ADVANCED INDUSTRIAL X-RAY COMPUTED TOMOGRAPHY FOR DEFECT DETECTION AND CHARACTERISATION OF COMPOSITE STRUCTURES

A thesis submitted to The University of Manchester for the degree of Doctor of Engineering
in the Faculty of Engineering and Physical Sciences.

2010

MATHEW AMOS

SCHOOL OF MATERIALS

Contents

Abbreviations

ART	Algebraic Reconstruction Technique
BPF	Back Projection Filtration
CCD	Charge Coupled Device
CFRP	Carbon Fibre Reinforced Plastic
CR	Computed Radiography
CT	Computer Tomography
DDA	Digital Detector Array
ESF	Edge Spread Function
FBP	Filtered Back Projection
FDK	Feldkamp Davis Kress
FOV	Field of View
FRP	Fibre Reinforced Plastic
FST	Fourier Slice Theorem
FWHM	Full Width Half Maximum
HE	High Energy
HVAC	Heating Ventilation Air-Conditioning
IQI	Image Quality Indicator
GFRP	Glass Fibre Reinforced Plastic
LE	Low Energy
MART	Multiplicative Algebraic Reconstruction Technique
MTF	Modulation Transfer Function
NDT	Non Destructive Testing
PSF	Point Spread Function
ROI	Region of Interest
SART	Simultaneous Algebraic Reconstruction Technique
SIRT	Simultaneous Iterative Reconstruction Technique
SNR	Signal to Noise Ratio
TFT	Thin Film Transistor
TOFD	Time of Flight Diffraction
UT	Ultrasonic Testing
WTB	Wind Turbine Blade

Abstract

X-ray Computer Tomography (CT) is well suited to the inspection of Fibre-Reinforced-Plastic (FRP) composite materials. However, a range of limitations currently restrict its uptake. The aim of the present research was to develop advanced inspection procedures that overcome these limitations and increase the scope of composite structures that can be inspected by industrial cone beam CT. Region of Interest (ROI) CT inspection of FRP laminated panels was investigated and two data completion methods developed to overcome reconstruction errors caused by truncated projection data. These allow accurate, highly magnified regions to be reconstructed on objects that extend beyond the Field-of-View (FOV) of the detector. The first method extended the truncated projection data using a cosine signal tailing off to zero attenuation. This method removed the strong 'glowing' artefacts but an inherent error existed across the reconstructed ROI. This did not affect the defect detectability of the inspection but was viewed as problematic for applications requiring accurate density measurements. The second method used prior knowledge of the test object so that a model could be created to estimate the missing data. This technique removed errors associated with ROI reconstruction thus significantly improving the accuracy. Techniques for extending the FOV were developed and applied to the inspection of FRP wind turbine blades; over 1.5X larger than the conventional scanning FOV. Two data completion methods were developed requiring an asymmetrically positioned detector. The first was based on the cosine tailing technique and the second used fan beam ray redundancy properties to estimate the missing data. Both produced accurate reconstructions for the 'offset' projection data, demonstrating that it was possible to approximately double the FOV. The cosine tailing method was found to be the more reliable. A dual energy image CT technique was developed to extend the optimum dynamic range and improve defect detectability for multi-density objects. This was applied to FRP composite/Titanium lap joints showing improved detectability of both volumetric and planar defects within the low density FRP. The dual energy procedure was validated using statistical performance measures on a specially fabricated multi-density phantom. The results showed a significant improvement in the detail SNR when compared to conventional CT scans.

Declaration

No portion of the work referred to in the thesis has been submitted in support of an application for another degree or qualification of this or any other university or other institute of learning

Copyright Statement

Acknowledgements

I would like to extend my eternal gratitude to all those who have helped in the project, at both the University of Manchester and TWI Ltd. The work could not have been completed without the help and support of the project supervisors Professor Philip Withers, Steve Kenny and Daniel Mitchard, as well as many other colleagues too numerous to mention here. Their technical support and insightful discussions during the project made this research possible. Andrew Ramsey and Sam Hawker of Metris X-tek Ltd are also acknowledged for their technical assistance in all aspects of tomography.

For the project funding, thanks and recognition must also be apportioned to The Engineering and Physical Sciences Research Board (EPSRC) and TWI Ltd.

And finally, I am forever in debt to my family and my partner Gemma for all their support and encouragement.

Chapter 1

Introduction

This introductory chapter will provide a brief description of the background to this thesis, including the basic concepts of X-ray Computer Tomography (CT) and its present limitations. The aim of the research and the organisation of the thesis are also described here to help guide the reader.

1.1 Motivation for Research

Fibre Reinforced Plastic (FRP) composites have gained increasing popularity in the engineering field due to their very high specific strength and stiffness properties, versatility, and resistance to corrosion. The application of these composite materials varies from sporting goods to areas of high technology in the power generation and chemical industries. In the aerospace industry one of the primary reasons for their extensive use is their benefits in fuel efficiency and to help satisfy environmental targets. However, FRP composites are quite susceptible to various types of defects and, like any other material, these defects can compromise the ability of the structure to perform its basic function. Common failure modes within FRP composites include, matrix cracking, delamination, and fibre breakage (Richardson and Wisheart 1996).

Defects in composites may be due to several factors including improper design, fabrication and manufacturing, and service induced damage. For laminated FRP composite materials, some defects are a major concern as they can evolve into a significant level of damage during the service life of a structure (Howard 2007). Delaminations are the most notable of these defects since they can significantly reduce the load carrying capacity of the laminate. Unlike metallic structures which are homogenous and have the ability to dissipate energy through yielding, composite structures exhibit weak interfacial strength between lamina. As a consequence they do not transfer interlaminar shear stresses and, under compressive loads, they can cause rapid and catastrophic buckling failure (ASNT 1991 as cited in Hasiotis *et al* 2007; Hayman 2007). Barely-Visible-Impact-Damage (BVID) is an area of extensive research due to the significant amount of delamination that can be caused by a low velocity impact. The major problem with BVID is that the defects arising from the impact may not be immediately apparent but can develop when load is applied and seriously compromise the

performance of the structure. The schematic diagrams provided in Figure 1.1 highlight the structure and propagation of some of the major defect types associated with low velocity impact of laminated FRP composites. It is widely acknowledged that during low-velocity impacts, damage is initiated by matrix cracks and fibre failures, which create delaminations at interfaces between plies with different fibre orientations (Abrate 1998). This initiates a pattern of damage propagation from either the top down (pine tree effect) or the bottom up (reverse pine tree).

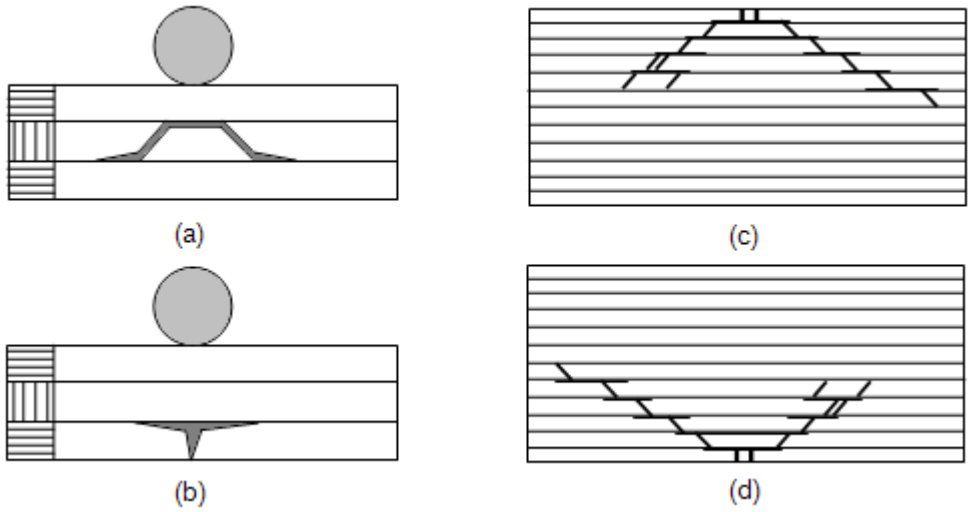

Figure 1.1: Schematic illustration of impact damage in FRP laminates. Two types of matrix cracks: a) shear crack, b) tensile crack and damage propagation patterns (c) pine tree affect, (d) reverse pine tree effect (Abrate 1998).

For these reasons, composite structures must undergo routine inspections and maintenance to ensure performance standards are met, thus extending the operational lifespan and maintaining a high level of safety. These inspections extend from design and manufacture optimisation through to in-service maintenance. Yet still, there is much concern over the capability to detect and characterise critical defects within FRP composites. With repeated occurrences of the aforementioned damage types and with ever more complex shapes being designed, there is an increasing call for new inspection techniques to be developed (Wong n.d.; Rao 2007).

For the manufacturers and users of these critical composite components it is not sufficient merely to identify the defects. One of the main challenges lies in determining the cause of the defect, its location, severity and impact on the performance of the structure as a whole. From this perspective, a Non-Destructive Testing (NDT) technique that can

accurately characterise a large range of defects is imperative to help relate the inspection results with analytical models and mechanical testing to gain information on structural reliability.

It is a well known fact that defect detection and characterisation in FRP composites is extremely challenging and presents more difficulty than metallic structures due to the mechanical anisotropy and heterogeneous composition (Howard 2007). Various NDT methods have been proposed to identify defects that can develop during manufacture, forming, installation, and/or in service. However, extensive research has shown that current NDT techniques have many limitations and defect assessment requires multiple techniques to gain the information required (Rao 2007).

Four commonly used methods are Ultrasonic Testing, Shearography, Thermography and Radiography. Ultrasonic Testing (UT) is the most established of these methods due to its ease of implementation and ability to detect planar defects. It is also more sensitive than Shearography and has advantages over Thermography as this technique can only reliably detect defects within a couple of millimetres of the surface (Rao 2007). However, UT struggles with complex shapes and the inspection is limited in penetration depth and contrast due to high attenuation and scattering in FRP composites. The use of a lower probe frequency can overcome some of these limitations but will reduce the resolution and detail detectability to the millimetre range (Hasiotis *et al* 2007; Rao 2007). On the other hand Radiography has high resolution and contrast sensitivity (typically 1-2% of the material thickness), excellent penetration and is directly related to detecting volumetric defects (Rao 2007). However, defect characterisation is extremely difficult as any defects present within the object are superimposed on a two-dimensional (2D) image without any indication of the flaw depth. This is because the object is placed perpendicular to the X-ray beam, thus making the detection of planar defects, such as delaminations and matrix cracks, near impossible.

CT inspection has shown to suit the inspection of composite materials and the defects that can be formed (Muralidhar and George 1999; Choudhry and Li 2008). It has all the benefits of conventional radiographic inspection but overcomes a major limitation by producing cross sectional images of the internal structure. This allows a detailed defect assessment to take place without the superimposition of features. Additionally, the CT inspection process requires that a full 360° of X-ray data is acquired to allow reconstruction of the 3D image. This means that previously undetected planar defects such as delaminations are now detectable due to the X-ray beam being correctly

orientated to them. However, due to inherent limitations with the technique, the only way to allow CT inspection of the majority of composite structures is to tailor the object to suit the CT inspection parameters. This can usually involve sectioning to remove undesirable parts, which is not an option for most non-destructive assessments.

1.2 Aims and Objectives

CT has the potential to be a very effective NDT technique for defect detection and characterisation in FRP composite materials. However the current commercially available industrial systems have inherent limitations that are not suited for the inspection of many composite structures. The aim of this research is to overcome many of these limitations and increase the scope of composite structures that can be accurately inspected using CT. Specific objectives of the research were as follows:

- To review the current state of the art of CT in both the medical and industrial field for overcoming the truncated data problem.
- To develop data completion methods for high resolution Region-Of-Interest (ROI) CT inspection of FRP laminated panels.
- To implement a method that extends the CT scan Field-Of-View (FOV) for the inspection of full width FRP Wind Turbine Blades.
- To develop a procedure capable of effectively increasing the optimum dynamic range of the CT inspection for FRP composite/Titanium Comeld^{TM} lap joints.

1.3 X-ray Computer Tomography

The research presented in this thesis will primarily focus on the development of advanced CT procedures for the inspection of FRP composite structures. CT is a powerful imaging technique that uses specialised reconstruction algorithms to produce cross-sectional and 3D volume images of an object from 2D X-ray projections. Characteristics of the internal structure of an object, such as dimensions, shape, internal defects, and density, are readily available from CT images.

1.3.1 Commercial Applications of X-ray Computed Tomography

In the medical field, CT has been used extensively for diagnostic imaging since the first CT scanner was implemented in 1972. More recently, CT has been developed for applications ranging from reverse engineering to palaeontology. The CT system

specifications vary greatly depending on the specimen being imaged. For instance medical CT and materials analysis work can require very low energy (<30keV[1]) and very high spatial resolution (sub-micron range). Whereas the other end of the scale you can find research institutions requiring LINAC[2] based CT systems using energies in the MeV range for inspection of industrial waste drums. Below is a brief review of the commercial CT applications:

1. Medical Diagnostic Imaging: The medical field is where CT scans or Computer-Axial-Tomography (CAT) scans were first implemented. CT imaging is capable of detecting very small density differences and is used to detect internal anomalies within the human body (Kalender 2006).
2. NDT inspection: As with X-rays, CT provides internal information of the object under inspection. It can be used for defect detection, sizing, damage characterisation, quality control and design process optimisation (Paul and Zhenhui 2008).
3. Density Analysis: Reconstructed CT images are displayed in grey levels that directly correspond to the density within the material. This allows a specific density range to be selected within the object and functions such as segregation to be performed (Ketcham and Carlson 2001). Such applications include airport baggage control and geological investigations.
4. Reverse Engineering and Metrology: CT is able to provide accurate external and internal measurements. This allows surface models to be exported and used in Computer-Aided-Design (CAD) packages for Reverse Engineering and Rapid Prototyping (Flisch *et al* 1999).
5. Biology and Palaeontology: The aforementioned benefits of CT can also be used to provide detailed internal information on biological specimens, bones, and fossils (Rowe *et al* 2003).

1.3.2 Current Limitations of Industrial X-ray Computed Tomography

CT inspection for industrial NDT is regarded as fairly new and is still establishing itself as a recognised inspection method. Its primary use is still considered to be in medicine and

[1] The electron volt (eV = 1.60217653 × 10^{-19} joules) is a unit of energy. In this context it refers to the maximum photon energy within the X-ray photon spectrum. Higher photon energy results in the penetrating power of the X-rays increasing.
[2] A Linear particle accelerator (LINAC) vastly increases the velocity of electrons allowing higher energy X-ray photons to be produced.

therefore the majority of research developments that try to overcome the current limitations lie within that field. The problem is that most of these recent innovations are based on specialised configurations, such as helical CT, which use very different scan geometries and algorithms than those commonly applied in the NDT industry. Therefore one of the major challenges facing industry is to use the knowledge gained from the medical field to develop methods that can be implemented with industrial systems. In terms of NDT, the significant limitations associated with CT inspection are listed below. These limitations are highly documented (Sivers 1995; Simon *et al* 2004; Wang and Yu 2008) and have restricted its uptake in many industrial applications. It should be noted that some of these are inherent to the technique itself and therefore apply to both medical and industrial applications.

1. Industrial CT suffers from a lack of standards[3] and guidelines on inspection optimisation and performance measurement. This drawback is potentially the main obstacle for industrial acceptance of CT as an established NDT technique.
2. The X-rays must sufficiently penetrate the object under inspection, limiting the inspection of highly attenuating objects to the maximum energy supplied by the system source.
3. A similarly related constraint (to the point above), is the limited effective dynamic range[4] of the commercially available detectors. This can result in reduced image quality due to artefacts from under-penetration and increased image noise from over-exposure. This is particularly the case for multi-density components or objects with regions of largely varying thicknesses.
4. The size of the object that can be inspected is limited to that which can fit in the detectors FOV. If the object function is transversely truncated in any view this will lead to a ringing or truncation artefact (described later in section 2.1.6.5). This is visualised as a glowing effect propagating from the point of truncation, masking important detail and inflating pixel values throughout the reconstructed image.
5. It is currently not feasible for use as an on-site inspection tool. Mainly due to issues with system portability, long exposure times resulting in a radiation hazard and the need for access to all sides of the object under inspection.

[3] The European Committee for Standardisation (CEN) is currently working on a set of NDT - Computed Tomography standards (EN – 16016 Parts 1-4). In February 2010 these were still at the draft stage of development.

[4] The effective dynamic range is the ratio of the maximum signal (provided by the X-ray exposure) that the X-ray detector can accommodate, to the minimum acceptable signal (surpassing the noise level) for reliable detection (Yaffe and Rowlands 1997).

1.4 Organisation of Thesis

The chapters presented in this thesis follow the research path from understanding the existing CT inspection parameters to developing advanced inspection procedures for difficult composite structures.

Following this introductory chapter, Chapter 2 covers the fundamentals of both Radiography and CT to introduce some key topics and theory to aid in the explanation of the research. A review of literature on the current state of the art in the field of CT is presented with a specific emphasis on the aspects related to the present research. An overview of some alternative NDT techniques and their application to FRP composites is also provided to support comparative studies described later in the thesis.

Chapters 3 and 4 both focus on overcoming the truncated data problem that is an inherent limitation for industrial CT systems using the standard circular cone beam geometry and FBP type reconstruction algorithm. ROI CT is the first area of the truncation problem addressed and this is presented in Chapter 3. Here, the data completion methods developed to suppress the truncation errors associated with ROI CT inspection of FRP laminates are described in full. In Chapter 4 the 'Offset CT' method for cone beam geometry is presented that overcomes a different side to the truncated data problem. This method extends the CT scan FOV allowing the reconstruction of FRP wind turbine blades that are considerably larger than the FOV of the detector.

The dual energy procedure developed to increase the effective dynamic range of the CT inspection is presented in Chapter 5. This includes the validation and application of this technique to multi density FRP composite/Titanium Comeld^{TM} joints.

The conclusions of the research are then discussed in Chapter 6, before recommending further work resulting from the research.

Chapter 2

Literature Review

In the following chapter, background theory identifying the fundamentals of X-ray interaction and the simplified assumptions used in CT reconstruction will be presented. Common reconstruction artefacts associated with CT and important image quality measurements used for performance analysis will be described. Recent innovations in the field of CT will be discussed concentrating on specific areas to which contributions have been made within this thesis. The Chapter will also provide a brief overview of alternative NDT techniques and their application to FRP composite inspection.

2.1 Non-Destructive-Testing

NDT is an evaluation tool that allows parts and materials to be inspected internally without damaging them. It plays a critical role in ensuring structural integrity of components and systems in all stages of the product life cycle, from design and manufacturing to in-service. For most applications it is no longer sufficient to simply detect any defects present. NDT techniques are now required to determine the characteristics of a defect such as its size, shape and orientation. This level of characterisation helps relate experimental data to fracture mechanics and analytical models so that critical defect sizes and damage modes can be determined.

The primary NDT techniques used in industry are considered to be Ultrasonic Testing, Radiography, Eddy Currents, Dye Penetrant and Magnetic Particle Inspection (MPI). These techniques are fully established, with industry recognised standards in place for inspection and training on a wide range of applications. However, modern components are often a challenge for NDT as they consist of new materials with more complex shapes. In response to these requirements the conventional techniques are being constantly updated and new advanced NDT techniques are now commercially available such as CT, Shearography, Thermography, and Phased Array Ultrasonics.

The experimental work presented in this thesis required feasibility studies and validation procedures to be undertaken that involved the use of other NDT techniques. These techniques are recognised inspection tools and were identified as the most suitable for

defect detection and characterisation in FRP composites inspection (see section 1.1). Specifically, Radiography, Ultrasonic Testing, and Thermography were short listed for their detection capabilities. An overview of these techniques and their capabilities with respect to FRP composites inspection is included in this chapter.

2.1.1 Radiography

This section will discuss the fundamentals of X-ray imaging including the different radiographic modalities and their application to FRP composites inspection. The different imaging modalities can be classified by their detection media which covers conventional film radiography, Computed Radiography (CR) using phosphor plates and digital radiography using Digital Detector Arrays (DDAs).

2.1.1.1 X-ray Physics

X-rays are a form of electromagnetic radiation and are generated by illuminating the target area of a positively charged anode with high speed electrons. The electrons are produced by heating the negatively charged cathode and are then accelerated through the tube towards the anode target area by a high potential difference. The resultant collision takes the form of several different processes to create a broad spectrum of X-ray energies. This spectrum consists of a polychromatic X-ray beam known as Bremsstrahlung radiation and mono-energetic peaks known as characteristic radiation (see Figure 2.1).

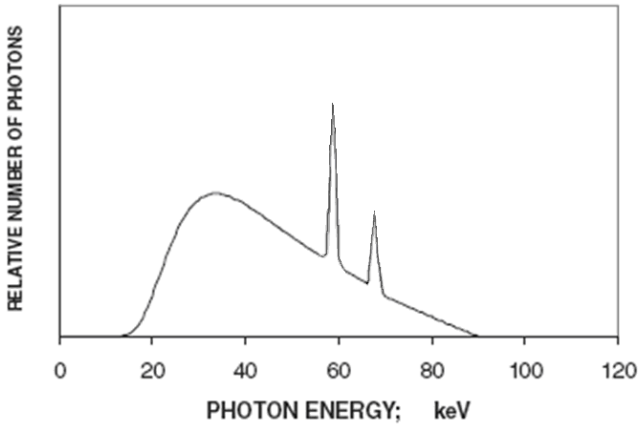

Figure 2.1: Typical X-ray Spectrum (tungsten).

All radiographic inspection techniques are based on effectively detecting the attenuation of X-ray photons[1] as they interact with the material under inspection. A fundamental property being that the measured linear attenuation coefficient is proportional to the

[1] The individual quantum of electromagnetic radiation is known as the photon and is symbolised by the Greek letter gamma.

material density. However, it is important to note that the linear attenuation coefficient carries a photon energy dependence that is a function of material composition. A simplified assumption used for X-ray attenuation is the Beer-Lambert law, which acts as the basis for all tomographic reconstruction:

$$I = I_0 \, exp(-\mu L) \tag{2.1}$$

For X-rays transmitted through an object the intensity I_0 is attenuated depending on the material linear attenuation coefficient μ and its thickness L.

The attenuation of X-rays as they interact with matter has been researched extensively (Evans 1955; Mackovski 1983; Beutel *et al* 2000) and is the result of several different interaction mechanisms. The majority of radiographic systems have a maximum X-ray energy <500 keV. For these systems the interactions are mainly limited to just two interactions known as photoelectric absorption and Compton scattering.

2.1.1.2 X-Ray Detectors

An X-ray detector is used to measure the attenuation of the emitted X-rays along the different ray paths. There are several types of X-ray detector technologies and these are used to classify the different radiographic modalities. Specifically, these are conventional film radiography, phosphor imaging plates and DDAs.

1. Conventional Film

Radiographic films consist of a silver halide emulsion that has been applied to an optically transparent substrate. The basic principle of radiographic film is the photochemical effect X and gamma rays have on the silver halide crystals contained in the emulsion. Specifically, when exposed to radiation some of the bromide ions are liberated and captured by the silver ions, creating a latent (hidden) image. A chemical solution is used to develop this image by making the exposed grains more sensitive to the reduction process. This changes the latent image into black metallic silver which can be visualised in the emulsion once a fixative has been applied to make the image of silver permanent. A light box is normally used to view the two-dimensional image present on the developed film.

Conventional film radiography is a well established technique with many standardised inspection procedures in place. The main benefits of this technique are its wide range of applications and the very high spatial resolutions (25µm) that can be achieved due to the small grain size of the film. The limitations of the technique are mainly poor film latitude,

long exposure (and processing) times, the use of hazardous chemicals and the inherent superimposition associated with 2D images of 3D objects.

2. Phosphor Imaging Plates (Computed Radiography)

Computed Radiography (CR) can be viewed as an alternative technology from digital and film radiography. Similar to the silver halide layer used in film radiography, a photosensitive phosphor plate is used to detect incident radiation. Here, the X-rays or gamma rays liberate electrons in the phosphor material which are subsequently captured in quantum wells creating a latent image. A laser is used to liberate these captured electrons to a higher energy state so when they fall back to their ground state, light is emitted. This light is then converted into a digital image using a photo multiplier tube. An example of a CR scanner system and a phosphor imaging plate is shown in Figure 2.2.

CR, like film radiography, is a well established technique that is used widely in the medical field. The benefits of phosphor plates compared to film inspection are mainly the improvement in dynamic range and the reduction in exposure times. Additionally, phosphor plates are re-usable and require no chemical processing, resulting in reduced cost of consumables. However, compared to digital radiography using DDAs, CR is slower and the dynamic range of the phosphor plates is not as high as some digital detectors.

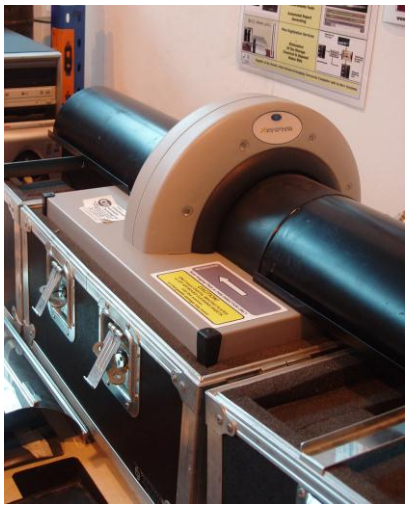
(a)

(b)

Figure 2.2: (a) CR scanner system (b) a phosphor imaging plate.

3. Digital Detector Arrays

There are several types of DDA technologies. The two types most commonly used for X-ray imaging and CT are Charge Coupled Device (CCD) detectors and Thin Film Transistor (TFT) based systems. Both are based on the conversion of absorbed X-ray energy into a corresponding electric charge.

A number of different detectors exist that are based on CCDs, in particular, linear arrays and optically coupled 2D cameras. A CCD linear array detector is generally composed of a 1D array of photodiodes mounted on CCDs and covered with a scintillation screen[2]. The Linear array is aligned to the X-ray beam and as the object is scanned the X-ray photons hit the scintillation screen, converting the photons to visible light (via luminescence). This causes the photodiodes to generate an electric charge (via the photoelectric effect) based on the X-ray intensity at that location. This charge is accumulated in the CCD and digitised into an output signal, thus capturing a single slice of the object. Camera based CCD systems use the same concept as linear arrays except they require some kind of optical coupling, such as an image intensifier. This reduces the size of the visible light image onto the CCD chip, which is physically very small. Compared to the linear array detectors, camera based systems are able to acquire the entire 2D projection of the object without the need to build up the projection slice by slice. In terms of CT scanning this means that the projection data can be acquired far quicker for the camera based systems greatly improving the inspection time. However, this type of system substantially reduces the number of photons that reach the CCD, causing an increase in image noise which degrades image quality. Additionally, the optical coupling can introduce geometric distortions and optical scatter (Chotas 1999).

The second group of DDAs are TFT based systems which consist of either 2D flat panels or 1D linear arrays. For TFT based systems there exists two main categories; indirect and direct. Direct conversion detectors have an X-ray photoconductor, such as amorphous Selenium that directly converts X-ray photons into an electric charge. Indirect conversion uses a two step process, whereby a scintillator is used to convert an incident X-ray photon into visible light (as with CCD based detectors). This light is then converted into an electric charge by means of photodetectors such as amorphous Silicon (Chotas 1999). Both indirect and direct systems are constructed with an active matrix consisting of a TFT for image readout. This allows the electric charge to be converted into a digital signal to produce a digital image. The digital image is visualised as an array of pixels each with an assigned grey value relating to the X-ray intensity found at that location of the detector array. The TFT based detectors are effective in producing images of very high quality and do not suffer from the same limitations as CCD based systems such as geometric distortion and increased image noise. However, the CCD based systems have faster

[2] A scintillation screen is a layer of material which exhibits the property of luminescence when excited by ionising radiation such as X-rays. These materials absorb the energy from the X-ray photon and re-emit the absorbed energy in the form of visible light.

readout time, resulting in real time radiography and are less prone to over exposed radiation damage (Elbakri 2003).

A third type of X-ray detector that uses inert gas can be found in some medical applications. An example of such a detector is the Xenon gas ionisation chamber. This type of detector records the electric charge which results from the ionisation of atoms.

2.1.1.3 Application to Fibre-Reinforced-Plastic Composites

Due to its high penetrating power, radiography can usually inspect the full thickness of most composite structures. It is considered ideal for the detection of non-planar, volumetric defects such as voids, porosity and solid inclusions. It is also useful in detecting changes in material composition or thickness and for locating unwanted or defective components hidden in the assembled parts.

The main limitations of radiographic inspection are that access to both sides of the specimen are required and that any defects or damage present within the specimen will be superimposed on a 2D projection. Meaning it is nearly impossible to determine the depths of any defects. In addition, voids and cracks can only be detected if they are of appreciable size in relation to the specimen thickness. This is typically a thickness change of 1-2%.of the total through thickness (Stone and Clarke 1975). Therefore, planar defects such as delaminations are almost impossible to detect unless another dimension is added to the inspection. This means the X-ray beam must be angled in the correct orientation to produce the required density difference. Figure 2.3 shows a radiograph of a CFRP laminate taken in the correct orientation to detect any delaminations present.

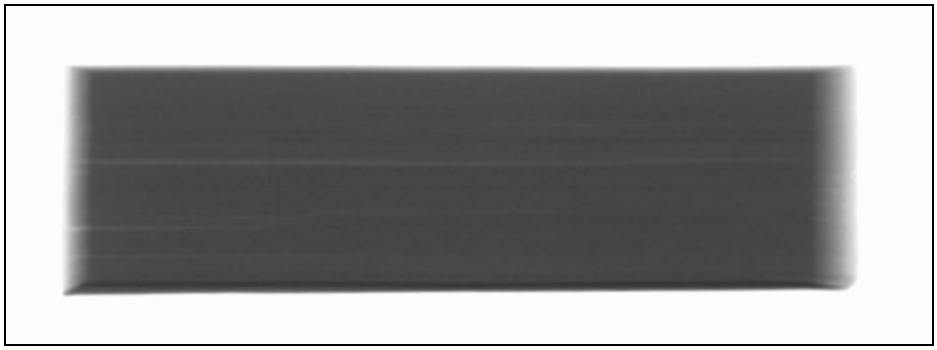

Figure 2.3: Radiograph of an impact damaged CFRP laminate. The X-ray beam was angled in the correct orientation to detect the delaminations. The sample dimensions were approximately 50x50mm with a through thickness measurement of 15mm.

2.1.2 Ultrasonic Testing

Ultrasonic Testing (UT) is an NDT technique that uses mechanical stress waves (at frequencies above 20 kHz) for a range of inspection applications. These include; defect detection, materials characterisation and thickness measurements. Figure 2.4 shows a typical UT setup consisting of a pulser/receiver unit, transducer and display unit. An electrical signal is sent from the pulse unit to a transducer. The transducer converts the electrical signal to a mechanical wave using a piezoelectric element. Providing there is sufficient coupling between the transducer and the test object surface, energy will be transferred to the test object in the form of mechanical stress waves. When a defect is encountered the propagating wave will be partially reflected back to the source, detected by the transducer and transformed into an electrical signal. This is interpreted by the receiver unit and displayed on an oscilloscope. Information including defect size, shape and position can then be obtained.

Ultrasonic systems send and receive signals in one of two ways. The first method is known as Pulse-Echo and only requires access to one side of the test surface, as the sending transducer is also designed to receive the reflected signal. In this instance, the oscilloscope normally shows the original pulse of the ultrasonic transducer (front surface echo) and the back reflection. So any extra indication can normally be interpreted as a reflection from a defect in the material, as illustrated in Figure 2.4. As the speed of the ultrasound through the material is known, the oscilloscope timing can easily be used to determine the depth of the defect below the surface. By contrast, Through-Transmission systems require access to apposing sides of the test object. A sending transducer generates the signal at one surface of the structure, while a receiving transducer on the back surface of the structure detects the signal after it has travelled through the material. In both cases, the received signal varies in amplitude, depending on what in-homogeneities or defects it encounters within the specimen.

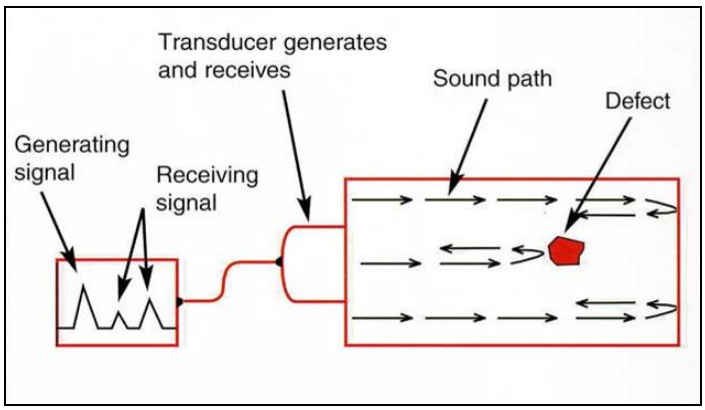

Figure 2.4: Illustration of ultrasound principle using a pulse-echo system.

UT results are presented in either A, B or C-scan mode. An A-scan shows signal amplitude against time (or distance) in the form of a graph. An example of an A-scan is shown in Figure 2.5. This is used to show information describing a one-dimensional scan of the test object. B-scan imaging shows a cross section of the test material and the location of any 'indications' within that section. Figure 2.6 shows an example of a B-scan where delaminations present in the impact damaged CFRP sample are causing obvious planar indications. The propagation of the delaminations from the impact site in the CFRP laminate is consistent with the pine tree pattern described earlier (section 1.1). C-scan presentation is also provided in Figure 2.6 showing a plan-type view of the CFRP sample, highlighting the location and size of any indications within that area. Depending on the mode of operation selected, the colour coding levels or grey levels on the image may represent relative signal amplitude or time-of-flight. In this instance, the grey scale C-scan shown in Figure 2.6 indicates relative signal amplitude so the light regions indicate a stronger reflection.

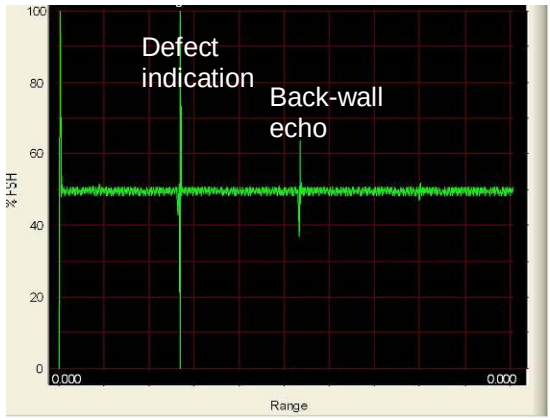

Figure 2.5: A typical A-scan obtained with a pulse echo UT test setup.

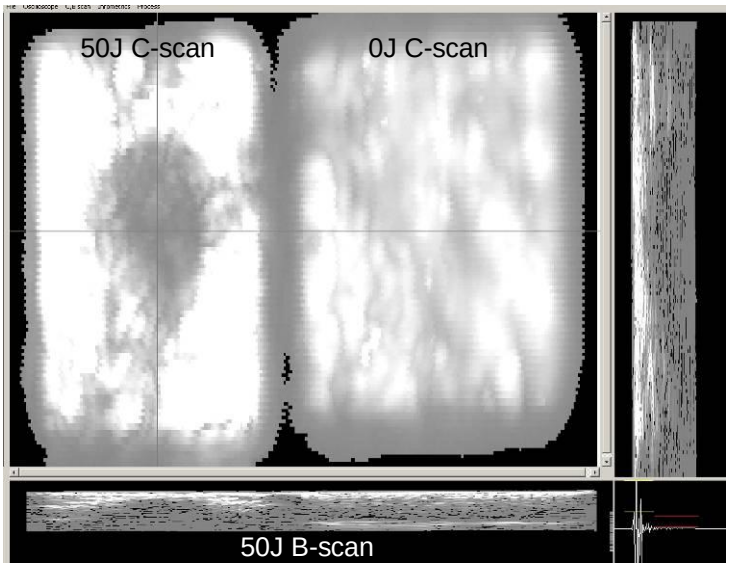

Figure 2.6: C-scan inspection of a CFRP laminate sample with and without impact damage. 50J impact on the left and without impact on the right. B-scan images at the sides show a cross-section of the 50J impacted sample. The sample dimensions were approximately 50x50mm with a through thickness measurement of 15mm.

2.1.2.1 Ultrasonic Inspection Methods

UT is one of the most commonly used inspection methods in NDT and as such a vast amount of research and development has taken place. This has resulted in a wide range of available UT techniques.

Immersion testing is a UT technique that uses pulse echo methods to transfer energy from the transducers to a test object. It differs from conventional pulse echo in that the test object is submerged in a couplant. This allows the transducers to operate remotely so there is no abrasion due to surface contact and there is always an even distribution of couplant. Water is commonly used as the coupling fluid because of its availability and low cost. However, water has a high attenuation coefficient which causes the inspection results to have a low SNR. Additional care also needs to be taken to ensure a constant temperature and pressure is maintained throughout inspection as both these factors will alter the wave velocity. An example of an immersion system is shown in Figure 2.7.

Figure 2.7: Immersion UT system with a 5-axis manipulator.

Scanning acoustic microscopy is also an immersion based testing technique that uses very high frequency ultrasound (up to 100MHz). The use of such high frequencies results in a highly focused inspection (high resolution) that offers improved detail detectability. The trade-off is penetration depth, as only features just below the surface can be inspected (typically less than 3mm). Typical results are displayed in Figure 2.8 for a set of impacted CFRP samples. These results were obtained using a high frequency 15MHz probe and are displayed as a C-scan grey scale image. The high frequency scan was able to detect delaminations, fibre breakage, fibre orientation and the impact site. The images also provided evidence of the delamination pattern of propagation found in literature for impact damaged CFRP laminates (Abrate 1998). Specifically, the delaminations are expected to be oblong shaped, stretched in the direction of the fibre orientation, as illustrated in Figure 2.8.

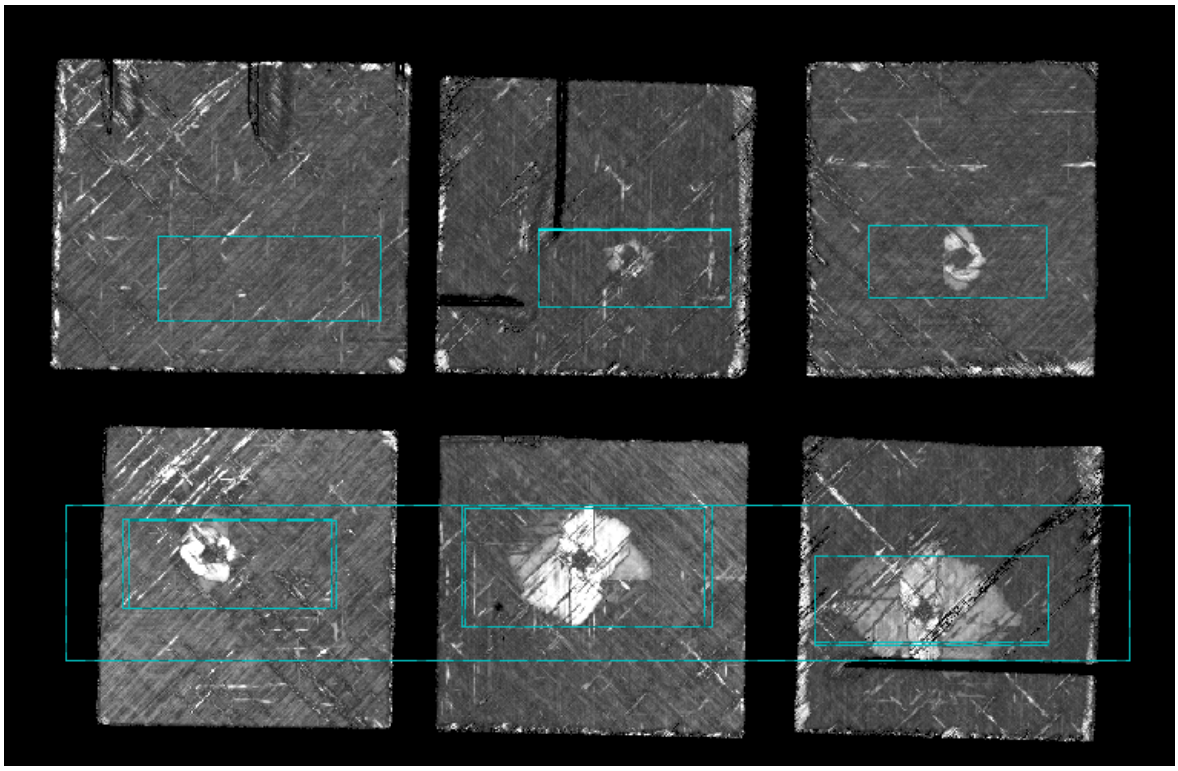

Figure 2.8: C-scan image of a set of impacted CFRP samples using a scanning acoustic microscope with a 15MHz probe. Top row shows 0J, 9J, 16J impacts (from left to right) and bottom row shows 30J, 50J, 64J impacts. The sample dimensions were approximately 50x50mm with a through thickness measurement of 15mm.

Time of flight diffraction (TOFD) is a commonly used technique for on-site inspection Figure 2.9(a) illustrates the principle of this technique. A wide beam signal is transmitted through the test object so a second transducer situated on the same face as the source will receive the reflected signal. The first signal to arrive is the lateral wave travelling along the material's surface. The second set of signals received will be from the 'tips' of any flaws present (top and bottom) and then finally a signal is received from the back wall. The time-of-flight of the lateral and back-wall echo signals serve to calibrate the speed of ultrasound in the material. The time of flight of the upper and lower flaw tip signals enable the positions of these tips, and hence the position and through wall height of the flaw, to be accurately determined. The advantages of TOFD over pulse echo UT is the accuracy of flaw sizing plus the fact that it is relatively tolerant to flaw orientation. Typical results are given in Figure 2.9(b), here the TOFD results have been displayed in C-scan mode with the colour coding representing the depths (time of flight) of the planar reflections (delaminations) within a set of impacted CFRP samples. The colour scale used here shows the green as representing a longer distance travelled by the signal, whereas the

orange represents a shorter travel distance. This shows that at increased impact levels (>16J) the signal is being almost entirely reflected by near surface delaminations.

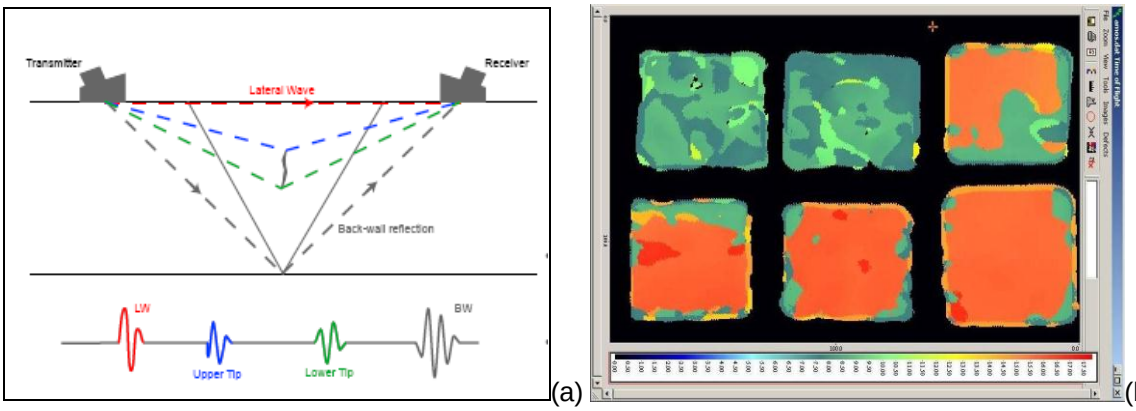

Figure 2.9: (a) The principle of time-of-flight diffraction (TOFD) and (b) typical results in C-scan display showing a 2MHz TOFD inspection of six impact damaged CFRP samples. Top row shows 0J, 9J, 16J impacts (from left to right) and bottom row shows 30J, 50J, 64J impacts. The sample dimensions were approximately 50x50mm with a through thickness measurement of 15mm.

2.1.2.2 Application to Fibre-Reinforced-Plastic Composites

Ultrasonic techniques have proven to be excellent for detecting planar defects such as delaminations in FRP composite structures (Lloyd 1989; Rao 2007; Jasiūnienė *et al* 2009a). They are also capable of detecting other defects such as fibre/ply mis-orientation, low level porosity, cracks and ply waviness, within a depth of 0.3 - 3mm from the surface (Wong n.d). Diagnosing these defects with UT is possible but requires a high level of operator skill. The reason being that all defects, including volumetric ones, cause planar type reflections which need to be interrogated from different angles to deduce the approximate dimensions and orientation. The major benefits of UT include; superior depth of penetration compared to other techniques (such as thermography and shearography), inspection can be carried out with access to only one side of the test object and information such as defect depth and location are easily extrapolated.

The main limitations of the technique are that UT requires a coupling medium and struggles with complex shapes. In addition, the inspection is limited in penetration depth and contrast due to the high attenuation and scattering effect in FRP composites. To be more specific, use of high frequency probes will provide a focused inspection with detail detectability in the micron range but they can only penetrate a depth of a few millimetres in FRP composites. The low frequency probes can penetrate the thick composites but have a much lower sensitivity with detail detectability in the millimetre range (Hasiotis *et al*

2007; Rao 2007). This results in small defects going undetected. In industries where FRP composites and laminates are getting thicker this is a major limitation of UT and is therefore an ongoing research area. However, the physics of ultrasonic wave propagation in such anisotropic material requires understanding of complex phenomena such as beam skewing (i.e. steering effect), material focusing/defocusing and unsymmetrical beam profiles. This ultrasonic behaviour is considered relatively insignificant for thin anisotropic composites, but cannot be neglected in thick composites (Balasubramaniam and Whitney 1996).

2.1.3 Infrared Thermography

Thermography is an NDT technique that generally uses infrared cameras to monitor surface temperature changes of a test object. The presence of surface and near surface discontinuities will change the thermal response from the object. The most common thermographic technique is infrared thermography and can be used either passively or actively. The passive approach inspects materials at their natural temperatures, whereas active inspection requires external stimulants to produce thermal contrasts within the test object (as illustrated in Figure 2.10). With both passive and active infrared thermography, the basic premise is to monitor the way heat is transferred through the object under inspection. When heat is applied to the surface of the object the thermal energy will naturally travel into the cooler interior. This reduction in surface temperature will be uniform providing the material properties are consistent. Therefore surface and subsurface discontinuities will affect the surface cooling rate which can be detected using the infrared camera. For active infrared thermography, the thermal images are normally taken with the infrared camera at microsecond intervals to capture the heat dissipation during the application of the external stimulus i.e. the flash of a heat lamp. These images are then used to construct a reference temperature/time curve which permits the approximation of the penetration depth to aid in locating defects. Typical results of infrared thermography are displayed in Figure 2.11. The images are taken at increasing time intervals to show the delaminations present at different depths within the impacted CFRP sample (50J impact). The images showed the delaminations to be oblong and stretched in the direction of the fibre orientation. This pattern of delamination propagation is expected for impact damaged laminates (Abrate 1998). The thermographs in Figure 2.11 also show that at increased penetration the image resolution significantly decreases due to heat dissipation.

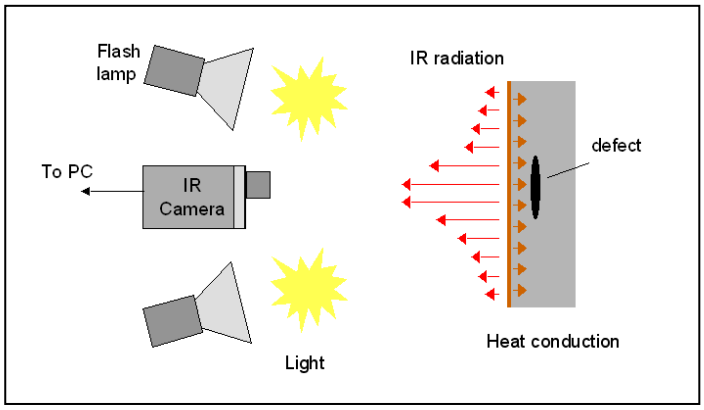

Figure 2.10: Illustration of infrared thermography using flash lamp as a pulsed stimulus.

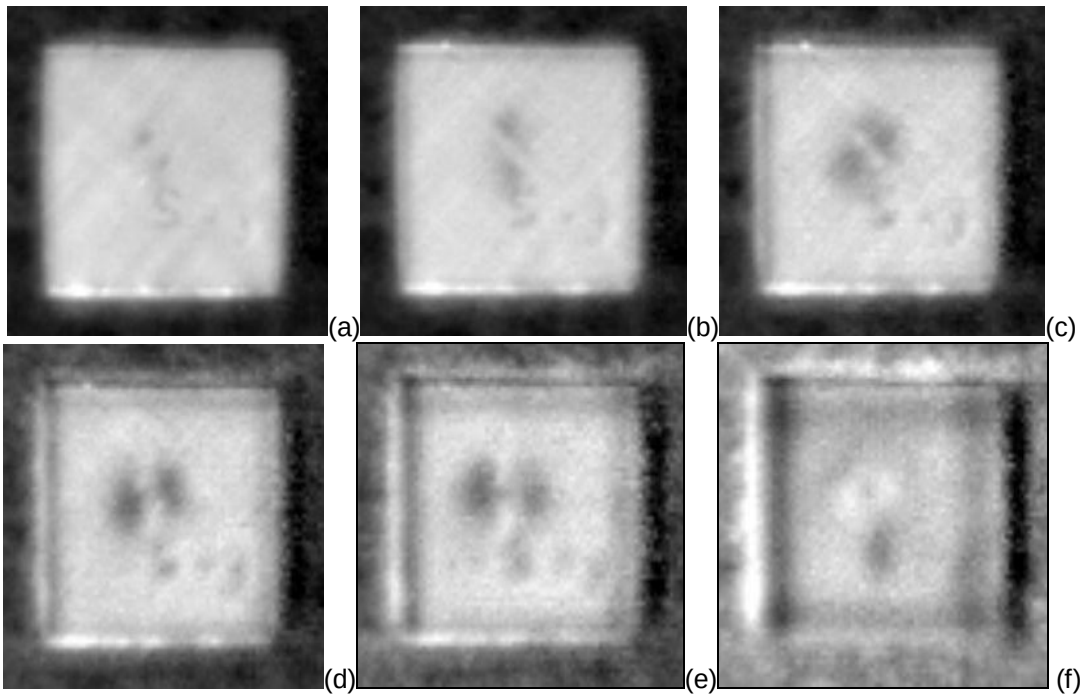

Figure 2.11: Infrared thermographic inspection of a impact damaged CFRP sample (50J impact). (a) to (f) showing increased time/penetration, starting with no time increase at (a).

2.1.3.1 Application to Fibre-Reinforced-Plastic Composites

Thermography requires no contact with the test object, it is very portable and the relatively fast data acquisition and easy interpretation makes it suitable for large area inspection. The method is useful for detecting near surface medium to large scale discontinuities (>6mm) (Dutta 2006) that have a significantly different conductivity compared to the base material. Such discontinuities include; delaminations, disbonds, moisture zones and voids. However, it is not able to provide accurate detail on the depth or size of these defects. In practise, to estimate the depth of any defects detected requires the contrast to be assessed against a reference temperature/time curve. This predicted depth is relative to the sample thickness and provides only qualitative data. In addition, this reference curve

can only be used if the sample heating is uniform, which is very difficult to achieve in large samples. This limitation also means that the change in thermal conductivity caused by smaller defects can not always be distinguished, limiting the detection capability to defects larger than 6mm (Dutta 2006). The defect detectability of IR thermography is considered to be largely qualitative and extensive operator skill is required for diagnosing defects and estimating their size. Another major limitation of thermography is that the resolution significantly decreases with increasing depth (as shown in Figure 2.11). This is due to heat dissipation and results in only surface and subsurface defects being reliably detected. For CFRP laminates this limitation is amplified as the conductivity in the laminate plane is about nine times that in the through-thickness direction (Stone 1987).

2.1.4 X-ray Computer Tomography

A full description of X-ray CT is provided in the following sections (section 2.2). In brief, X-ray CT is a radiographic based inspection technique that produces cross-sectional and 3D volumetric images of the linear attenuation coefficient of a scanned object. These attenuation coefficients directly relate to the material densities present within the object under inspection.

Figure 2.12 and Figure 2.13 show reconstructed CT slices taken from the impact damaged CFRP sample (50J impact). The cross sectional CT images highlight with great detail the damage propagation in the CFRP sample. Shear cracks, fibre breakage, and delaminations have all been detected. The pine tree affect can be identified in Figure 2.12 by the delaminations progressively spreading out and getting larger with increasing depth. These delaminations appear to be rotating as the slices progress through the thickness of the sample. This is again due to the oblong shape delaminations being stretched in the fibre lay-up direction. The pine tree effect is more pronounced in Figure 2.13 due to the axial direction of the cross sectional images. In these images the pine tree effect plus the intra-ply shear cracks that connect the delaminations (Abrate 1998) have been detected. The inspection results also found that in this sample (50J impact) there was a metal wire near the back wall which was not detected by any other NDT technique. This wire caused artefacts in the form of scatter due to the X-ray energy being too low to penetrate the denser material (Figure 2.13).

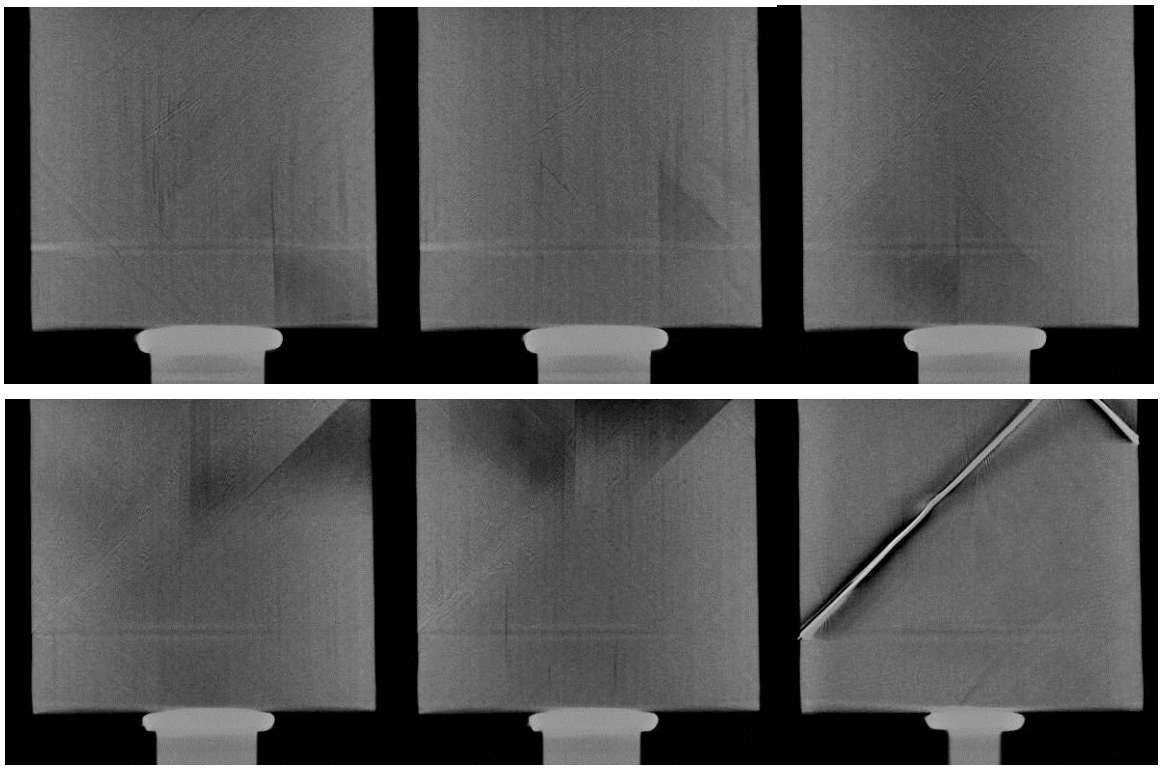

Figure 2.12: Cross-sectional CT slices in the frontal direction of an impact damage CFRP sample (50J). The sample dimensions were approximately 50x50mm with a through thickness measurement of 15mm.

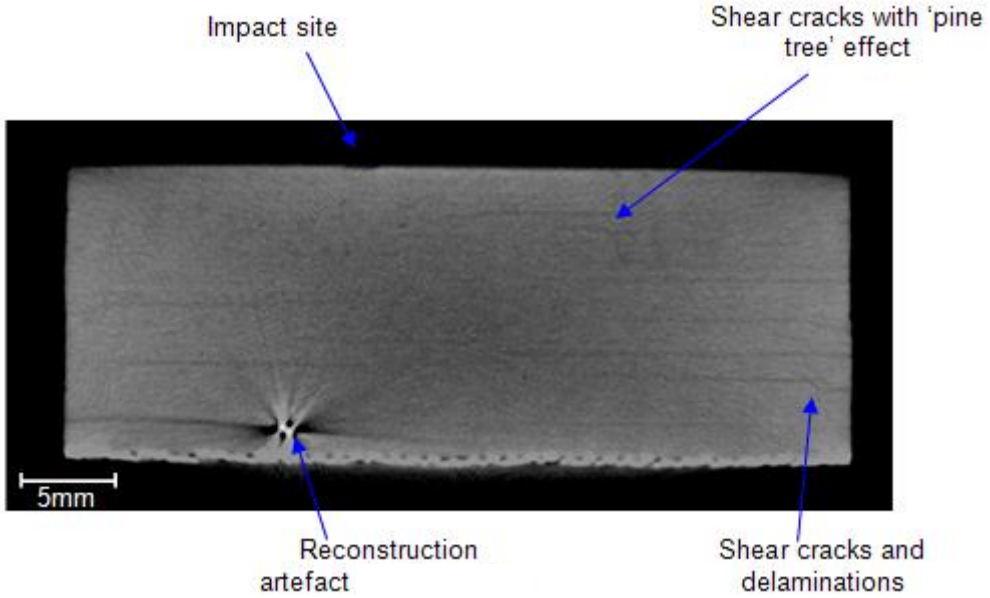

Figure 2.13: Axial cross sectional CT slice of an impact damaged CFRP sample, highlighting the range of defects detected. The sample dimensions were approximately 50x50mm with a through thickness measurement of 15mm.

2.1.4.1 Application to Fibre-Reinforced-Plastic Composites.

The main benefit of CT over conventional radiography is that it removes the inherent superimposition; improving the subject contrast and the probability of detection. Furthermore, the many angles of X-ray projections used in the CT reconstruction means that planar defects become detectable due to the increased probability of the X-ray beam being well orientated to them. These beneficial properties have proven to be very effective for inspection of FRP composite materials (Muralidhar and George 1999; Choudhry and Li 2008). Similar to radiography, CT is excellent for detecting volumetric flaws such as porosity, inclusions and thickness changes. Its high penetrating power means it is able to inspect the full thickness of most composite structures and the use of micro-focus sources allows very high spatial resolutions to be achieved; resulting in defect detectability on a micron scale (<15μm). Unlike radiography, CT is able to reliably detect planar defects such as delaminations and cracks. Plus accurate depth measurements are easily attainable from the cross sectional images.

The main limitations of CT inspection are those inherent to radiographic techniques in general, i.e. access to both sides of the specimen is required and for volumetric flaws to be detected they need to be of an appreciable size in relation to the specimen thickness. This is typically a thickness change of 1-2%.of the total through thickness (Stone and Clarke 1975). The other limitations are inherent to the CT technique and have been discussed in section 1.3.2. In terms of FRP composite inspection, the main limitations are the truncated data problem and the limited effective dynamic range of the detector. The truncated data problem limits the size of objects that can be inspected to those that fit within the Field-of-View (FOV) of the detector (see section 2.2.5 for more details). This limitation can be extending to Region-of-Interest (ROI) inspection at high geometric magnifications. Many defects formed in FRP composite materials are on a micron scale and require the use of high magnifications to achieve that level of defect detectability. At present this problem is circumvented by sectioning and cutting the sample down around the ROI. Clearly, this destructive method is not an option in many applications.

2.1.5 Summary of NDT Capabilities with respect to FRP Composites.

Table 2.1 summarises the defect detection and characterisation capabilities of Radiography, Ultrasonics, Thermography and CT, when applied to FRP composite structures

.

Table 1: Summary table for NDT of FRP composites

NDT Method	Advantages	Disadvantages	Types of defects
CT	• Same advantages as listed for Radiography • Cross sectional imaging so superimposition of features is removed and contrast is improved. • Planar defects are detectable.	• Object size is limited to that which fits within the FOV of the detector. • Geometric magnification and thus spatial resolution is also limited by the object fitting within the detector FOV. • Difficult to obtain sufficient contrast between the fibres and epoxy resin due to the similarities in density.	As with radiography, CT inspection is very good for volumetric flaws, such as voids, inclusions and thickness changes. It also has increased probability of detection (compared to radiography) for planar type defects such as delaminations and cracks. CT is also capable of detecting BVID, fibre breakage and fibre/ply orientation.
Radiography	• Very effective for determining nature and size of volumetric defects • High penetrating power • No contact or surface preparation required • Defect detectability in the micron range with contrast sensitivity between 1-2% of the total through thickness.	• Traditional radiographic techniques produce a 2D projection of a 3D object resulting in superimposition of features and reduced contrast • Detection of planar defects such as cracks and delaminations require the X-ray beam to be correctly orientated to the defect. • Radiation Hazard.	Main application is for the inspection of volumetric flaws like voids, porosity and solid inclusions. Also capable of detecting changes in material composition or thickness.
Ultrasonics	• Superior sensitivity and depth of penetration compared to thermography • Information on defect depth and location easily extrapolated. • Inspection only requires access to one side of the object. • Portable • No health / environmental risks	• Most inspection methods require some form of coupling medium. • Compared to other materials, the penetration depth and contrast is limited in FRP composites due to scattering. • The depth of penetration is limited to ~3mm for defect detectability in the micron range. • Majority of UT methods struggle with inspection of complex shapes.	Very good for detection of planar defects like delaminations and disbonds. For near surface inspection, UT is capable of detecting other defects such as fibre/ply mis-orientation, low level porosity, cracks and ply waviness.
Thermography	• Fast data acquisition and easy interpretation • No contact required • Capable of large area inspection • Portable • No radiation hazard	• Limited to defects larger than 6mm • Limited to the detection of only surface and sub-surface defects (<5mm depth) • Only capable of detecting anomalies that result in a measurable change in thermal properties. • Mainly a qualitative technique so not effective for accurate defect characterisation	Near surface discontinuities such as delaminations, disbonds, impact damage, moisture zones and voids.

2.2 X-Ray Computer Tomography

CT is an imaging method that produces cross-sectional and 3D volume images of the linear attenuation coefficient of a scanned object. It is an established technique in the medical field and has more recently been developed for industrial applications such as NDT and reverse engineering. Figure 2.14 illustrates the concept of a simple CT scanner. Here, an X-ray source generates an X-ray beam that propagates through the object under inspection. The resulting intensity of the X-ray beam is measured using an X-ray detector and is based on the attenuation properties of the object. This process is repeated over many angles to obtain a stack of X-ray projections. These projections are input into a reconstruction algorithm that produces two-dimensional (2D) cross sectional and three-dimensional (3D) volume images.

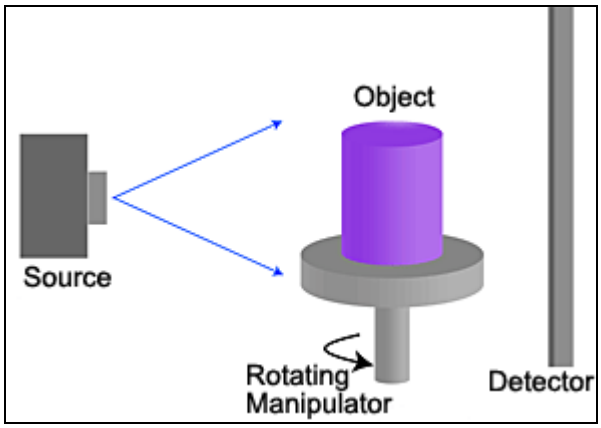

Figure 2.14: The basic set-up of a CT system. The component rotates through an X-ray beam, whilst a digital detector collects attenuation information.

2.2.1 A Brief History of X-Ray Computer Tomography

The field of X-ray imaging was created in 1895 when Wilhelm Conrad Röntgen discovered a new type of radiation that allowed the bones in his wife's hand to be visualised. This discovery was awarded the Nobel Prize for Physics in 1901. Today, conventional radiography still remains one of the major imaging techniques used in the medical field. However, the use of X-rays for medical imaging has expanded well beyond conventional radiography. Conventional radiography suffers from the limitation that it only produces 2D projections of a 3D object. This causes a reduction in spatial information and contrast due to the inherent averaging process when superimposing features. The concept behind the development of CT was the need to eliminate this superimposition. This led to the solution

of the inverse problem[3] associated with producing cross-sectional CT images using 2D X-ray projections. These findings were first published by the mathematician Johann Radon in 1918 (Radon 1917/1986). However, due to the complexity and depth of the publication, the consequences of these ground-breaking results were not revealed until the mid-20th Century.

Allen MacLeod Cormack re-addressed the problem and his work on image reconstruction was published in 1963 (Cormack 1963). However, it was not until 1972 that Sir Godfrey Hounsfield appreciated the significance of Cormack's work and used computer technology to apply it to diagnostic imaging (Hounsfield 1972). The first clinical images were published in 1972 (Hounsfield 1972) and, both Cormack and Hounsfield were awarded the Nobel Prize for Medicine in 1979.

The invention of CT by Hounsfield is one of the major innovations in diagnostic imaging. The first CT machine to be installed was called the EMI scanner, built by EMI Medical Inc. This system was limited to only making tomographic sections of the brain, using a water-filled Perspex tank to reduce the dynamic range of the radiation reaching the detectors. These images were also relatively low resolution, being composed of a matrix of only 80 x 80 pixels (Nosach 2006). Since then, improvements in CT equipment, such as computing power, large area detectors and reconstruction algorithms have been constant; providing a reduction in inspection times and greatly improved image quality. These developments have revolutionised the technique resulting in CT being used extensively in medicine and many other industries.

2.2.2 X-ray CT Scanning Geometries

As previously mentioned, the first stage of the CT process involves the acquisition of the X-ray projection data. These X-ray projections of the object need to be gathered at many angular orientations to allow reconstruction of cross sectional CT images. In principle, it makes no difference whether the object is moved relative to the source and detector or vice versa. The decision is usually based on the practical and physical considerations of the application. For medical applications, moving the patient accurately without any additional un-calibrated movement would be very difficult. The obvious choice is to move the source-detector pair and keep the patient stationary. However, this is not a problem

[3] The general nature of an inverse problem is to deduce a cause from an effect. For CT this involves deducing the object function i.e. 3D volume (cause) from the gathered X-ray attenuation data i.e. 2D X-ray projections (effect). Whilst taking into account the necessary system parameters. The CT reconstruction process is described in full in section 2.2.3.

for most industrial CT applications as inspection would involve an inanimate object that can be mounted and the movement accurately calibrated.

Currently five different generations of CT systems exist. Their classification relates to the configuration of the mechanical equipment and the relative motion it provides between the object, source and detector.

First-generation scanning geometry is Hounsfield's original configuration (Hounsfield 1972). This setup consisted of a narrow pencil beam being linearly displaced along the length of the object to produce each X-ray projection. This process is repeated for a number of angular positions as shown in Figure 2.15. The advantages of this configuration are its simplicity and its ability to accommodate a range of object sizes. In addition, compared to other configurations, it is less susceptible to image degradation caused by scatter. The major disadvantage is a much longer scanning time compared to later generations.

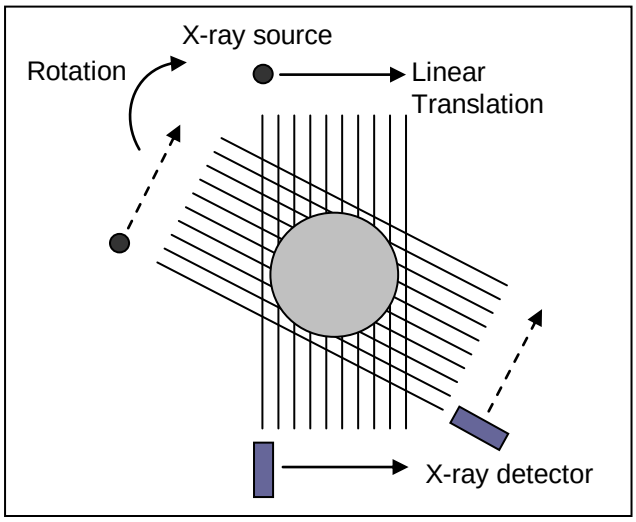

Figure 2.15: First generation parallel beam CT scanning geometry.

Second-generation CT (Figure 2.16) uses the same translate/rotate scanning procedure about the object and can be considered as the commercial adaptation of the first generation design (Hounsfield 1974) The difference is that a narrow fan beam replaces the pencil beam and the single detector is replaced by a small linear or arc shaped detector array. As a result, the rate of data acquisition is significantly faster. These systems, like first generation, also have the flexibility to accommodate a wide range of object sizes.

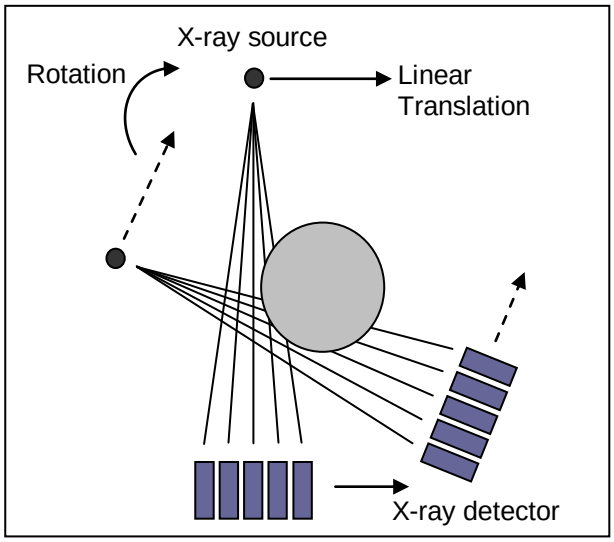

Figure 2.16: Second generation fan beam CT scanning geometry.

A typical third generation CT (also known as circular or rotate only CT) scanning geometry is illustrated in Figure 2.17. Here, the fan beam and X-ray detector are wide enough to contain the whole object. This generation of machines use a rotate only geometry instead of the translate-rotate configuration of the first and second generation (Brooks and Di Chiro 1976a). The result is considerably faster acquisition times due to the X-rays being utilised more efficiently. The vastly improved scan times and simplicity of this design has meant that this configuration is used extensively for both medical and industrial applications. However, the spatial resolution in a third generation CT system depends on the size and number of sensor elements in the detector array. Therefore, this reduction in acquisition time is achieved at the cost of having to use more sensors than with other generations of CT systems. Consequently, very strict requirements are placed on detector performance since all the sensors contribute to a single X-ray projection. The resulting disadvantages include the necessity of normalising the detector response and ring like artefacts (see section 2.2.4.5). These artefacts are produced from various non uniformities in the calibration and system setup (Schneberk *et al* 1990).

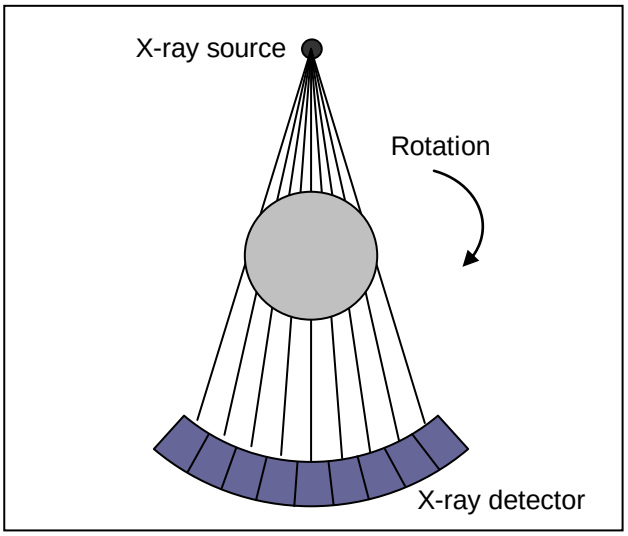

Figure 2.17: Third generation CT scanning geometry.

Fourth generation CT systems consist of a fan beam source that rotates around the object being imaged with a stationary circular array of detectors (As shown in Figure 2.18). Although this configuration is a more complex and costly approach compared to other generations, it does offer resistance to ring-like artefacts (similar to first and second generation) and faster acquisition times (similar to third generation). However, these systems require the object to fit within the fan of the X-ray beam and are more prone to scattered radiation.

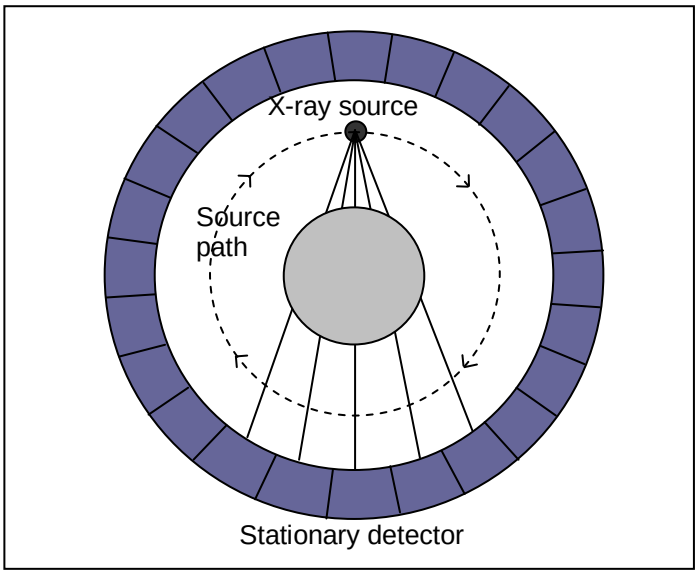

Figure 2.18: Fourth generation CT scanning geometry

Fifth generation CT scanning is different from the previous four generations in that no mechanical movement is required (Robb and Ritman 1979). As illustrated in Figure 2.19, the system consists of a circular array of X-ray sources and detectors, that are

electronically triggered to switch on and off in sequence. This allows the acquisition of the X-ray projections and the reconstruction of the cross sectional CT data to take place simultaneously. This type of system is very complex and is specifically used for reconstructing precise images of a rapidly moving part (i.e. beating heart) and is generally known as Electron Beam CT (EBCT) (Kropas-Hughes and Neel 2000).

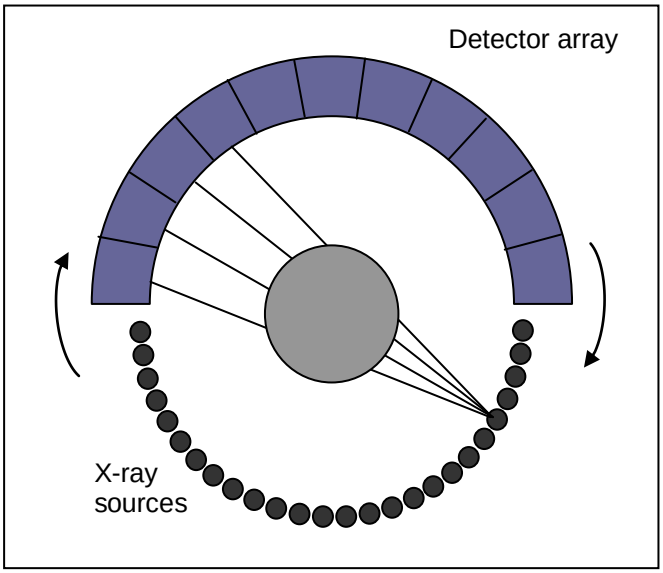

Figure 2.19: Fifth generation CT scanning geometry.

Third generation rotate-only CT systems are by far the most commonly used in both medical and industrial applications. This is due to their simple design and significantly faster scan times compared to previous generations. In medicine, the improved scan times are important for both reducing the radiation exposure to the patient and reducing the time required to remain motionless. For industrial applications, the considerations are not the same. But faster scan times are still the main driver in system configuration due to the obvious business benefits. However, there is a significant difference between the third generation CT systems used in the medical field and those found in industry. The majority of medical systems employ a scanning geometry known as Helical CT (Kalender *et al* 1990). Here, the source follows a helix trajectory as it rotates around the object. This technique enables long objects to be scanned but requires more complex and costly equipment compared to the conventional third generation (circular) CT systems used for industrial applications.

More recently, direct 3D reconstruction has been developed using cone beam X-ray sources that provide greater geometric coverage compared to the fan beam arrangement. This configuration can be applied to the same scanning geometries listed previously. The only difference is that a planar detector with a 2D array of sensors replaces the linear

series of detector elements. This allows for much faster data acquisition, as the data acquired in multiple fan slices can be acquired in one cone beam projection. However, it is also computationally more intensive and prone to distortion, as most cone beam reconstruction algorithms are an approximation (discussed in more detail in sections 2.2.3.5).

2.2.3 CT Reconstruction

2.2.3.1 General Principles

Fundamentally, tomography deals with the reconstruction of an object from its projection data. These projections are essentially a set of measurements of integrated attenuation values belonging to each individual ray path of the X-ray beam (called line integrals). The Beer-Lambert Law forms the basis of this reconstruction by allowing the transmitted X-ray intensities (acquired using the detector) to be related to the line integrals along each ray path. The Beer-Lambert law has been defined previously in section 2.1.1.1, Equation 2.1.

By modifying Equation 2.1, it can be shown that for each ray of X-ray photons transmitted through an object, the intensity, I_0, is attenuated depending upon the integral of the linear attenuation coefficients, μ, and the material thickness, L, along the path of the ray:

$$I = I_0 \cdot exp\left[-\int_L f(x,y)dL \right] \tag{2.2}$$

The function *f(x,y)* represents the value of the linear attenuation coefficient, μ, at the point *(x,y)* along the selected ray path of the X-ray beam, as shown in Figure 2.20.

So for each intensity measurement the corresponding line integral can be determined by a simple log operation:

$$ln\left(\frac{I_0}{I}\right) = -\int_L f(x,y)dL \tag{2.3}$$

A projection is formed by combining the set of line integrals for a single angle of rotation, as shown in Figure 2.21. Repeating these measurements along a large number of ray paths and over many angles within the same slice defines the Radon transform of the object (Radon 1917/1986). Finding the inverse of this transform enables a cross-sectional attenuation slice of *f(x,y)* to be reconstructed.

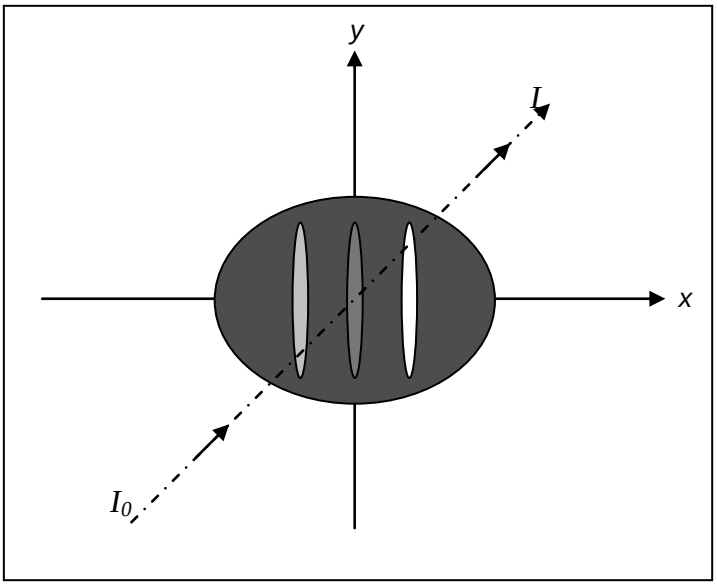

Figure 2.20: An X-ray beam passing through an object with four different linear attenuation coefficients.

For simplicity, the parallel beam geometry will be used to derive the mathematical basis of tomographic reconstruction. The coordinate system is illustrated in Figure 2.21.

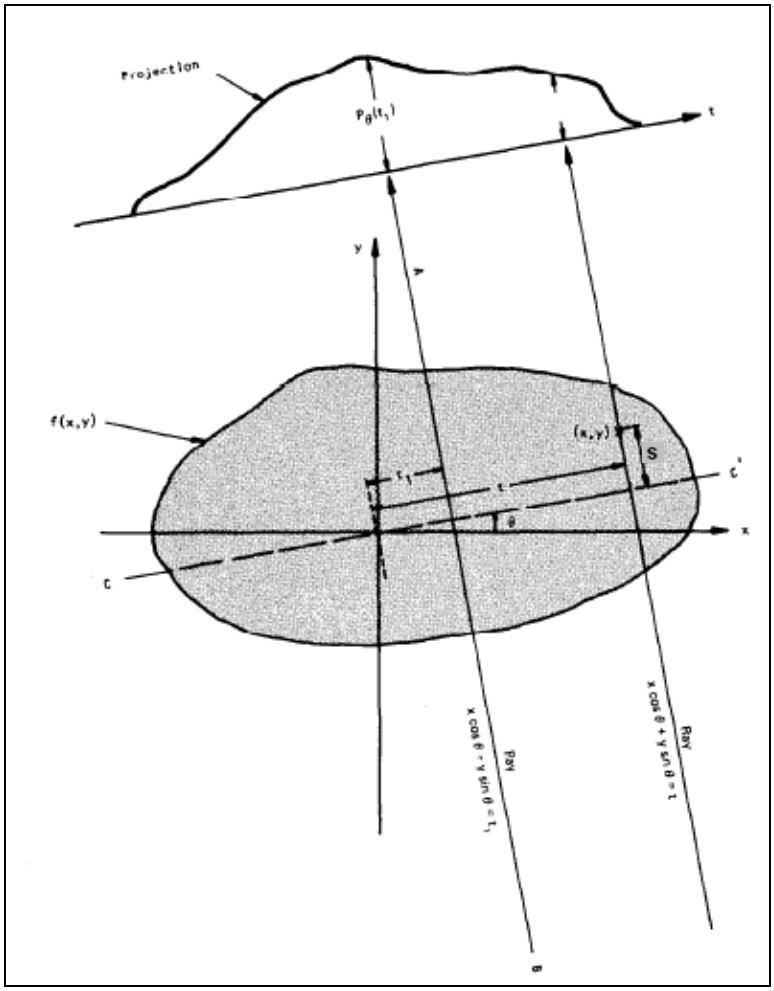

Figure 2.21: Parallel beam geometry and co-ordinate system for an object *f(x,y)* and its projections, $P_\theta(t)$ (Kak and Slaney 1987).

Firstly, the coordinate system will be used to define the line integrals and projection functions. In this example the object is again represented by a two-dimensional function, *f(x,y),* and each line integral by the *(θ,t)* parameters. Where *θ* is the angle between the x-axis and the perpendicular to the ray and *t* is the algebraic distance from the axis of rotation to the ray. The equation of the line *AB* is:

$$x\cos\theta + y\sin\theta = t \tag{2.4}$$

Using the Beer-Lambert relationships given in Equation 2.2 and 2.3 the corresponding line integral, $P_\theta(t)$, for each intensity measurement is given by:

$$P_\theta(t) = \ln\frac{I_0}{I_\theta(t)} = \int_{(\theta,t)line} f(x,y)ds \tag{2.5}$$

$P_\theta(t)$ is used to define a line integral or a projection (set of line integrals) along a ray given by *(θ,t)*, as shown in Figure 2.21. Thus, the function $P_\theta(t)$ calculated over many ray paths and angles is known as the Radon transform of the function *f(x,y)* (Radon 1917/1986):

Commonly used CT reconstruction algorithms such as Filtered Back Projection (FBP) (full details in section 2.2.3.3) have been developed based on the above assumptions surrounding the Beer-Lambert law (Equations 2.2 and 2.3). These algorithms use a significant tool for the inversion of the Radon Transform, known as the Fourier Slice Theorem (FST).

2.2.3.2 Fourier Slice Theorem

One of the important properties of the Radon Transform, $P_\theta(t)$, of an object *f(x,y)*, is its relationship to the Fourier Transform, *F(u,v)* of *f(x,y)*, usually termed the FST. It states that the 1D Fourier Transform of a parallel projection $P_\theta(t)$ is the 2D Fourier Transform of the original object function *f(x,y)* (Kak and Slaney 1987). It follows that using the projection data it should be possible to estimate the object function *f(x,y)* by simply performing a 2D inverse Fourier transform.

The 2D Fourier transform of the object function is defined as (Kak and Slaney 1987):

$$F(u,v) = \int_{-\infty}^{\infty}\int_{-\infty}^{\infty} f(x,y)\cdot exp[-j2\pi(ux+vy)]\,dxdy \tag{2.6}$$

Where *(u,v)* are the coordinates of the object in the frequency domain and *(x,y)* the coordinates in the spatial domain, as defined in Figure 2.22. *j* is the square root of negative one. The Fourier transform $S_\theta(\omega)$ of a projection at an angle *θ* is defined as (Kak and Slaney 1987):

$$S_\theta(\omega) = \int_{-\infty}^{\infty} P_\theta(t)\cdot exp[-j2\pi\omega t]\,dt \tag{2.7}$$

where *ω* is the spatial frequency.

The proof of the theorem is straight forward and can be shown by taking the simple example of a projection at *θ=0* for the object function *f(x,y).*

The projection $P_{\theta=0}(x)$ is related to the original function by the equation:

$$P_{\theta=0}(x) = \int_{-\infty}^{\infty} f(x,y)dy \tag{2.8}$$

Taking the Fourier transform with respect to x on both sides gives:

$$S_{\theta=0}(u) = \int_{-\infty}^{\infty} P_{\theta=0}(x) \cdot exp[-j2\pi ux]\,dx = \int_{-\infty-\infty}^{\infty\infty} f(x,y) \cdot exp[-j2\pi ux]\,dxdy \tag{2.9}$$

The 2D Fourier Transform of $f(x,y)$ is given by:

$$F(u,0) = \int_{-\infty-\infty}^{\infty\infty} f(x,y) \cdot exp[-j2\pi ux]\,dxdy = S_{\theta=0}(u) \tag{2.10}$$

Therefore it can be concluded that $S_{\theta=0}(u) = F(u,0)$. This result is the simplest form of the FST but the same process will apply regardless of the angle of orientation. This can be shown in Figure 2.22, using the projection $P_{\theta}(t)$ defined in Equation 2.5. As the coordinate system is rotated by θ, the Fourier transform of the projection is equal to the 2D Fourier transform of the object, $F(u,v)$, along a line, BB, rotated by θ. This indicates that acquiring projections of the object function at many angles and applying a Fourier transform to each will determine the values of $F(u,v)$. Thus, allowing the object function $f(x,y)$ to be recovered using the inverse Fourier transform. This was defined by (Kak and Slaney 1987) as:

$$f(x,y) = \int_{-\infty-\infty}^{\infty\infty} F(u,v) \cdot exp[\,j2\pi(ux+vy)]\,dudv \tag{2.11}$$

More formal derivations of the FST using coordinate system rotations are available in Kak and Slaney (1987).

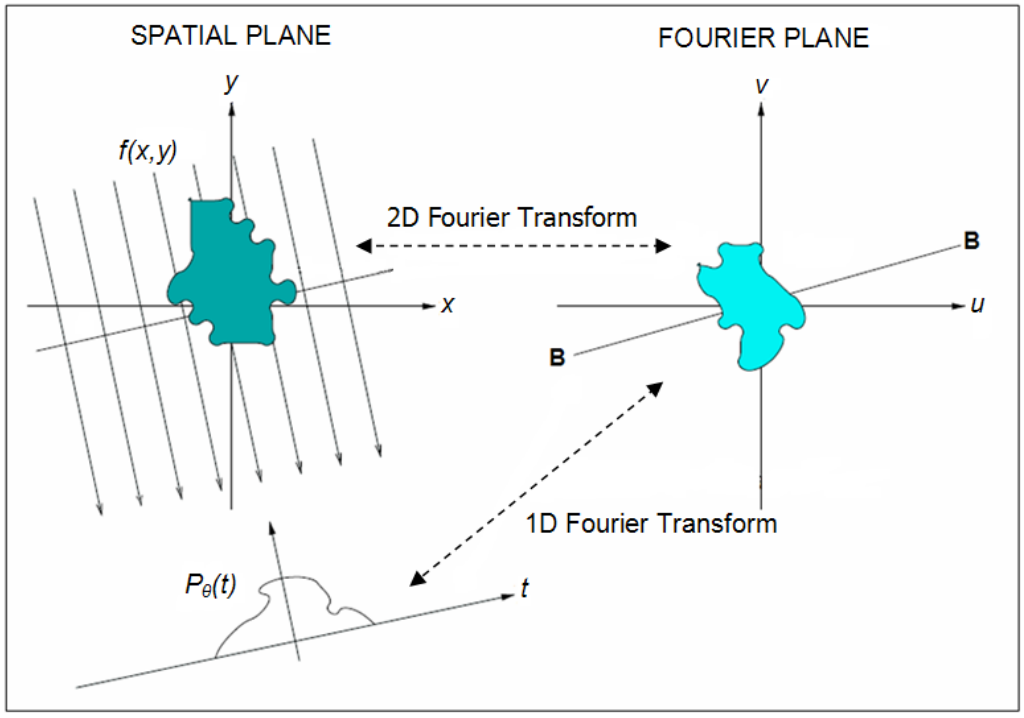

Figure 2.22: Illustration of the Fourier Slice Theorem, relating the Fourier transform of a projection to the Fourier transform of the object along a radial line.

2.2.3.3 Filtered Back Projection

The FST is shown to relate the Fourier Transform of a projection to the Fourier Transform of the object function along a single radial line. Thus obtaining projection data at enough angles would mean the FST could provide a straight forward method of reconstructing an estimate of the object function. However, practical implementation of Fourier reconstruction faces significant challenges due to the sampling pattern produced in the Fourier space (Elbakri 2003). Therefore, a different approach known as the FBP algorithm developed by Herman (1980) is commonly used in most tomographic applications.

There are two steps to the FBP algorithm. The first is the filtering of the projection data, which can be viewed as a simple weighting of each projection in the frequency domain. The second involves projecting the measurements back along the same line (or equivalent same θ) from where they were obtained.

The inverse Fourier transform, defined in Equation 2.11, enables the object function $f(x,y)$ to be recovered from the Fourier transform of the set of projections in the frequency domain. To take advantage of the FST, this equation is manipulated by changing the coordinate system from rectangular (u,v) to polar coordinates (ω,θ), giving:

$$f(x,y) = \int_0^{2\pi} \int_0^{\infty} F(\omega,\theta) \cdot exp[\, j2\pi\omega(x\cos\theta + y\sin\theta)]\, \omega d\omega d\theta \tag{2.12}$$

The Fourier transform of the projection data at angle θ, defined in Equation 2.7 as $S_\theta(\omega)$, is substituted in place of the two dimensional Fourier transform $F(\omega,\theta)$. The expression is simplified using Equation 2.4 and the resulting FBP formula is obtained:

$$f(x,y) = \int_0^{\pi} [\int_{-\infty}^{\infty} S_\theta(\omega)|\omega| \cdot exp[\, j2\pi\omega t\,] d\omega\,] d\theta \tag{2.13}$$

The integral in the equation above can be expressed as (Kak and Slaney 1987):

$$f(x,y) = \int_0^{\pi} Q_\theta(x\cos\theta + y\sin\theta) d\theta \tag{2.14}$$

where:

$$Q_\theta(r) = \int_{-\infty}^{\infty} S_\theta(\omega)|\omega| \cdot exp[\, j2\pi\omega t\,] d\omega \tag{2.15}$$

Equation 2.15 represents a filtering operation, where the Fourier transform of the projection data $S_\theta(\omega)$, is multiplied by the frequency response of the ramp filter given by $|\omega|$. So $Q_\theta(\omega)$ is interpreted as a filtered projection. The resulting inverse Fourier transforms of the filtered projections for all angles of θ can then be added to form the estimate for $f(x,y)$. This final step is known as back projection, as it can be perceived as the smearing of each filtered projection over the image plane.

The result of back projecting the projection data is shown in Figure 2.23. The reconstruction of the Shepp-Logan head phantom (Shepp and Logan 1974) is shown for increasing number of projection views illustrating the back projection process.

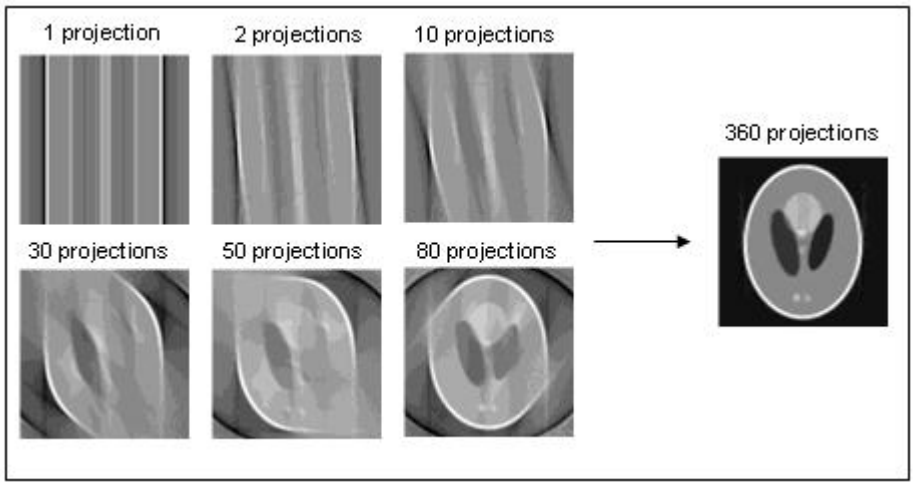

Figure 2.23: Simulated FBP images of the Shepp-Logan head phantom from various numbers of projection views.

For parallel beam geometry, projection measurements taken over 180 degrees are sufficient to represent the Radon Transform (as the remaining 180 degrees of projection data is just mirror images) (Radon 1917/1986). Additionally, the view sampling i.e. the angle between each successive projection measurement must be addressed. This will ensure that a sufficient number of line integrals are known within the object function. In reality, projection measurements are not acquired with infinitely thin rays. Instead, each ray has a width that is determined by the focal spot size of the X-ray source, the size of the detector sensor elements and the system magnification. Consequently, the angular step used to acquire the projection data must be small enough to provide a sampling that is consistent with these inspection parameters. At a minimum, one projection ray needs to pass through each voxel. At the centre of rotation this is not a problem, but voxels located along the circumference of the reconstructed circle will have fewer projections passing through them. Therefore, the number of points needed along the circumference of this circle to satisfy the sampling condition is $q\pi$, where q is the diameter of the object in pixels. Since each projection profile provides two points along this circumference the minimum number of projections is one-half this value i.e. $q\pi/2$ (Kak and Slaney 1987).

A sinogram is commonly used to display a stack of projection measurements in a 2D image format. Figure 2.24 gives an example of a sinogram using a set of projection measurements $P_\theta(t)$ over 180°.

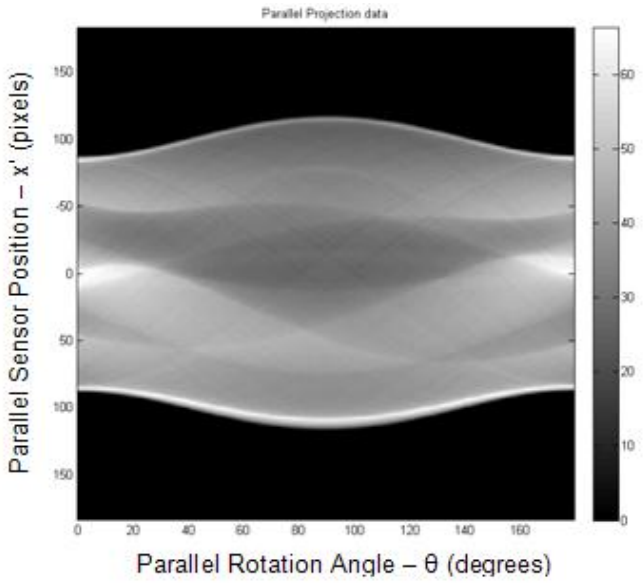

Figure 2.24: Sinogram produced by a fan beam reconstruction of the Shepp-Logan head phantom.

2.2.3.4 2D Fan Beam Reconstruction

There are two types of fan projections depending upon whether a projection is sampled at equi-angular or equi-spaced intervals, i.e. whether the detector array lies on a circular arc or with the detector elements on a straight line, respectively. The equi-spaced fan beam geometry is the most widely used in industry due to the use of linear detector arrays. In addition, the commonly used FDK reconstruction algorithm for cone beam geometry is based on fan beam algorithms used for equi-spaced data (Feldkamp *et al* 1984).

For the case of equi-spaced sampling on a straight line, each ray integral in the fan projection data is denoted by the function $R_\beta(s)$ as shown in Figure 2.25 (Rosenfeld and Kak 1982). Here, β is the angle that the source S makes with a reference axis, and s is the distance along the straight line corresponding to the flat detector array.

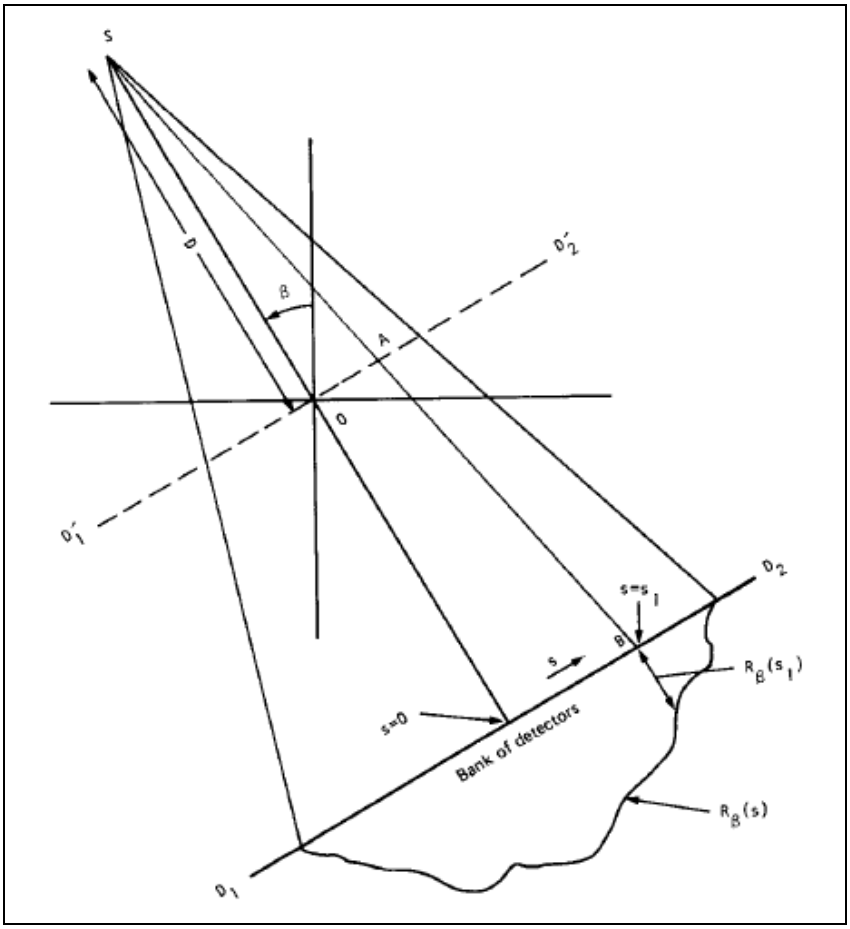

Figure 2.25: A fan beam projection $R_\beta(s)$ for an equi-spaced detector array on a straight line (Rosenfeld and Kak 1982).

The mathematical derivation of the algorithm uses a fan projection $R_\beta(s)$ associated with an imaginary detector line D_1',D_2'. So the ray *SB* is now *SA* as in Figure 2.25 and the value of *s* for this ray is the length of *OA*. If parallel projection data were created for the same object, the ray *SA* would belong to a parallel projection $P_\theta(t)$ with θ and *t* as shown in the Figure 2.26. The relationship between the fan beam acquisition parameters (β,s) and the parallel case (θ,t) is given by (Kak and Slaney 1987):

$$\theta = \beta + \gamma \qquad \theta = \beta + tan^{-1}\frac{s}{D}$$
$$t = s\cos\gamma \qquad t = \frac{sD}{\sqrt{D^2 + s^2}} \tag{2.16}$$

where *D* is the distance from the source *S* to the origin *0*.

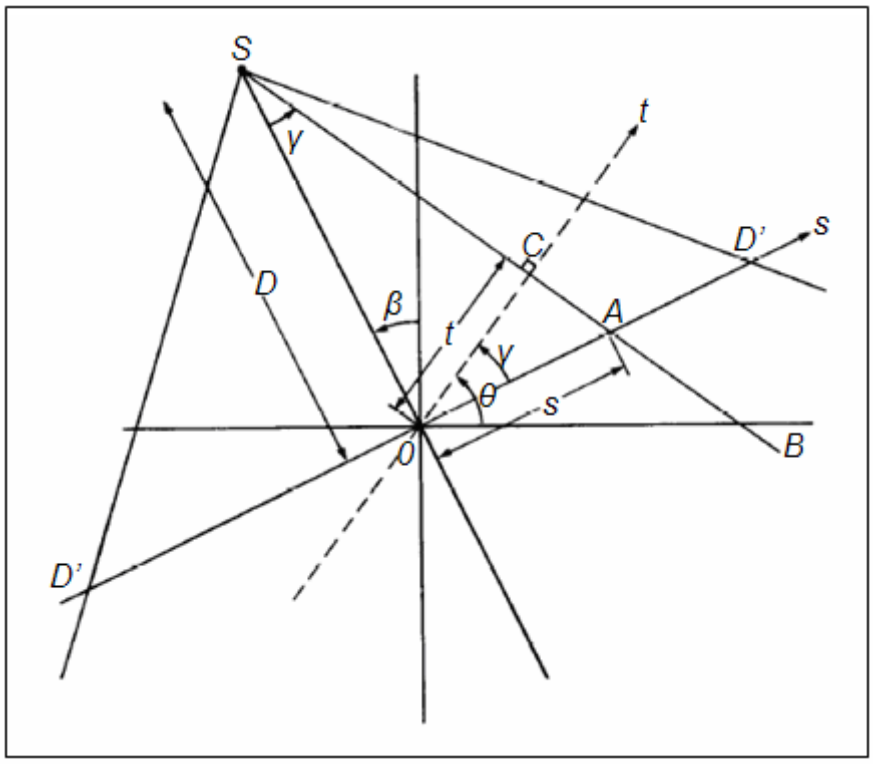

Figure 2.26: A fan beam projection with corresponding parallel projection for ray *SA*, illustrating the parameters used in the derivation of the fan beam FBP algorithm (Rosenfeld and Kak 1982).

The FBP algorithm for fan beam data consists of the following steps (Kak and Slaney 1987):

(1) Pre-weight the fan projection data, $R_\beta(s)$ to find $R_\beta'(s)$. This is done according to the relative position of the corresponding equi-angular projection data using the function *(D/√(D²+s²))*.

$$R_\beta'(s) = R_\beta(s)\frac{D}{\sqrt{D^2+s^2}} \tag{2.17}$$

Note, the weighting factor $R_\beta'(s)$ that modifies each fan projection can be interpreted as the cosine of the angle between the projection ray under consideration and the central ray.

(2) Filter each weighted projection $R_\beta'(s)$ with $g(s)$ to produce the corresponding filtered projection, $Q_\beta'(s)$, using the filtering kernel:

$$g(s) = \frac{1}{2}h(s) \tag{2.18}$$

where *h* is the impulse response of the ramp filter and

$$Q_\beta(s) = R_\beta(s) * g(s) \tag{2.18}$$

(3) Perform a weighted back projection on the filtered projections along the corresponding fan ray with the weight *U.* This is the ratio between the parallel projection of a pixel at the position *(x,y)* onto the central ray *SP* and the source to origin distance *D* (as shown in Figure 2.27).

$$U(x,y,\beta) = \frac{D + x\sin\beta - y\cos\beta)}{D} \tag{2.19}$$

The resulting FBP formula is given below, where *s'* is the value of *s* for the ray that passes through the point *(x, y).*

$$f(x,y) = \int_0^{2\pi} \frac{1}{U^2} \int_{-\infty}^{\infty} Q_\beta(s').ds d\beta \tag{2.20}$$

The sum of all the back projections is the reconstructed image.

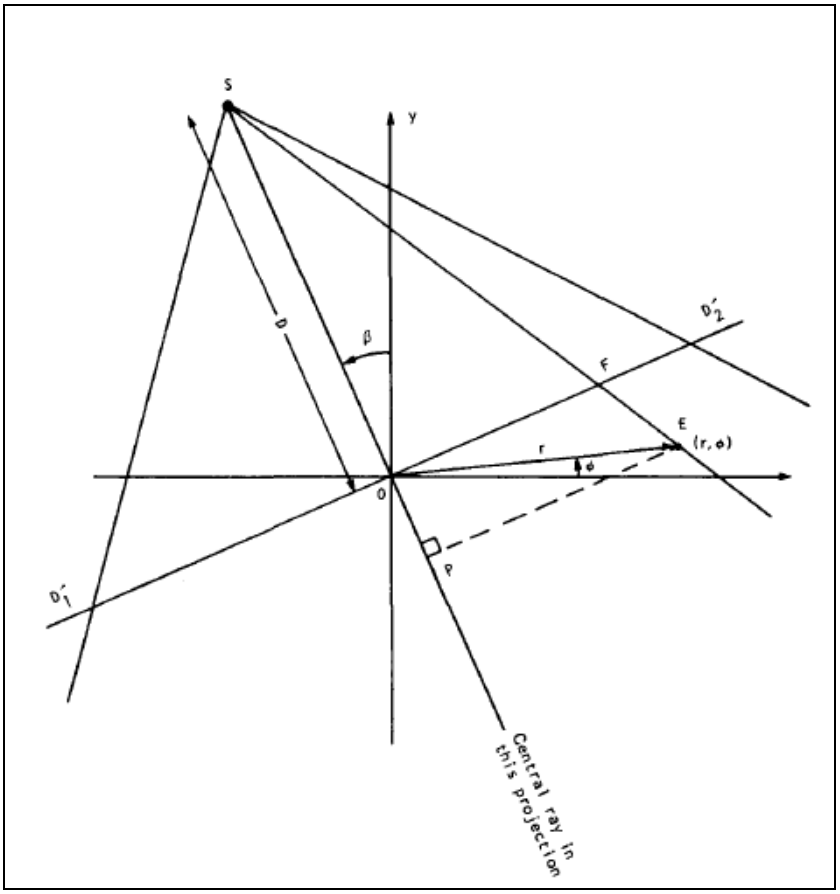

Figure 2.27: Illustration of the parameters used in deriving the variable weighting factor *U*, which is the ratio of *SP* to *D* (Rosenfeld and Kak 1982).

2.2.3.5 3D Cone Beam Reconstruction

The conventional way to obtain a 3D CT image of an object was to scan successive slices within the object using a fan beam X-ray source. A 2D fan beam reconstruction algorithm, as described previously, could then be used to reconstruct each plane separately and stack them up to obtain a 3D image. However, it has become common place to use a more efficient approach via cone beam CT systems. The majority of reconstruction algorithms for cone beam geometry are based on the FDK algorithm developed by Feldkamp, Davis and Kress in 1984. This algorithm is a generalisation of the 2D fan beam algorithms based on FBP (Feldkamp *et al* 1984). The main advantage of cone beam tomography over fan beam is the reduction in the data acquisition time. In the time it takes to measure a single slice of the object function using fan beam CT, the entire set of line integrals through every point in the object can be collected using cone beam CT. The limitation of this technique is that no exact solution exists, meaning the FDK reconstruction algorithm is an approximation outside of the mid-plane. This is due to the fact that Tuy's sufficiency condition (Tuy 1983) is only met for line integrals that intersect the source trajectory (Kak and Slaney 1987). When this condition is not satisfied there will be incomplete information for a stable solution to the inverse problem. Figure 2.28 provides an illustration of the source trajectory location within the cone beam setup. Here, for a circular scanning geometry only the ray paths that intersect the object through the horizontal plane in which the source lies can be exactly reconstructed. In cone beam geometry this is only the case in the mid-plane (where it can be viewed as a fan beam slice). Therefore all line integrals outside the mid-plane are an approximation. The FDK algorithm accurately approximates these line integrals by measuring the tilted fan beams. This basically means that the FDK projects the off scanning plane/tilted projection data into the scanning plane and then follows the 2D fan beam FBP algorithm. The disadvantage of this technique is that the approximation becomes increasingly inaccurate for large cone angles. The result is image quality degradation, visualised mainly as blurring in the axial direction. These cone beam artefacts have been described in a number of different ways in literature. One Fourier based description relates the artefacts to a shift variant cone of missing spatial frequency components (Bartolac *et al* 2009). This description implies that the artefacts depend on multiple parameters including the imaging geometry, the position of the object, its shape and the density. For example, it has been shown that a planar disk based phantom (i.e. Defrise phantom) will degrade rapidly at relatively small cone angles, whereas as spherical type features are preserved at the same locations (i.e. cellular) (Bartolac *et al* 2009). This can be explained as follows: when lines of absent frequency components correspond to features in the real object it is expected that the resolution of surfaces normal to these directions will be most affected

(i.e. degraded). Therefore, spherical features may appear less degraded as only the upper and lower most surfaces are likely to be affected. It should be noted that regardless of the shape of the feature cone beam artefacts will still be present to some extent. Numerous techniques have been proposed to overcome the missing data problem with cone beam CT and ensure data completeness. Finch (1985) proposed a theoretically exact and stable inversion procedure for cone beam trajectories that do not satisfy Tuy's condition. However, this inversion procedure does not include a closed form solution and does not lead to a computationally feasible algorithm. In fact, if it was possible to develop a numerical reconstruction based on these procedures it is likely to be computationally inefficient and result in significantly longer reconstruction times (Yan and Leahy 1991). The majority of techniques overcome the missing data by employing some novel non-planar scanning trajectory to satisfy Tuy's sufficiency condition. These include circle and line, circle plus arc, dual ellipses and double orthogonal (Hu and Zhang 2009).

Despite the aforementioned limitations of the FDK algorithm and cone beam circular scanning geometry it is still one of the most widely employed methods for 3D X-ray CT. The circular configuration allows high rotation speed due to its mechanical simplicity (no axial movement as in helical) and the FDK algorithm is extremely efficient; exploiting the available projection data in a mathematically rigorous manner (Ebert 2001; Schretter 2010). Its simplicity and very fast execution speed are the two key factors for its widespread adoption. In fact, for discrete data, the FDK algorithm, near to the mid-plane, has proven to be more accurate than potentially exact shift-variant filtered back projection of complete cone beam data because it involves fewer interpolations (Ebert 2001). It has also been shown that even if an exact solution is used, it may not offer improved performance over the approximate reconstruction due to sub-optimal noise characteristics (Wang and Yu 2008).

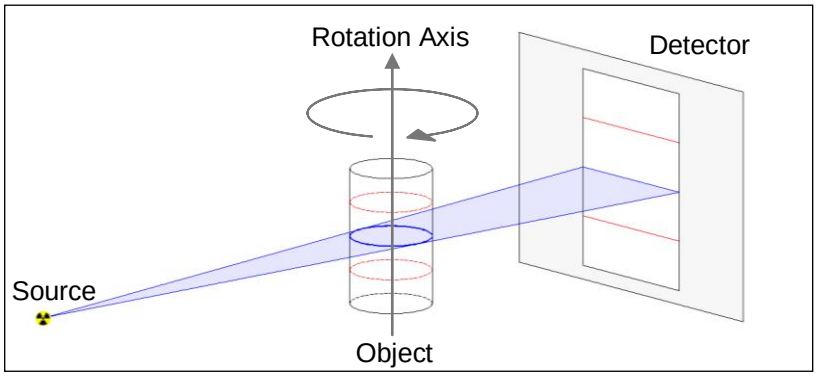

Figure 2.28: Circular cone beam CT setup showing the plane that intersects the source trajectory and satisfies Tuy's sufficiency condition for exact reconstruction.

The following derivation briefly describes the FDK algorithm but a more detailed derivation can be found in Kak and Slaney (1987). The projection data in three dimensions, $R_\beta(t,r)$, are now a function of the source angle, *β*, and the horizontal and vertical positions on the detector plane, *t* and *r* as in Figure 2.29 (Feldkamp *et al* 1984; Kak and Slaney 1987).

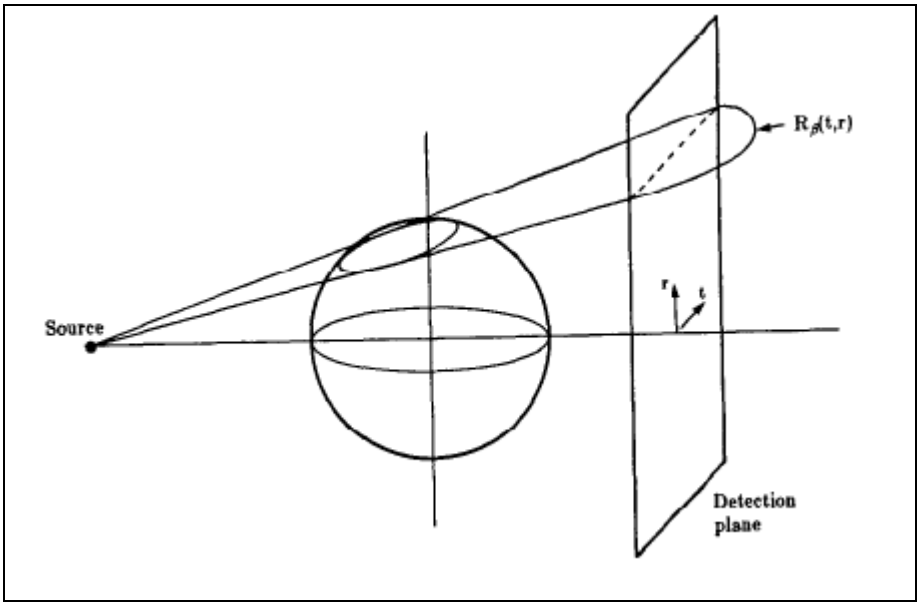

Figure 2.29: Cone beam geometry projection data (Kak and Slaney 1987).

Therefore a three dimensional parallel projection of an object can be expressed by the following integral (Kak and Slaney 1987):

$$P_{\theta,\gamma}(t,r) = \int_{-s_m}^{s_m} f(t,s,r)ds \tag{2.21}$$

In order to define the cone beam geometry, the original coordinate system *(x,y,z)* is rotated twice resulting in the new coordinate system *(t,s,r),* as defined in Figure 2.30 (Feldkamp *et al* 1984; Kak and Slaney 1987). The first rotation, as in the fan beam case, is by *θ* degrees around the *z*-axis to give (*t,s,z*)-axes and the second is rotation is in the (*t,s*)-plane around the *t*-axis by an angle γ. The specified ray is now being described using four variables; *(t,θ)* locates a ray in a given tilted fan i.e. the distance and angle in the x-y plane and *(r,γ)* is used to do this in the s-z plane; to specify the location of the tilted fan itself.

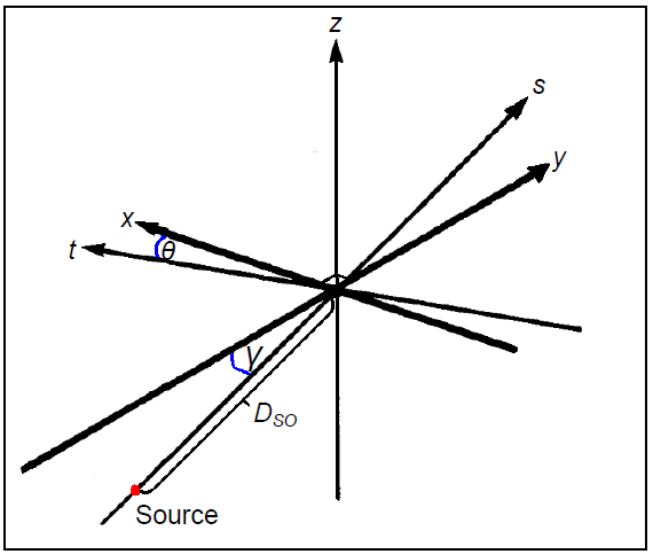

Figure 2.30: Cone beam coordinate system defining the *(t,s,r)* axes. The *r*-axis is not shown but is perpendicular to the *t*- and *s*-axes (Feldkamp *et al* 1984; Kak and Slaney 1987

In a cone beam system the source is rotated by *β* and ray integrals are measured on a detector plane described by $R_\beta(p,\zeta)$. Where *p* is the distance along the horizontal straight line corresponding to the flat detector array and *ζ* corresponds to each elevation within the cone beam. So for a given cone beam ray, $R_\beta(p,\zeta)$, the equivalent parallel projection ray is given by (Feldkamp *et al*, 1984; Kak and Slaney 1987):

$$t = p\frac{D_{SO}}{\sqrt{D_{SO}{}^2 + p^2}}$$
$$\theta = \beta + tan^{-1}(p / D_{SO}) \qquad (2.22)$$

where *t* and *θ* locate the ray in a given tilted fan and D_{SO} indicates the distance from the centre of rotation to the source.

Reconstruction for cone beam projection data using FBP algorithms involves filtering and back projecting each plane separately within the cone. The final reconstruction is then obtained by summing the contribution to the object from all the tilted fan beams (Feldkamp *et al* 1984).

The FDK cone beam reconstruction algorithm can be broken down into the following three steps (Kak and Slaney 1987):

(1) Pre-weight the projection data, $R_\beta(p,\zeta)$ to find $R_\beta'(p,\zeta)$. This is done according to its position within the 3D cone using the function $(D_{SO}/\sqrt{(D_{SO}^2+\zeta^2+p^2)})$

$$R_\beta'(p,\zeta) = \frac{D_{SO}}{\sqrt{D_{SO}^{\ 2} + \zeta^2 + p^2}} R_\beta(p,\zeta) \tag{2.23}$$

(2) Filter each weighted projection, $R_\beta'(p,\zeta)$, along the horizontal detector lines using the same filtering kernel as for the 2D fan beam data $h(p)/2$ (Equation 2.18). This step is performed separately for each elevation, ζ, giving the result $Q_\beta(p,\zeta)$.

(3) Back project each weighted projection over the three dimensional reconstruction grid;

$$g(t,s,z) = \int_0^{2\pi} \frac{D_{SO}^{\ 2}}{(D_{SO}-s)^2} Q_\beta(p,\zeta)\,dp\,d\beta \tag{2.24}$$

2.2.3.6 Iterative Reconstruction Techniques

Reconstruction by FBP is used by most manufacturers because of speed, ease of implementation, and relatively few parameters. However, iterative reconstruction methods, such as Algebraic Reconstruction Technique (ART), are a different group of algorithms that are attracting a lot of interest. The basic premise of this type of reconstruction is to start with an initial guess for the reconstructed object and then perform a sequence of iterative grid projections and correction back projections until the reconstruction has converged to some criterion (Pan *et al* 2009). Iterative methods have allegedly a number of advantages over FBP, such as better noise tolerance, versatility and better handling of sparse and non-uniformly distributed projections (Subbarao 1997; Mueller 1998; Mueller *et al* 1999b). Another important advantage is their ability to correction for scatter, non-uniform attenuation and other physical factors (Mueller 1998; Mueller *et al* 1999b). The main problem with these iterative methods is their computational cost and slow speed (Mueller 1998; Mueller *et al* 1999b; Chlewicki 2001; Pan *et al* 2009).

Different types of iterative reconstruction methods exist. The main types are ART, Simultaneous Iterative Reconstruction Technique (SIRT), Simultaneous ART (SART) and Multiplicative ART (MART). The Algebraic Reconstruction Technique (ART) can be classed as the original iterative technique and was developed by Gordon *et al* (1970). It has been shown that ART only requires approximately half the number of projections as

FBP (Guan and Gordon 1996). This clearly has benefits in the medical industry where toxicity and dose limitations restrict the number of projections that can be acquired. However, ART produces strong aliasing artefacts when applied for cone angles exceeding 20 degrees (Mueller *et al* 1999b) and is very poor at distinguishing between materials of similar densities compared to FBP (Ali *et al* 2004). SIRT was developed by Gilbert (1972) to suppress the noise and overcome some of the limitations associated with ART reconstruction. The problem with SIRT was the long time it needed for convergence (Mueller *et al* 1999b). So Anderson and Kak (1984) tried to combine the positive aspects of both techniques and produced the SART approach. The main advantages of this technique were the removal of the strong aliasing artefacts associated with ART and the improvement in efficiency (Mueller *et al* 1999b). The main drawback with the SART algorithm is that ART is considerably easier to accelerate and reduce the reconstruction time (Mueller *et al* 1999a). A further iterative algorithm was proposed by Gordon *et al* (1970) known as MART. This method has similar efficiency to ART but has the advantage that a voxel can never be corrected to values less than zero (which is not in the solution space) (Chlewicki 2001).

Iterative based reconstruction methods provide many improvements compared to FBP type algorithms. Yet the FBP algorithm is still largely favoured for the majority of CT applications. The principle reason for its popularity can be attributed to the FBPs convenient analytical formulation which enables fast computation of predictable duration (Mueller *et al* 1999b).

2.2.4 Image Quality

CT systems can never exactly duplicate the object under inspection. The degree to which the CT image does reconstruct the object is mainly determined by the competing influences of spatial resolution, contrast, noise and artefacts (Dainty and Shaw 1976). The relationship between conventional image quality parameters is illustrated in Figure 2.31 (Stenstrom 2000). The Modulation Transfer Function (MTF) (see section 2.2.4.3) is used to express the relationship between contrast and resolution. The Signal-to-Noise Ratio (SNR) (see section 2.2.4.2) describes the relationship between contrast and noise and the Noise Power Spectrum (NPS) illustrates the relationship between noise and resolution.

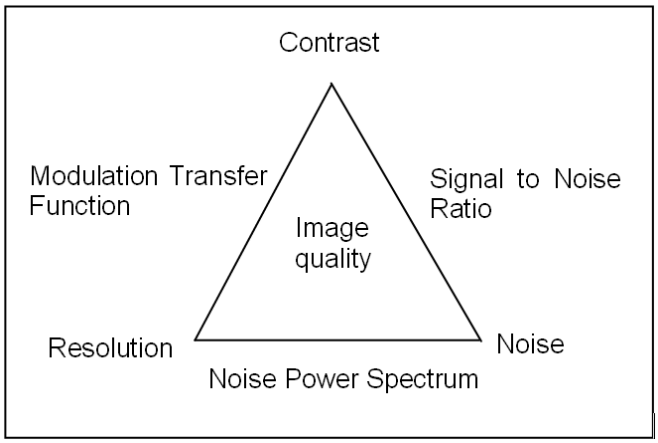

Figure 2.31: A schematic illustration of the relationship between the image quality parameters, contrast, resolution and noise (Stenstrom 2000).

2.2.4.1 Contrast

The contrast in a CT image depends on both the imaged object and numerous properties of the CT system. It can be described as the difference in the linear X-ray attenuation coefficients between the detail and the surrounding material. Specifically, for a detail to be distinguishable, it must have a linear attenuation coefficient μ_d that is sufficiently different from the linear attenuation of its surrounding material μ_m, as shown in Figure 2.32.

The contrast of a CT image, $\Delta\mu$, is then defined as the percentage difference between the detail and the surrounding material such that;

$$\Delta\mu(\%) = \frac{|\mu_m - \mu_d|}{\mu_d} \times 100 \tag{2.25}$$

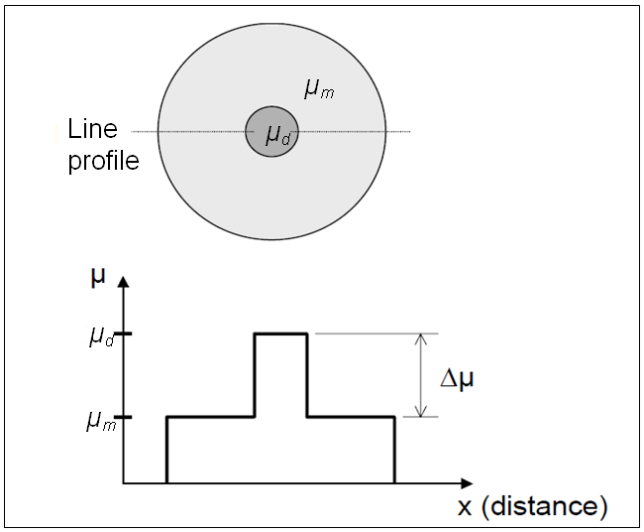

Figure 2.32: Intensity profile used to estimate image contrast for a detail within an object material.

The effective linear attenuation coefficient of the material depends greatly on the incident X-ray spectrum and therefore, contrast depends on the spectrum of incident radiation. This makes it a very important parameter for consideration in the setup of an inspection. Primarily, the generated spectrum is defined by the target material of the source anode and the energy settings applied to the X-ray tube. It can also be refined with the use of filters, which assist by removing the unwanted photons, and narrowing the spectrum. This reduces detrimental image noise and thereby increases the contrast. Lower energy settings also maximise contrast of low density features but are generally detrimental to the SNR (Macdonald 2004). The difficulty lies in finding the optimum trade-off between these factors. It should be noted that several other factors exist for limiting the image contrast outside of the radiation spectrum. These include, but are not restricted to, the limited dynamic range of detector and non-linearities such as artefacts.

2.2.4.2 Noise

Noise is always present in CT images and degrades image quality by impairing the detectability of small details. Noise is defined as the uncertainty in the signal due to random fluctuations. The random nature of generating and detecting X-ray photons is known as quantum noise and is separate to electronic noise found in the detector.

Electronic noise is usually in the form of random electrical currents often produced by thermal activity within the device. This can be mitigated by proper cooling and digitising the signal early in the supply chain. Other detector specific effects that can contribute to image noise are caused by dark currents and sensor circuit gain. These can be corrected through proper calibration, known as ‘offset’ and ‘gain’ corrections. The primary method of reducing quantum noise is by increasing the number of incident photons, thus reducing their random nature. Other methods exist such as filtering the X-ray beam (to remove unwanted photons) and increasing the number of frames acquired. However, even if these measures are taken, quantum statistics dictate that there will inevitably be variation in the X-ray photons detected from the source. This is known to obey Poisson statistics (Bushberg *et al* 2002). Therefore, it can be characterised by the fact that the variance of the signal is equal to its mean and noise can be specified as the standard deviation.

The SNR provides a measure of both noise and contrast (refer to Figure 2.31) and is an important parameter for characterising image quality. The detail SNR of a CT image is defined as (Graeff and Engelke 1991):

$$SNR_{\Delta S,CT} = \frac{\Delta S}{\sigma_{\Delta S}} = \frac{\left| m_{S2} - m_{S1} \right|}{\sqrt{\left(\sigma_1^{\,2} + \sigma_2^{\,2} \right)}} \tag{2.26}$$

Where m_{S2}, σ_2^2 and m_{S1}, σ_1^2 are the expected value and variance of the signals in the detail and the surrounding base material of the object, respectively, as defined in Figure 2.33 (Mangard 2000). In CT images, the signal, *S*, is proportional to the linear X-ray attenuation coefficient, μ.

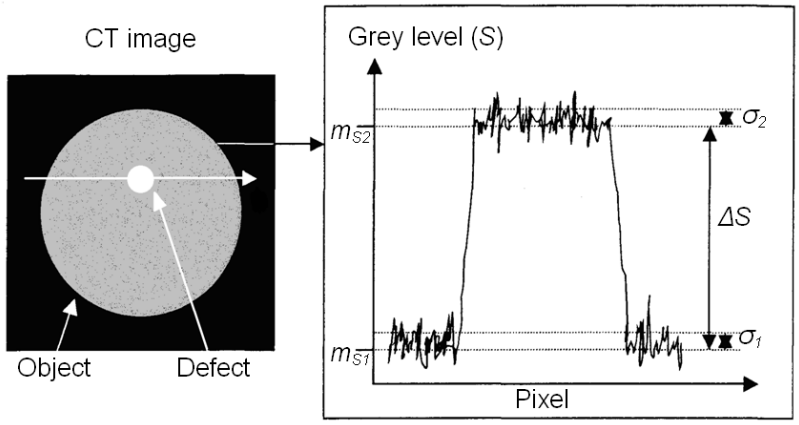

Figure 2.33: Defining the detail signal-to-noise ratio in a CT image. (Mangard 2000).

Using the Beer-Lambert law previously defined (Equation 2.1); the raw X-ray projection data can be described as representing the negative logarithm of the transmitted signal intensities. This leads to the expression for calculating the detail SNR in the acquired X-ray projection data, $SNR_{\Delta proj}$, as (Graeff and Engelke 1991; Hammersberg *et al* 1995):

$$SNR_{\Delta proj} = \frac{\left| ln(m_{P2}) - ln(m_{P1}) \right|}{\sigma_{\Delta proj}} \tag{2.27}$$

Where:

$$\sigma_{\Delta proj}^{\;2} = V\left[ln\left(\frac{P_2}{P_0}\right) - ln\left(\frac{P_1}{P_0}\right) \right] \approx \frac{\sigma_{P2}^{\;2}}{m_{P2}^{\;2}} + \frac{\sigma_{P1}^{\;2}}{m_{P1}^{\;2}} + \frac{2\sigma_{P0}^{\;2}}{m_{P0}^{\;2}} \tag{2.28}$$

Figure 2.34 defines the signals P_0, P_1 and P_2 with respect to the object and the detail. P_0 is defined as the signal produced from the X-ray path adjacent to the object. P_1 is the signal produced from the X-ray path passing through the object and next to the detail. The signal P_2 is defined as that produced from the X-ray path passing through both the object and a detail in the centre of the object. *V* is the number of views or projections acquired during the CT scan. *m* and σ^2 are the expected value and variance respectively of the corresponding signal.

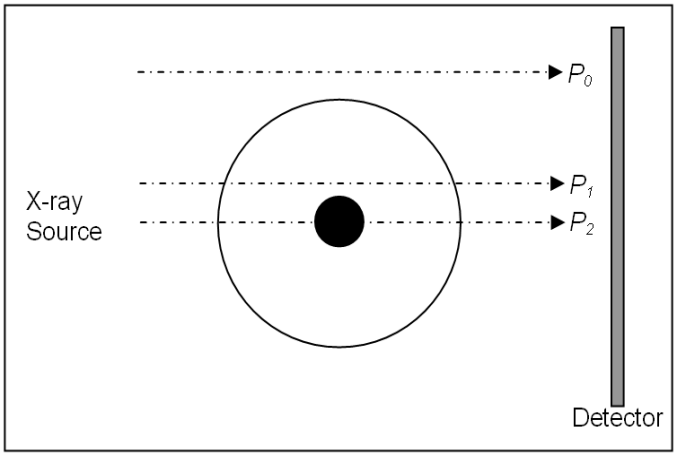

Figure 2.34: Definition of the signals P_0, P_1 and P_2 with respect to the object and the detail (Graeff and Engelke1991).

To maximise the detail SNR in the X-ray projection data, $SNR_{\Delta proj}$, the difference between signals P_1 and P_2 should be as large as possible, together with a low level of noise. However, an important constraint in reconstructing a CT image from the X-ray projection data is the requirement of the signal level beside the object, P_0, to be within the dynamic range of the digital detector system (see Figure 2.35). This means the detector cannot be saturated by the X-rays, thus restricting the maximisation of the detail SNR (Graeff and Engelke 1991).

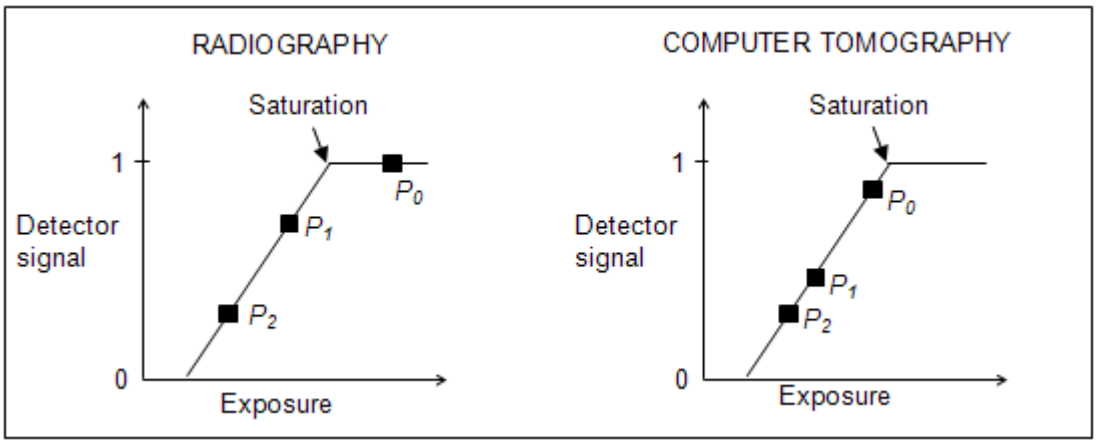

Figure 2.35: In contrast to radiography, CT requires all signals, including those passing beside the object, P_0, to be within the dynamic range of the detector (Stenström 2000).

The relationship between the detail SNR in the X-ray projection data, $SNR_{\Delta proj}$, and the detail SNR in the CT image, $SNR_{\Delta S,CT}$, can be expressed by (Mangard and Hammersberg 1998):

$$SNR_{\Delta S,CT} = \left(\frac{\sqrt{V}}{c_{noise}} \right) SNR_{\Delta proj} \tag{2.29}$$

This implies that the maximum detail SNR for both the CT projection data and the CT image is obtained using the same optimum CT inspection settings. Where c_{noise} describes the connection between the noise in the CT image and the noise in the CT projection data and originates from the data acquisition and reconstruction process.

2.2.4.3 Spatial Resolution

Spatial resolution is generally described in terms of the smallest separation at which two points can be distinguished as completely separate (Oster 1999). The spatial resolution of a CT image is determined principally by the size of the source focal spot, the magnification and the size and number of detector elements. Calculating the maximum spatial resolution of a system is an important performance parameter as it allows the user to determine the ability of the system to resolve small details. This can be done using the Modulation Transfer Function (MTF) and is usually represented in terms of line pairs per millimetre (lp/mm).

The MTF describes how the system transfers the input signal, i.e. the raw X-ray projection data, into the output reconstructed image as a function of spatial frequency. The MTF is primarily used to quantify the systems ability to reproduce spatial frequencies. In other words, to determine the contrast as a function of spatial frequency. However, the edge method for calculating the MTF can also provide a measure of the maximum spatial resolution of the system.

Dainty and Shaw (1976) defined a system as that which produces a set of output functions from a set of input functions. For a digital radiography or CT system, the input is an array of spatially varying signal intensities and the output (or image) is a spatial representation of the linear attenuation coefficients. Suppose that the input signal is a one-dimensional sinusoidal function as defined by:

$$f(x) = a + b\cos(2\pi\omega x + \varepsilon) \tag{2.30}$$

where ω is the one-dimensional spatial frequency, and ε is a measure of the phase, *a* is the shift in the function in the *y*-axis and *b* is the half-amplitude. The output image is also sinusoidal with the same spatial frequency as the input, but with a change of amplitude, or modulation. The ratio of the output modulation to the input modulation depends on the

spatial frequency and is equal to the modulus of the one-dimensional Fourier Transform of the system's Line Spread Function, LSF (also known as the Point Spread Function, PSF). It is this ratio of output to input modulation that is called the Modulation Transfer Function (MTF).

The input modulation is defined by:

$$M_{input} = \frac{f_{max} - f_{min}}{f_{max} + f_{min}} = \frac{b}{a} \tag{2.31}$$

The output function, *g(x),* is also sinusoidal, and has the same frequency as the input:

$$g(x) = a + M(\omega)b\cos(2\pi\omega x + \varepsilon + \phi(\omega)) \tag{2.32}$$

where *M(o)* and $\phi(\omega)$ are the modulus and phase of the Fourier Transform of the line spread function. The output modulation is defined by:

$$M_{output} = \frac{g_{max} - g_{min}}{g_{max} + g_{min}} = M(\omega)\frac{b}{a} \tag{2.33}$$

Thus the ratio of the output modulation to the input modulation is equal to $M(\omega)$:

$$M(\omega) = \left| \int_{-\infty}^{+\infty} l(x).exp[-2\pi i\omega x]\,dx \right| \tag{2.34}$$

The MTF is usually normalised to unity at zero spatial frequency:

$$M(0) = \left| \int_{-\infty}^{+\infty} l(x_1)dx_1 \right| = 1 \tag{2.35}$$

Figure 2.36 illustrates the process of obtaining the MTF using the Edge Spread Function (ESF) from the image of a simple cylinder. The use of a cylinder is preferred because, once its centre of mass is determined, profiles through this point are perpendicular to the cylinder edge. Many profiles can be traced and averaged to reduce noise on the ESF. The LSF is estimated by taking the discrete derivative of the ESF and finally, the MTF is obtained by calculating the Fourier transform of the LSF. The resulting function is normalised to unity at zero spatial frequency and plotted in terms of spatial frequency, usually expressed in line pairs per millimetre (lp/mm). The quantitative value of the measured MTF is taken as the frequency at 10% modulation and from this a value for the spatial resolution can be inferred (ASTM E1695, 2006). However, the main problem in the analysis of edge traces is the influence of un-sharpness and image noise.

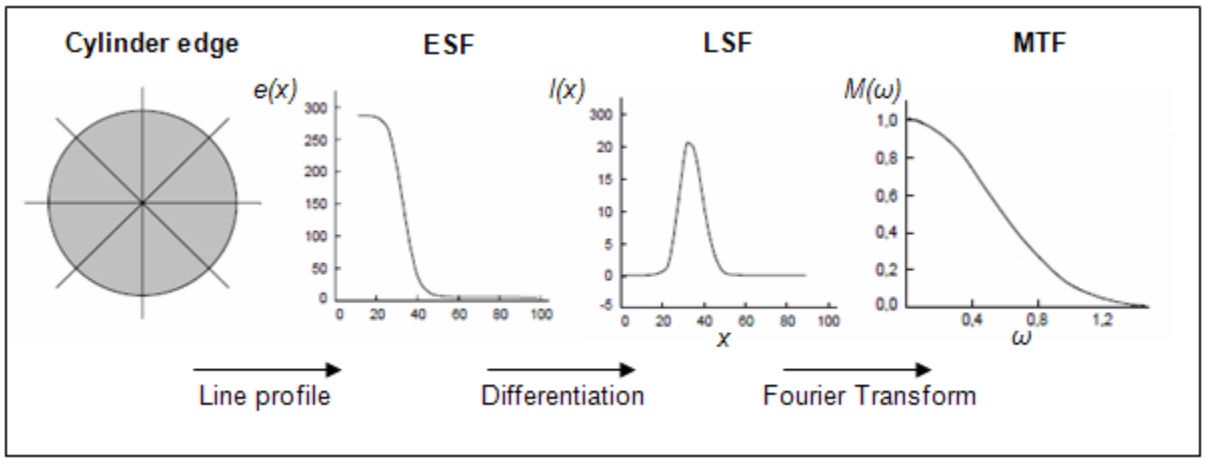

Figure 2.36: Illustration of the process of deriving the MTF from the edge response function (ASTM E1695, 2006).

2.2.4.4 Detection Sensitivity

The detectability of details depends on numerous factors including; spatial resolution, detail size, noise, contrast and image observation conditions (environment and observer). Detection sensitivity has been extensively researched and numerous relationships have been published (Tasto and Schomerg 1978; Cohen 1979; Hanson 1979). The definition widely used for detection sensitivity is the minimum detail SNR (or contrast) required to distinguish a given detail with attenuation, μ_d, with respect to the surrounding material with attenuation, μ_m, with a 50% probability of success.

For example if $(\Delta\mu)_{con}$ is the minimum contrast required, a detail will be distinguishable with a probability of at least 50 % if $(\Delta\mu)_d \geq (\Delta\mu)_{con}$.

In practice detection sensitivity is not only based on threshold criteria, the human observer factor must be taken into account. Several publications (Cohen 1979; Hanson 1979) have reported that the required contrast, $(\Delta\mu)_{con}$, which the human eye can detect with a 50% probability of success follows the relationship:

$$(\Delta\mu)_{con} \cong c.\sigma.\frac{\Delta p}{D} \tag{2.36}$$

Therefore, $(\Delta\mu)_{con}$, depends on the object diameter, D, image noise, σ, and the size of the pixels, Δp, Where c is an empirically determined constant depending on various factors (human, environmental, etc.).

Mangard (2000) provided a theoretical approach on detectability within a CT image, by determining the required value of the detail SNR ($SNR_{\Delta S,CT}$) for 50% probable detection. It stated that the detail size, τ , the MTF of the CT system, MTF_{CT}, and the pixel size, Δp, in the image must be known. Plus the perception factor G based on the number of pixels used to represent the detail. If these parameters are known then the following calculation can be used to find the minimum detail SNR for 50% probability of detection:

$$SNR_{\Delta S,CT} = \frac{G\Delta p}{\sqrt{2}.\tau.MTF_{CT}\left(\frac{1}{2\tau}\right)} \tag{2.37}$$

In Figure 2.37, a typical detail SNR detectability curve as a function of detail size is shown (Mangard 2000). A detail of size τ above the curve is detectable. A detail on the curve will be detectable with a 50% probability and a detail below the curve will go un-detected. As stated previously, the limiting resolution is determined as the frequency at 10% modulation of the measured MTF (ASTM E1695, 2006).

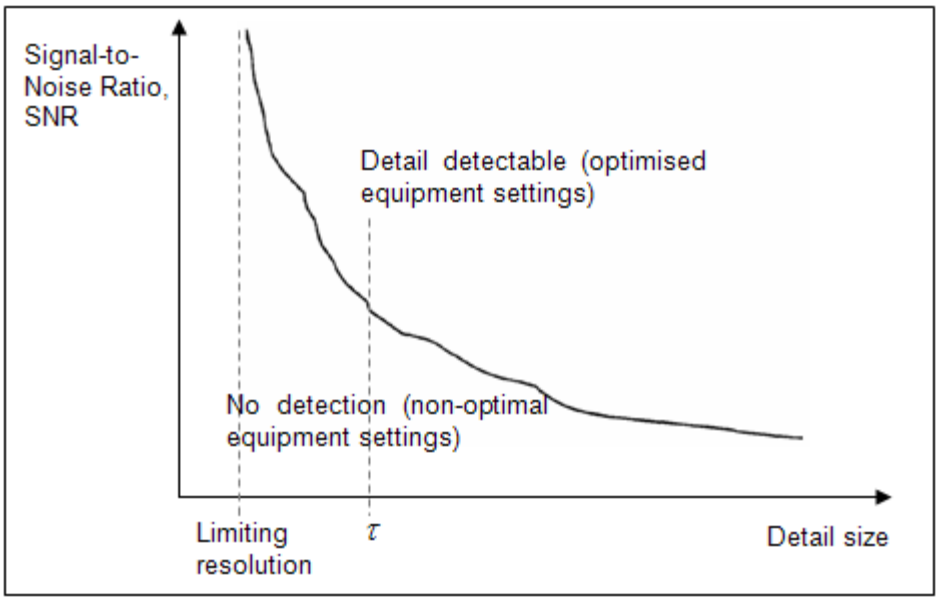

Figure 2.37: A representation of an SNR ($SNR_{\Delta S,CT}$) - detail detectability curve.

These relationships exist to provide threshold criteria for the minimum probability of detection. But essentially to increase the detectability of a detail in the final CT image, the differences in the signals between the detail and the surrounding base material must increase. Therefore, the correct X-ray spectrum has to be chosen with a tube potential and shaped with filters so that the contrast from a detail within an object increases more than the image noise. This will be different for each individual object, depending on its

geometry, the detail and its base material. Thus making it very difficult to find the optimum inspection settings for each imaging task.

2.2.4.5 Artefacts

Artefacts are the appearance of details in an image that do not correspond to a physical feature in the test object. All imaging systems, whether CT or conventional radiography, display artefacts. Some artefacts induced in CT imaging, such as those related to scattered radiation and noise, can be reduced or eliminated by data processing or improved physical acquisition conditions. Other artefacts, such as partial volume effects and high density edge effects are inherent to the technique. Understanding the difference between the artefacts and how they affect the inspection performance allows the experienced operator to disregard their presence.

The beam hardening artefact is a common problem in CT imaging and is caused by the polychromatic nature of the X-ray beam. Specifically, the lower energy photons within the spectrum are more easily attenuated causing the spectrum to change as it passes through the object. This results in a relative increase of the mean energy along that ray path. This process is known as beam hardening (Brooks and Di Chiro 1976b). As a result, the number of photons taken away from the beam in that same voxel for different projection angles will be different. This will cause a false linear attenuation coefficient gradient to be formed. The most common beam hardening artefact is the cupping effect (Brooks and Di Chiro 1976b). This term is used to describe the artefact as it reconstructs inflated grey level values at the edges of an object with a uniform density distribution. These false attenuation measurements prevent true density measurements from taking place. Figure 2.38 illustrates the beam hardening artefact. Both the reconstructed slice through a uniform density steel cylinder and the grey level intensity profile extracted across the slice reveal it to be denser at the centre than at the edges. The effects of beam hardening can be minimised by correct filtration of the incident X-ray beam. This will remove the problematic low energy photons from the spectrum thus reducing the overall hardening effect caused to the polychromatic beam. However, these methods do not overcome beam hardening, they simply aim to reduce its impact on the final image. More sophisticated pre-processing methods are currently being developed to calibrate the effect of beam hardening on the projection data and then correct it prior to reconstruction (Hammersberg and Mangard 1998; Badel *et al* 2003).

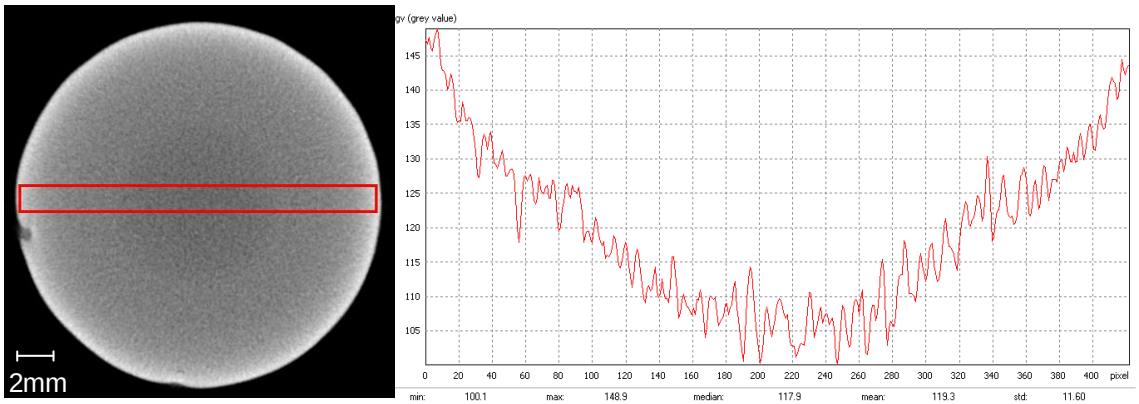

Figure 2.38: A reconstructed slice through a 9mm diameter carbon steel cylinder, showing an apparent density gradient across the object. (b) A grey level profile across the slice in (a) showing the 'cupping effect' across the object.

The centre of rotation artefact is another frequently encountered problem. This is caused by the centre of rotation not being correctly defined when acquiring the X-ray projection data for a CT inspection. The FBP algorithms used for CT reconstruction require accurate knowledge of the point at which the centre of rotation passes for all of the projections. This is because the accurate reconstruction of a voxel depends on the attenuation measurements for each ray value being correctly aligned in relation to the centre of rotation. If the defined centre of rotation is incorrect, the ray values that do not intersect at a voxel position within the object are then mistakenly included in the back projection sum. This causes a double edge blur to be reconstructed, as shown in Figure 2.39. Most CT systems use two measures to correct for this artefact. The first is during setup prior to acquisition. Here, the object is replaced with a straight rod that the system can use to calibrate the centre of rotation of the object in relation to the centre point of the reconstruction. The second measure is usually included as part of the reconstruction setup. Here, the double edge blur is used as a reference to adjust the centre of rotation setting until a single sharp edge is achieved.

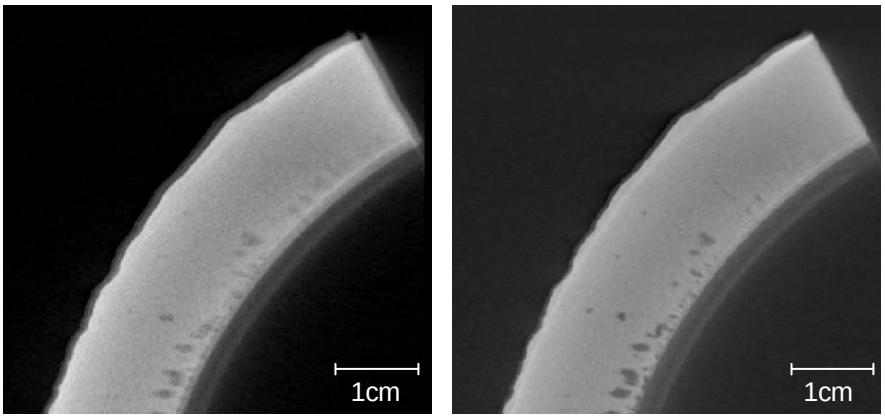

Figure 2.39: Centre of rotation artefact visualised as a double edge blur in the CT image (right). Normal artefact free reconstruction (left).

Ring artefacts generally only occur in third generation rotate-only scanning and are visualised as concentric circles within in the image centred on the axis of rotation (Figure 2.40) (Shepp and Stein 1976). This artefact is a direct result of uncalibrated detector elements and nonlinearities in the 2D detector array. The attenuation measurements acquired by an individual detector element at each angle of rotation make up the vertical lines in a sinogram as the projected ray sums. If the gain or offset for these detector elements has not been calibrated then an imbalance exists that will cause incorrect vertical lines to appear in the sinogram. These lines will produce concentric rings in the reconstructed image making it difficult to distinguish low contrast features. Conventionally, two methods are used in the acquisition stage to overcome ring artefacts. The first is simply to re-calibrate the detector prior to CT scanning. The second method is based on shuffling the object under inspection with small calibrated movements during acquisition of the projection data. This changes the position of underperforming elements within the detector array so that rings are not reconstructed in the final CT image.

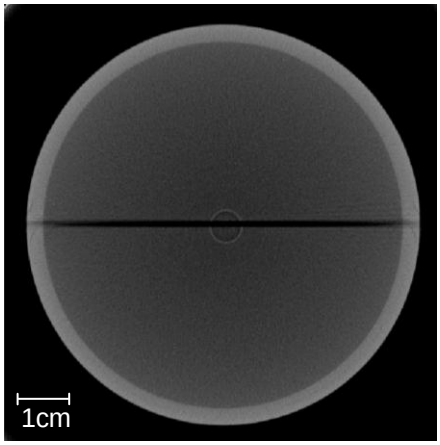

Figure 2.40: Ring artefacts displayed as concentric rings near the centre of the reconstructed CT image.

Truncation artefacts, otherwise known as 'ringing' artefacts (Lewitt and Bates 1978), are created when the object function does not fit within the FOV of the detector for all the projection views. The data outside the detector FOV is assumed to be zero and therefore truncated projection data produces a very sharp transition at the truncated edge. This can only be represented by a range of very high frequencies. As a result, the high frequencies are overrepresented in the Fourier Transform and this causes the ringing artefact. This is visualised as a cupping effect or 'glowing' due to inflated pixels propagating from the truncated edge (Schillnger *et al* 2004), as shown in Figure 2.41. This artefact is the result of an inherent limitation with the majority of CT systems. Developing methods to overcome this limitation is currently an area of extensive research and is reviewed in detail in section 2.2.5.

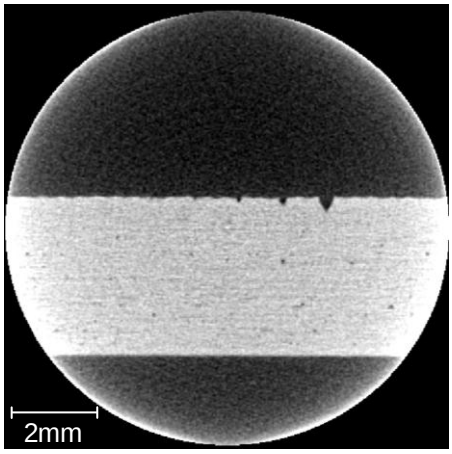

Figure 2.41: Truncation artefacts displayed as strong regions of inflated pixels propagating from the truncated edges.

As mentioned previously some artefacts that appear are inherent to the CT technique and cannot be removed, such as the partial volume effect. This problem arises when a voxel within the object contains a number of different material densities. The resultant voxel value is then an average of these densities. This is known as the partial volume effect. Additionally, due to the inherent resolution limitations of CT reconstruction, material boundaries are blurred to some degree. This can potentially cause the density in one voxel to influence the reconstructed grey values of neighbouring voxels.

A variety of other artefacts can occur during certain inspection situations. If the object under inspection includes regions that are highly attenuating compared to the surrounding material, a "starburst" artefact can be introduced (De Man *et al* 1999). This causes light and dark streaks to propagate from the high density region into the surrounding material, potentially masking details within the image (Figure 2.42(a)). These artefacts are more

likely to occur due to improper penetration of the high density regions. Another artefact that can occur during inspection is due to view under-sampling, usually visualised as arc shaped bright streaks propagating from higher density regions, as shown in Figure 2.42(b).

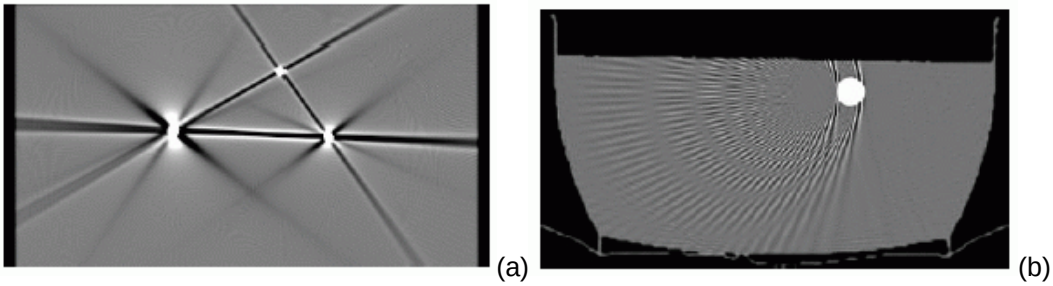

(a) (b)

Figure 2.42: (a) Lack of penetration and (b) View under-sampling (streaks appear) (De Man 1999).

2.2.5 Truncated Data Problem

For the purpose of this thesis, a literature research was performed that focused on CT algorithms and techniques within both medicine and industry that aim to overcome the truncated data problem, or to be more specific, truncated projection data. This problem presents itself when the object function does not fit within the detectors FOV i.e. the resultant projection measurements do not cover the entire object. If such projection measurements were reconstructed using conventional algorithms strong artefacts and inaccuracies would dominate the final CT image (see Figure 2.43). The associated limitations of the truncated data problem were initially highlighted in Chapter 1 (section 1.3.2). The methods contributed by this thesis in relation to the truncation problem are presented in Chapters 3 and 4.

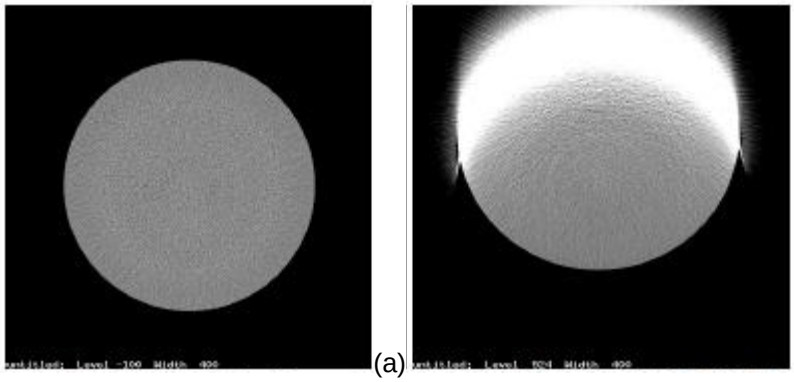

(a) (b)

Figure 2.43: Two CT images of a reconstructed phantom 50cm in diameter. (a) shows the true image of the phantom with no truncation. (b) shows the artefacts produced when the

top edge of the phantom is truncated by 8cm outside the FOV and reconstructed using a conventional algorithm (Li and Heish 2007).

The truncated data problem is currently an area of extensive research within the medical field and has been subdivided depending on the desired outcome. The two main areas are ROI CT and FOV extension. ROI CT aims to reconstruct a ROI from a set of truncated projection data, whereas, the second category aims to not only reconstruct the ROI but extend the scanning FOV i.e. reconstruct the entire object from only ROI scan data. Many techniques have been proposed to reduce or overcome the effects associated with truncated projection data for both ROI CT (Chun *et al* 2004; Schillinger *et al* 2004; Simon *et al* 2004; Sourbelle *et al* 2004; Leng *et al* 2005; Ravishakar *et al* 2005; Li *et al* 2007) and extending the scanning FOV (Nassi *et al* 1982; Sivers 1995; Ohnesorge *et al* 2000; Li and Heish 2007; Zamyatin *et al* 2007; Anoop and Rajgopal 2009).

Helical cone beam and circular fan beam source geometries (third generation) have dominated commercial medical CT systems. Therefore the majority of the current methods for overcoming the truncated data problem have only been developed for these systems and have not been applied to circular cone beam geometry. This has resulted in a new area of research focused on adapting medical methods, which can handle truncated projection data, to circular cone beam geometry (Ramamurthi and Prince 2003; Weigert *et al* 2004; Cho *et al* 2006; Yu *et al* 2006; Neutsch *et al* 2008; Wang and Yu 2008). The main reasons for the recent interest in cone beam scanning methods using approximate reconstruction algorithms can be attributed to improvements in flat panel detectors and increased acquisition speed (more details provided in section 2.2.3.5).

2.2.5.1 Region-of-Interest CT

It is not uncommon in X-ray CT imaging that the FOV of the CT system is smaller than the object. In fact, the imaging task may require an ROI to be reconstructed that fully covers the FOV but is significantly smaller than the object size. Developing methods so that these ROI scans can be reconstructed would effectively increase the spatial resolution of the CT scan and allow regions of large objects to be accurately imaged.

Recent developments within helical CT scanning have allowed the reconstruction of ROIs within truncated projection data. The condition being that the ROI to be reconstructed must not be truncated in any views (Leng *et al* 2005). This means that the object function can be truncated but the ROI that lies within the object function cannot be truncated in any views. These recent algorithms fall into two classes. The first class of algorithms are all

FBP type and are based on Katsevich algorithm (2002a, b). The second class of algorithms are based on the Zou Pan Back Projection Filtration (BPF) algorithms[4] (Zou and Pan 2004a, b).

The ROI problem for 2D parallel beam and fan beam CT has also been widely investigated (Faridani *et al* 1992a, 1992b, 2001; Ramm and Katsevich 1996; Wang *et al* 1996 cited in Anastacio *et al* 2007; Faridani and Ritman 2000; Chun *et al* 2004; Sourbelle *et al* 2004; Ravishakar *et al* 2005), but it has been identified by Anastacio *et al* (2007) that the 3D ROI CT problem for circular cone beam scanning continues to be largely unexplored.

The developed algorithms for ROI CT in circular geometries can again be categorised into two groups, similar to recent developments described for helical CT scanning. The first class are based on novel data rebinning schemes for FBP type algorithms and the second are based on BPF algorithms using PI lines.

1 FBP based methods

Conventional FBP algorithms for both circular fan beam and cone beam scanning require some form of novel data rebinning scheme to complete the projection data and overcome the truncation. The data completion approach has shown that an exact reconstruction of an ROI is often impossible but a fairly accurate ROI is achievable (Weigert *et al* 2004). This is because the missing portions of the cone beam projections only provide a small contribution to the exact result within the ROI. This suggests that rebinning or extending the projections so that truncated projections become non truncated projections and reconstructing with a conventional FBP type algorithm (such as the FDK) would give satisfactory results.

Data completion methods were first implemented for parallel beam projection data. Its basic concept is to fill out the missing portion of the projection data prior to applying one of the conventional reconstruction algorithms. The estimation of the missing data is normally based on extrapolating information available about the object (Anoop and Rajgopal 2009). Numerous methods exist that involve some kind of novel data rebinning to complete the projection data and remove the undesired consequences of truncated projection data (Lewitt and Bates 1978; Ramamurthi and Prince 2003; Chun *et al* 2004; Sourbelle *et al* 2004; Weigert *et al* 2004; Ravishakar *et al* 2005; Neutsch *et al* 2008). An early approach

[4] The BPF reconstruction algorithm acts by first computing the back projection of the data derivatives onto the PI lines and then performing a 1D filtering operation along them (Yu *et al* 2006). A PI line is a line segment (or chord) connecting any two points on a helix source trajectory (Cho *et al* 2006).

suggested by Lewitt and Bates (1978) to extend parallel beam truncated data was to make plausible assumptions about the shape of the object and the X-ray attenuation coefficients inside. This information was then extrapolated to fill out the missing projection data. The simple assumption that the object is a water cylinder and has a constant X-ray attenuation coefficient has been shown to give good results. The size of this estimated lateral extension is controlled by an extension factor. This is the ratio of the lateral size of the full non-truncated projections to the lateral size of the truncated projections (Weigert *et al* 2004). However, this simplified data completion approach has shown to give strong truncation artefacts when imaging regions with highly attenuating objects outside the detector FOV.

Similar to Lewitt's (1978) technique, Sourbelle *et al* (2004) and Ravishakar *et al* (2005) estimated the missing data using information extrapolated from within the ROI. Both of these methods took advantage of using parallel beam sampling geometry whereby the total attenuation for each ideal projection remains constant over all views.

For cone beam configurations, the vast majority of the concepts and assumptions used in parallel and fan beam cannot be directly applied. This is the primary reason for the limited amount of ROI techniques converted for circular cone beam CT. The majority of methods identified for cone beam ROI CT are a based on extending the truncated projection data using prior non truncated CT data of the whole object (Ramamurthi and Prince 2003; Chun *et al* 2004; Weigert *et al* 2004; Neutsch *et al* 2008). Specifically, these methods first involved reconstructing an intermediate CT image by extending the truncated data using extrapolated data. This intermediate CT image is then registered with the prior larger CT image of the whole object to produce a more accurate reconstruction. Note that in these methods the extended projection data outside the ROI is not reconstructed. It is only needed for the filtering step of the FBP algorithm, to provide an accurate estimate of the line integrals outside of the detector FOV. These prior CT based data completion methods for ROI imaging have shown to reduce the typical artefacts associated with truncated data. However, small ring shaped in-homogeneities are commonly reconstructed due to imperfect image matching.

2 BPF based methods

The second class of ROI CT algorithms are based on the BPF algorithm developed for helical cone beam CT (Zou and Pan 2004). Noo *et al* (2004) published a circular fan beam algorithm based on this approach, where the main idea adopted from Zou and Pan (2004) was backprojecting the derivative of the projections. Here, the derivative of the projections

is taken rather than the usual ramp filtering with conventional FBP. This results in a backprojected image that corresponds to a Hilbert image[5] rather than the correct image. Therefore the correct image can be recovered by inverting the Hilbert image using the 1D Hilbert transform. The main benefit of Noo *et al* (2004) two-step Hilbert transform method over conventional FBP is the ability to handle truncated projections. The two step approach allows the derivative of the remaining projection to be calculated even when truncated; so at least part of the backprojected image remains unaffected by the truncation. This means that in certain situations a ROI within an object can be accurately reconstructed even though the projection data is truncated. The conditions of ROI reconstruction within an object using the two step Hilbert method are (1) that the ROI lies within the FOV for all projections and is not truncated and (2) that the ROI lies within the union of all straight lines that do not intersect a truncated region of the object.

Only one adaptation of the BPF algorithm for circular cone beam geometry could be found. This method, developed by Cho *et al* (2006), consists of an approximate BPF algorithm for ROI imaging based on the exact BPF algorithm for helical cone beam CT (Zou and Pan 2004). It has been shown that the ROI BPF algorithm can reconstruct an exact ROI within the mid-plane and approximate an ROI off the mid-plane. An exact solution within the mid-plane exists as this is where the source trajectory is located, meaning the BPF algorithm can be adapted to reconstruct along the PI lines (helical CT). To utilise this concept for outside the mid-plane, stacked virtual source trajectories together with virtual PI lines have been introduced, as illustrated in Figure 2.44 (Clackdoyle *et al* 2004). These reconstructed images are free from the typical truncation artefacts, such as inflated pixel values, that dominate ROI imaging when using the FDK algorithm.

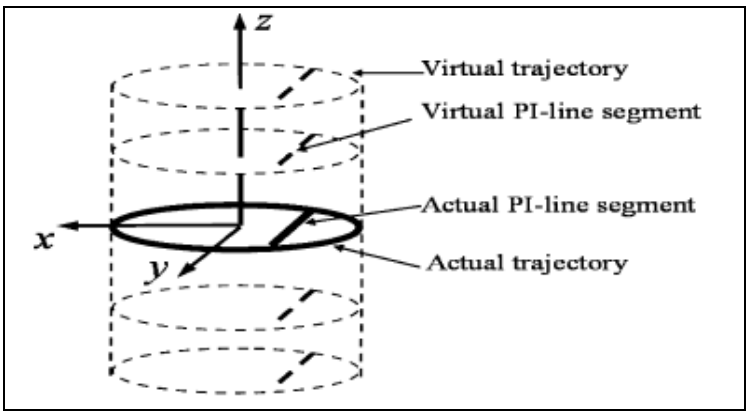

Figure 2.44: Illustration of the actual and virtual circular source trajectories including actual and virtual PI-line segments (Yu *et al* 2006).

[5] The Hilbert image is a Hilbert filtered version of the correct image.

The main drawbacks of this technique are: (1) the BPF algorithm for circular cone beam data, like the FDK, is an approximation and (2) an ROI can only be reconstructed if that ROI is non-truncated in all views (similar to the conditions for the two step Hilbert method). This could be an explanation for the results produced by Yu *et al* (2006) using the BPF algorithm for circular cone beam, as shown in Figure 2.45. The central non-truncated ROI within the object has been accurately reconstructed, but certain edges within the image still display strong 'glowing' artefacts as the 1D filtering lines in these locations intersect with truncated regions of the object.

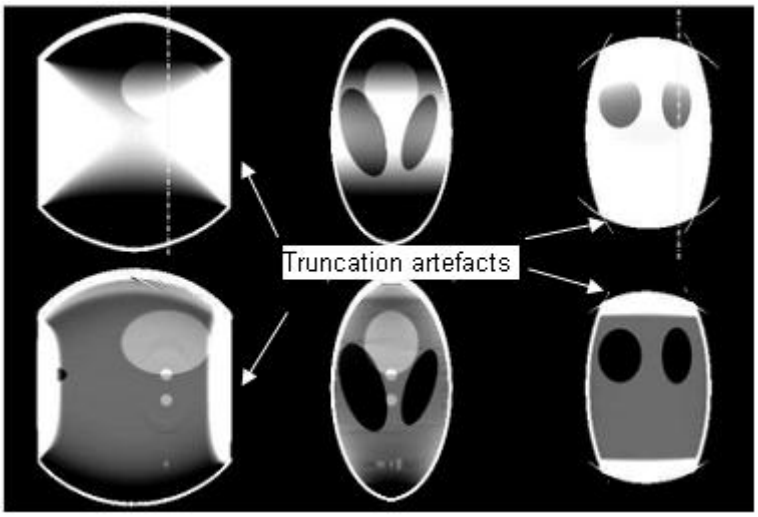

Figure 2.45: 2D cross sectional CT images of the Shepp Logan phantom. The columns represent 2D slices from different viewing planes (frontal, sagittal and axial). The top row is reconstructed using the FDK algorithm with truncated cone beam data. The second row is reconstructed using the BPF ROI algorithm with truncated cone beam data.

2.2.5.2 Extending the CT Scan Field-of-View

CT imaging a large patient or object using conventional methods results in a considerable portion of the peripheral region being outside the detector's FOV. Therefore, it is of great interest in both the medical and industrial field to develop methods that not only remove the typical truncation artefacts but also extend the reconstructed FOV beyond that of the detector.

Numerous methods have been developed to extend the CT scan FOV (Nassi *et al* 1982; Sivers 1995; Ohnesorge *et al* 2000; Heish *et al* 2004; Fu and Lu 2005; Dongbo *et al* 2006; Zamyatin *et al* 2007; Fu *et al* 2007; BIR ACTIS 2008; Anoop and Rajgopal 2009). They are all based on an FBP type algorithm, using some form of data completion to estimate

the missing data. Most of these methods have only been applied to conventional fan beam and cone beam helical trajectories. For the fan beam case the majority of data completion methods are based on some kind of novel detector shift and rebinning scheme (Fu and Lu 2005; Dongbo *et al* 2006; Fu *et al* 2007; BIR ACTIS 2008). Whereas, helical cone beam algorithms for extending the FOV are mainly based on estimating the missing data through linear prediction models (Anoop and Rajgopal 2009). The only method found that was not based on FBP type algorithms, is by Leng *et al* (2005). This used the Filtered Back Projection Differentiation (FPBD) algorithm on fan beam projection data acquired from an asymmetrically positioned detector. This algorithm is categorised under the BPF type as it utilises the chord concept (i.e. PI lines) within source trajectories.

To review the relevant literature on the data completion techniques for extending the FOV, the techniques were split into two groups. The first group of algorithms involve shifting the detector and the second group estimate the missing data outside the FOV without the need to shift the detector.

1 Extending the FOV using detector shifting

As previously mentioned, the majority of methods developed for extending the FOV have been for fan beam geometries and are based on shifting the detector and rebinning the projection data. A method developed by Fu and Lu (2005) falls under this category. This algorithm was based on the short scan redundancy theorem by Parker *et al* (1982) and used fan beam projection data acquired from an asymmetrically positioned detector. Fu and Lu (2005) showed that to meet the minimum sampling requirement a full 360 degree rotation is needed. The premise being that rebinning the data to parallel beam geometry will allow the missing half of the projection to be sampled after a 180 degree rotation. So basically, each truncated projection is extended to give a full non-truncated projection using data already acquired. This allows a reconstruction to be performed that extends the CT scan FOV. Several adaptations of this method have been produced with similarly effective results (Dongbo 2006; BIR ACTIS 2008)

Another method based on a data completion approach using an asymmetrically positioned detector has been developed by Nassi *et al* (1982). In this instance, the missing projection data is estimated using sinogram reflection and then iteratively improved with a method of reprojection known as Iterative-Reconstruction-Reprojection (IRR).

Only a small number of FOV extension techniques were identified for use with circular cone beam geometry (Sivers 1995; Zeng *et al* 2007). These techniques were based on

novel detector shifting schemes that did not require an asymmetrically positioned detector. Specifically, they involved multiple CT scans at different detector positions being merged together to convert a number of partial data sets into one complete data set.

2 Extending the FOV without shifting the detector

The second group of algorithms extend the FOV without shifting the detector. These approaches have again been implemented for fan beam geometries, whereby an important aspect is the rebinning to parallel beam data. The advantage of using this sampling configuration is that the total attenuation of each ideal projection remains constant over all views. This means that truncated projections can be identified in the sinogram and the amount of truncation can be estimated. Different methods exist that exploit this property to extend the reconstructed FOV (Ohnesorge *et al* 2000; Heish *et al* 2004; Zamyatin *et al* 2007). It has been shown that these algorithms, to some extent, can suppress the truncation artefacts and approximate structures outside the FOV. The performance of these three reconstruction algorithms for extending the FOV were compared by Li and Heish (2007). The first algorithm, developed by Ohnesorge *et al* (2000) uses symmetric-mirroring of the sinogram to estimate the missing data within the truncated projections. The second (Zamyatin 2007) is a sinogram decomposition algorithm that completes the missing parts of the sinogram by interpolating between the boundary values. The final algorithm developed by Heish *et al* (2004) is a water cylinder fit method based on Lewitt's data completion method for ROI tomography (Lewitt and Bates 1978) (see section 2.2.5.1). Figure 2.46 illustrates some of the reconstruction results used to compare the performance of these algorithms. Li and Heish (2007) concluded that the water cylinder fit method produced the better results. Typical glowing truncation artefacts were suppressed and structures outside the FOV were reasonably approximated with only small inaccuracies. However, darker shading artefacts were introduced at the point of truncation in all three algorithms.

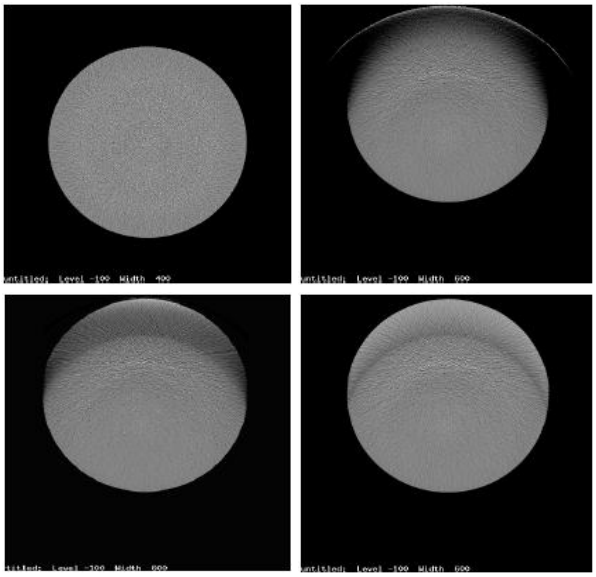

Figure 2.46: Example CT images resulting from the three FOV extension methods evaluated (Li and Heish 2007). Top left – True image; top right – sinogram mirroring (Ohnesorge *et al* 2000); bottom left: sinogram decomposition (Zamyatin 2007); bottom right: water cylinder fit (Li and Heish 2007). The phantom is 50cm in diameter and the top edge was truncated by 8cm outside the FOV.

2.2.5.3 Current Industrial Techniques for ROI CT and Extending the Field-of-View

The medical industry is leading the field in expanding the capabilities of X-ray CT with industrial research organisations struggling to compete in terms of resources and expertise. Some novel yet limited techniques have been developed in recent years to suppress truncation artefacts. But as expected, the majority of industrial developments have been made through adapting medical CT imaging methods.

For ROI CT imaging, Weigert *et al* (2004) adapted a technique developed initially in the medical field by Ramamurthi and Prince (2003). This uses prior non-truncated cone beam CT data of the whole object to extend and complete the truncated projection data (see section 2.2.5.1). However, this has shown to be susceptible to imperfect image matching leaving ring shaped artefacts. A second ROI technique found to be used for industrial cone beam CT applications was published by Schillinger *et al* in (2004). This method is a very simple post processing step that multiplies the single plane 2D reconstruction data by a quadratic mask. The diameter of this mask is slightly smaller than the reconstructed FOV, basically removing the worst of the truncation artefacts found at the edge of the FOV. The techniques contributed by this thesis in the field of ROI CT imaging are presented in Chapter 3. Specifically, two different data completion methods were

developed and their performance compared for application with high resolution ROI inspection of CFRP laminates.

The limited number of techniques found in the industrial field for ROI CT imaging are based on cone beam geometry. This is the geometry found in most industrial CT systems. However, techniques for extending the FOV are still largely limited to fan beam sources. This is due to the fact that cone beam techniques for extending the FOV are still an ongoing research area even in the medical field.

Nearly all the current industrial methods for extending the FOV are based on detector shifting and ray redundancy methods for fan beam geometry (Fu and Lu 2005; Dongbo *et al* 2006; Fu *et al* 2007; BIR ACTIS 2008). Some cone beam methods have been developed that require multiple scans with novel detector translation schemes. These are based on a combination of 2nd and 3rd generation acquisition configurations to obtain the partial data sets needed to reconstruct the entire object (Sivers 1995; Zeng *et al* 2007). The FOV extension techniques contributed by this thesis are presented in Chapter 4. In this work, two different data completion methods were investigated for use with an asymmetrically positioned detector in a cone beam CT system. The performance of these two techniques was investigated for application with large wind turbine blade inspection.

2.2.6 Setup of the CT system

2.2.6.1 CT Instrumentation

The majority of the work presented within this thesis used a commercially available, third generation X-ray CT system (HMX 225) supplied by Metris X-tek Ltd. The system comprised:

- A micro-focus X-ray source based on cone beam geometry with 4 different anode targets available (Tungsten, Silver, Molybdenum, and Copper). Minimum focal spot size of 10-15µm, a maximum tube potential of 225kV, and maximum tube current of 2mA.
- A 5 axis rotating manipulator capable of handling up to 25kg load, a source to detector distance of up to 1059mm and geometric magnification up to160x.
- A detector system consisting of an image intensifier coupled to a Charge Coupled Device (CCD) based digital camera. The image intensifier had a field of view of approximately 220mm diameter with a CsI scintillator covered by a carbon fibre

front screen. The camera was a Thales CCD high resolution 12 bit digital detector with 900x900 pixels and 160µm pixel size.

- The control console consisted of an AMD Opeteron™ processor, 2.01Ghz and 3GB of RAM. The source, manipulator, detector and CT data acquisition was controlled by X-tek InspectX software that digitised the radiographic images to 16 bit format. The CT reconstruction software was provided by Metris X-tek (CTpro) and the CT visualization software was VGStudioMax, which generated the CT images in 8 bit format.

A schematic diagram of the imaging arrangement in the CT system is shown in Figure 2.47(a). Photographs of the actual system, identifying the X-ray source, manipulator and detector system are shown in Figure 2.47(b).

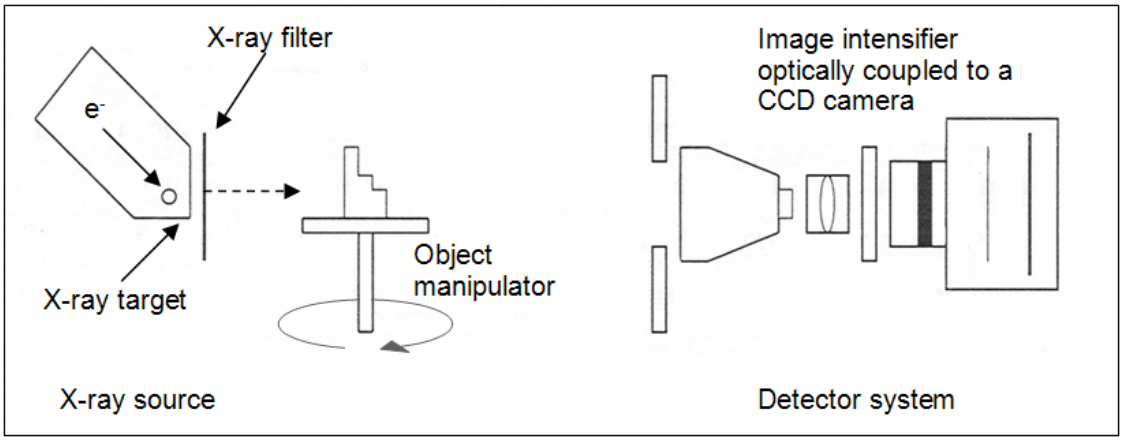

(a)

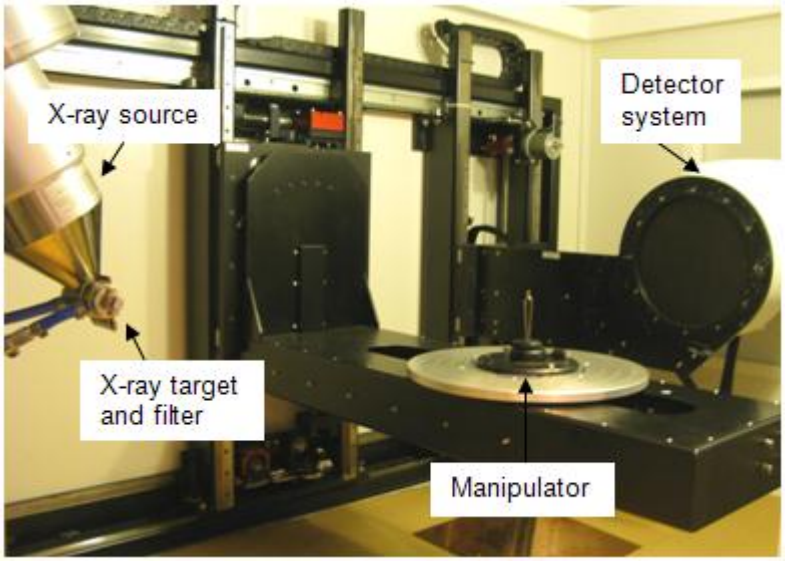

(b)

Figure 2.47: (a) Schematic of the CT imaging setup and (b) Photograph showing the key instrumentation.

2.2.6.2 Setup and Calibration

Before acquisition of the CT projection data it was very important to ensure all the imaging instrumentation (X-ray source, manipulator and detector) was accurately set up and calibrated relative to each other. If the necessary calibrations are not completed then the CT reconstruction will be distorted and dominated by artefacts. The three main calibration procedures carried out as part of the CT scan setup were as follows:

(1) Spatial distortion correction. This calibration is necessary to correct the non-linearities in the imaging system. The procedure consisted of imaging a linearity plate to measure the horizontal and vertical distortions introduced by the imaging system. The CT acquisition routine then identifies the distortion within this reference image to correct the raw projection data. If this calibration was not performed the non-linearities would result in reconstruction artefacts such as ring artefacts (see section 2.2.4.5)

(2) Shading correction. Similar to the point above, this calibration is necessary to correct for shading non-linearities in the detector system. For Thin Film Transistor (TFT) based flat panel detectors, this is to correct for the gain and offset within the detector electronics (see section 4.4.1.3). For image intensifier based systems, the correction is needed due to the intensifier focusing higher concentrations of light photons at the centre of the CCD camera. The calibration procedure requires the acquisition of white and black reference images at every tube potential setting. This can be performed automatically with the acquisition software.

(3) System alignment. This calibration is imperative to the CT process as the reconstruction algorithm defines the ray paths relative to the centre line of the cone beam. Therefore, the X-ray source and detector must be aligned, both horizontally and vertically, along the principal axis of the CT system. This is defined by the line joining the X-ray focal spot to the centre of the detector front screen. It is also important that the axis defining the centre of the rotation of the turntable was accurately aligned perpendicular to the principal axis of the system.

Once all of the calibration procedures were complete, collection of the raw projection data could be performed.

2.3 Summary

The first part of this literature review highlighted the potential benefits of CT as a defect characterisation tool for FRP composites. Several techniques that are commonly used for composite inspection were discussed and their capabilities regarding composite inspection was compared. It was confirmed that many of the weaknesses identified could potentially be overcome using CT inspection.

The focus of the literature review was then X-ray CT and identifying the limitations of this technique that effects its application to FRP composites. One area that requires further attention is the inspection setup due to the lack of standards and guidance on the subject. It has been shown in literature that choosing the correct inspection settings can optimise the image quality achieved for radiographic inspection (section 2.2.4). However, CT acquisition and reconstruction has different constraints and conditions that need to be met in order to achieve an accurate CT image free from artefacts. One of these constraints is the limited effective dynamic range of the CT inspection. This presents a significant problem when inspecting multi density objects or objects with a large thickness latitude. The difficulty lies in achieving optimum inspection settings for the different materials present whilst still keeping within the constraints of the dynamic range (described in section 2.2.4).

The truncated data problem and the current methods that aim to overcome the different aspects of this problem were discussed in detail in section 2.2.5. It has been identified that the majority of techniques for both ROI imaging and extending the FOV are in the medical field and are based on system geometries used predominantly within this field. Therefore, most of these techniques cannot be directly applied to circular cone beam geometry, the most commonly used configuration in industry. For ROI imaging, the small number of methods that have been applied to cone beam geometries are limited in their application and still display artefacts near the site of truncation (Ramamurthi and Prince 2003; Chun *et al* 2004; Weigert *et al* 2004; Neutsch *et al* 2008;). These techniques are mainly based on completing the missing projection data using prior CT images of the entire object. Clearly, this approach requires the entire object to be able to fit within the FOV so that the prior CT data can be acquired. Therefore, ROI inspection of a large object cannot be achieved, which is one of the primary reasons for developing such techniques. Extending the CT scan FOV is a different side to the truncated data problem. Again, current techniques found in literature are mainly based on fan beam geometries utilising ray redundancy properties (Fu and Lu 2005; Dongbo *et al* 2006; Fu *et al* 2007; BIR ACTIS

2008). At the time of writing this literature review no FOV extension techniques could be found for application with circular cone beam geometries.

Chapter 3

Development of Region-of-Interest CT Techniques for Defect Characterisation in CFRP Laminates.

3.1 Introduction

This chapter describes the development and validation of two different data completion methods for high resolution Region-of-Interest (ROI) CT inspection of Carbon-Fibre-Reinforced-Plastic (CFRP) laminates. The aim of this work was to overcome the artefacts and reconstruction errors associated with truncated projection data so that ROI CT inspection could be utilised for CFRP composites.

Since the widespread use of CFRP composite materials for product application is still in its infancy, (compared to the use of metallic structures) it is not sufficient to simply detect any defects present. It is very important to determine the cause of the defect, the defect location, severity and impact on the performance of the structure as a whole. From this perspective, it is imperative that accurate inspection results are related to analytical models and mechanical testing to gain information on structural reliability (more details in section 1.1). However, the mechanical anisotropy and heterogeneous composition of CFRP composites makes them more complex than metallic structures. As a result, defect detection and characterisation in CFRP composites is very challenging.

Currently, inspection of composite based structures requires multiple NDT techniques to detect and characterise the most significant defects (see section 1.1). The limitations of these conventional NDT techniques with regard to FRP composites have been discussed in section 2.1. CT has shown to overcome many of these problems and provide a very effective inspection tool for defect characterisation in FRP composite materials (Choudhry and Li 2008; Muralidhar and George 1999). However, inherent limitations of CT reconstruction restrict its uptake for use with many composite inspections. This is due to the majority of industrial CT systems using Filtered Back Projection (FBP) (see section 2.2.3) to reconstruct the projection data. This algorithm cannot accurately reconstruct transversely truncated projection data (see section 2.2.5), which places a constraint on the inspection such that the test object must fit within the Field-of-View (FOV) of the detector for each view angle. If the object extends beyond the FOV, the projection data

becomes truncated which causes truncation artefacts and missing data errors to dominate the final reconstruction (see section 2.2.4.5). These are caused by the sharp boundary at the site of truncation and the missing projection data (more details in section 3.4). This presents a significant problem when the imaging task requires an ROI to be reconstructed that fully covers the FOV but is significantly smaller than the object size. This type of reconstruction is very beneficial from an inspection point of view for two reasons: Firstly, it would allow ROI scans to take place on an object larger than the detectors FOV. Secondly, it would allow the use of higher geometric magnifications, resulting in increased spatial resolution and improved detectability of small features. This is particularly beneficial in terms of FRP composite inspection, as many defects such as fibre breakage and matrix cracking arise at the micro level and cannot be detected without the use of such high magnifications.

ROI CT aims to overcome the truncated data problem by suppressing the truncation artefacts and removing the inherent errors associated with the missing data. Research surrounding methods to overcome the truncated data problem have been reviewed in section 2.2.5. This literature review helped identify data completion methods[1] as the most applicable approach to overcoming the truncation problem. An important issue in this context is that, they could be implemented with the majority of industrial CT systems utilising the FBP type FDK reconstruction algorithm.

This chapter describes the development and validation of two different data completion methods for application with CFRP laminates. In the first method the missing projection data is completed using a simple low frequency curve based on the attenuation at the truncated edge. The low spatial frequency curve provided a simplified estimate to the object shape and a low spatial frequency tail off to zero attenuation. This removed the sharp boundary caused by the truncated edge and allowed filtration within the FDK algorithm to take place without the usual truncation artefacts. A more sophisticated approach was employed in the second method with the missing data estimated on the basis of a pre-defined model of the test object, this required prior knowledge of the test object such as dimensions and magnification.

[1] The basic concept of data completion approach is to fill out the missing portion of the projection data prior to reconstruction

The performance of both of these techniques was assessed quantitatively using error maps based upon an ideal reconstruction from un-truncated projection data. It should be noted that the development and validation of these techniques was first performed in Matlab (Matlab 2009b) for fan beam geometry. Application to cone beam projection data using commercial reconstruction software was conducted subsequently once the approach had been validated.

3.2 Objectives

The aim of this research was to develop new methods of data completion, and to establish their effectiveness in reducing or eliminating the errors associated with ROI CT of CFRP laminates. The ultimate aim of the ROI CT technique is to be able to accurately reconstruct:

- Regions of objects that are larger than the FOV of the detector.
- Regions of objects with very high geometric magnification.

The specific objectives for the research presented in this chapter were:

- To investigate and identify the source of errors in ROI reconstructions.
- To develop a data completion method for fan beam geometry that overcomes the truncation artefacts associated with ROI CT inspection of CFRP laminates.
- To develop a data completion method for fan beam geometry that overcomes all reconstruction errors associated with ROI CT inspection of CFRP laminates.
- To quantitatively validate the performance of both data completion methods.
- To implement the data completion methods for cone-beam ROI CT.

3.3 Fabrication of CFRP Laminated Samples

The investigative work in this chapter required a set of CFRP laminated samples to be fabricated for algorithm validation purposes. The aim being to fabricate a range of sample sizes having large aspect ratios in order to represent the most challenging situations in terms of CT inspection. An Image Quality Indicator (IQI) was introduced into a small region at the centre of the sample comprising laser drilled holes with a range of differently sized diameters and equivalent depths. Specifically, five holes were introduced with sizes; 500µm, 250µm, 100µm, 50µm and 30µm, using two different laser systems; the

Femtosecond and the Laservall[2]. The Laservall is a diode pumped solid state laser system with a 532nm wavelength. This system was used to drill the majority of the holes with an energy setting of 980mJ/cm^2. The Femtosecond laser has an 800nm wavelength and was only used to drill the 30µm. The energy setting used for this laser was 2J/cm^2. These laser drilled holes allowed performance measurements to be taken and the image quality resulting from different ROI techniques to be compared. This set of samples consisted of three different size panels, 50 x 50mm, 100 x 100mm and 150 x 150mm, each having a total 48 ply lay-up resulting in a sample thickness of 5mm.

The carbon fibre pre-impregnate (pre-preg) was Hexply 8552, supplied by Hexcel composites. This consisted of uni-directional carbon fibres and a toughened epoxy matrix (Hexcel n.d.). This pre-preg had a high cure temperature (180°C/356°F curing matrix) and is primarily used in the aerospace industry due to its excellent mechanical properties (Hexcel n.d.). The samples were cured using the Quickstep system available at the Northwest Composites Centre[3]. The Quickstep curing process (see below section 3.3.1) is different from using a conventional autoclave, as it involves a unique fluid-filled heated floating mould technology that applies the required pressure to the composite being cured (see Figure 3.1).

3.3.1 Sample Lay-up and Curing

The composite lay-up chosen for this set of samples was $(0/90)_{12S}$, where (0/90) means that one ply of pre-preg was laid up with the fibres orientated in the 0° direction, followed by another ply perpendicular at 90°. This was repeated 24 times, where at the halfway point the pattern was mirrored to make the entire lay-up symmetrical. The samples were cut and laid up in the required size prior to curing. As stated earlier, the samples consisted of three different size panels, 50 x 50mm, 100 x 100mm and 150 x 150mm, with the total 48 ply lay-up resulting in a sample thickness of 5mm.

During the lay-up process, the laminate samples were debaulked at regular intervals to ensure the pre-preg conformed to the correct shape and was consolidated over the entire surface area. The debaulking process required the samples to be covered with a

[2] The laser drilled holes were introduced based on the Author's specification by Dr. David Whitehead of the School of Mechanical, Aerospace and Civil Engineering, The University of Manchester.
[3] The CFRP samples were laid up and cured by the Author under the guidance of Dr. Alan Nesbitt at the Northwest Composite Centre at The University of Manchester.

perforated release film plus a nylon breather fabric and a low cost membrane and placed under vacuum for approx 10 minutes (see Figure 3.2(b)). This was repeated every 3 to 4 plies.

The Quickstep process used to cure the CFRP samples is a relatively new manufacturing technique for composites. It was developed to overcome some of the major operational difficulties with autoclaves, in particular, the slow production rates, the high costs and the high pressure requirements (Coenen 2005). Figure 3.1 shows the schematic of the Quickstep system. The pressure chamber uses a fluid filled bladder for heat transfer rather than air as used in an autoclave. This mechanism of heat transfer through a flexible bladder is beneficial due to the higher thermal conductivity of the Heat Transfer Fluid (HTF) and the shape flexibility of using liquids. This allows the temperature to ramp up very quickly and cure times to reduce. It also results in a lower resin viscosity which allows sufficient wetting of fibres without the high pressure required in an autoclave.

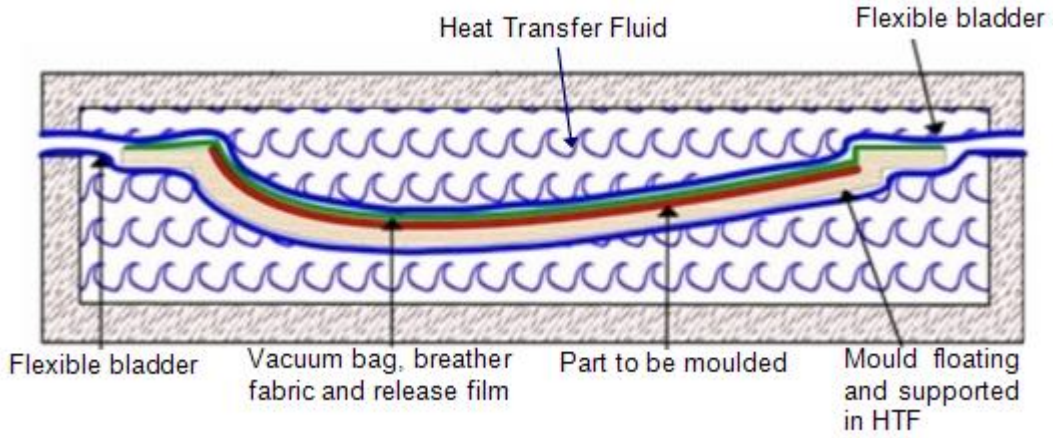

Figure 3.1: Schematic drawing of the Quickstep curing process (Coenen 2005).

Quickstep curing requires the composite samples to be vacuum packed for the entire process. Therefore, the same setup described earlier for debaulking was used except cork edging was applied to help prevent resin bleed out (Figure 3.2(a)). The entire setup was then placed inside the Quickstep system with the vacuum paths extended away from the main lay-up to allow the attachment of a vacuum pump and pressure gauge (Figure 3.2(b)).

The cure cycle for the Hexply 8552 pre-preg consisted of the following heating schedule (Hexcel n.d.):

- Heat at 1-3ºC/min to 110ºC ± 5ºC
- Hold at 110ºC ± 5ºC for 60 minutes ± 5 minutes
- Heat at 1-3ºC/min to 180ºC ± 5ºC

- Hold at 180ºC ± 5ºC for 120 minutes ± 5 minutes
- Cool at 2-5 ºC per minute

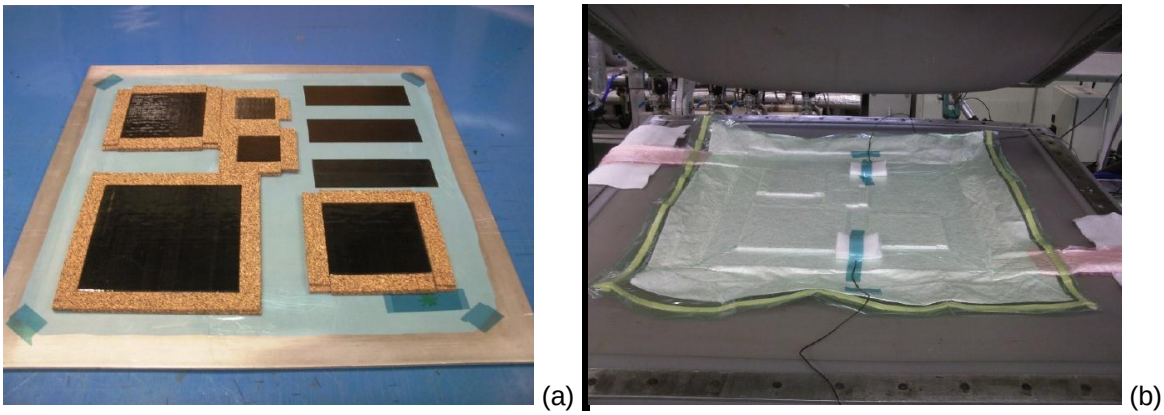

(a) (b)

Figure 3.2: (a) Final sample lay-up with cork edging and (b) vacuum packed samples in the Quickstep system ready for curing.

The final set of samples is shown in Figure 3.3 including a magnified photograph of the laser drilled IQI described earlier in section 3.3.

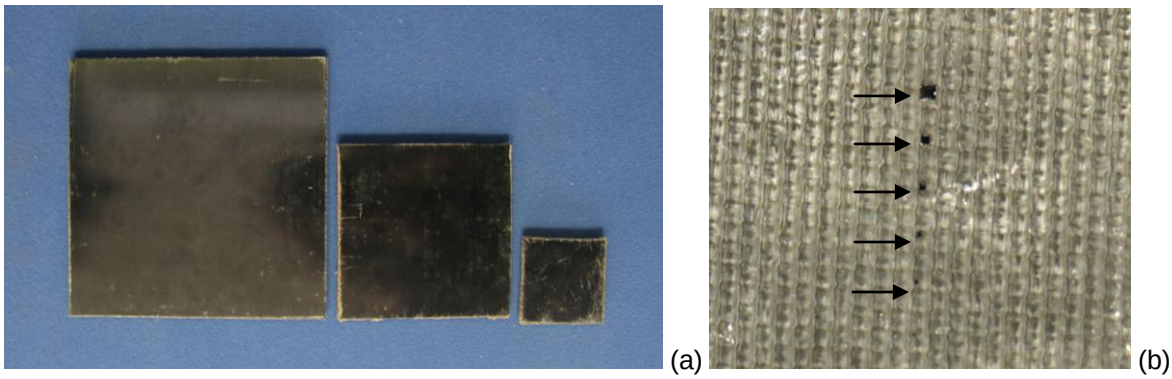

(a) (b)

Figure 3.3: (a) The fabricated CFRP laminated samples and (b) the six laser drilled holes forming the IQI.

3.4 Region of Interest CT

As stated previously, one of the basic requirements of conventional CT scanning is that the object being inspected must fit within the detector's FOV at all times during the scan. In an ROI CT scan the object extends beyond the FOV of the detector, so the condition is not satisfied and the projection data is truncated in many views. Direct reconstruction of this projection data using the common FBP type algorithms will result in images of the object that have inherent errors caused by the missing data and truncation artefacts

(described in full in the following sections 3.4.1 and 3.4.2). These combined errors can mask significant information about the object and can stop accurate density measurements or volume segregation taking place.

The errors within the reconstruction can be broken down into two categories. The first is related directly to the missing attenuation information from the parts of the object that extended outside the FOV. The second is the ringing or truncation artefacts caused by the processing of the truncated edge in the FBP algorithm.

3.4.1 Errors Arising from Missing Data

The following example illustrated in Figure 3.4 oversimplifies the FBP algorithm (particularly for cone beam geometry), but is useful in demonstrating why missing or incomplete data results in reconstruction errors. Consider ROI CT applied, with fan beam geometry, to a single density panel with an aspect ratio of A:1. If the ROI covers 50% of the width of the panel then projections taken at 90° have 25% of the projection data missing from both sides.

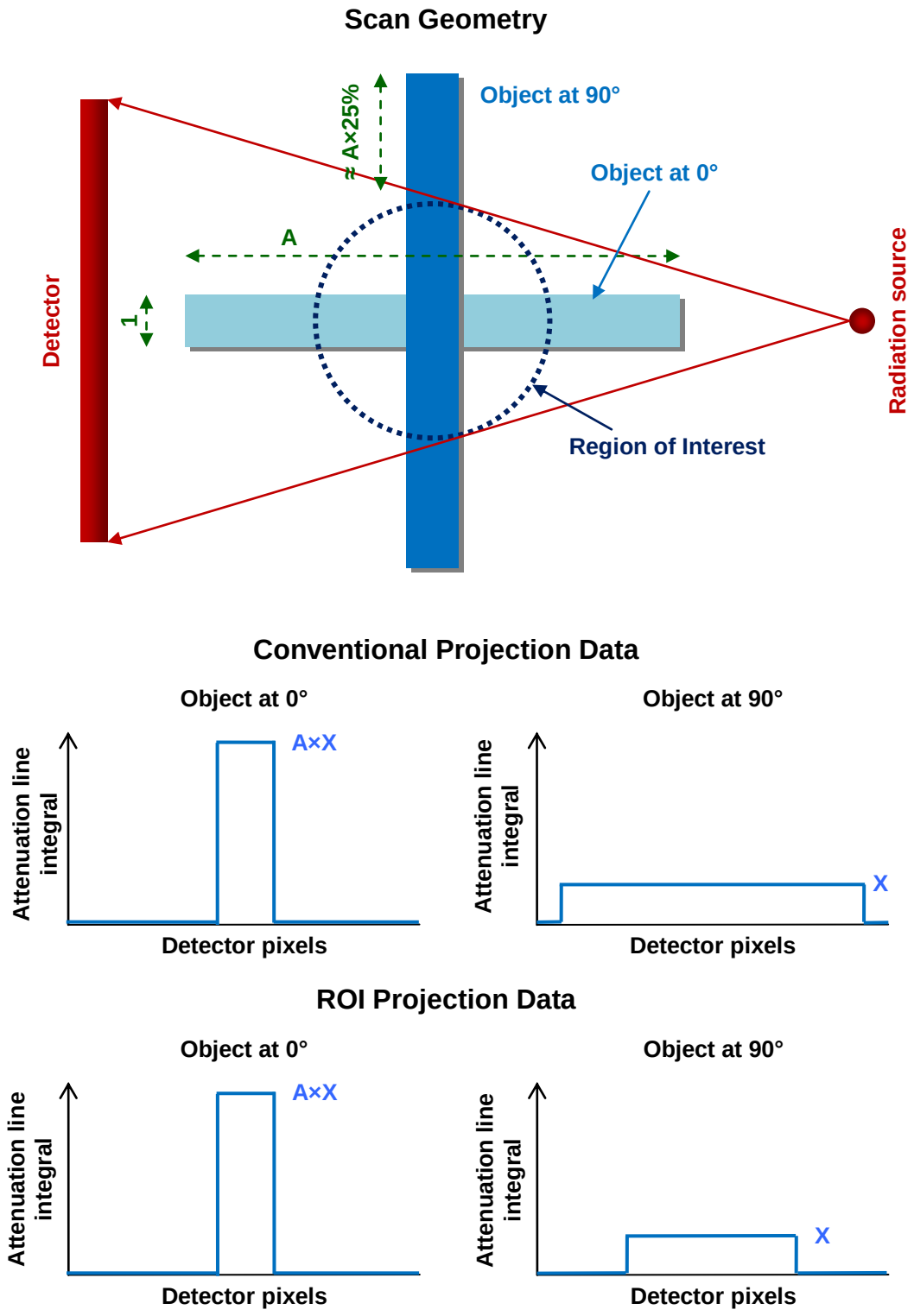

Figure 3.4: Illustration of the missing data problem associated with a ROI CT scan.

At this projection angle (90°), all the pixels of the detector measure the sum of the object attenuation to be ≈ X. At 0° i.e. an end-on projection, the pixels of the detector measure the sum of the object attenuation to be ≈ A×X. In a conventional CT scan the area under the line profile for the 0° projection would equal the area under the line profile for the 90°

projection[4]. In an ROI scan, this is not the case. In this example, the area under the line profile for the 90° projection is only 50% of the area under the line profile for the 0° projection.

When the FBP algorithm is applied to these projections, it does not take into account that 50% of the object is outside the FOV. Therefore, the object density values cannot be correctly resolved in the reconstruction. The result is a reconstructed image where the attenuation coefficients do not match those in an equivalent reconstruction using the full (un-truncated) projection data.

3.4.2 Truncation Artefacts

Truncation or ringing artefacts are a second form of reconstruction error associated with ROI CT. These artefacts are visualised as inflated pixels or 'glowing' regions propagating from the truncated edges within the reconstructed CT images. They are caused by the presence of the sharp boundary introduced at the edge of each of the truncated projections (see section 2.2.4.5). Specifically, the filtering of this sharp transition during application of the FBP algorithm is the cause of the truncation artefacts (Weigert et al 2004). As discussed in section 2.2.3, the FBP algorithm uses the inverse Radon Transform with a ramp filter. The basic inverse Radon transform has an inherent point spread function, which has the effect of blurring the final reconstructed image. The ramp filter is the inverse of that point spread function, and when included in the algorithm it reverses the point spread function, resulting in a crisp, defined, reconstructed image. However, the ramp filter is a high pass filter. This means high frequency elements of a given signal will be emphasised when the filter is applied. For truncated data, the projection signal drops sharply from the attenuation found at the edge, to zero, in the width of one pixel. This sharp transition is represented in the frequency domain by very high frequency components. Therefore, when the ramp filter is applied to truncated data, it creates a massive spike in the projection data at the point of truncation. Figure 3.5 shows an arbitrary projection profile for a single row of detector pixels (shown in red). A second line (in blue) shows the same data, but truncated. This represents the projection data from an ROI scan i.e. object data extends beyond the FOV of the detector.

[4] This condition is true for parallel beam geometry and is utilised for some data completion methods whereby the fan beam data is rebinned to parallel beam geometry (see section 2.2.5).

Note that this projection profile is shown as attenuation line integrals, not radiation intensity. Radiation intensity is the direct pixel output of the radiation detector i.e. the raw X-ray projection images. These are converted to attenuation line integrals prior to reconstruction by taking the negative logarithm of the ratio of the transmitted and incident radiation intensity. This is derived from the Beer Lambert law for X-ray attenuation (Equation 2.2 - see section 2.2.3 on reconstruction theory). The projection data presented in this chapter, unless explicitly stated otherwise, is represented as attenuation line integrals, which has no units.

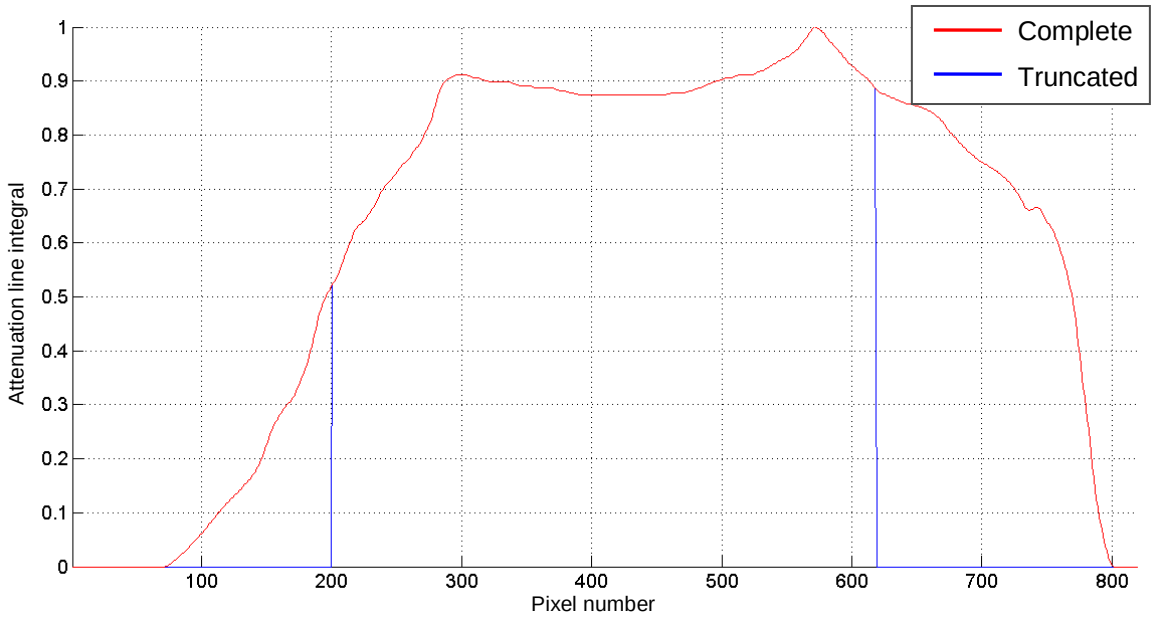

Figure 3.5: Example of an arbitrary projection profile for a single row of detector pixels. Full projection (red) and truncated projection (blue).

Figure 3.6 shows the results of applying the ramp filter to the signals in Figure 3.6. There are two points of interest to observe in this graph. Firstly, note how the filter has entirely changed the visual appearance of the ideal (un-truncated) signal (in red). The slowly changing signal that is lifted high for most of its width is represented by low frequency elements. In contrast, all the points where the signal changes sharply are represented by high frequency elements and are strongly emphasised.

The second feature is the difference between the ideal, and the truncated signal. It has already been observed that the filter emphasises rapid changes in the signal, and the artificial edge created by the truncation is an extreme example of this. The sudden decent of the signal to the background level (an un-attenuated radiation path which, in this instance is 0) causes huge spikes in the filtered signal at the points where the projection

was truncated. The effect of these spikes permeates a substantial distance into the adjacent areas of the signal. This is known as ringing (hence the alternative name; ringing artefacts). Based on the resulting difference between the two signals, errors can be expected upon reconstruction of the truncated projection data.

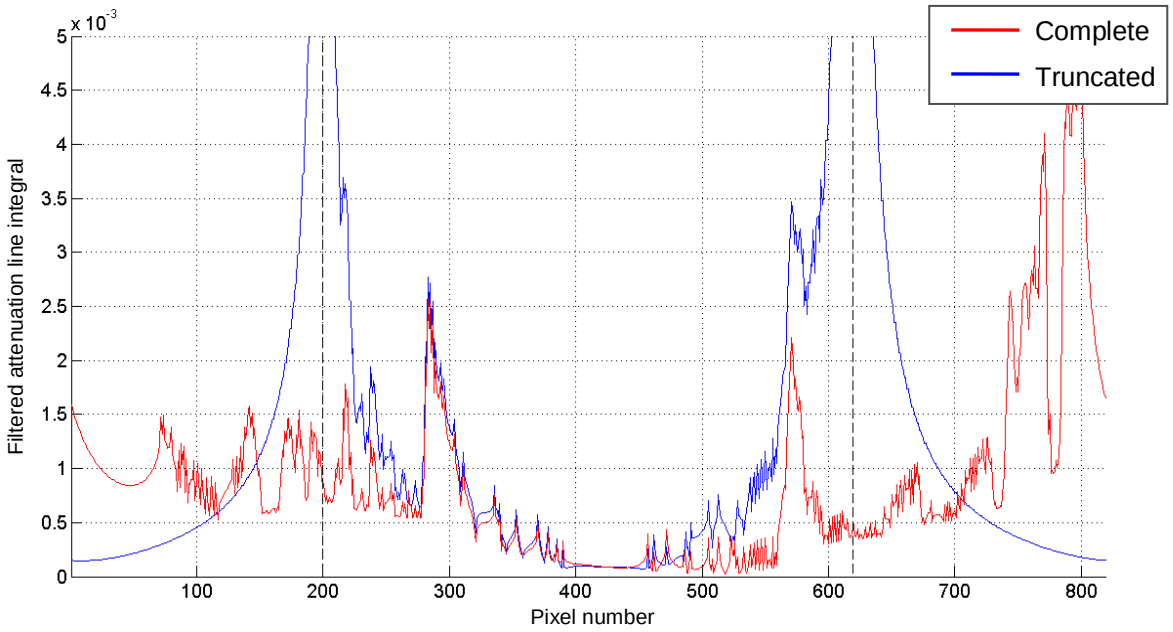

Figure 3.6: Resultant filtered projections based on the projection profiles shown in Figure 3.5. Full projection (red) and truncated projection (blue).

The projection data acquired during a CT scan will also contain locations where the signal changes very sharply, such as at the boundary of an object. These will result in sharp spikes in the filtered data as shown above. However, when the signal transitions occur because of a real object feature within the projections, they will:

1. not occur in every projection;
2. correspond with the edge location data in projections from other angles, and;
3. tend to be a more gradual change (thus represented by slightly lower frequency components).

Whereas, the artificial edges introduced by truncation:

1. occur in every projection where non-zero data is truncated;
2. do not match the edge locations in the other projections, and;
3. drop to the background level in the width of 1 pixel.

The result of reconstructing with these errors present is the truncation artefact. This typically presents itself as a bright glowing around the edge of the ROI, which propagates

or fades towards the centre of the image (see artefacts section 2.2.4.5). This artefact is illustrated in Figure 3.7 on a CFRP laminate sample.

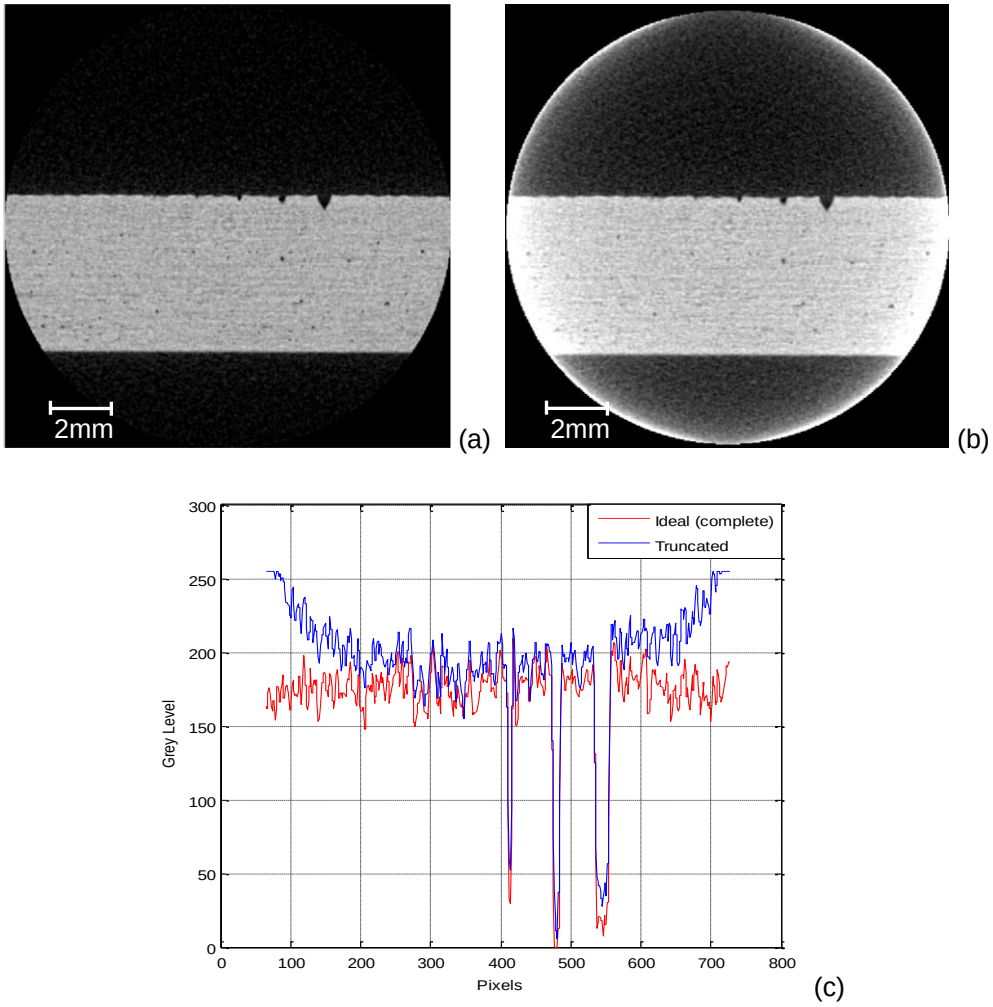

Figure 3.7: Reconstructed cross sectional CT images of a CFRP laminate panel. (a) Ideal reconstruction with complete projection data, cropped to match ROI scan results. (b) ROI reconstruction from truncated projection data. (c) Intensity line profile comparison.

The impact of truncation errors depends heavily on the application. For most industrial NDT applications, the most important aspect of the inspection is defect detectability. In this sense, truncation artefacts are the most problematic effect of ROI CT. This is highlighted in Figure 3.7, where the truncation artefacts mask large amounts of detail at the edge of the object within the reconstructed image. Additionally, the false intensity gradient, highlighted by the line profiles in Figure 3.7(c), makes it very difficult for accurate thresholding and segregation to take place. This poses a problem for inspections where accurate volume fractions are required.

The missing data errors are only problematic for inspections that require accurate measurement of the attenuation coefficients. One such application can be found in industry where accurate density measurements are required to verify models used for stress distributions in cast ceramics (Sawicka et al 1991). For the simple geometry objects investigated in the present research, the missing data has been shown to cause a small relative error between the image pixels but a significant absolute error is present. The small relative error means that defect detectability is not significantly affected by the missing data. This is because the pixels share an approximately common error value.

The objective for the majority of inspection work performed using CT is accurate defect detectability, rather than relative attenuation measurements. However, there are certainly inspection applications in industry that would require both of these criteria. The following experimental work describes the development and validation of data completion methods for ROI CT that consider both requirements.

3.5 Experimental Approach

The current state of the art for ROI CT has been reviewed in Chapter 2, section 2.2.5. From this data completion methods were identified as the most applicable approach to overcoming the truncated data problem for ROI CT. The basic concept of the data completion is to fill out the missing portion of the projection data prior to reconstruction. The experimental approach required that data completion methods be developed, and then evaluated for their effectiveness in terms of reducing the reconstruction errors produced. The process was often iterative in that success or failure of a particular idea led to a new understanding of the way the completion method effected the reconstruction, which in turn led to an improved method for data completion.

The basic procedure for assessing each data completion method was to:

1. Take a set of complete (un-truncated) projections.
2. Reconstruct those projections to create an ideal image for comparison.
3. Truncate the ideal projections to simulate an ROI scan.
4. Apply the data completion method to the truncated projections and reconstruct.
5. Assess the difference between the ideal image and the ROI reconstruction.

This process is illustrated in Figure 3.8.

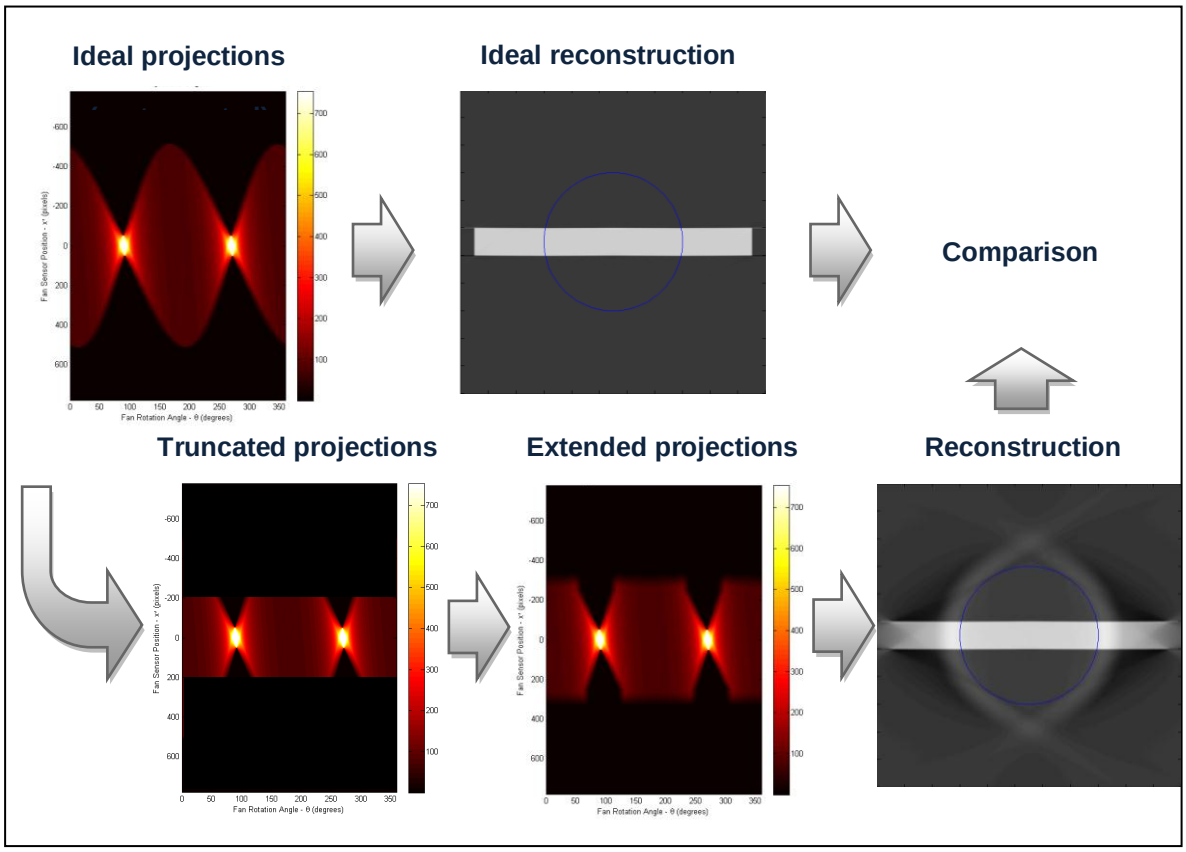

Figure 3.8: Experimental approach for assessing each data completion method.

3.5.1 Processing in Matlab

Data completion, reconstruction, and assessment of results were undertaken in Matlab. Fan beam functions were used to develop and validate the techniques prior to implementation with cone beam CT. All simulations used fan beam geometry with an equi-spaced (straight) detector (see section 2.2.3.4) and the FBP algorithm with a ramp filter. This is the same type of reconstruction algorithm and filter used in the cone beam setup provided by X-Tek Metris' CT system (see section 2.2.6).

The Matlab Image Processing Toolbox contains the required forward and back-projection algorithms, known as the `fanbeam` and `ifanbeam` functions, respectively. The `fanbeam` function produces the radon transform of the input data, using fan beam geometry. The input to this function is a cross sectional image and the output is projection data represented as linear attenuation integrals. The `ifanbeam` is the inverse of that function, taking projection data represented as linear attenuation integrals as an input and outputting a CT image of attenuation coefficients.

3.5.2 Projection Datasets

Two sets of projection data were used for all experiments. One was a set of projection data captured from a conventional CT scan of a CFRP laminate panel. The other was a simulated phantom with the same geometry as the CFRP sample data.

(1) CFRP Laminate Panel

The CFRP laminate panel was 50 x 50mm with a thickness of 5mm. The sample lay-up and fabrication process is explained in section 3.3. The CT system used to acquire the projection data is described in full in section 2.2.6. The radiographic settings used were 65kV, 122uA with a 1mm Aluminium filter placed on the source. Projection data was captured at 1500 equally spaced angles, which produced an image stack of cone beam projection data. To reduce this to a set of fan beam data (for use in Matlab) required the row of pixels in the horizontal mid-plane i.e. the cone mid-plane) to be extracted from each projection. This projection data was represented as radiation intensity received by the detector pixels (quantised and stored as 16-bit integers). Therefore, before the inverse radon transform (`ifanbeam` function) could be applied to the raw projection data, the radiation intensity values had to be converted into linear attenuation integrals (see section 3.4.2).

(2) Simulated Phantom

The simulated phantom of the CFRP panel was created in Matlab. This had the same size as the CFRP sample, and the same number of equally spaced projections. The phantom image had uniform density, and a uniformly zero background, with no added noise. The projection data was created by applying the `fanbeam` function to the phantom image, so the projection data was represented as attenuation line integrals from the outset; no conversion from radiation intensity was required.

The creation of both projection data sets is illustrated in Figure 3.9. Both sets of projection data (the simulated phantom, and the CFRP sample) are represented as attenuation line integrals (in sinogram format (see section 2.2.3.3)) in all the following experiments.

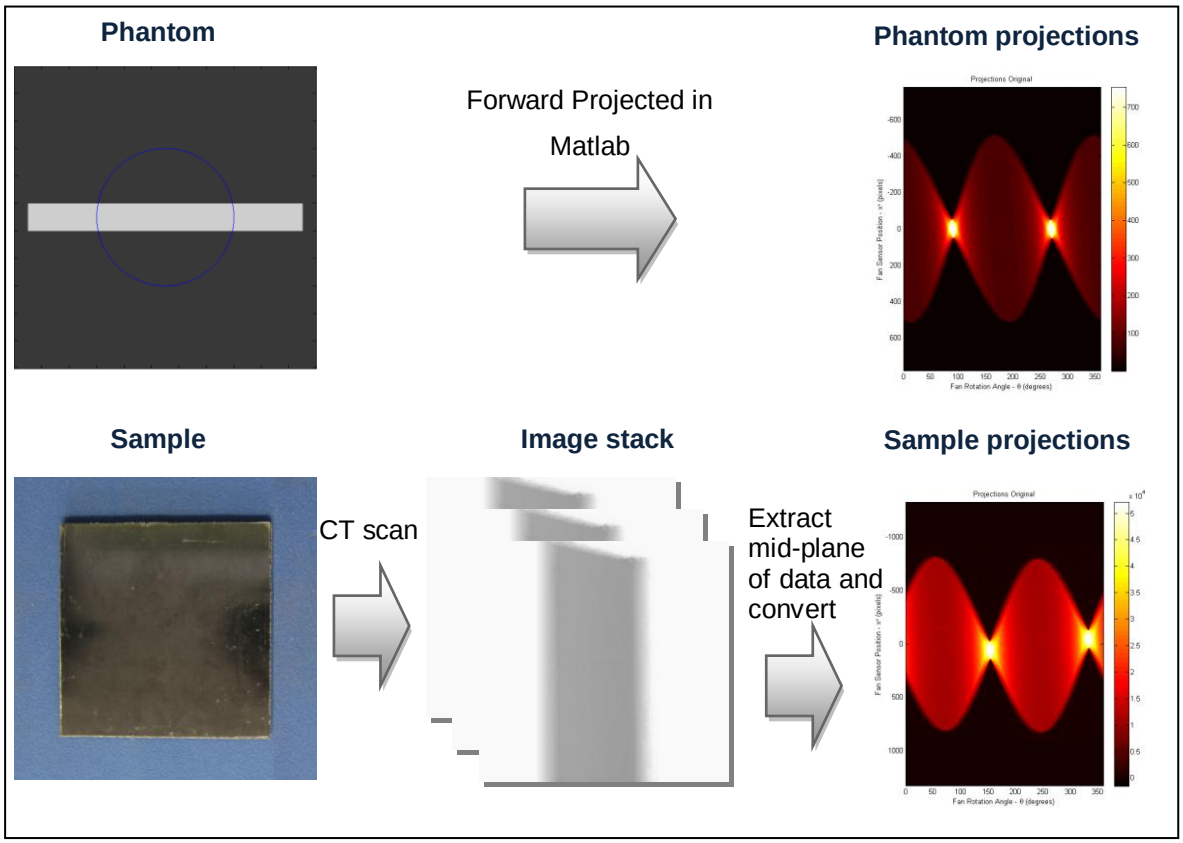

Figure 3.9: Illustration showing the creation of the simulated phantom projection data and the CFRP sample projection data.

To ensure the reconstruction results from the two data sets were directly comparable, all controllable aspects were kept the same, including:

- The number of projection angles (1500).
- The source to object distance (7772 pixels - 249.5mm)
- Number of pixels truncated (734 on both sides - 80% of the object).
- The number of pixels in the extended projections (1836 - the same as the un-truncated projection width).

3.5.3 Error Analysis

In order to quantitatively assess the performance of a data completion method two types of error comparison were established. The first provides an overall picture of the errors. An image is created where the pixel values are the absolute difference between the ROI CT reconstruction and the same area of the ideal reconstruction. This map of the errors is normalised by the mean value of a central area of the panel in the ideal reconstruction. Therefore, a 0.1 value in the error map corresponds to a reconstruction error equal to 10% of the ideal panel's attenuation coefficient. This ensures that the error values are

comparable between different reconstructions, even if the scale of the attenuation coefficients in each reconstruction is entirely different. Finally, the error map image is masked so that only the ROI area is shown. This removes any distracting artefacts and makes unbiased interpretation easier. This process is illustrated in Figure 3.10.

Wherever possible, error maps shown in this report use a common normalised error scale. In some maps this means that the maximum errors are out of range. Any error that is higher than the maximum value in the image scale (shown to the right of the error map) is visually limited to the maximum of the image scale.

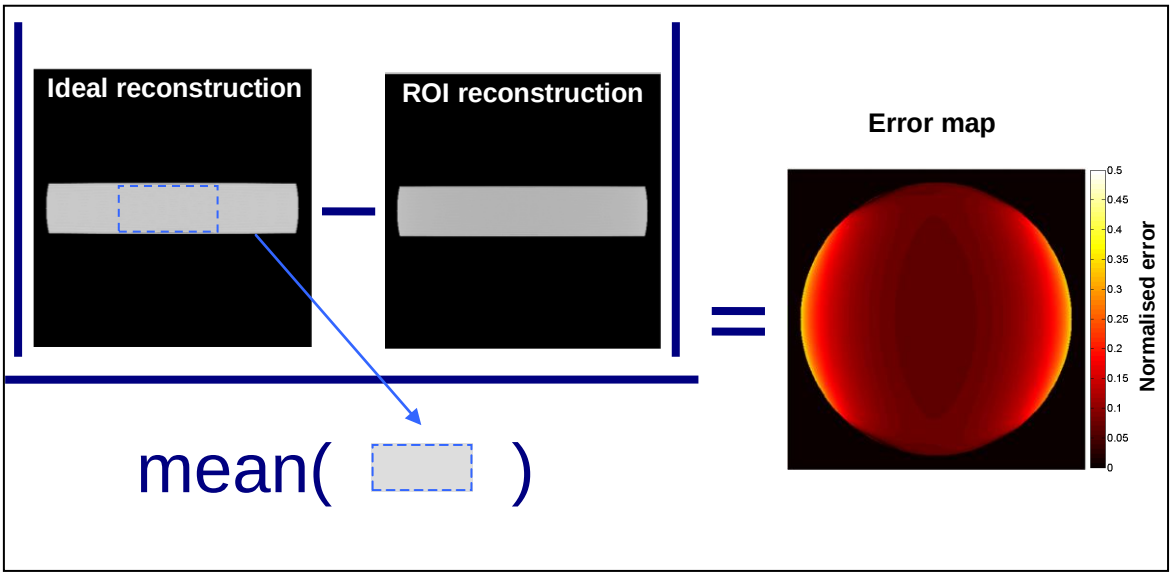

Figure 3.10: Illustration showing the process used to produce the error maps.

The second error comparison method was to statistically analyse all the pixels within the unmasked area of the error map and establish quantitative measurements. This included the mean, maximum, and minimum error values; and also the standard deviation. This provides quantifiable metrics that can be used to compare between data completion methods, while the error map provides a good picture of where the errors occur.

The ideal and truncated reconstructions and the resultant error maps are shown in Figure 3.11 and Figure 3.12. The process is illustrated for both the simulated phantom projection data and the CFRP sample projection data.

The first reconstructions produced for both datasets were ideal images using the full (un-truncated) projection data. Then the projection data was truncated by 80% leaving the central data intact (i.e. 40% removed from either side). The truncated projection data was

then reconstructed to demonstrate an ROI reconstruction without the employment of any data completion method. The results are shown in Figure 3.11 and Figure 3.12, for both the phantom and sample projection data. Note that while the simulated phantom was perfectly homogenous, some detail is visible in the ideal reconstruction. This reflects the inaccuracy of the projection and back-projection algorithms. As the number of the detector pixels and projection angles increases, these undesirable details will reduce and the ideal reconstruction will approach the perfect phantom.

The results show a distinct difference between the ideal reconstruction and the reconstruction from truncated projections for both the phantom and sample projection data. The truncation artefact (as described in section 3.4.2) is visible as glowing near the edges of the reconstructed region. Defects near the edges of the ROI could easily be obscured by this artefact. The significance of the errors across the entire reconstruction (from truncated projections) is even more evident in the error maps, as shown in Figure 3.11(c) and Figure 3.12(c).

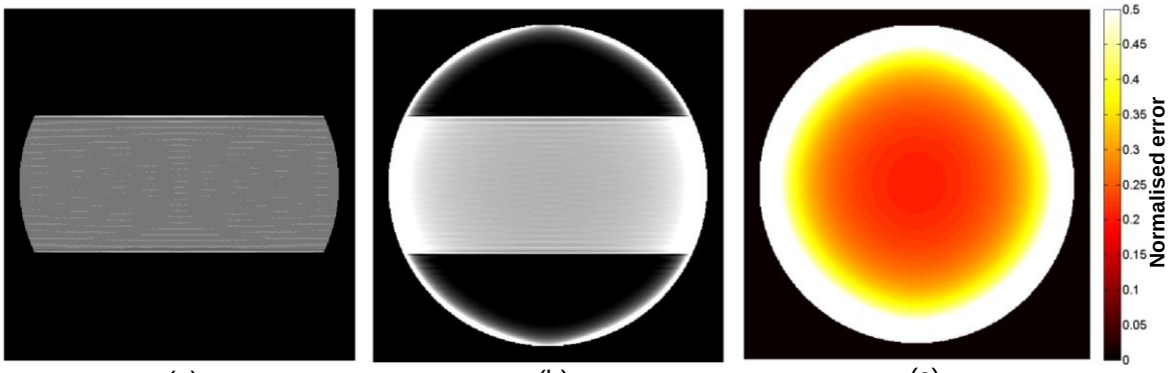

(a) (b) (c)

Figure 3.11: Simulated phantom reconstruction results. (a) Ideal (un-truncated) full projection data, (b) truncated projection data (80% truncation) and (c) corresponding error map.

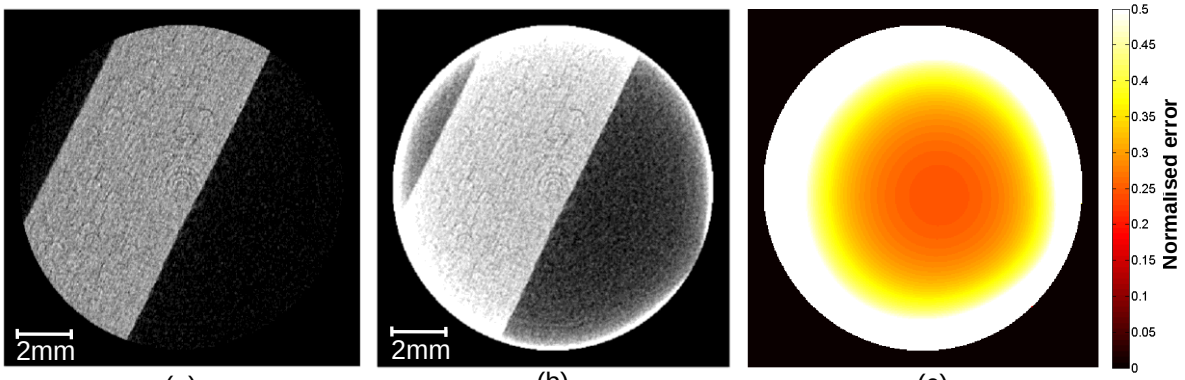

(a) (b) (c)

Figure 3.12: CFRP sample reconstruction results. (a) Ideal (un-truncated) full projection data, (b) truncated projection data (80% truncation) and (c) corresponding error map.

It should be noted that the image quality of the reconstructions for the CFRP sample data (Figure 3.12(a)) is not as high as that produced by the commercial 'CTpro' reconstruction software supplied Metris X-Tek. This is because the algorithms implemented in Matlab do not allow for a centre of rotation correction to be employed. Centre of rotation correction is used in commercial CT systems to allow for the fact that the centre of the object manipulator (usually a turntable) is not centrally aligned with the source and the detector (see section 2.2.6). The result of not performing this correction is that some of the internal features of the panel appear softer (less sharp) than they should. This does not affect the phantom projection data, as this dataset was created by forward-projection in Matlab (the `fanbeam` function), so it has no centre of rotation offset.

The centre of rotation problem does not detract from the accuracy of the experimental results because all of the reconstructions employing data completion methods are compared to an ideal reconstruction which is also affected by the same incorrect centre of rotation. Therefore, the error maps and error statistics are fully valid results.

3.6 Simple Data Completion by Edge Extension

The first type of data completion method investigated was a simple extension of the projection data with a signal that prevents the truncation artefacts described in section 3.4.2. Similar methods were identified in the literature review (section 2.2.5.1) based on parallel beam properties (Lewitt and Bates 1978; Hsieh *et al* 2004; Ravishankar *et al* 2005; Sourbelle *et al* 2005). These methods utilised the property described in section 3.4 that the area under each projection profile (i.e. total attenuation) remains constant for all

views. This allows the attenuation of the missing data to be easily extrapolated from the sinogram and used together with an approximation of the object shape. However, cone beam CT does not exhibit the same properties. Therefore, the simple data completion method developed in this section extended the projection data based on information extrapolated from the object edge.

The objective of this investigation was to develop a data completion method that minimised the truncation artefacts. The criteria for such an extension were established as follows:

- The method should not modify the captured ROI data in any way.
- The extension must have low spatial frequency.
- The method cannot assume detailed prior knowledge of the sample.
- The extension should add no new artefacts into the reconstructed image.

The following sections present the developed method based on cosine extensions and investigate its effectiveness in terms of meeting the above objectives. Included in this investigation is a comparison between the developed cosine tail method and a similar approach found in literature based on level extensions (Kyrieleis et al 2010).

3.6.1 Cosine Tail Extensions

The cosine tail completion method adds a half-period of a cosine wave to each end of the projection data. The signal starts at the last un-truncated pixel on the end of a projection and finishes at the background level. The equation used to calculate this curve was:

$$y = \frac{y_1 + y_2}{2} + \frac{(y_1 - y_2)}{2} cos\left((x - x_1)\frac{\pi}{d} \right) \tag{3.1}$$

Where y_1 is the start pixel value, y_2 is the end pixel value, x is the pixel number, x_1 is the first pixel number and d is the length of the tail.

This is illustrated in Figure 3.13, where cosine tail extensions have been applied to an arbitrary projection that has been truncated. The purpose of the cosine tail is to provide a low spatial frequency tail off to zero attenuation (i.e. removing the sharp transition at the truncated edge) and provide a simplified approximation to the object shape. In addition, this method does not require any prior knowledge of the object geometry. However, if this is known the length of the tail can be adjusted to help reduce the error (discussed in the following section 3.6.1.1).

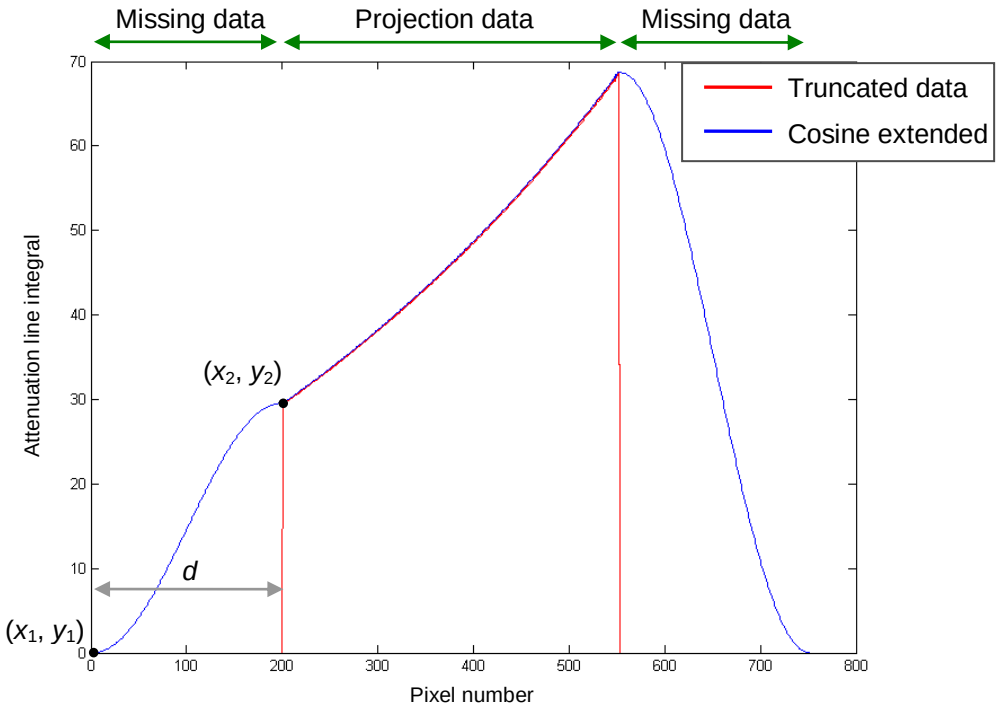

Figure 3.13: Example of cosine tail extension being applied to a projection profile. Truncated projection (red) and truncated projection extended with cosine tails (blue).

3.6.1.1 Cosine Extension Length

The length of the cosine tail affects the reconstruction error. In order to determine the optimal tail length, an experiment was designed to test a wide range of extension lengths on a range of truncation levels.

The test subject was the simulated phantom described in section 3.5.2. A number of truncated projection datasets were created by applying a range of crop lengths to the ideal un-truncated projections. The truncation levels corresponded to removing a specific percentage of the object width from the projection data, e.g., a 40% truncation removed 40% of the object width, leaving 60% of the panel within the FOV. The truncations levels were set at 20% increments from 10% to 70%.

For each set of truncated projections a series of cosine tail extensions were applied. For each length of tail extension different lengths of zero-padding were also applied, i.e., the signal was further extended on both ends with zeros. For each combination of tail length and zero-padding length the projection data was reconstructed and the mean error assessed. This produced an output, like the one shown in Figure 3.14, showing the mean

error as a function of tail length and zero-padding length. This process was repeated for all 4 levels of truncation; results of which can be found in the Appendix A.

The image in Figure 3.14 shows the mean errors measured for 50% truncation. This shows the typical characteristics that were found for all the truncation levels:

- As the cosine tail length increases the error initially drops; this is evidence of the truncation artefacts being removed by the cosine tail.
- At a cosine tail length of approximately 60 pixels, the mean error is at a minimum. This is approximately the length of the panel that was cut from the ROI.
- As the cosine tail length increases beyond 60 pixels, the error increases again. At longer tail lengths the total attenuation in the projections is exceeding the ideal. This is similar to the missing data problem described in section 3.4.1, except in this case the resultant projection data now describes more attenuation than the ideal projections.
- The length of the zero padding had very little effect on the reconstruction error.

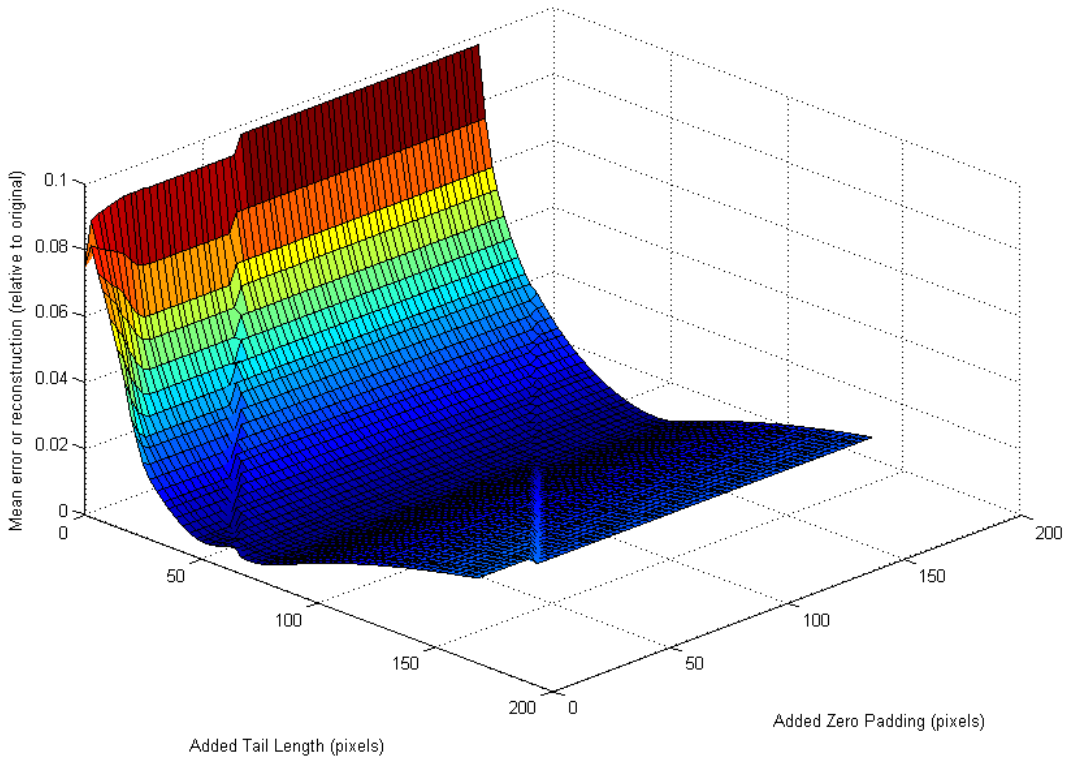

Figure 3.14: Reconstructed mean error results for 50% truncation with cosine tail and zero padded extension.

After reviewing all the results for the varying levels of truncated projection data a guideline for minimising the reconstruction error was established: *The length of the cosine tail*

should be approximately equal to the length of the object that has been cut from the FOV. Note that this guideline has only been tested on a panel with an aspect ratio of 10:1. For objects with different geometries an alternative guideline may be more appropriate. However, similar results on the extension length were reported by Lewitt and Bates (1978) on their data completion method (details of this method are provided in section 2.2.5).

3.6.2 Level Extensions

As mentioned previously, the performance of the cosine extension method was compared with another approach based on Kyrieleis et al (2010) method using level extensions. Figure 3.15 illustrates the two completion methods when applied to a set of truncated projection data. The cosine completion method extends the truncated data using a cosine signal starting at the value of the last un-truncated edge pixel which tails off to the background level (full details in previous section 3.6.1). Whereas, the level extension method filled out the missing data with a constant value equal to the value of the last un-truncated edge pixel (Kyrieleis et al 2010).

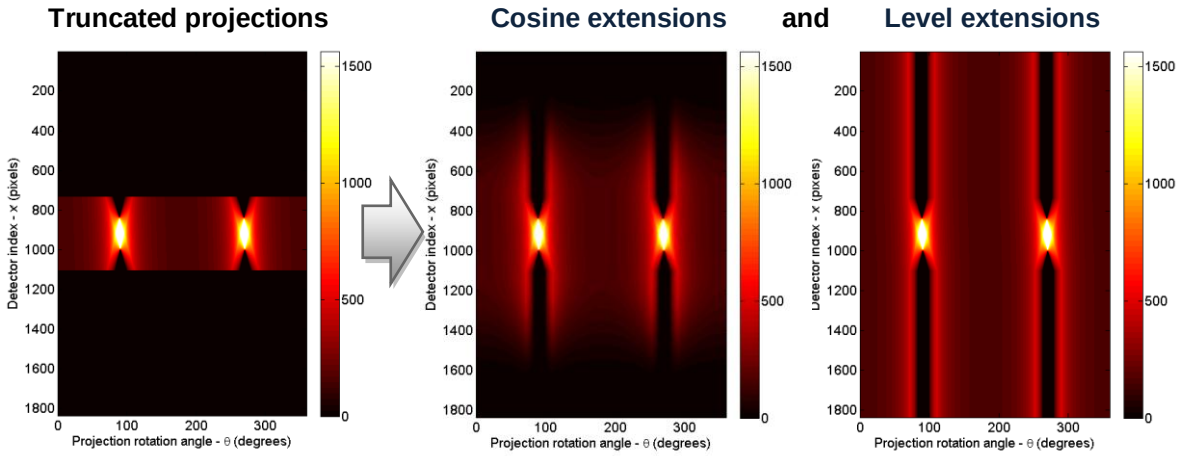

Figure 3.15: Sinograms showing the cosine and level extensions being applied to the truncated phantom projection data. The colour axis shows the value of the projected attenuation line integral at each pixel in the projection data.

The main purpose of the level extension method (Kyrieleis et al 2010) is to: (1) extend the data with a signal that adds no sharp transitions and (2) move the point of truncation far enough away from the truncated data so that no ringing type (truncation) artefacts caused by the ramp filter can permeate into the ROI (see section 3.4.2). This means the accuracy of the reconstruction is strongly dependant on the length of the extension. The level

extension length was set at the same length as the ideal un-truncated projection data; similar to that used by Kyrieleis et al (2010).

3.6.3 Results and Discussion

Figure 3.16 and Figure 3.17 show the reconstruction results for both the simulated phantom and the CFRP sample projection data, following application of the cosine extension method. The reconstruction results for the level extension method (Kyrieleis et al 2010) applied to the simulated phantom and the CFRP panel are shown in Figure 3.18 and Figure 3.19, respectively. The level of truncation was 80% of the object width in all cases. Note that the scale of the reconstructed images has been adjusted so that the central region of pixels has approximately the same value in each image set. Also, the upper and lower visual limits have been set to give a reasonable contrast level; a process normally controlled by the radiographer by adjusting the image histogram. Common imaging settings have been applied to all the reconstructions from each set of projection data, i.e., all the phantom reconstructions share the same settings, and likewise for all the sample panel reconstructions.

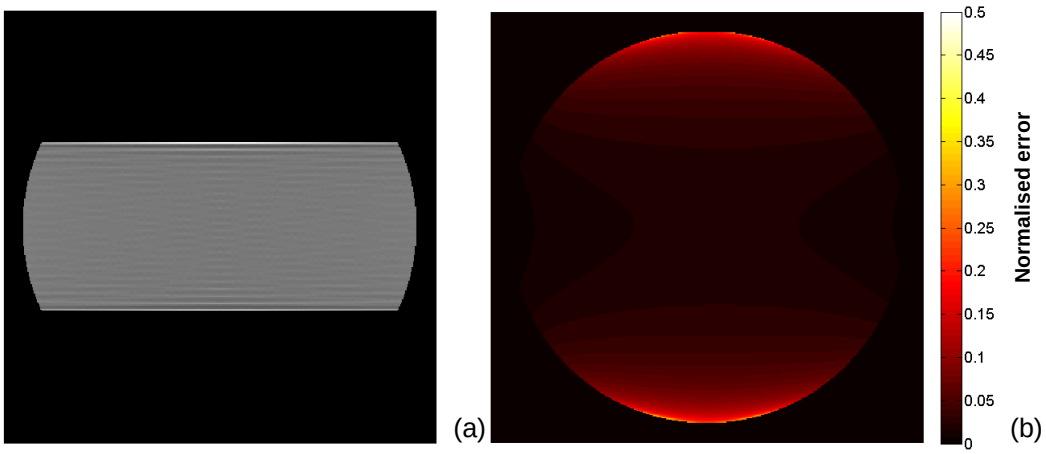

Figure 3.16: (a) Simulated phantom reconstruction following application of cosine tail extensions. The level of truncation was 80% of the object width. (b) Corresponding error map (defined in section 3.5.3).

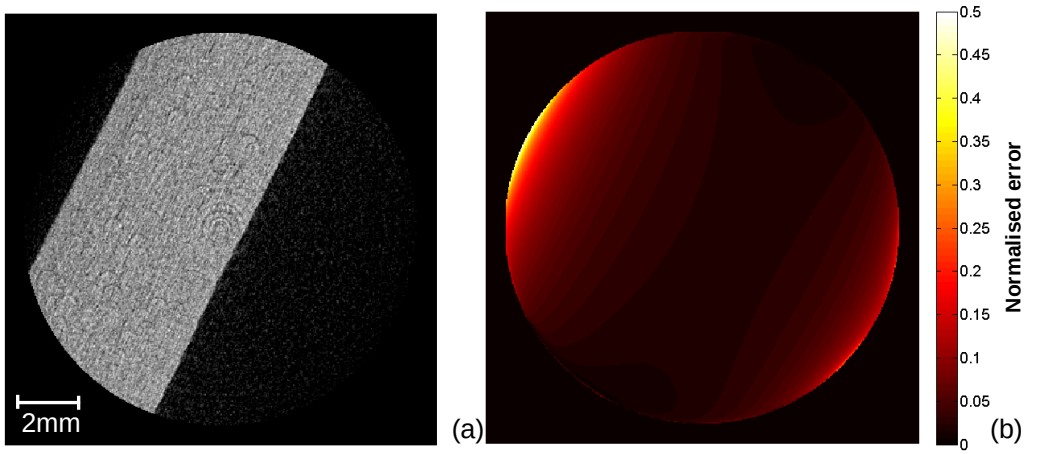

Figure 3.17: (a) CFRP sample reconstruction following application of cosine tail extensions. The level of truncation was 80% of the object width. (b) Corresponding error map (defined in section 3.5.3).

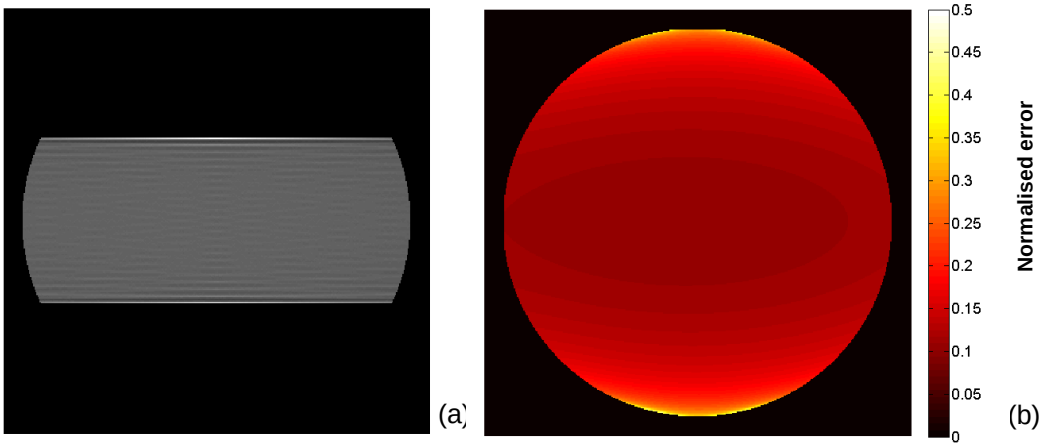

Figure 3.18: (a) Simulated phantom reconstruction following application of level extensions. The level of truncation was 80% of the object width. (b) Corresponding error map (defined in section 3.5.3).

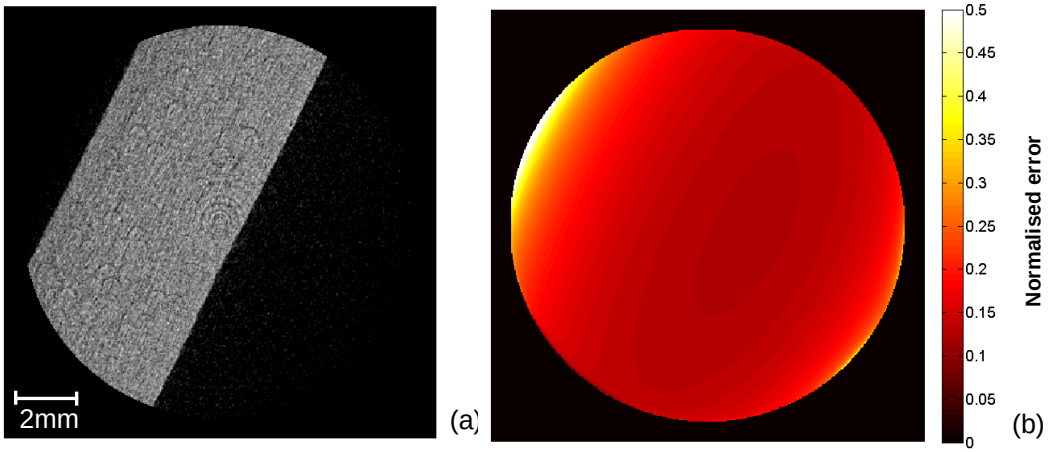

Figure 3.19: (a) CFRP panel reconstruction following application of level extensions. The level of truncation was 80% of the object width. (b) Corresponding error map (defined in section 3.5.3).

Comparing the cosine reconstructions in Figure 3.16(a) and Figure 3.17(a) with the ideal reconstructions in Figure 3.11(a) and Figure 3.12(a), there is little or no difference. This means the cosine extension method has been successful in suppressing the significant truncation artefacts within the reconstructed ROI. However, the error maps (Figure 3.16(b) and Figure 3.17(b)) reveal that there are still considerable differences between these reconstructions and the ideal case. The eradication of these errors is addressed in the following section 3.7.

The reconstructed CT images in Figure 3.18(a) and Figure 3.19(a) for the level extension method also show no significant artefacts when compared to the ideal reconstructions in Figure 3.11(a) and Figure 3.12(a). With adjustment of the imaging parameters, it is possible to make faint artefacts visible, but none that are likely to mask potential defects in the material. However, it is evident from the level extension error maps (Figure 3.18(b) and Figure 3.19(b)) that the general error covering the entire ROI is significantly worse than that reconstructed using the cosine extension method (Figure 3.16(b) and Figure 3.17(b)). The general error displayed for both methods is similar to the problem of missing attenuation data described in section 3.4.1. Except with level extensions, the resultant projection data now describes significantly more attenuation than the ideal projections.

Statistical analysis of the reconstruction errors from the error maps is presented in Table 3.1. This further highlights the difference between the reconstruction based on truncated projection data and the reconstruction using the two simple data completion methods

discussed so far. It also shows that the cosine method is superior to the level extensions method in both the mean and maximum errors.

Table 3.1: Reconstruction error statistics for simple data completion methods (error analysis procedure defined in section 3.5.3).

Error:	**Minimum**	**Mean**	**Maximum**	**Std Deviation**
Phantom projection data				
Truncated	0.1378	0.5237	9.7282	0.6157
Level extension	0.1030	0.1299	0.4338	0.0351
Cosine extension	0.0028	0.0332	0.3204	0.0304
Sample projection data				
Truncated	0.1802	0.6215	13.1255	0.7150
Level extensions	0.0620	0.1594	0.7403	0.0520
Cosine extension	0.0002	0.0430	0.5839	0.0436

3.7 'Estimation from Model' Data Completion

The data completion method described in this section approaches the ROI problem from another angle. It assumes that some prior knowledge of the object is available and attempts to use this knowledge to create a more accurate replacement for the missing data. While the cosine tail method is very good at suppressing artefacts, it still leaves the reconstruction with significant errors. The aim of this technique is to remove not only the truncation artefacts, but also the errors from missing data (see sections 3.4.1 and 3.4.2 for more details on the distinction between the two).

3.7.1 Method

The technique for estimating missing data from a model incorporates three phases: creating the model from the available information, applying a Radon transform to the model to generate projection data, and combining that projection data with the actual truncated projection data. This process is illustrated in Figure 3.20.

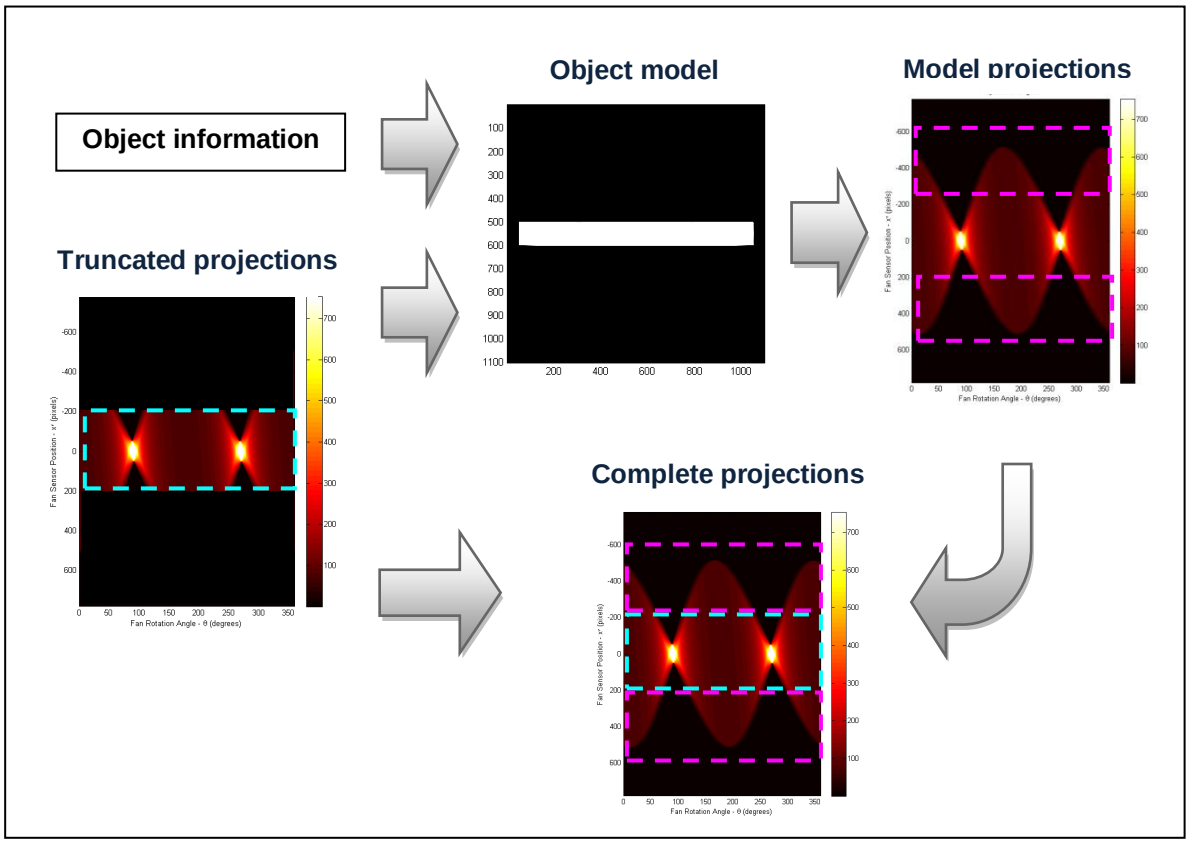

Figure 3.20: Basic process of 'estimation from model' data completion.

For the case of a homogenous panel, the object model is a binary image, showing the cross sectional geometry of the object. The model should exhibit the same geometry and alignment as the ideal reconstruction. This is achieved by using prior knowledge of the object, and a reconstruction of the truncated projections with cosine extensions applied.

The correct dimensions for the object model are established (in pixels) using prior knowledge. Specifically:

- The measured object size.
- The source to object distance.
- The source to detector distance.
- The number and size of the pixels in each row of the detector.

The correct orientation and location of the object model is established using an initial reconstruction of the truncated data with cosine tail extensions applied. An unmasked reconstruction of the test panel from truncated projection data, with cosine tail extensions applied, is shown in Figure 3.21(a). Superimposed upon this image is a bounding box for the object model. The dimensions of the box are pre-determined from prior knowledge (see above). The box is aligned by a human operator making adjustments to the x-y

position and angular rotation. The rotation angle and the positioning of the bounding box to align with the short axis of the panel are simple and accurate. The alignment of the long axis of the panel, the ends of which are outside the FOV, remains an estimation. However, several factors help in this respect:

- If it is known that the panel was placed centrally in the scan setup, then this constitutes prior knowledge and the bounding box can be placed centrally as well.
- The poorly reconstructed image outside the FOV may contain artefacts which indicate approximately the location of the panel edges (see Figure 21(a)).
- The positioning of the long axis is very tolerant of misalignment (in terms of reconstruction errors). Even if the model is misaligned in this way the total attenuation through the object is still correct across either axis. Errors may occur around the reconstructed edges of the object, but they will be well outside the ROI and therefore do not present a problem.

Once the bounding box has been defined an image of the object model is created that takes the attenuation coefficient value zero in the background regions, and one inside the bounding box. This is shown in Figure 3.21(b).

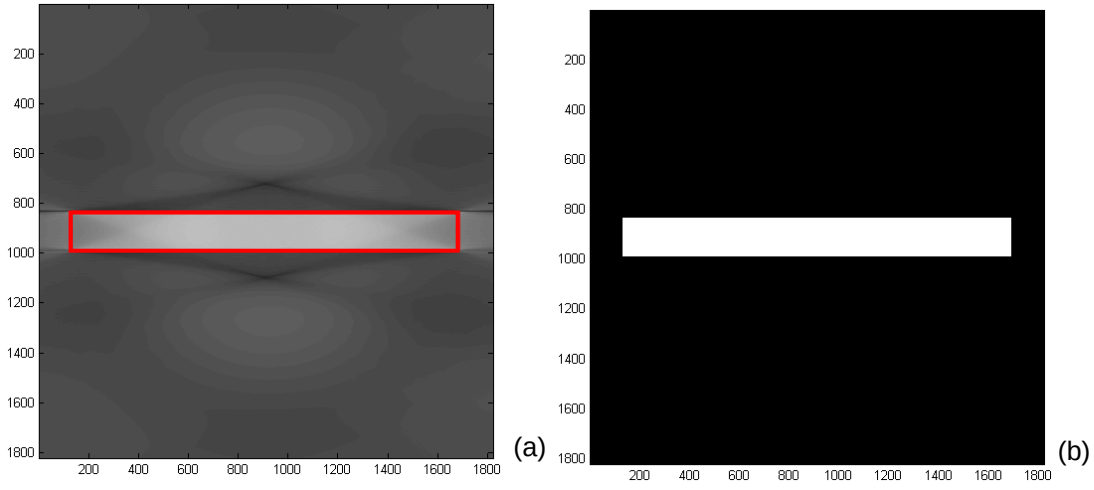

Figure 3.21: Establishing the correct orientation and location of the object model using a bounding box. (a) Reconstruction of the phantom panel using cosine extensions with model box overlaid. (b) Resultant binary object model.

The Radon transform is then applied to the cross sectional image of the object model. The inputs to the transform are set to create the same number of projections with the same geometric settings (source to object distance, source to detector distance, etc.) as the

truncated data already captured, but simulating a larger detector. This simulated detector can be created as wide as required so that the entire object can be fitted within the FOV.

The new set of estimated projections had the following characteristics:

- The projection data is for a homogenous object with the same size, location, and orientation as the actual test panel.
- It has the same geometric settings as the already captured (but truncated) data, except that the whole object is within the FOV.

However, the scale of the pixel values (attenuation line integrals) in the model projection data does not match the truncated projection data because the attenuation coefficient of the model was set to one, rather than the actual attenuation coefficient of the test panel, which is not yet known.

In order to re-scale the model projections to match the truncated projections, the mean value of the truncated projection data was evaluated as μ_1 and the mean value of the model projection data, for same region, was evaluated as μ_2. The model projection data was then scaled by μ_1/μ_2, yielding a new set of model projections for a full (un-truncated) FOV. This scaling process is illustrated in Figure 3.22.

The scaled, model projections and the truncated projections were then combined to form a final set of complete projections. The complete projection data used the unaltered ROI data within the truncated projections, while the missing data outside the truncated FOV was filled with the data from the model. The model projection data scaling and combination is illustrated in Figure 3.22.

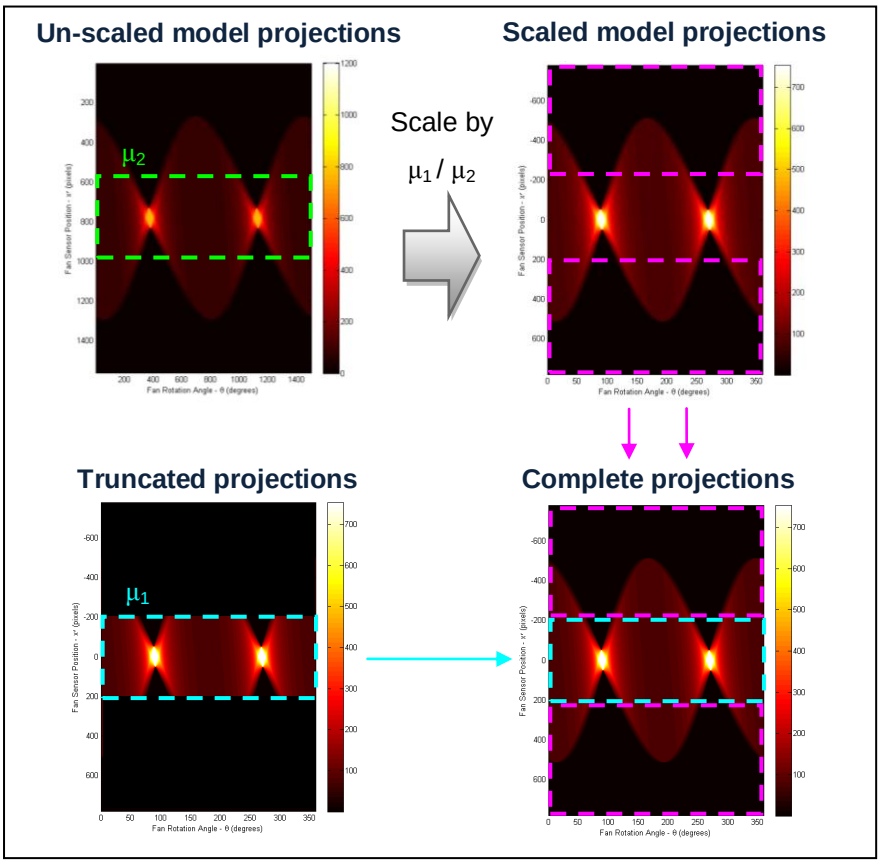

Figure 3.22: Projection data scaling and combination.

3.7.2 Results and Discussion

Simulated Phantom

The first experiments were done with the projection data from the simulated phantom panel. The reconstruction of the combined projection data using the 'estimation from model' technique (described above) is shown in Figure 3.23, along with the corresponding error map. Unsurprisingly, the reconstruction results are almost perfect, with the error map showing only a very small error at the bottom of the image (Figure 3.23(b)). This is because the ideal projection data was made using a homogenous phantom, and the orientation and size were known very precisely. Therefore, the estimated data used to complete the truncated projections is almost a perfect match to the ideal (un-truncated) projection data.

Comparing the results obtained for the 'estimation from model' technique with the results obtained for the cosine extension (Figure 3.18), it is very clear that the model technique has substantially reduced the error across the whole ROI.

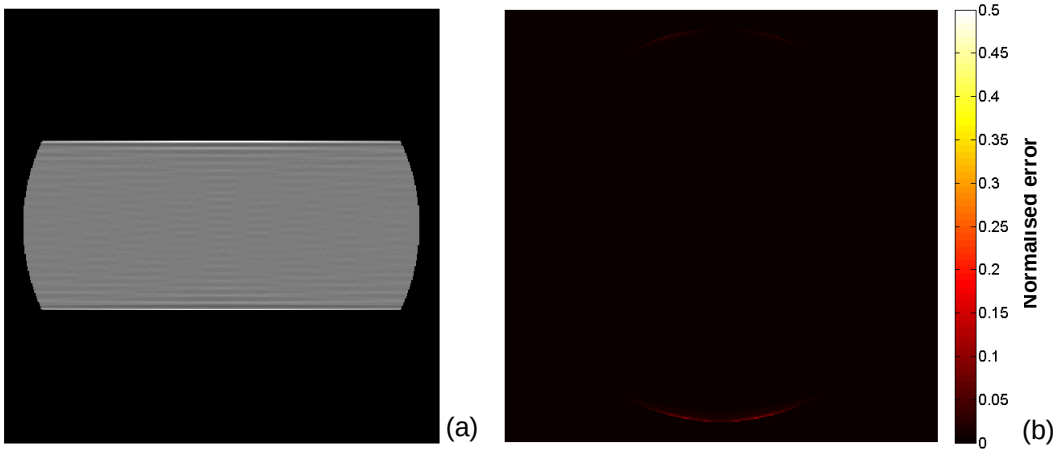

Figure 3.23: (a) Simulated phantom reconstruction following 'estimation from model' completion. The level of truncation was 80% of the object width. (b) Corresponding error map (defined in section 3.5.3).

The model was then re-created with deliberate misalignment to test the tolerance of the data completion technique to a poor operator alignment. The model bounding box was rotated by 1% then offset down and right by 0.5% of the image size. The misaligned bounding box is shown in Figure 3.24. The projection data from the misaligned model was scaled and combined with the truncated projections as described in the previous section (section 3.7.1). The resulting reconstruction and corresponding error map are shown in Figure 3.25. It is evident from the error map that the misalignment has created a truncation artefact type error in the reconstruction. This error is only located at the very edges of the ROI and does not propagate into the image. Therefore, it will not substantially effect image interpretation. Based on these observations and the fact that the alignment mismatch tested was far worse than any operator would be expected to make; this data completion technique can be considered very tolerant of model misalignment.

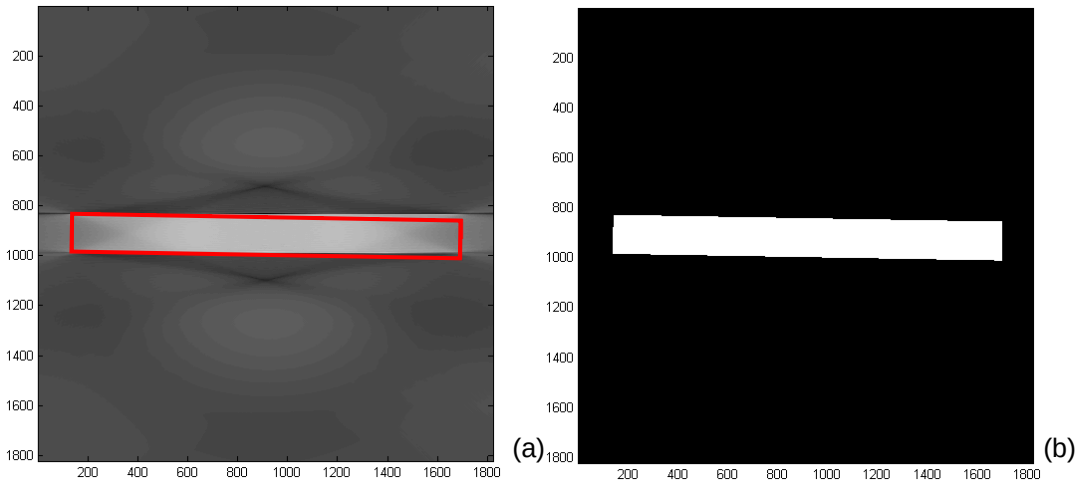

Figure 3.24: Example of misaligned bounding box. (a) Reconstruction of the panel using cosine extensions with model box overlaid. (b) Resultant binary object model.

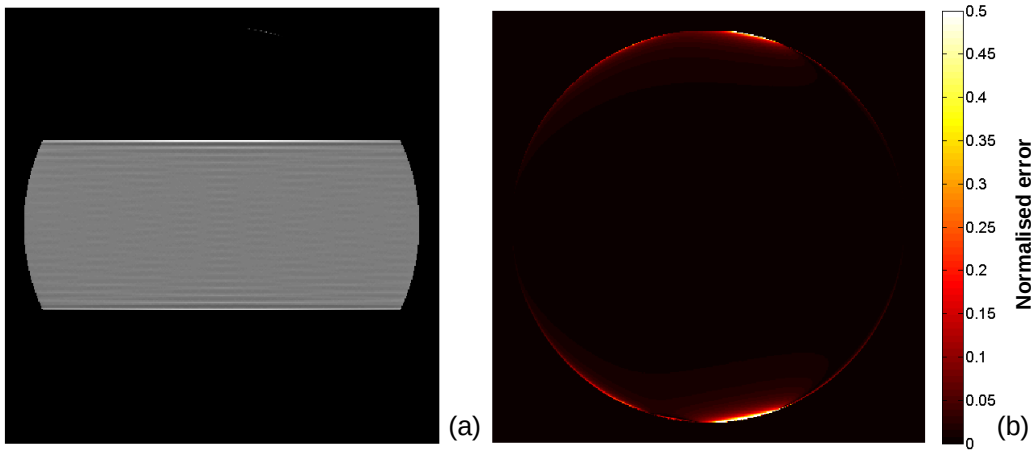

Figure 3.25: (a) Simulated phantom reconstruction following estimation from misaligned model completion. The level of truncation was 80% of the object width. (b) Corresponding error map (defined in section 3.5.3).

CFRP Panel

The 'estimation from model' data completion method was then applied to the truncated projection data from the CFRP panel (as illustrated in Figure 22). The reconstruction result and corresponding error map are shown in Figure 3.26. Again, comparing these results with Figure 3.19, the reconstruction of the CFRP panel using cosine extensions, the difference between the two techniques is evident in the error maps. The 'estimation from model' technique results in a lower general error throughout the ROI because the extended data is a better representation of the total object attenuation. However, the

truncation artefact (visualised as an error occurring at the edge of the ROI) is much stronger in the estimated from model reconstruction.

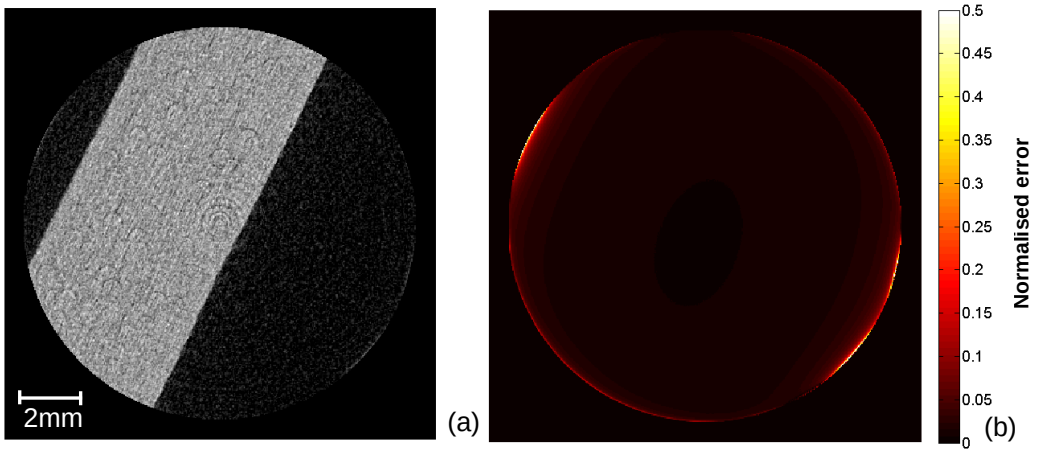

Figure 3.26: (a) CFRP sample reconstruction following 'estimation from model' completion. The level of truncation was 80% of the object width. (b) Corresponding error map (defined in section 3.5.3).

The observations discussed above, for both the simulated phantom and CFRP sample, were confirmed following analysis of the image statistics for all error maps produced so far. These statistics are presented in Table 3.2.

The mean and maximum errors of the reconstructions for both the phantom and sample datasets are substantially lower for both data completion techniques when compared to the corresponding reconstruction for the truncated data. Another point to note is that the mean error resulting from the cosine extensions is higher than for the estimated from model extensions. However, the reverse is true for the maximum errors. This follows from the fact that the cosine tail extension method ensures that the extended data is well matched to the truncated data at the site of the truncation, but does not accurately represent the total attenuation of the object.

The 'estimation from model' extensions more accurately represent the total attenuation of the object when compared to the cosine extensions. The statistics in Table 3.2 demonstrate this fact, as the misaligned model applied to the phantom data and the model applied to the sample data both exhibit the lowest mean error. However, it should also be noted that the misaligned model exhibits a higher maximum error than the aligned model and the cosine extensions. This is due to the misalignment causing a few of the

projections to be sharply truncated to the background level; resulting in a truncation artefact and thus a higher maximum error.

A similar error was noted in the estimated from model extensions for the sample projection data. Again, the maximum error was higher than that exhibited for the cosine extensions. However, in this instance the model was accurately aligned so the cause of the increased maximum error was not truncation artefacts as for the phantom results. Further investigation found a mismatch in the combination of the model projections with the actual truncated data. The reasons for this mismatch are discussed in the following section (section 3.7.3).

Table 3.2: Reconstruction error statistics including 'estimation from model' (error analysis procedure defined in section 3.5.3)

Error:	**Minimum**	**Mean**	**Maximum**	**Std Deviation**
Phantom projection data				
Truncated	0.1378	0.5237	9.7282	0.6157
Level extension	0.1030	0.1299	0.4338	0.0351
Cosine extension	0.0028	0.0332	0.3204	0.0304
Estimated from model	0.0000	0.0010	0.1274	0.0034
Estimated from misaligned model	0.0000	0.0083	1.5343	0.0320
Sample panel projection data				
Truncated	0.1802	0.6215	13.1255	0.7150
Level extension	0.0620	0.1594	0.7403	0.0520
Cosine extension	0.0002	0.0430	0.5839	0.0436
Estimated from model	0.0001	0.0164	0.7231	0.0235

3.7.3 Revised 'Estimation from Model' Method

The estimation by model method produced better results for the phantom data than for the sample panel. This is evident when reviewing the mean error statistics in Table 3.2. With the phantom projection data the cosine extensions reduce the mean error to 6.3% (when compared to the truncated projection data). The sample data with cosine extensions reduces the error to 6.9%. With the level extensions applied to the phantom data the error is reduced to 24.8%, for the sample projection data the reduction is to 25.6%. With the 'estimation from model' method the phantom data reduces the error to 0.19%, but for the sample projection data the error reduction is only 2.6%. For the cosine and level

extensions, the error improvement is comparable between the two data sets, but for the model estimations there is an order of magnitude between them. The cause of these errors and the methods implemented to overcome them is discussed in the following sections.

3.7.3.1 Individual Projection Magnitude Matching

On close inspection of the projection data profiles in the sinogram, a very slight scaling mismatch is visible between the model data and the truncated projections for the CFRP panel. This does not occur when comparing the projections for the phantom and can be attributed to an effect known as beam hardening (see section 2.2.4.5). It only effects the sample projections because it arises from the radiation attenuation in the CT scan. The polychromatic nature of the incident X-ray beam means that low energy photons are preferentially attenuated compared to high energy photons as they pass through the object. This causes the average energy of the transmitted X-ray beam to increase or harden as it passes through increased thicknesses of material; resulting in non-linear attenuation. Therefore, the attenuation line integrals do not represent linear attenuation.

The cause of this mismatch was confirmed by comparing the attenuation of rays that passed through the length of the panel with rays that passed through the panel at 90 degrees to the length. When the attenuation values were compared for the phantom data, the ratio between the two measurements was 9.91, approximately the same as the aspect ratio of the panel; indicating linear attenuation. The same process was applied to the CFRP panel projections and resulted in a ratio of 8.4; indicating non-linear attenuation.

With the attenuation being non-linear, the scaling process illustrated in Figure 3.22 does not produce estimated projections that are well matched to the data within the truncated projections. In order to circumvent this problem, a new method for scaling the model projections individually was applied.

Each model projection was scaled individually by μ_{1k} / μ_{2k}, where k is the projection number. μ_{1k} is the mean of the truncated data, for the k^{th} projection, and μ_{2k} is the mean of the un-scaled model projection data for the same region. The model projection, once scaled by μ_{1k}/μ_{2k}, will match the average intensity of the truncated projection data[5].

[5] Refer to Figure 3.22 for an illustration of the old scaling process. The only exception in this instance is that it was applied individually to each projection angle.

It should be noted that this process does not compensate for any errors caused by the beam hardening itself. It merely ensures that the extended data matches the missing data as closely as possible, which is essentially non-linear attenuation. The geometry of the panel used in this investigation means that the missing projection data is typically in a region of the panel with a flat attenuation profile. For other objects, where the model projection profile has more variation, this simple technique may not produce equivalent results. In these instances, a calibrated beam hardening correction may be necessary (Hammersberg and Mangard 1998; Badel *et al* 2003).

3.7.3.2 Individual Projection Cosine Blending

In order to mitigate possible truncation errors caused by marginal misalignment of the model, a short cosine tail was added to blend the model data to match the intensity found at the edge of the truncated data. In situations where the model might be slightly misaligned with the truncated data, the meeting point of the model data and the truncated data may have a steep transition. This transition will cause a truncation artefact as a result of the ramp filtering (see section 3.4.2 for details). The cosine tail blend limits the steepness of the transition, and hence the size of the truncation artefact.

A long blend length will provide a high tolerance to misalignment, but will degrade the accuracy of the model data. The bounding box alignment tool developed in this work is considered user friendly and accurate, therefore only a very short blend length was introduced (around 1% of the total image size). Figure 3.27 shows an arbitrary projection that has been individually scaled and blended.

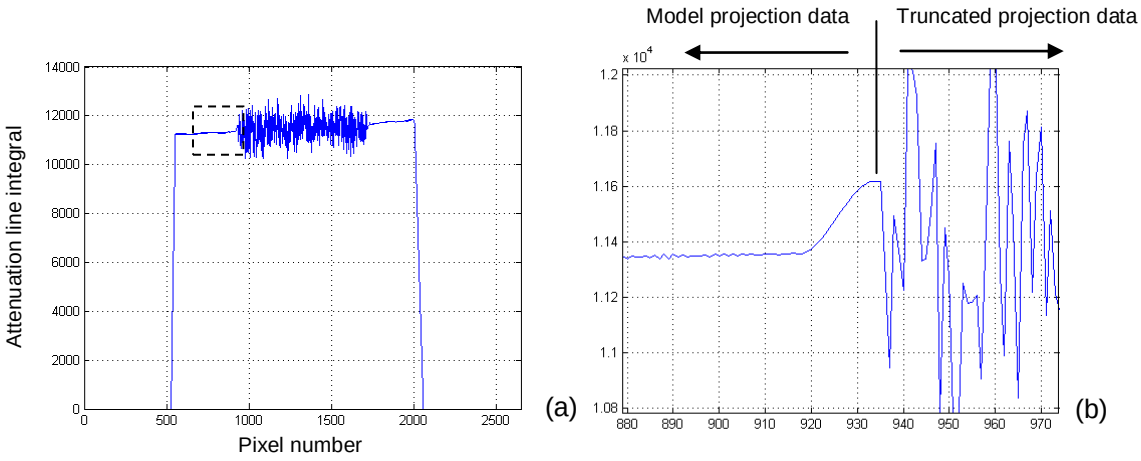

Figure 3.27: Complete projection with individual projection cosine blending. (a) Projection profile extended with 'estimation from model' method and (b) magnified view of short cosine blend.

3.7.3.3 Results and Discussion

The revised 'estimation from model' method used both individual projection magnitude matching, and the individual projection blending described in section 3.7.3 and 3.7.3.2, respectively. This method was applied to both sets of truncated projection data; the phantom and the CFRP panel. The reconstruction results and the corresponding error maps are shown in Figure 3.28 and Figure 3.29. The virtually blank error maps show that the revised method produces a very low error, for both the phantom and the sample panel data.

This is further demonstrated with the statistics presented in Table 3.3, showing that the revised method produces smaller errors than the initial 'estimation from model' method, for both the phantom and the sample panel. The mean error associated with the sample data is cut to one third of that for the initial 'estimation from model' method. This can be attributed to the magnitude matching which now causes the model to exhibit beam hardening effects similar to the truncated data. The maximum errors for both the phantom and sample projections have also dropped to approximately one fifth (compared to the initial 'estimation from model' method). This can be attributed to the cosine blending which limits the effect of small truncation artefacts caused by imperfect model alignment.

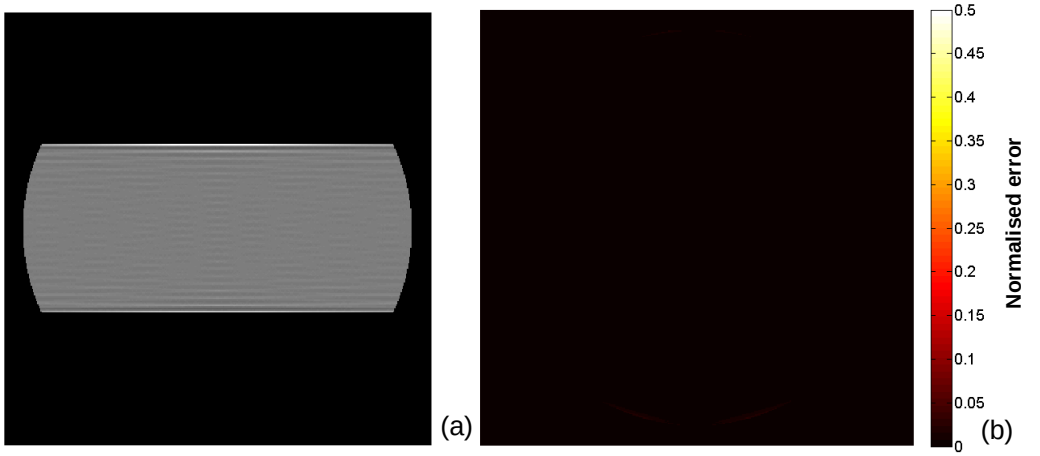

Figure 3.28: (a) Simulated phantom reconstruction following revised 'estimation from model' completion. The level of truncation was 80% of the object width. (b) Corresponding error map (defined in section 3.5.3).

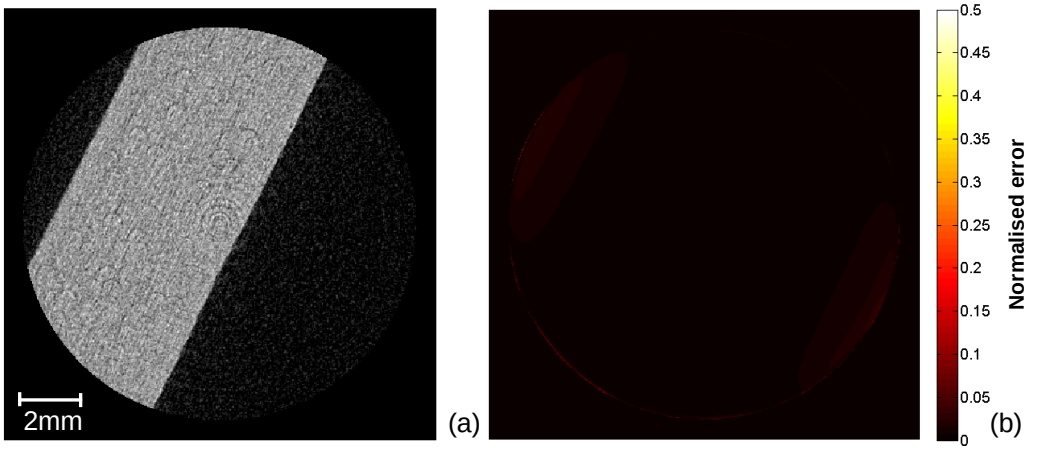

Figure 3.29: (a) CFRP sample reconstruction following revised 'estimation from model' completion. The level of truncation was 80% of the object width. (b) Corresponding error map (defined in section 3.5.3).

Table 3.3: Error statistics for all reconstructions (error analysis procedure defined in section 3.5.3).

Error:	**Minimum**	**Mean**	**Maximum**	**Std Deviation**
Phantom projection data				
Truncated	0.1378	0.5237	9.7282	0.6157
Level extension	0.1030	0.1299	0.4338	0.0351
Cosine extension	0.0028	0.0332	0.3204	0.0304
Initial estimated from model	0.0000	0.0010	0.1274	0.0034
Estimated from misaligned model	0.0000	0.0083	1.5343	0.0320
Revised estimated from model	0.0000	0.0007	0.0245	0.0013
Sample panel projection data				
Truncated	0.1802	0.6215	13.1255	0.7150
Cosine extension	0.0620	0.1594	0.7403	0.0520
Level extensions	0.0002	0.0430	0.5839	0.0436
Initial estimated from model	0.0001	0.0164	0.7231	0.0235
Revised estimated from model	0.0000	0.0054	0.1107	0.0045

A final set of comparative results are shown in Figure 3.30 and Figure 3.31. These show the error maps for the cosine extensions, the initial model method, and the revised model method, applied to both sets of projection data. Note that the error maps are plotted using the 0 – 0.1 scale, rather than the 0 – 0.5 scale used in all the previous images. This scale emphasises the differences in accuracy between the three methods. Figure 3.30 shows the resultant error maps based on the simulated phantom projection data. Here, it is evident that both the initial and the revised model extensions provided a significant reduction in reconstruction error compared to the cosine extension method. This is also apparent in Figure 3.31 for the sample projection data. In addition, the marked improvement between the initial model and the revised model for the CFRP panel is evident. The reasons for this have been discussed above.

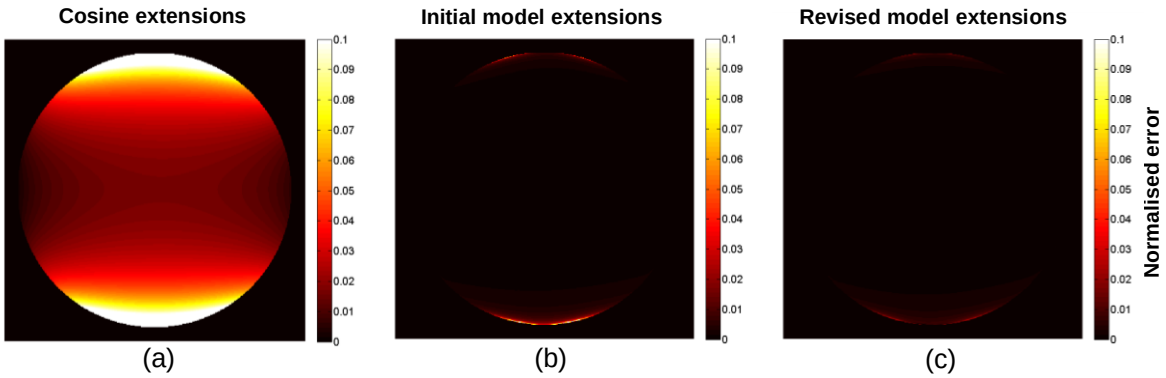

Figure 3.30: Error map comparison for the three data completion methods applied to the simulated phantom projections. (a) Cosine extensions (b) initial 'estimation from model' completion and (c) revised 'estimation from model' completion. The error maps are plotted with a smaller error range (0-0.1) to those previously shown.

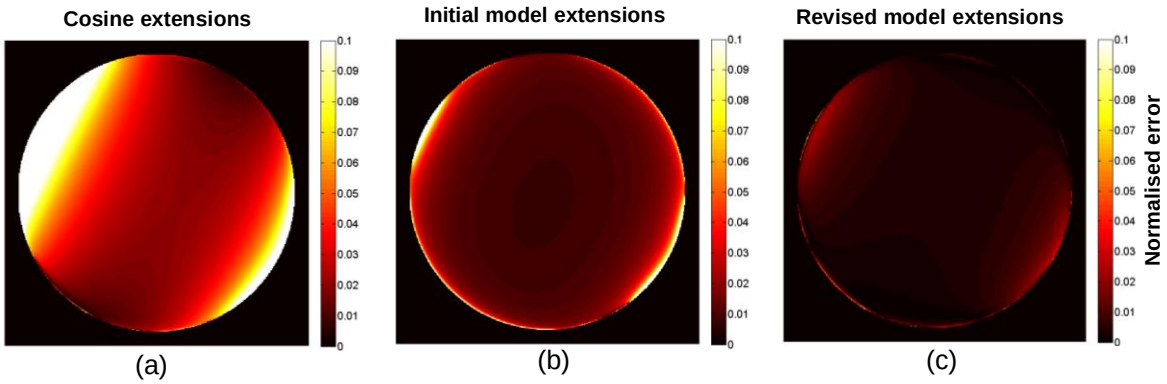

Figure 3.31: Error map comparison for the three data completion methods applied to the CFRP sample projections. (a) Cosine extensions (b) initial 'estimation from model' completion and (c) revised 'estimation from model' completion. The error maps are plotted with a smaller error range (0-0.1) to those previously shown.

3.8 Application of the Developed ROI CT Techniques to Cone Beam Geometry

Both the cosine extension method and the 'estimation from model' method were successfully applied to cone beam geometry. The results were successful in terms of visual image quality, but were not qualified quantitatively as for fan beam geometry in the previous sections. The commercial software used to implement the reconstruction and view the outputs (see section 2.2.6 for equipment and software details) required manual setting of the image histograms to set the limits and gradient of the visual range. The

result is that each image has slightly different visual settings which would result in a false error calculation if compared using the error map method from the previous sections.

Cone beam projection data allows reconstruction of 3D volumes using a series of tilted fan beam slices through the object (see section 2.2.3.5 for full details on cone beam reconstruction). For fan beam data each projection results in a 1×n array of attenuation values, where n is the width of the detector. For cone beam data each projection results in an array of m×n attenuation values, where n is the width of the detector and m is the height of the detector. Figure 3.32 shows a volumetric 3D image reconstructed using cone beam projection data for the CFRP panel.

Figure 3.33 shows two cross sectional CT images in the axial plane, reconstructed using the ideal (un-truncated) projection data. The axial cross-sectional plane in relation to the sample geometry is illustrated in Figure 3.32. Figure 3.33(a) is a cross sectional slice extracted near the mid-plane where the IQI holes are located (description of laser drilled IQI in section 3.3). Figure 3.33(b) is a cross sectional slice taken at a large cone angle within the sample. These two slices are compared for all data completion methods and were purposely chosen to validate the techniques application to cone beam geometry. The mid-plane i.e. central slice can be considered as fan beam geometry (see section 2.2.3.5), so the estimation by model technique should perform exactly the same as shown in previous sections. However, at increasing cone angles the estimation of the missing data based on a fan beam model will become increasingly inaccurate. Potentially, this could cause artefacts and errors within the reconstruction.

The truncated ROI data with no data completion method applied is shown in Figure 3.34. The truncation artefacts are clearly illustrated; visualised as a strong glowing around the edge of the ROI masking the object detail within those regions.

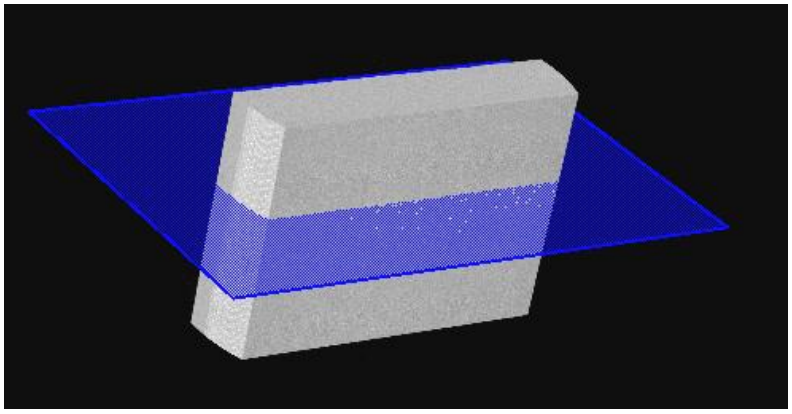

Figure 3.32: Volumetric 3D CT image of the CFRP panel, reconstructed from cone-beam projection data. The blue plane illustrates the axial cross sectional direction.

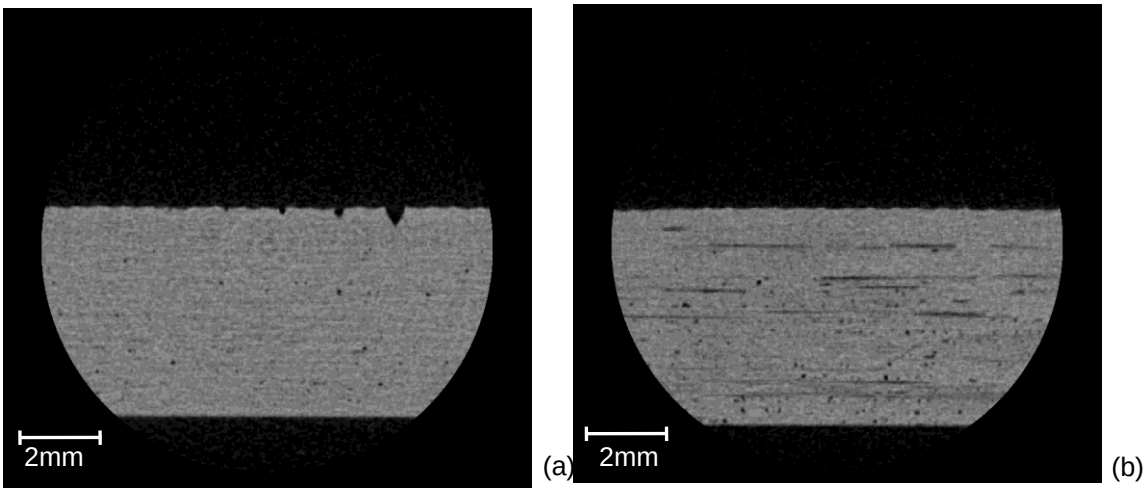

Figure 3.33: ROI cone beam reconstruction with ideal (un-truncated) projection data. (a) Cross sectional CT slice extracted near the mid-plane and (b) cross sectional CT slice extracted at a large cone angle.

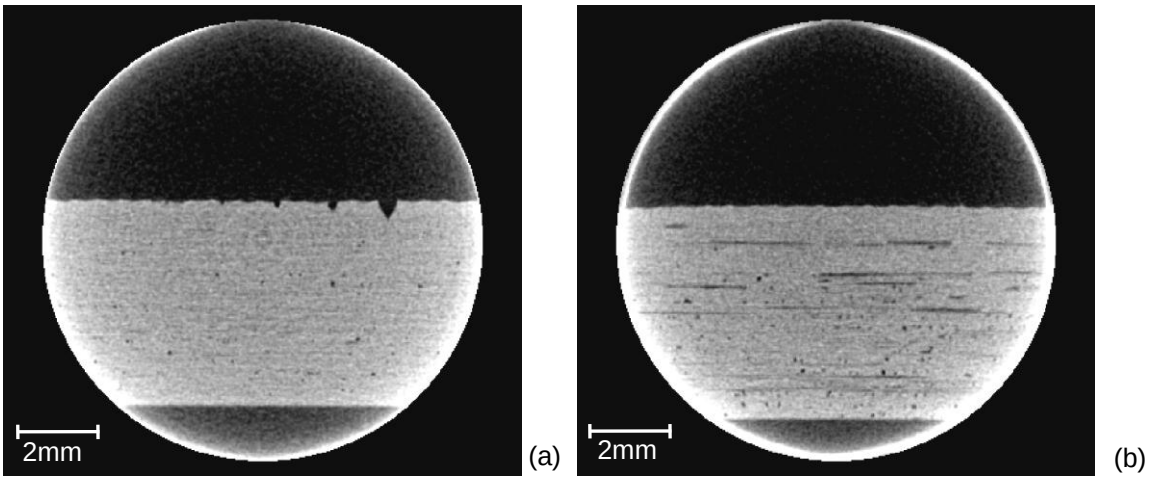

Figure 3.34: ROI cone beam reconstruction with truncated projection data (80% truncation). (a) Cross sectional CT slice extracted near the mid-plane and (b) cross sectional CT slice extracted at a large cone angle.

The data completion methods were applied independently to each elevation or row (each value of m) within the raw projection images collected by the cone beam scan. For the cosine tail method this required applying the extension to both sides of the truncated region for each row in the projection image. The projection images were then reconstructed to produce a 3D volumetric dataset. The same two cross sectional images were extracted from this dataset and are shown in Figure 3.35. Comparing these CT images with those produced by the truncated ROI (no data completion) in Figure 3.35, it is clear that the cosine tail extension has made a major improvement to the reconstruction quality.

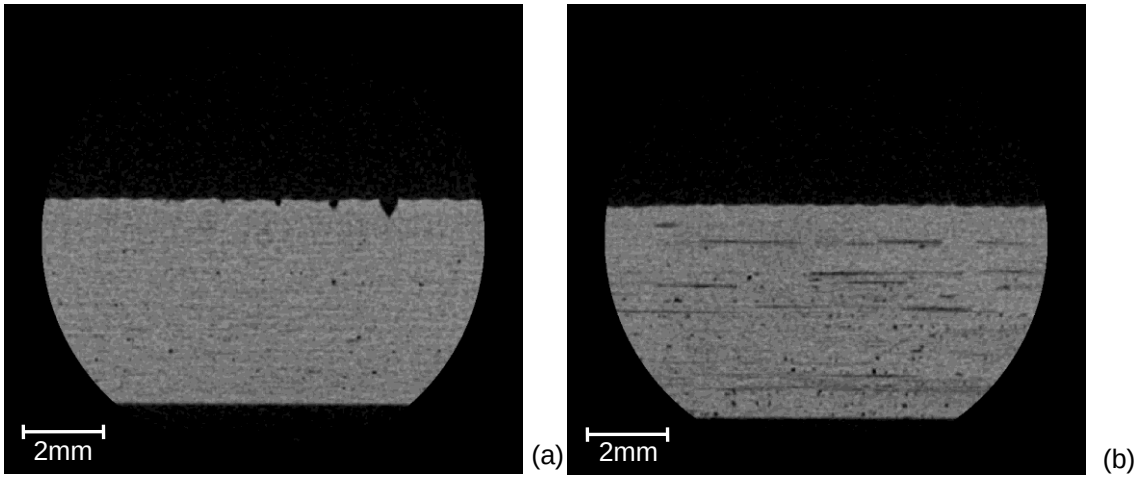

Figure 3.35: ROI cone beam reconstruction with cosine extended projection data. The level of truncation was 80% of the object width. (a) Cross sectional CT slice extracted near the mid-plane and (b) cross sectional CT slice extracted at a large cone angle.

For the 'estimation from model' method, a single cross sectional model was produced using the object geometry in the cone mid-plane (i.e. the central slice where it can be viewed as fan beam data). The model projections were then created as described in section 3.7.3. The missing data was then completed for each row in each projection image, individually matching the magnitude of the projections with the ROI truncated region and applying the cosine blending method. As mentioned previously, the single model being used for all cone angle elevations (i.e. detector rows) is based on the fan beam data in the mid-plane, therefore the model projections outside the mid-plane are an imperfect model.

The results of the model extensions applied to cone beam data are shown in Figure 3.36. Similar to the cosine extension results above (Figure 3.35), the 'estimation from model' method has also produced excellent results with no visible artefacts or errors present.

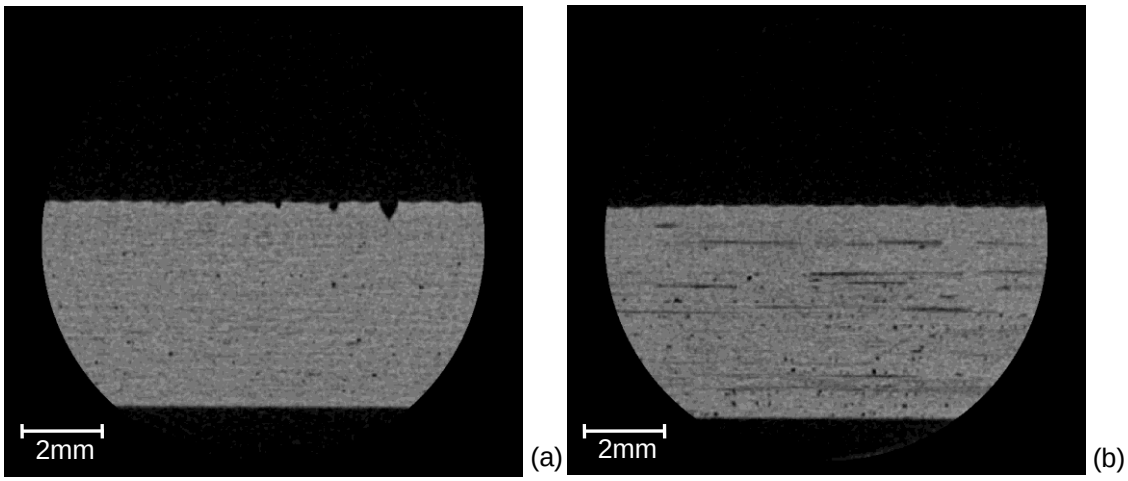

Figure 3.36: ROI cone beam reconstruction following application of the revised 'estimation from model' data completion. The level of truncation was 80% of the object width. (a) Cross sectional CT slice extracted near the mid-plane and (b) cross sectional CT slice extracted at a large cone angle.

The line profiles shown in Figure 3.37 and Figure 3.38 further illustrate the reduction in the reconstruction errors associated with truncated ROI data. The line profiles were extracted across the cone beam CT slices shown previously. Figure 3.37 shows the line profiles extracted from the CT slices near the mid-plane and Figure 3.38 shows the line profiles extracted from the CT slices at a large cone angle. In both Figure 3.37 and Figure 3.38, the line profiles from the cosine and model extended reconstructions are virtually indistinguishable from the ideal reconstruction using the ideal (un-truncated) data. On the other hand, the truncated data projections produced a reconstruction with significant artefacts, which shows in the line profiles as lifting towards the edges.[6]

Both the data completion methods investigated produced reconstructions that are virtually indistinguishable from the reconstruction that utilised the full (un-truncated) projection data. This is consistent with the results from the fan beam reconstructions in the previous sections. In addition, no significant difference was seen between the reconstructed model results at the mid-plane and the model results at the large cone angle. This provides

[6] Note that the data is shown in the exported grey values, which have been scaled manually by the adjustment of the image histogram. The same standard histogram setup procedure was used for each to ensure reasonable contrast levels, but this is applied to different output histograms so the absolute level of each cannot be compared. Nonetheless, the similarity of the profiles can still be evaluated i.e. the relative intensity levels.

evidence that although the model was an imperfect match outside of the mid-plane it did not significantly affect the accuracy of the reconstruction.

It should also be noted that the reconstructions using the cone-beam algorithm were able to employ a centre of rotation correction, which was not implemented in the fan beam reconstructions (see section 3.5.3). Therefore, the cone-beam results appear sharper than the fan beam results. By implementing a centre of rotation correction in the fan beam reconstruction algorithm, a similar level of sharpness would be expected.

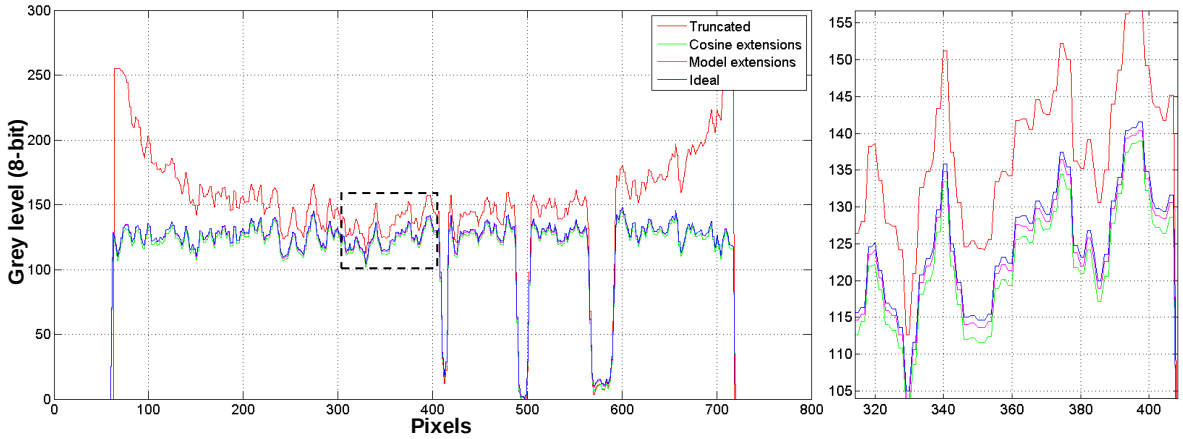

Figure 3.37: (a) Comparison of line profiles extracted across the IQI holes near the mid-plane. (b) Magnified view of region within the line profile comparison.

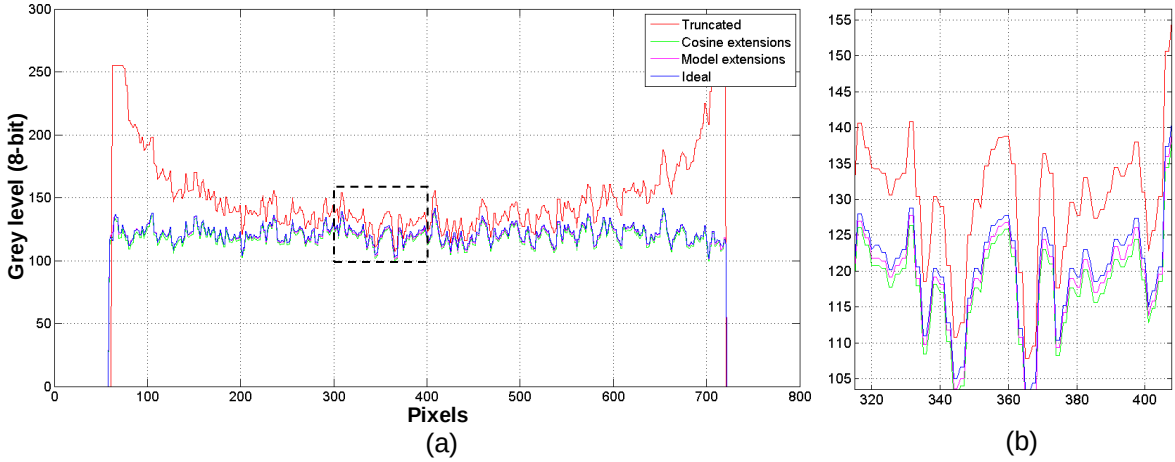

Figure 3.38: (a) Comparison of line profiles extracted across the CT slices taken from a large cone angle. (b) Magnified view of region within the line profile comparison.

3.9 Conclusions

The data completion methods developed in this work make it possible to perform ROI reconstructions of CFRP laminates with a similar accuracy to that obtained with conventional CT. This makes ROI CT an effective inspection tool by removing the image errors that previously compromised the quality of the results and reduced the potential application of post processing.

The opportunity to use ROI CT for cone beam geometry directly extends the capabilities for CT inspection of CFRP laminates. It makes it practical to scan and accurately reconstruct:

- Regions of objects that are larger than the FOV of the detector.
- Regions of objects with a very high geometric magnification.

The investigation presented in this chapter shows that the size of the detectors FOV is no longer a barrier to inspect regions of large objects. The data completion methods described previously make it possible to perform ROI CT on objects larger than the size of the detectors FOV without suffering from truncation artefacts and errors in the reconstruction. Similarly, the maximum geometric magnification that can be set in a CT scan is no longer limited by the size of the FOV. The data completion methods also make it possible to set up an ROI CT scan of an object with very high geometric magnification. This is done without compromising image quality when the magnified object extends beyond the detectors FOV. This is particularly beneficial for CFRP inspection as the use of the very high magnification is required for the detection and characterisation of very small defects such as matrix cracking, fibre breakage and Barely-Visible-Impact-Damage (see section 1.1). This can now be achieved accurately, regardless of object size.

The research carried out in this investigation was focussed solely on the simple geometry of a homogenous panel that could be applied to CFRP laminated panels. Clearly, this does not cover the full spectrum of desirable inspection subjects. However, the next logical step is to apply the data completion methods to more complex geometries and multi-density objects. There is potential for an imported CAD model of the object to be used in the ‘estimation from model’ data completion technique. This could increase the scope of the technique to any possible object geometry. Additionally, the cosine extension method could be improved by matching the cosine tail length with the amount of missing data for each individual projection. This would increase the accuracy of the resultant sinogram prior to reconstruction.

The ‘estimation from model’ technique has strong similarities to data completion methods for ROI CT discussed in the literature review (section 2.2.51). These methods also require the use of prior knowledge to complete the projection data (Ramamurthi and Prince 2003; Chun *et al* 2004; Weigert *et al* 2004; Netsch *et al* 2008). The basis of these techniques is to initially scan the object using conventional CT and then use the full un-truncated projections to approximate the missing data in the subsequent ROI CT scan. The most significant difference between these prior knowledge ROI techniques and the use of the ‘estimation from model’ technique is the need to acquire an initial CT scan. Firstly, this scan takes time. The ‘estimation from model’ method requires only the one ROI scan to complete the reconstruction. It does require more computation time, but this will not slow down the throughput of the CT system. All of the computation can be performed offline, after the ROI scan has been captured. Secondly, a conventional CT scan must be possible. One of the major reasons to develop ROI CT is to enable inspection of objects that cannot fit within the detector’s FOV. In applications where this is the case the ROI techniques based on prior conventional CT scans cannot be used.

The research presented in this Chapter was highly successful in meeting all of the stated objectives, and the results of the final data completion methods exceeded expectations. The main achievements include:

- Two distinct underlying causes of errors in ROI reconstructions were identified. This knowledge was then used to focus the development of the two data completion techniques.
- The cosine data completion method was developed with the specific aim of reducing the truncation artefacts in the reconstructed image. This was successful.
- The ‘estimation from model’ technique eliminates almost all of the image error relating to the ROI truncated data. This includes both the truncation artefacts as well the error relating to the missing data.
- The error analysis approach provided a quantitative method of validating the performance of both data completion ROI techniques.
- Both data completion methods were successfully applied to cone-beam geometry for the ROI CT inspection of CFRP laminates.

The cosine extension method is suitable for any ROI CT application where the primary need is to suppress the truncation artefacts. This will be the case in any inspection where

the strong artefacts are masking defects near the edge of the ROI. It does not remove all of the missing data error because the tail is a simplified approximation of the missing data. For most NDT applications, this error reduction is sufficient to allow an uncompromised inspection. Defects will not be significantly affected by the remaining error and will be far more visible because of the magnification benefits of the ROI scan. The time added to an inspection is very low, requiring only some additional computation time.

The 'estimation from model' method is exceptionally effective in suppressing all reconstruction errors associated with ROI CT. With little to no transition at the truncation point, the truncation artefacts are removed and as the model projection data is an excellent substitute for the data outside the FOV, the missing data error is likewise removed. This improvement over the cosine method comes at the cost of greater complexity and the requirements of prior knowledge. Therefore, this technique is likely to find applications in more demanding inspections where subtle density changes need to be identified.

Overall, the research presented in this chapter was highly successful. It resulted in the development of two techniques for error suppression in ROI CT that allowed accurate high resolution volumetric inspection of CFRP composite panels. It has also highlighted that industrial CT has not yet reached its full potential and that there are still a number of avenues of applied research yet to be investigated.

Chapter 4

Extending the CT Scan Field-of-View for Inspection of GFRP Wind Turbine Blades

4.1 Introduction

This chapter describes the development of a novel CT scanning technique known as Offset CT using a prototype high energy micro-focus X-ray system. The aim of this work was to extend the CT scan Field-of-View (FOV) in cone beam CT systems. This would allow Glass-Fibre-Reinforced-Plastic (GFRP) Wind Turbine Blades (WTB) to be inspected that were significantly larger than the detector's FOV.

The industrial need for inspection methods that can provide extensive information on defects (and damage) within critical FRP composite components has been discussed in Chapter 1. A reliable NDT technique that can accurately detect and characterise a large range of defects is imperative to help relate inspection results to analytical models and mechanical testing. This is especially true for the wind turbine industry where efficiency of design and structural reliability are of the up-most concern. Faults within the composite structure can result in catastrophic failure endangering life and reducing public confidence. This will restrict future wind turbine developments and significantly impact on current initiatives to increase sustainable and renewable energy sources (Jasiūnienė *et al* 2009).

CT has shown to be a very effective NDT technique for damage characterisation in FRP based composite structures (Choudhry and Li 2008; Muralidhar and George 1999). It has all the benefits of conventional radiographic inspection but overcomes two major limitations by removing the 2D superimposition of features and allowing planar defects such as delaminations to be detected. However, the inherent limitations of CT reconstruction restrict its uptake as an inspection technique for large structures such as WTBs. This limitation is due to the resulting truncated projection data which cannot be reconstructed accurately using the common Filtered Back Projection (FBP) type FDK algorithm (section 4.5.1). Only two methods can potentially overcome this problem, Region of Interest (ROI) CT and extending the scan FOV (see sections 2.2.5). ROI CT will not image the whole object but, instead, produces a CT image of the region that fits within

the FOV. This is being developed to increase the magnification and spatial resolution of imaged regions and to allow regions of large objects (larger than the detector FOV) to be accurately inspected (details of this were described in Chapter 3). FOV extension methods are different in that the whole object will be reconstructed using only the data present within an ROI. The main problem with both techniques is the truncated projection data and resultant incomplete sampling and the effect this has on the subsequent reconstruction; this was reviewed in section 2.2.5.

Various methods have been developed to extend the FOV with most using data completion methods to estimate the missing data (see section 2.2.5.2). The vast majority of these methods are based on fan beam geometries that utilise ray redundancy properties to complete the missing data (see section 2.2.5 and section 4.5). However, these methods for extending the CT scan FOV cannot be directly applied to cone beam configuration as no ray redundancy exists, except in the mid plane where the source trajectory is located and it can be viewed as fan beam geometry.

This chapter describes the development and validation of an 'Offset CT' technique for extending the FOV in cone beam configurations. This technique exploited aspects of Fu and Lu's (2005) fan beam method described in section 2.2.5.2 and incorporated the concept of a virtual source trajectory used by Clackdoyle *et al* (2004) for the Back Projection Filtration (BPF) algorithm. This resulted in an asymmetrically positioned detector and each elevation within the cone beam projection, i.e. a 1D horizontal pixel array, being treated as a virtual fan beam trajectory. This allowed the approximation of redundant ray paths which could then be used to complete the missing half of the projection data. An estimation of the missing data was sufficient as it was only required for the purposes of filtration. Following the filtration process a blanking function was implemented within the FDK reconstruction algorithm to ensure only the measured data was back-projected.

The chapter also compares the performance of this technique to a second simpler data completion method for Offset CT based on the cosine ROI technique described in Chapter 3 (see section 3.6). For the purposes of the Offset CT work, the two data completion methods will be referred to as 'tailing' and 'estimation', where tailing describes the Cosine based assumption method developed for ROI CT and estimation describes the data redundancy based method above. Both of these methods were implemented using projection data acquired from a prototype high energy X-ray system. This system allowed the required horizontal detector shift (asymmetrically positioned) and a full width GFRP

WTB to be mounted and scanned. In relation to the inspection of WTBs, the scope of work also included an initial feasibility study into detection capabilities of radiographic inspection compared with ultrasonic testing. This work was performed prior to developing the advanced offset CT inspection procedures for WTBs.

4.2 Objectives

The aim of this work was to develop a FOV extension method that could be implemented into a cone beam CT setup so that WTBs significantly larger than detectors FOV could be inspected. Specifically to;

- Provide an initial feasibility study on the use of digital radiography compared to ultrasonic testing for the detection of defects in a WTB.
- Calibrate the prototype X-ray system to a sufficient level to allow the offset projection data to be accurately collected.
- Develop and implement two different data completion methods to estimate the missing data and overcome the truncation problem.
- Modify the FDK reconstruction algorithm to allow only the measured data to be reconstructed following filtration.
- Successfully reconstruct the full width of a GFRP WTB that is larger than the detectors FOV.
- Validate the Offset CT technique using accurate full data sets to simulate offset CT projections and quantify the performance.

4.3 Feasibility Study: NDT of Wind Turbine Blades using Radiographic and Ultrasonic Techniques.

The objective of this pre-study was to investigate whether radiographic techniques are a viable option for inspection of WTBs. Currently, Ultrasonic Testing (UT) is one of the most commonly used NDT techniques for both manufacturing quality control and lab based fatigue and damage investigations. The use of UT c-scan imaging enables area mapping of both composite delamination and interface disbonds. However, the interference of overlapped reflections, scattering and attenuation of the reflected ultrasonic waves from the multi-layered structure often affects results. The scattering effect also has a negative impact on the propagation of ultrasonic waves in general and requires the use of lower frequencies which significantly reduces the spatial resolution (Gieske and Rumsey 1997). These inherent limitations with UT has meant extensive research is still ongoing to

develop reliable inspection techniques for defect detection and characterisation at all stages of the blades life cycle; from design to in-service. Therefore, an investigation was conducted comparing the inspection results obtained using Radiography and UT on a range of manufactured and natural occurring defects within a WTB sample. Evaluating the ability of these techniques to identify and characterise various defects helped prove that CT, as a radiographic based technique, could potentially be developed to overcome the limitations of conventional inspection of WTBs.

4.3.1 Blade Sample

The study was carried out on a 1005mm x 870mm GFRP WTB sample as shown in Figure 4.1. A drawing of the same sample identifying the artificial defects and other areas inspected in the investigation are shown in Figure 4.2.

All of the artificially produced defects were circular flat bottom holes with various diameters which simulated lack of bonding/glue, structural defects and delaminations (ultrasonics only). These were fabricated into three different areas of the blade, the main spar (diameters 19mm, 49mm and 81mm), the trailing edge (5mm, 15mm and 25mm) and the leading edge (5mm and 15mm).

Aside from the artificial defects, scan lines were also chosen along the sample to search for naturally occurring in-homogeneities within the sandwich structure, similar to those shown in Figure 4.1. These inspected areas are highlighted in Figure 4.2 as lines *AA* and *BB*.

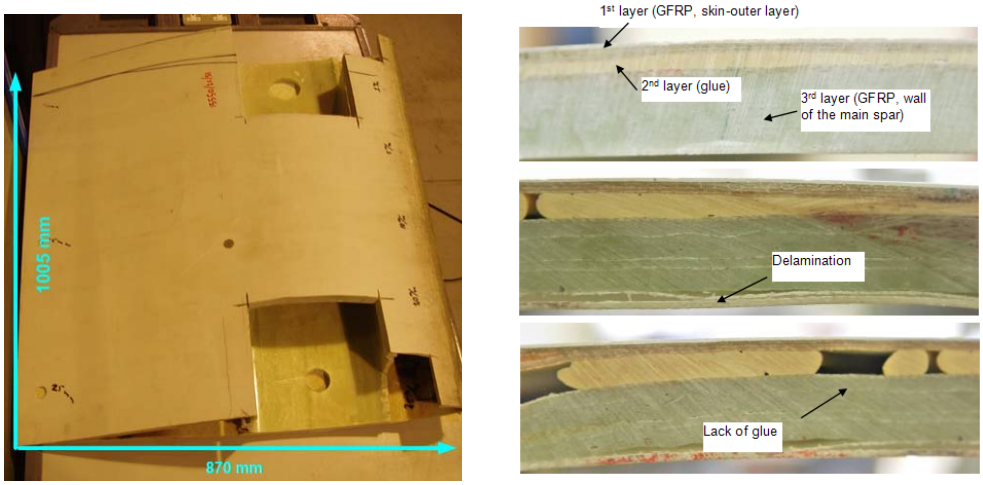

Figure 4.1: Photograph of the wind turbine blade sample used in the study (left). Cross sections through the Main spar showing the blades sandwich structure and some manufacturing defects (right).

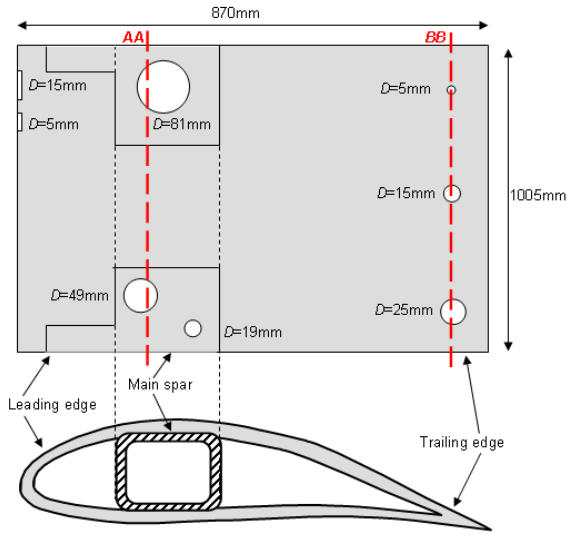

Figure 4.2: A drawing giving dimensions and identifying defects in the sample.

4.3.2 Ultrasonic Testing Setup

UT scanning of the wind turbine blade is a complicated task due to the arbitrary curved surface of the blade. Its implementation requires a precise set-up and continuous monitoring of many parameters. The transducer should be positioned at the same distance strictly perpendicular to the surface throughout the scan as variations can affect the results. The UT technique employed for this study was pulse-echo immersion testing utilising a moving water container. Two different transducers (focused *f*=2.2 MHz and planar *f*=400 kHz) was used and the inspection setup for each transducer was as follows:

- The focussed transducer had a frequency of 2.2MHz and a diameter of 22mm. The transducer was excited by 1 period bursts with amplitude 200V. The gain of the system was set at 37dB.
- The planar low frequency transducer had a frequency of 400kHz and a diameter of 26mm. The transducer was excited by 1 period bursts with amplitude 17V. The gain of the system was set at 7dB. All the measurements were collected using a scanning step of 1mm.

This UT scanning procedure was developed and the results collected by the Ultrasound Institute of Kaunas University of Technology, Lithuania (Jasiūnienė *et al* 2009). The UT work was part of a collaborative project[1] involving TWI Ltd (Wales). The experimental setup for this technique is shown below in Figure 4.3.

Figure 4.3: The experimental set-up for the pulse-echo immersion technique (Jasiūnienė *et al* 2009).

4.3.3 Radiographic Setup

A prototype high energy micro-focus X-ray system located at TWI Ltd was used for the radiographic investigation. The X-ray source was capable of 450kV and 2mA, with a Tungsten target and a focal spot size of approximately 50μm. The detector used to acquire the data was an image intensifier coupled to a 12 bit CCD camera, 1012 x 1012 pixels with 160μm Pixel size. The source to detector distance was approximately 1.8m and the source to object distance was modified according to the area under inspection. The photograph in Figure 4.4 shows the inspection setup including the mounted blade sample.

[1] Concept was a collaboration between the following organisations: Metris X-tek, GenVolt, Innoxpexion, Kaunas Technical University, London South Bank University and TWI Ltd. The project was co-ordinated and managed by TWI Ltd and was partly funded by the EC under the Cooperative Research, Project ref: FP6-COOP-CT-2006-032949.

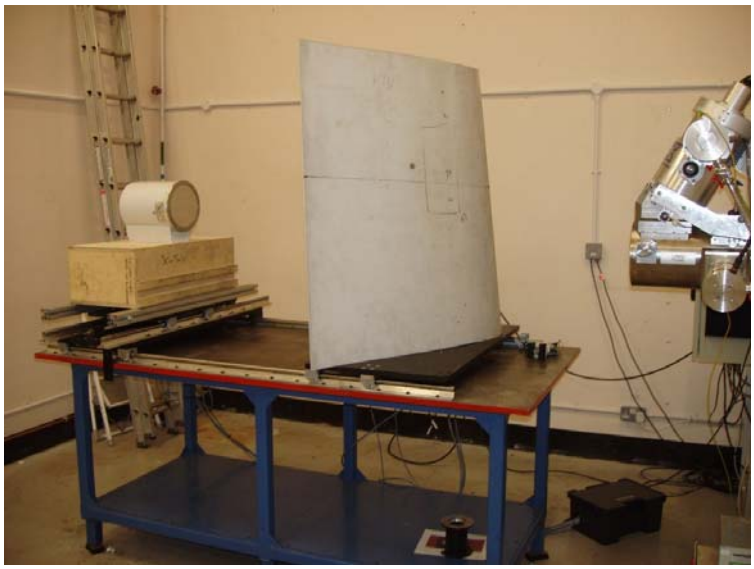

Figure 4.4: The experimental set-up for radiographic testing of the wind turbine blade.

4.3.4 Experimental Results

4.3.4.1 Main Spar – 81mm Defect

A photograph of the artificial 81mm circular defect with regions containing lack of glue is shown in Figure 4.5. This defect was inspected using the pulse echo immersion technique (*f*=2.2 MHz and *f*=400 kHz) and radiographically using the X-ray settings 80 kV and 100 μA with the image intensifier CCD camera.

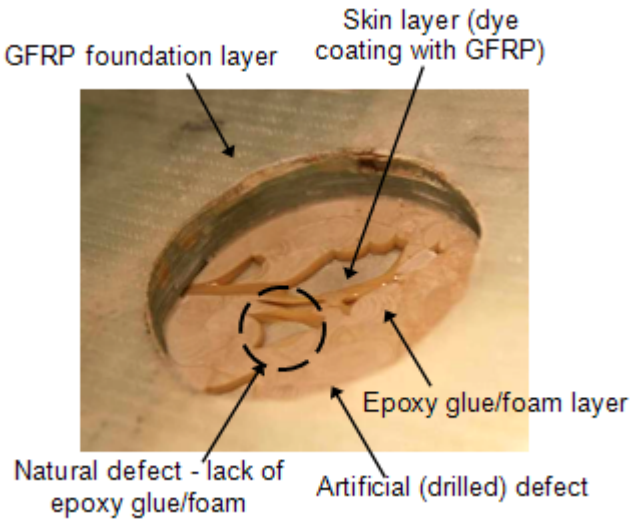

Figure 4.5: Photo of the artificially made defect (diameter 81 mm) on the third layer (GFRP foundation, wall of the load carrying box).

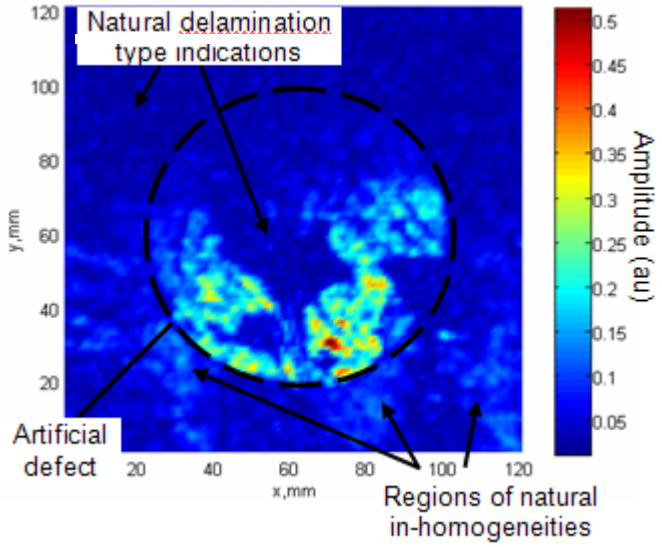

Figure 4.6: Ultrasonically obtained C-scan image using focused ultrasonic transducer (2.2MHz) of the artificially made internal defect (diameter 81 mm). The colour scale represents the amplitude of the signal reflected and then received by the transducer (Jasiūnienė *et al* 2009).

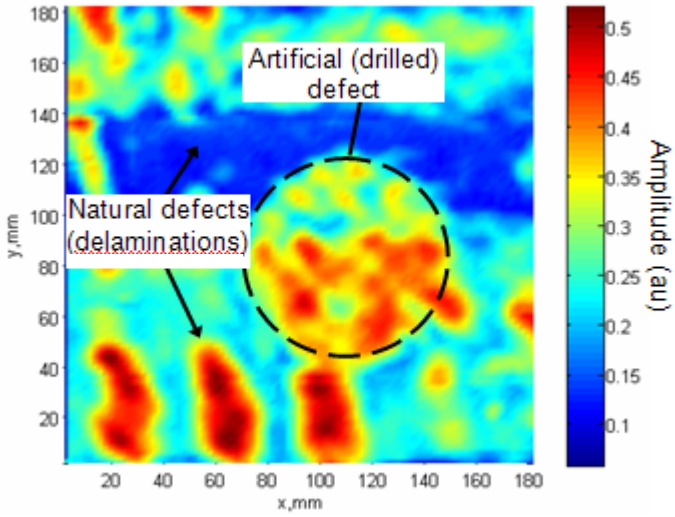

Figure 4.7: An ordinary (raw) C-scan image using planar 400 kHz transducer of the internal artificially made defect 81 mm in diameter The colour scale represents the amplitude of the signal reflected and then received by the transducer (Jasiūnienė *et al* 2009).

Figure 4.6 shows a C-scan image of the 81mm defect using the focussed 2.2 MHz transducer. In this case, the highly focused transducer has allowed, in some parts, to visualise the dimensions of the void caused by the missing glue. However, the shape and diameter of the 81mm circle cannot be fully defined because it is overshadowed by the amplitude at the interface between the outer skin (1st layer) and the epoxy (2nd layer).

There are two possible reasons for this increased amplitude. The first is that it could be due to the shorter wavelength being more sensitive to the acoustic barrier of the interface. The second explanation is that it could be due to a natural occurring delamination between the layers.

Figure 4.6 also shows that outside of the circular defect are some regions of naturally occurring in-homogeneities. These areas go almost undetected using the focussed transducer and cannot be characterised in anyway in terms of type of defect or size. By contrast, the lower frequency transducer (*f*=400kHz) allows these defects to be visualised and the size approximated, as shown in Figure 4.7. This is due to the fact that low frequency transducers allow for an increased depth of penetration and thus increasing the transmission of sound between the materials internal interfaces However, as mentioned previously the use of the lower frequency waves results in a reduced spatial resolution. This is clear when comparing the actual shape of the missing glue regions (within the 81mm defect) in Figure 4.5 compared to the ultrasonically obtained image in Figure 4.7. The shape has not been accurately reconstructed and obtaining extensive information on the defective region is not possible.

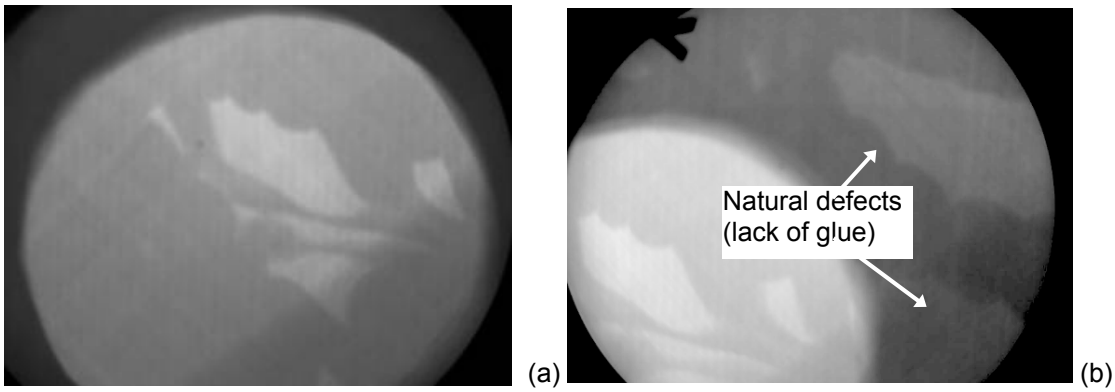

Figure 4.8: (a) A 2D digital radiograph of the 81mm defect and (b) the defects in the outer region. The radiographic settings used were 80kV and 100µA with a source to object distance equal to approximately 400mm.

Figure 4.8 shows radiographic images acquired with the CCD detector coupled to an image intensifier. This detector was used as it is capable of real time radiography which was beneficial for optimising the beam angle for any defects present. The images acquired show very good contrast allowing accurate measurements to be taken of the geometry of the defects. The lack of glue regions within the drilled hole are clearly visible and the natural in-homogeneities detected using UT (Figure 4.7) have been validated using X-rays (Figure 4.8). Additionally, the radiographic inspection was able to

characterise these indications as being a lack of glue within the blade structure and not delaminations.

4.3.4.2 Main Spar - Scanning Cross Section AA

The scan line *AA* was chosen along the length of the main spar between the artificial defects 81mm and 49mm (as shown in Figure 4.2). In between these defects, naturally occurring in-homogeneities within the sandwich structure were detected and compared between the two inspection techniques. The pulse echo low frequency UT setup (*f*=400kHz) was used to allow the required depth of penetration and radiographically the X-ray settings were the same as those used for the inspection of the 81mm defect (80kV 100μA).

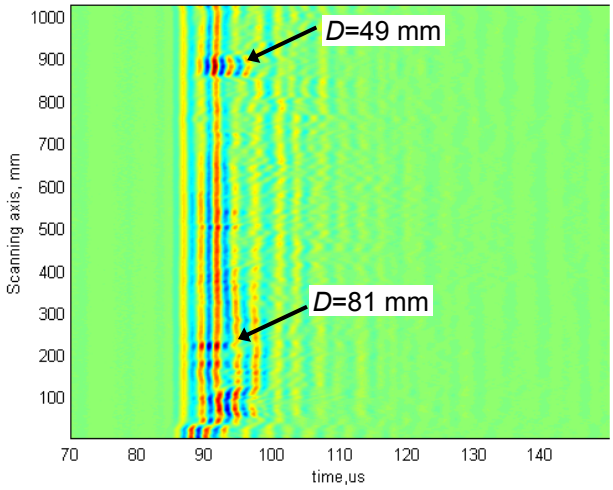

Figure 4.9: The raw B-scan image made along the scanning cross-section AA using the low frequency ultrasonic transducer (*f*=400kHz) (Jasiūnienė *et al* 2009).

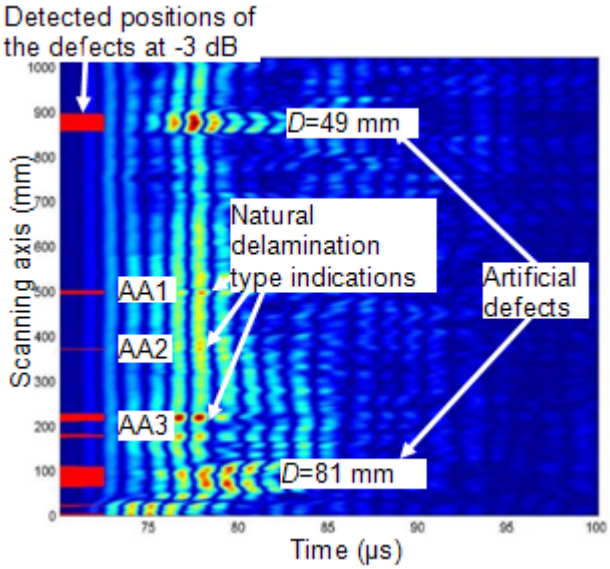

Figure 4.10: The processed B-scan image made along the scanning cross-section AA using the low frequency ultrasonic transducer (Jasiūnienė *et al* 2009).

Figure 4.9 shows the raw B-scan image collected along the scanning cross section AA using the low frequency transducer. Figure 4.10 is a processed B-scan image along the same scanning cross section AA. The image processing allows easier identification of any in-homogeneities by subtracting the reference signal from the raw B-scan data. The reference signal is the averaged response from the multilayered medium. The processed B-scan identified the two artificial defects (81mm and 49mm) and indicated three areas of natural delamination type defects, as highlighted in Figure 4.10.(*AA*1, *AA*2, *AA*3).

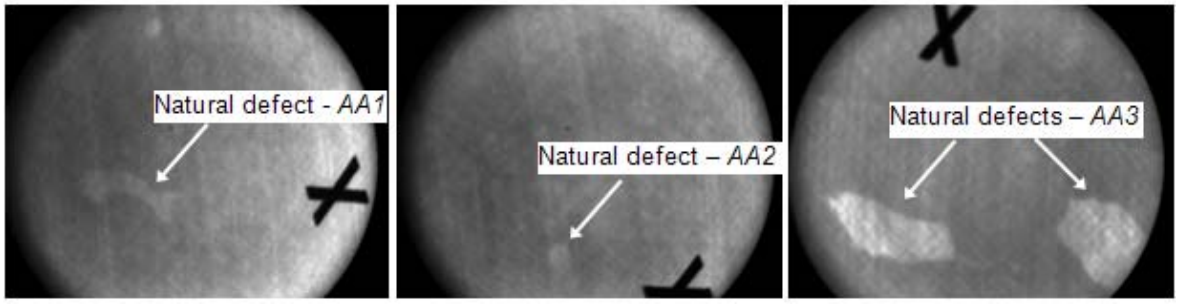

Figure 4.11: 2D digital radiographs taken of the scanning cross section *AA*. Defect *AA1* (left), defect *AA2* (middle), defect *AA3* (right). The radiographic settings used were 80kV and 100µA with a source to object distance equal to 400mm.

The radiographic inspection results in Figure 4.11. show that it was also able to detect all three of the naturally occurring in-homogeneities (*AA1*, *AA2*, *AA3*) identified in cross section *AA* by the UT scan (Figure 4.10). The radiographs confirmed these defects to be a lack of glue and not delaminations as indicated by the UT results. Additional information

such as the shape of these defects and the fibre orientation is also available in the radiographic results obtained.

4.3.4.3 Trailing Edge - Scanning Cross Section *BB*

The inspection scanning line *BB* was chosen along the length of the trailing edge encompassing the artificial defects 5mm, 15mm and 25mm (as shown in Figure 4.2). In between these defects, naturally occurring in-homogeneities were detected and compared between the two inspection techniques. The inspection setup for both techniques remained the same as for the scanning cross section *AA*.

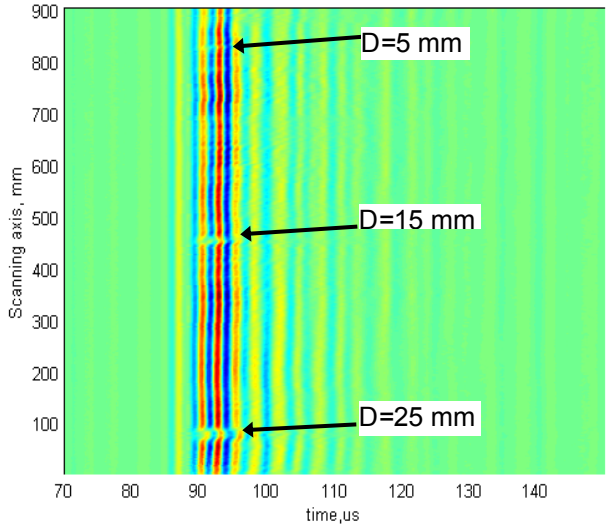

Figure 4.12: The raw B-scan image made along the scanning cross-section *BB* using the low frequency ultrasonic transducer (*f*=400kHz) (Jasiūnienė *et al* 2009).

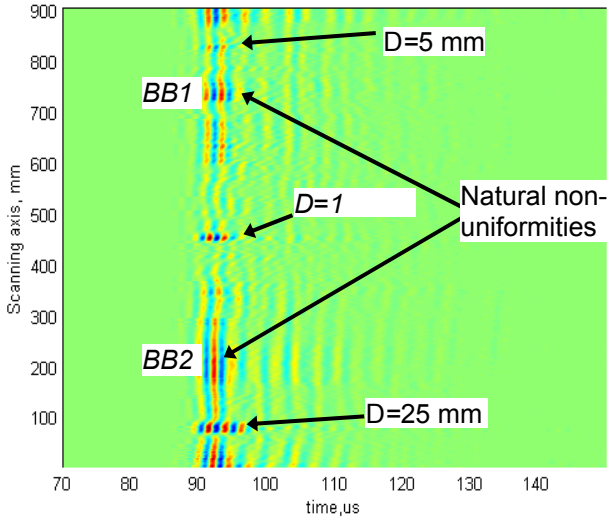

Figure 4.13: The processed B-scan image made along the scanning cross-section *BB* using the low frequency ultrasonic transducer (*f*=400kHz) (Jasiūnienė *et al* 2009).

The raw B-scan image collected along the scanning cross-section *BB* is shown in Figure 4.12 with all three of the artificial defects being detected (5mm, 15mm and 25mm). The subtraction was again performed to produce the processed B-scan data shown in Figure 4.13. This image accurately identified the position of two naturally occurring in-homogeneities (*BB1* and *BB2*) between the artificial defects.

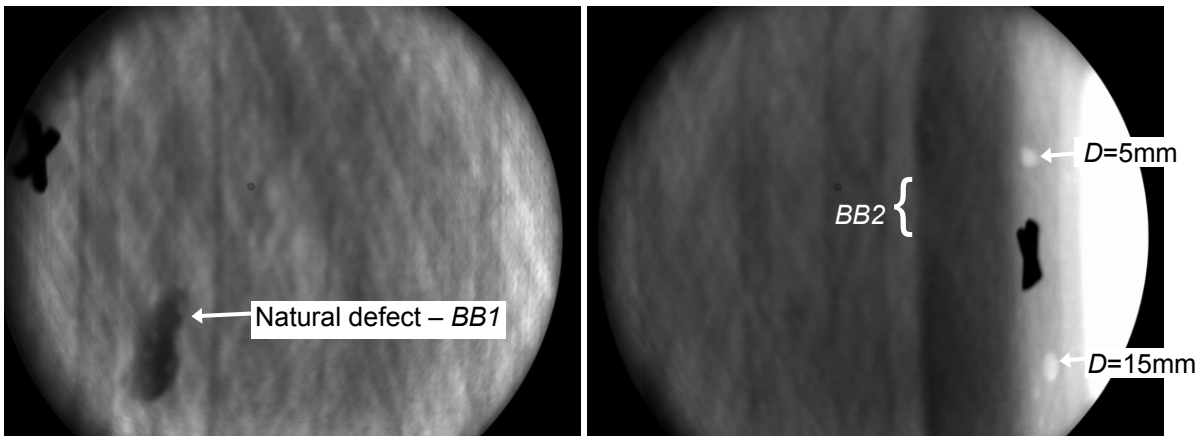

Figure 4.14: 2D digital radiographs taken of the scanning cross section *BB*. The detected inclusion, *BB1* is shown on the left and the non-uniformity in the blade structure, *BB2*, is shown on the right. The radiographic settings used were 80kV and 100μA with a source to object distance equal to 400mm.

The X-ray images were also able to detect all three of the artificial defects and the two naturally occurring in-homogeneities identified by the UT scan. Figure 4.14 shows that the indication *BB1* detected in the UT scan is actually an inclusion of a higher density material. Information regarding the density of such in-homogeneities is not possible using ultrasonic techniques. Figure 4.14 also shows that the indication *BB2* can be defined as a non uniformity in the blade structure. This is visualised in the radiograph as a short break in a continuous layer of slightly higher density material (dark line). This indication is a good example of why some quality control processes require the use of multiple NDT techniques. The UT inspection easily identified the indication but with no prior knowledge it could have been easily overlooked within the radiographic inspection results. On the other hand, the UT results could not identify the source of this indication whereas the radiographic inspection results could easily visualise the cause as a non uniformity in the blade structure. This is a common problem with UT and is the reason why sometimes such techniques are limited to the detection of hotspots and not for full defect characterisation.

4.3.5 Conclusions

The objective of this study was to evaluate the defect detection and characterisation ability of Digital Radiography and Ultrasonic Testing for the inspection of GFRP WTBs. A range of artificial and naturally occurring defects were inspected and compared in a variety of locations on the blade structure. The Ultrasonic results showed that this technique is able to reliably detect the position of defects and non-uniformities within the blade structure. It also requires access to only one side of the component and has no radiation restrictions. However, the results also highlighted the limitations of the technique for inspecting the complex multi-layered structure. The focussed transducer enabled the shape of defects to be visualised but the increased sensitivity resulted in strong reflections from the layer interfaces which masked the underlying defects. The low frequency planar transducer reduced this affect but the lower resolution meant that it was not possible to accurately characterise the shape or size of the naturally occurring defects (such as lack of glue). A range of natural defects were detected during the investigation, this included, a higher density inclusion, lack of glue, structure non-uniformity and excess glue. However, the UT techniques were not able to characterise between the types of defects as the signal reflections caused by them are the same as any delamination type defect.

The radiographic images proved the technique is capable of detecting volumetric defects such as lack of glue and internal structural irregularities. All of the defects identified using the UT technique were validated and further characterised using radiography. Additional information on the defect type and shape were readily available from the radiographic images. However, as mentioned previously, the radiographic inspection was essentially inspecting hotspots identified by the UT results. The potential risk is that planar defects, such as structural non-uniformities and delaminations, may go undetected or overlooked by a radiographer if no prior knowledge was available to investigate that area with multiple X-ray angles. This is the main reason why the current solution to NDT of GFRP WTBs is to combine a number of different techniques (Raišutis *et al* 2008). The combination of UT and Radiography has been recommended in several papers (Lading *et al* 2002; Borum *et al* 2006; Chia *et al* 2008; Jasiūnienė *et al* 2009).

However, the use of radiography as a method to characterise damage or defective hotpots still has inherent limitations. A radiograph is a 2D image of a 3D object resulting in superimposed details and no method of accurately positioning through thickness object features such as defects. This is a major problem when inspecting a WTB as the perpendicular angle of the X-ray beam will make it near impossible to locate the position

of any defects within the multilayered structure. This problem with imaging and locating planar structures can be partly overcome by correctly orientating the X-ray beam so that they are parallel to the photon path. However, this does not remove the problem of superimposition which will be significantly worse at these angles due to the increased amount of material being penetrated.

X-ray CT is being increasingly used for defect characterisation purposes because the restrictions of conventional radiography discussed above do not apply. The elimination of the superimposition of features and the 360 degrees worth of X-ray data means that CT can provide cross-sectional information on planar defects and multilayered structures. This makes CT an ideal inspection technique for the complex structure of a WTB. However, CT also has restrictions that limit its uptake for inspecting large objects such as WTBs. These restrictions have been discussed in section 1.3.2 and section 2.1.7.

This study has provided sufficient evidence that radiographic testing is a viable option for the inspection of WTBs. It has also added further weight to the argument that developing X-ray CT for the inspection of WTBs would provide defect characterisation abilities that currently cannot be achieved by any other NDT technique.

4.4 Offset CT – Acquisition of the Projection Data

A prototype high energy micro-focus X-ray system built at TWI Ltd was used to develop the Offset CT technique. The enclosure allowed very large objects (up to 3.5m in height) to be inspected (such as WTBs) and the manipulator permitted the required detector shift to an asymmetrical position (such that the centre of rotation is within the FOV of the detector), as illustrated in Figure 4.15. However, the prototype high energy X-ray system was built mainly for the purpose of developing the high energy micro-focus source, meaning the entire system was not fully integrated or calibrated. Therefore, to perform a CT scan, every aspect of the X-ray system had to be calibrated and checked before acquisition of the CT data could take place.

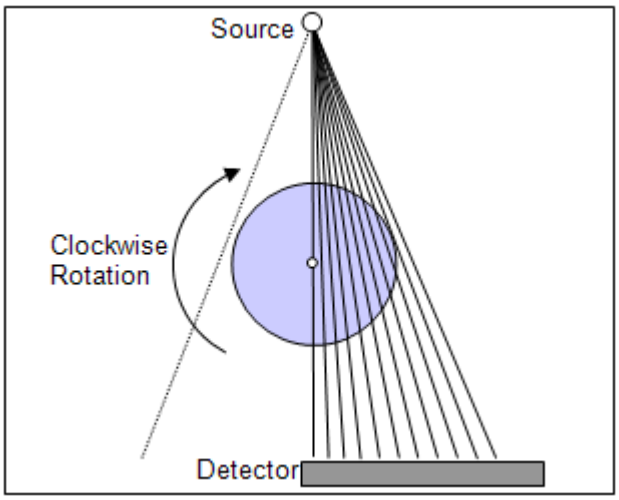

Figure 4.15: Drawing of Offset CT setup.

4.4.1 X-ray System Calibrations

4.4.1.1 Manipulator

The manipulator required full calibration as the software represented the movement with count values instead of angles. These values needed to be transformed so that the angular increments are known for each of the CT projections. In addition, this calibration had to account for the errors in the rotational movement to improve the accuracy of the defined increments.

The manipulator software showed the input movement and the actual movement (in units of 'counts'), allowing for an error percentage to be calculated. The average of these errors and the standard deviation of the actual movements were calculated at different distances, speeds and directions, to deduce the best combination for the accuracy and repeatability. The findings proved that slower speeds and larger distances resulted in the smallest error and clockwise rotation provided the optimum in terms of repeatability.

An angular reference was fabricated to calibrate the number of counts required to turn the manipulator table by 1 degree. This comprised a CAD drawing with 360 degree increments fitting exactly onto the manipulator table (of diameter 190mm) and a needle placed stationary at 0 degrees (as shown in Figure 4.16). It was observed that an input value of 34,000 gave the most accurate 1 degree increment. This input value resulted in an average actual movement of 34,988 counts giving an average error of 2.9% per movement (calculated over a sample of 20 movements). Based on this, the input value was deduced for 0.72 degree increments (500 projections) which also accounted for the error in the movement. Specifically, the input value of 24,000 counts was shown to

produce the desired actual movement of 25,191 counts (34,988 x 0.72). This meant the extra distance moved by the manipulator (i.e. the error) was included in the input value to improve the accuracy of the angular movements. This was validated using the CAD angular reference by rotating through 360 degrees and observing that, at these increments, the manipulator returned to its original starting position.

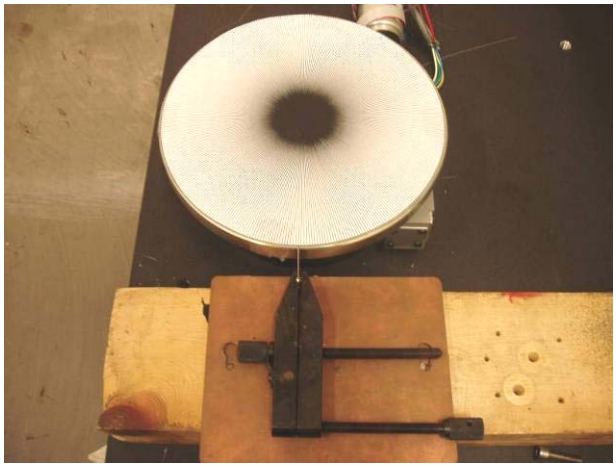

Figure 4.16: CAD angular reference on manipulator with needle mounted in position.

4.4.1.2 Source

The combination of a separate prototype high voltage unit and micro-focus X-ray tube resulted in a very unstable source requiring a time consuming conditioning period. The best way to achieve higher stable voltages was to increase the voltage in 2kV increments and allow it to stabilise for 10 minutes. Once the desired voltage had been met, the beam current was then increased in the same way.

The source focus required calibration to improve the sharpness of the radiographic image. A look up table was set up as a reference to obtain the optimum focus output for the tube potential being used. This involved placing a circuit board chip on the source for maximum magnification and altering the focus output power supply until the beam was properly focused on the 25µm wires inside the chip. This was repeated at 5kV increments and a curve of focus output as function of tube potential (kV) was plotted for reference use. A radiograph of the magnified chip is shown in Figure 4.17.

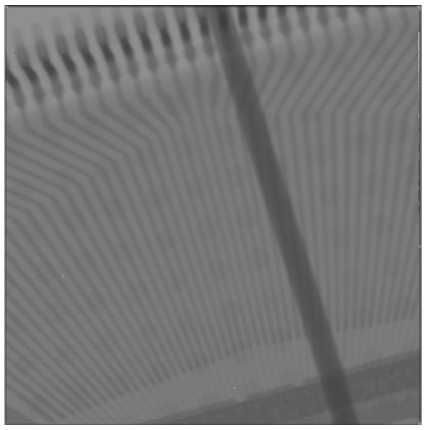

Figure 4.17: Radiograph showing the highly magnified circuit board chip that was used to optimise the source focus.

For CT scanning, the system alignment has to be accurately calibrated to ensure the reconstruction algorithm correctly defines the ray paths relative to the centre line of the cone beam. This requires both the X-ray source and detector to be aligned, both horizontally and vertically, along the principal axis of the CT system. This calibration involved initially aligning the source, manipulator and detector using a laser pointer. The alignment of the source focal spot to the centre of the detector was then refined using a rod fitted to the manipulator in an off-centre position and observing it through rotation to ensure that the height did not alter as the magnification changed. This calibration procedure is described in full in section 2.2.6.

4.4.1.3 Detector

The detector used for the experiment was a Perkin Elmer 16 bit XRD1621 with 2048 x 2048 pixels and a pixel size of 200µm. A series of corrections needed to be performed to eliminate detector specific effects and obtain good quality results. Each image was ‘offset’ and ‘gain’ corrected, including an underperforming pixel correction. The X-ray detector needs an offset correction to account for the dark current of each pixel. Additionally, a gain correction is required to homogenize differences in pixel sensitivities and to take into account the X-ray beam illumination. The pixel correction allows a ‘software repair’ of underperforming pixels to enhance image quality. These underperforming pixel values are replaced with the averaged value of the surrounding eight adjacent good pixels.

The calibration of the offset distance was necessary to align the centre of rotation to the edge of the detector FOV, as shown in Figure 4.18. To perform this calibration a homogenous aluminium cylinder was used. The cylinder was 50mm diameter and the inspection setup included a source to object distance of 230mm and a source to detector

distance of 1,477mm. The cylinder was placed at the centre of the manipulator and the width of the cylinder (in pixels) was measured at the centre of the detector FOV, equalling 1,375 pixels. To successfully reconstruct the offset CT data, it was necessary for the centre of rotation to be just inside the FOV. Therefore the detector was offset so that the centre of the cylinder was just visible on the edge of the FOV. To avoid an increase in artefacts, the centre of rotation was shifted by 11 pixels further into the FOV, as this was the amount of underperforming pixels found at the edge of the detector.

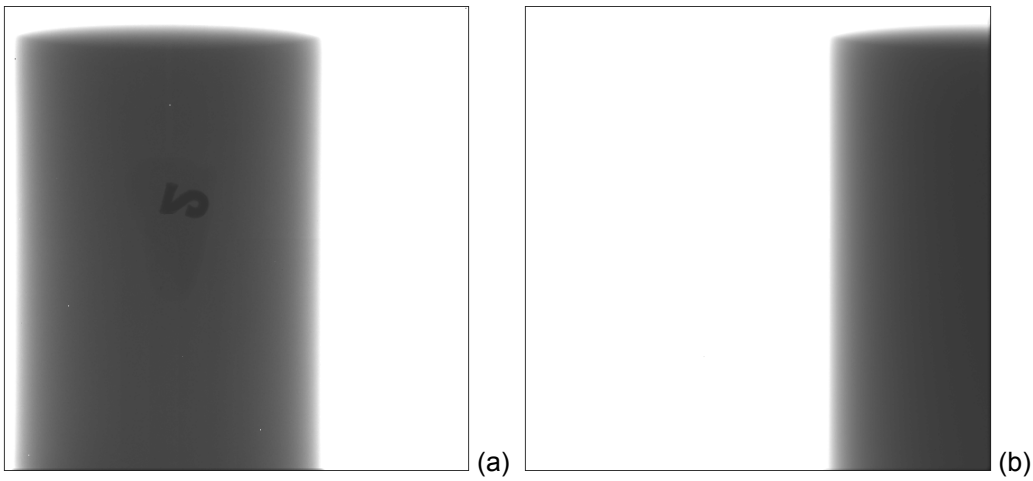

Figure 4.18: X-ray projections of aluminium calibration cylinder; (a) full projection with lead letter to ensure sufficient penetration (b) Offset projection with centre of cylinder just inside the FOV.

4.4.2 Acquisition Method

Three separate Offset CT scans were acquired:

(1) Homogenous aluminium calibration cylinder with a reference marker (washer)

(2) Homogenous aluminium calibration cylinder without a reference marker

(3) Full width of a WTB

The homogenous aluminium cylinder was chosen as an ideal calibration object for the developmental CT scan, as artefacts and anomalies added by the reconstruction can be easily identified and possibly corrected. This has obvious benefits when trying to optimise an experimental reconstruction method. The reference marker on the first scan was used as a further tool for calibrating the angular increments of the manipulator. This was removed for the second scan to provide a fully homogenous cylinder. The aim again being to use the first two scans to optimise the offset reconstruction process and then implement a final version for the more difficult WTB projection data. The aluminium cylinder was 50mm in diameter but was highly magnified for acquisition of the offset projection data.

The offset CT setup used for the aluminium cylinder is shown in Figure 4.19 and the WTB setup is shown in Figure 4.20. The WTB had to have a specially fabricated mount that was able to secure the large blade centrally to the manipulator table and be stable so that no image blur was induced. The imaged section of the WTB had a cord length of 550mm and a maximum width of 70mm. It should also be noted that the detector used had an active FOV of approx 400mm x 400mm.

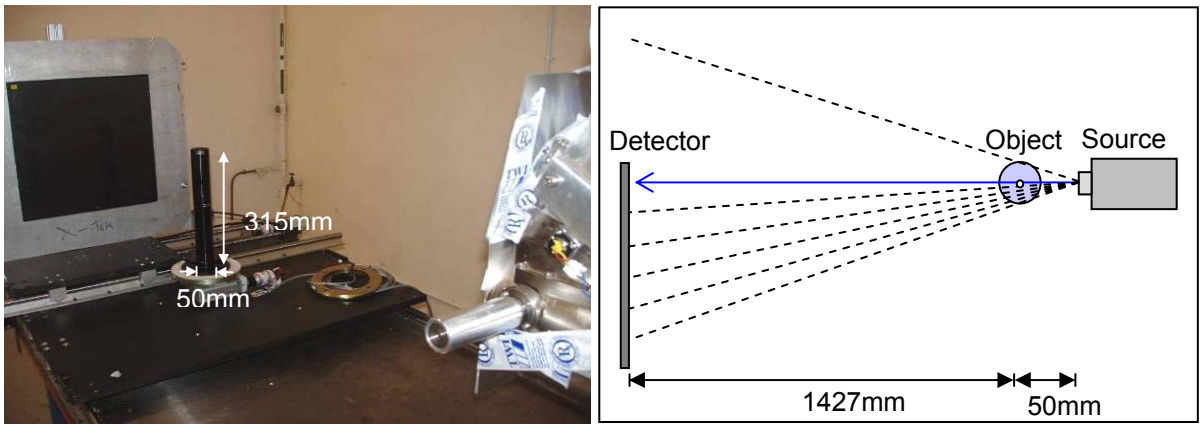

Figure 4.19: Photograph of the aluminium calibration cylinder in the offset position (left). Schematic diagram showing the offset setup used to acquire the projection data for the aluminium cylinder (right).

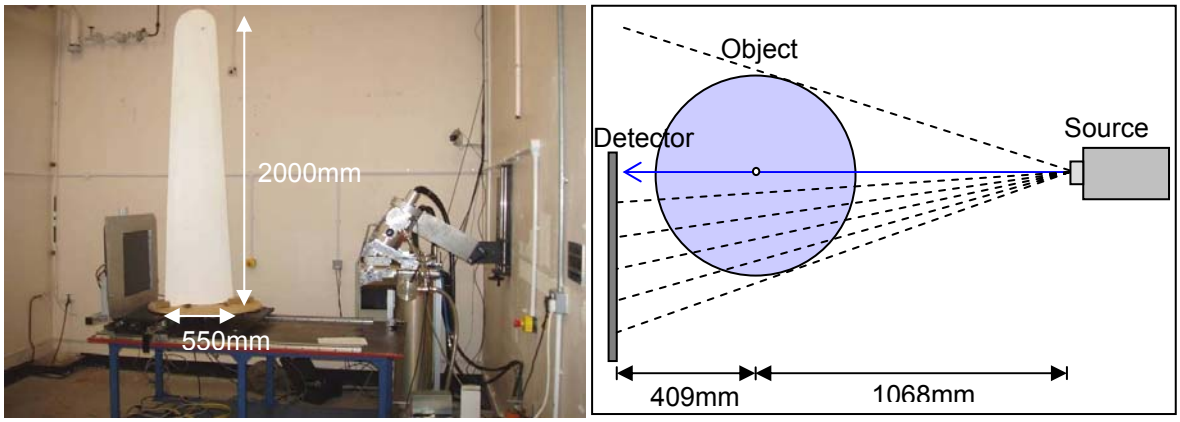

Figure 4.20: Photograph of the prototype X-ray system with a WTB mounted in the offset position (left). Schematic diagram showing the offset setup used to acquire the projection data for the WTB (right).

The following method was repeated for each of the three scans;

(1) The sample was placed on the manipulator table, and the X-ray source and detector parameters set such that sufficient penetration through the component

was achieved without saturating the background. The detector had an internal trigger exposure time set to 5 seconds.

(2) The sample was then removed so that the detector corrections could be performed.

(3) The X-rays were turned off and the detector allowed to stabilise so that an offset dark correction image could be acquired.

(4) The X-rays were turned back on and a gain correction sequence acquired. The sequence involved taking gain images at different tube potentials so that the average grey value of each gain correction image represents the range of grey levels that will be present in the actual image. Once these separate images have been acquired a gain sequence can then be built and both the gain and offset dark correction image can be linked in to correct future images.

(5) A new corrected image was acquired at approximately 80% Full Signal Range (FSR) which equalled 52,000 grey levels (16 bit depth). The homogeneity is then checked by adjusting the brightness and contrast to ensure the gain and offset corrections have been performed satisfactorily.

(6) This corrected image is used to create the pixel mask for underperforming pixels. By taking note of the grey values of such underperforming pixels an ideal range is inputted and the pixels out of the range will be replaced with the average of the surrounding 8 good pixels.

(7) A black reference image and white reference image for the CT scan was acquired by averaging 3 frames at 5 seconds per frame.

(8) The sample was replaced on the manipulator in the central position and the X-ray source parameters returned to the required setting.

(9) The actual projection data had to be acquired manually by rotating the manipulator 0.72 degrees and taking 3 averages for each of the 500 projections.

The settings used for the two scans of the aluminium calibration cylinder were 188kV, 140μA, 3mm Aluminium filter at source, source to object distance of 230mm, and the detector in the offset position with a source to detector distance of 1,477mm.

The X-ray settings had to be altered for imaging the WTB, including reducing the magnification. Due to the range of different densities and thicknesses in the WTB, it was difficult to find the adequate settings. In order to achieve sufficient contrast on the thinnest section of glass fibre and penetration on the thickest sections, it required using a large amount of filtration which could have resulted in under penetration in some parts. The final settings used for the WTB was 180kV, 125uA, 2mm Aluminium plus 1mm Copper filter at

the source, source to object distance 1,068mm, and the detector in the offset position with a source to detector distance of 1,477mm.

4.4.3 Results and Discussion

Figure 4.21 shows a conventional full projection of the aluminium cylinder and an example projection in the offset position where the centre of rotation is just inside the FOV. Figure 4.22 shows the offset projection data acquired for the WTB.

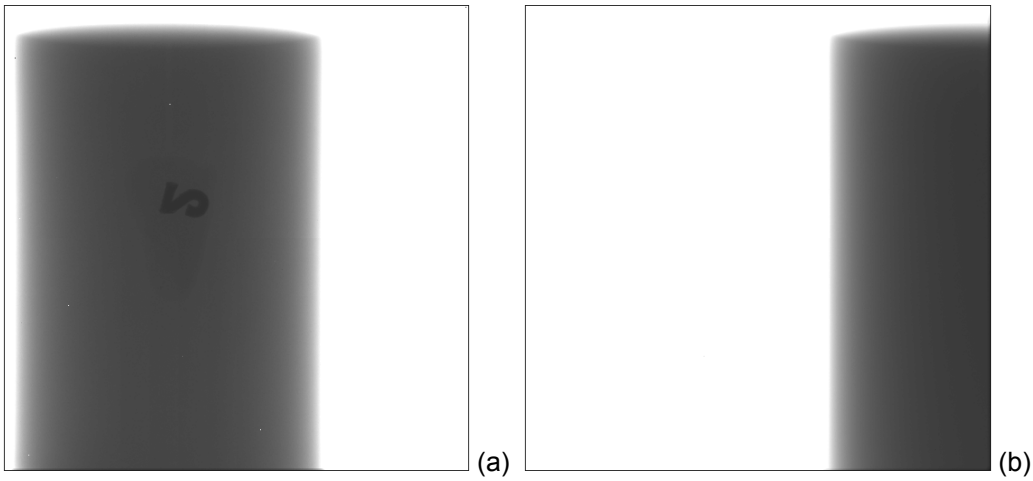

Figure 4.21: X-ray projections of an aluminium calibration cylinder; (a) full projection with lead letter to ensure sufficient penetration (b) Offset projection with centre of cylinder just inside the FOV.

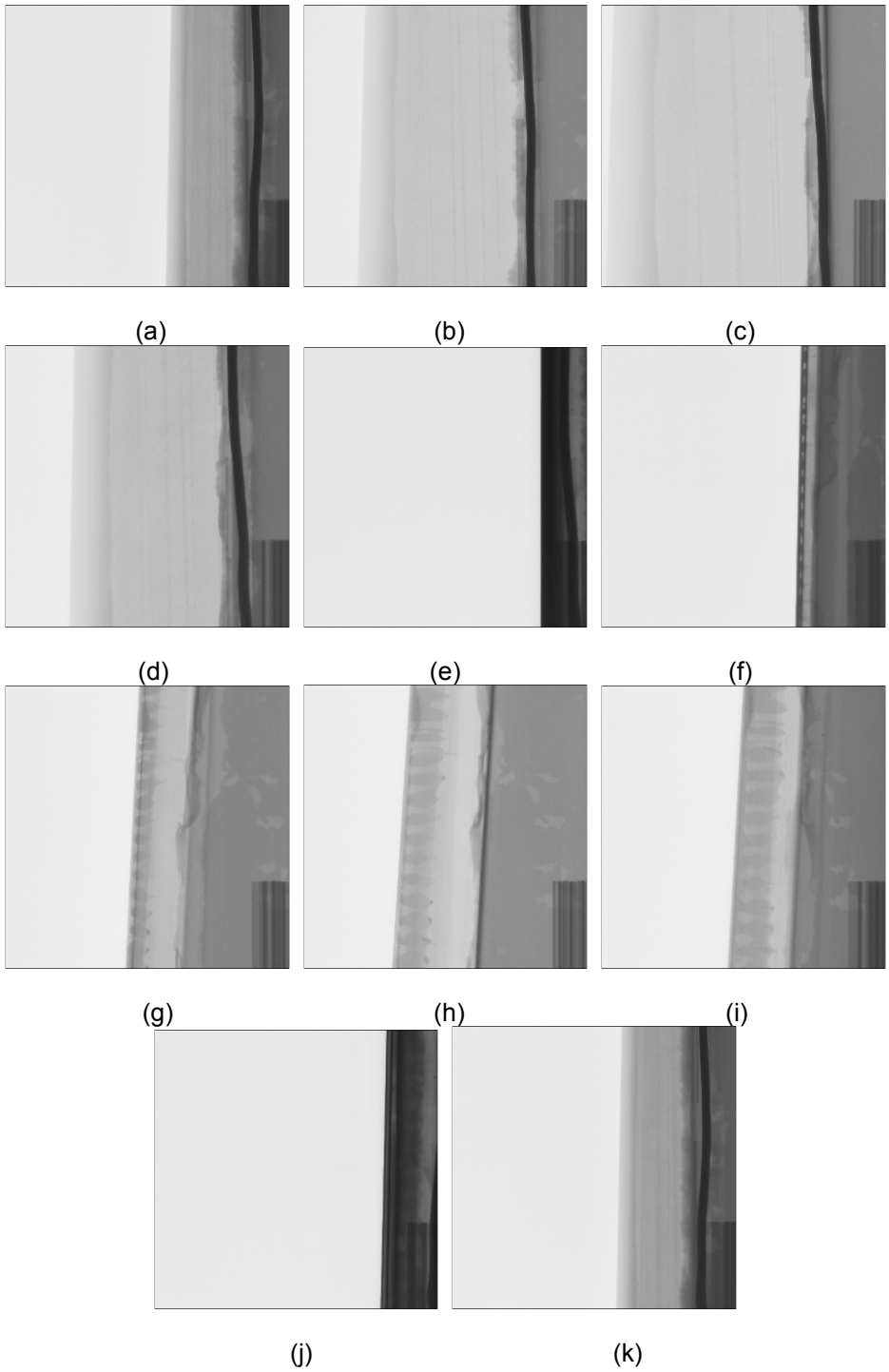

Figure 4.22: Sample of Offset WTB projections taken from the total 500 acquired (a) – (k), projection 0001 (0º), 0050 (36º), 0100 (72º), 0150 (108º), 0200 (144º), 0250 (180º), 0300 (216º), 0350 (252º), 0400 (288º), 0450 (324º), and 0500 (360º), respectively.

A manual Offset CT scan was achieved with 360 degrees of projection data acquired. However, due to the instability of the X-ray source, the X-ray beam sometimes fluctuated during image acquisition, which resulted in reduced exposure for that projection. This could result in possible artefacts and reduced quality in the CT image, and with further

analysis it became apparent that the reduced exposure projections caused the gain correction files to be poorly linked.

The number of projections within the image stack was limited to 500 due to the manual nature of the acquisition process. This meant the projection data was insufficiently sampled which can result in possible under-sampling artefacts and reduced SNR (for more details see section 2.1.6.5). For projections of this size with a detector width of 2048 pixels, the required sampling for an accurate reconstruction would require between 1500-3000 projections. This is based on the sampling rule that the number of projections must equal between $\pi/4$ and $\pi/2$ multiplied by the number of voxels (see section 2.2.3.3). However, this was unavoidable as the experiment required the use of a prototype X-ray system that did not have the level of integration required to perform a CT scan.

4.5 Offset CT Reconstruction

Developing a method that extends the FOV of the CT scan requires the reconstruction of the full object function from a truncated projection data set. However, the FBP algorithm requires that the projection data is not truncated in any view for an accurate reconstruction to take place. This problem has two elements that need addressing, the incomplete sampling and the truncation artefacts. Incomplete sampling leads to inconsistencies in the final projection data set that are subsequently reflected in the reconstructed image (Kak and Slaney 1988) and the truncation leads to strong high frequency ringing artefacts that will also be included in the final CT image.

The key to solving the sampling problem is finding a way to complete the sampling properly. This is the primary reason for the asymmetrically positioned detector within the offset CT setup; it allows utilisation of fan beam ray redundancy properties. It has been well documented that a parallel beam scan taken over a 180 degree angular range provides sufficient information to reconstruct the object (see section 2.2.5.2). This is due to the fact that opposite parallel beam scans are mirror images of each other, therefore there is no additional information content in a 360 degree parallel beam scan. It can also be shown that a 360 degree fan beam scan is equal to a 360 degree parallel beam scan. Using these facts it can be proven mathematically that when CT imaging using a fan beam geometry, a 180 degree scan plus the fan angle has the same information content as a 180 degree parallel beam scan. Therefore, such a scan contains sufficient information content to reconstruct the object (Tam 1988). Consequently, Offset CT for fan

beam geometry has also been shown to satisfy the minimum sampling requirements, as 360 degrees of data has been captured but only in half of the view (Fu and Lu 2005).

As explained in Chapter 2 (section 2.1.7), cone beam CT does not exhibit ray redundancy (except at the mid-plane) and therefore short scan methods that have recently been developed (Zhu *et al* 2007) utilising ray redundancy properties are purely an approximation. However, it has been shown that exact reconstruction algorithms might not offer improved performance compared to the approximate algorithms due to suboptimal noise characteristics (Wang and Yu 2008). Therefore, for the purpose of cone beam Offset CT it can be assumed that these sampling conditions are sufficiently met and a complete data set is acquired even with truncated projections. The problem was now reduced to the matter of finding a way to complete the offset projections using simulated data, so that the truncated projections become non-truncated projections. This would allow the algorithm to process and reconstruct the measured data without inducing the usual truncation artefacts.

4.5.1 Completion of the Projection Data

The offset CT projections were firstly converted from the raw image format produced using the prototype detector into 16 bit tiff file format and doubled in width by adding a zero attenuation image of equal size. This is because the reconstruction software requires the centre of rotation to be near the centre of the image for correction purposes.

If the standard FDK algorithm was used to reconstruct this offset projection data the truncation near the centre of rotation would introduce artificial high frequency noise to the central regions of the filtered projections. This is known as ringing or truncation artefacts and can mask important object detail within the final CT image. The truncation artefact is due to the basic principles of how the FBP algorithm processes the projection data and is described in detail in section 2.2.4.5 and section 3.4. Figure 4.22 shows a CT image resulting from the aluminium cylinder being directly reconstructed using offset truncated projection data completed with only an image of zero attenuation; the truncation artefact is clearly illustrated.

Data completion methods were identified as the most applicable approach to overcoming the truncation problem. This was mainly because they can be implemented with the majority of industrial CT systems that utilise the FBP type FDK reconstruction algorithm. Two approaches were developed (‘estimating’ and ‘tailing’) that extend and complete the

projection data to allow filtration to take place without inducing artefacts. It is well known that the simulated data used to complete the projection will affect the accuracy of the measured data during filtration. Therefore a sufficient estimate of the missing data is essential. In this instance, the extended data is required for filtration purposes only, as the FDK reconstruction algorithm was altered so that the simulated data was not included in the back projection. This allowed only measured data to be reconstructed.

Figure 4.23 shows how the truncation artefacts are visualised in an Offset CT reconstruction when the data is only completed using an image of zero attenuation. These artefacts appear differently to the truncation artefacts identified in Chapter 3 for ROI imaging. This is because Offset CT causes the truncated edge to be continuously located in the middle of the component. Therefore, upon reconstruction artificial high frequency noise is added to the central regions resulting in truncation artefacts within the object.

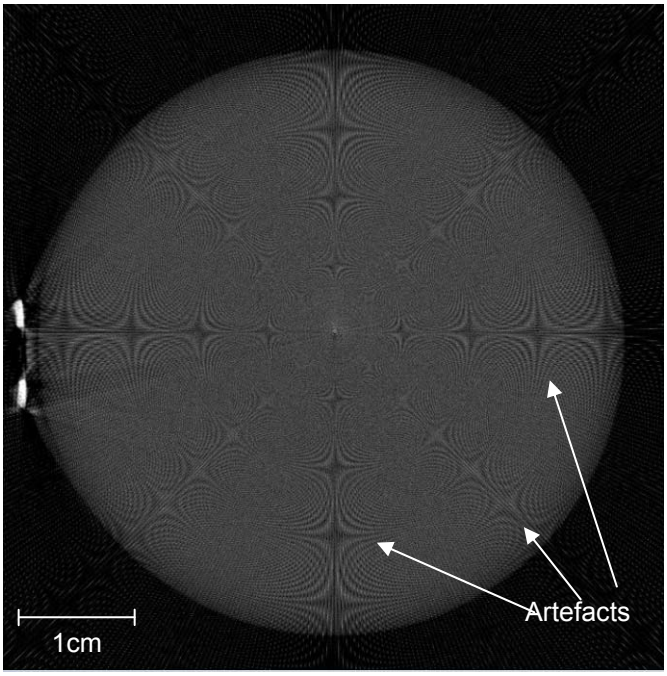

Figure 4.23: A CT image showing the ringing artefacts produced in an Offset CT reconstruction when the data is only completed using an image of zero attenuation.

4.5.1.1 Offset Data Completion Method 1 – Tailing

The cosine 'tailing' data completion method was initially developed for ROI scanning of CFRP laminates and was described in full detail in section 3.6. The ROI data completion method was adapted for the offset projection data so that the low spatial frequency cosine curve was fitted to the edge pixel on only the truncated side of the projection data (located near the centre of the offset object). Similar to the ROI implementation with cone beam

data (section 3.8), this tailing curve was fitted for each 1D horizontal array of pixels within the cone beam projection image. This accounted for the fact that the high pass ramp filter within the FDK algorithm processes the projection data in 1D horizontal lines. Therefore, the cosine tailing provides a simplified extension to the object data and the low spatial frequency curve will remove the sharp transition at the truncated edge; resulting in minimal degradation to the measured data.

Theoretically, the projection data after it has been extended using the tailing function could be reconstructed using the FDK algorithm. This is because the simulated data i.e. cosine tail should be completely removed by the ramp filter. However, this would result in data being averaged across the filtered out simulated data, causing the density to be halved over all voxels. So a 'blanking' function was implemented into the FDK reconstruction algorithm to ignore the simulated data after filtration had been performed. This ensured full density pixels were reconstructed and that only the measured data was back projected. (Blanking is fully described in section 4.5.2).

The following images in Figure 4.24 to Figure 4.27 highlight the tailing extension applied to the projection data of the aluminium cylinder (with washer) and the WTB. Figure 4.24(a) shows an original offset projection of the aluminium cylinder (with washer) with Figure 4.24(b) being the same projection after it has been extended using the tailing technique. The next projection image, Figure 4.25, is taken at approximately 90 degrees where the washer crosses the truncation threshold. This image highlights the variable tail off produced in the simulated data by the cosine curve being fitted to the truncated edge pixel. An intensity line profile, CD, in Figure 4.26 has also been drawn across the cylinder to further illustrate the tail off to zero attenuation. The reference marker at the centre of the line profile signals the start of the cosine fit. Additionally, Figure 4.27(a) shows the original offset WTB projection and Figure 4.27(b) is the resultant projection after attenuation tailing has been applied.

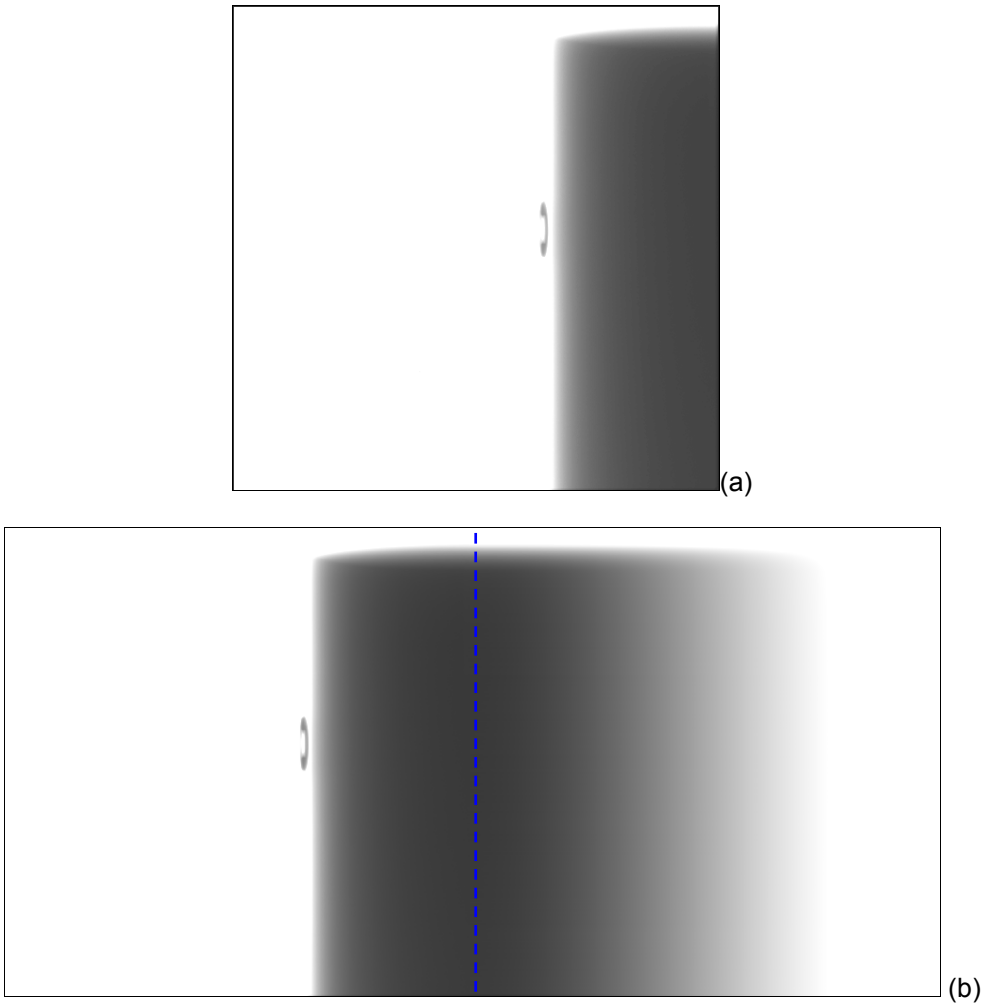

Figure 4.24: (a) Original offset projection image taken of the aluminium cylinder with the washer attached as a reference. (b) New offset projection of the cylinder following extending and tailing.

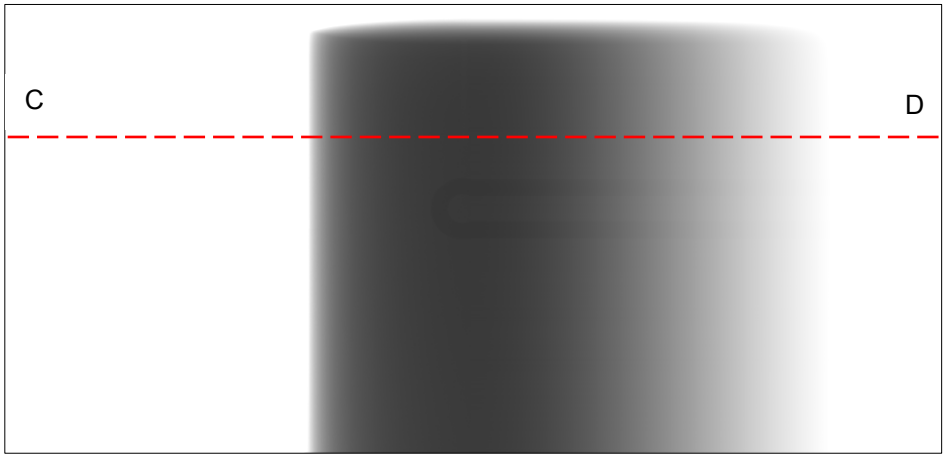

Figure 4.25: New offset projection image with the washer at 90 degrees to highlight the 'tailing' produced when the cosine function is applied. The line profile CD is drawn to illustrate the attenuation tail off to zero attenuation, as shown in Figure 4.26.

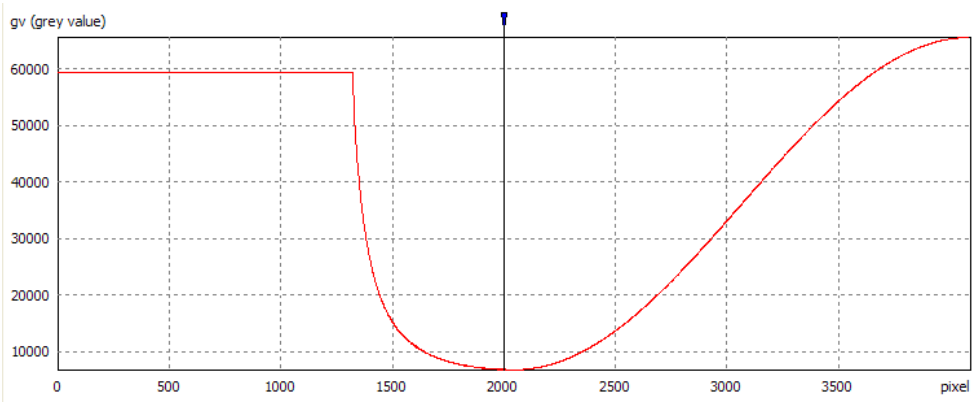

Figure 4.26: The intensity line profile CD illustrating the tailing data completion method. The marker in the centre of the line profile shows the start of the tail off to zero attenuation (set at 64000 grey level).


(a)

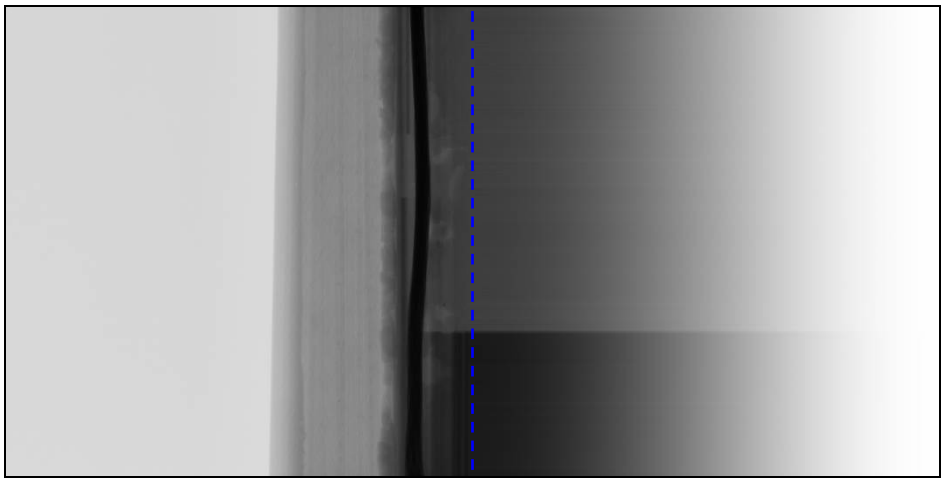
(b)

Figure 4.27: (a) Original offset projection image of the WTB. (b) New offset projection image of the WTB following extending and tailing.

4.5.1.2 Offset Data Completion Method 2 – Estimation

As mentioned previously, the main aim of these data completion methods is to provide a sufficient estimate of the missing data. This allows the filter used in the FDK algorithm to be performed without introducing artefacts in the measured data. Therefore, a second more complicated data completion algorithm was also investigated to accomplish this task. The method involved estimating the missing data from the known projection data using fan beam ray redundancy properties. However, unlike offset techniques for fan beam configurations (Fu and Lu 2005; BIR ACTIS 2008), the estimation algorithm developed for this work did not require the computationally intensive task of rebinning the projection data to parallel beam sampling geometry. Furthermore, the utilisation of the virtual trajectory concept (Clackdoyle *et al* 2004) meant the algorithm was applied to each elevation within the cone beam projection, as illustrated in Figure 4.28 to produce a complete data set. This meant the entire data set appears correct to the FDK filter, eliminating the possibility of induced artefacts prior to back projection.

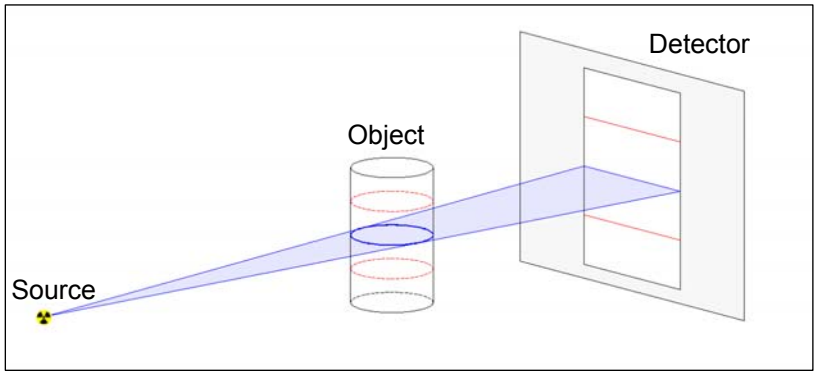

Figure 4.28: Cone beam CT setup showing fan beam sampling at the source trajectory (mid-plane) and the assumed virtual source trajectory (out of mid plane).

The method used for locating the exact ray path through an object given the coordinates of its intersection with the detector plane have been previously derived by Feldkamp *et al* (1984). It has been shown that to locate the correct ray path, the angle of the ray path and the perpendicular distance between the ray path and the centre of rotation must be known. The offset CT estimation method uses these conditions as well as the fan beam redundancy theorem (Parker *et al* 1982) to estimate the missing data by locating the equivalent redundant ray path in the measured data.

Figure 4.29 shows the offset CT setup at the projection angle, θ_1, where the desired ray path through the object intersects the detector plane at X_1 (within the missing data). The

object centre of rotation is slightly out of line with the centre of the source (distance *OD*) to make it more representative of an actual CT scan setup.

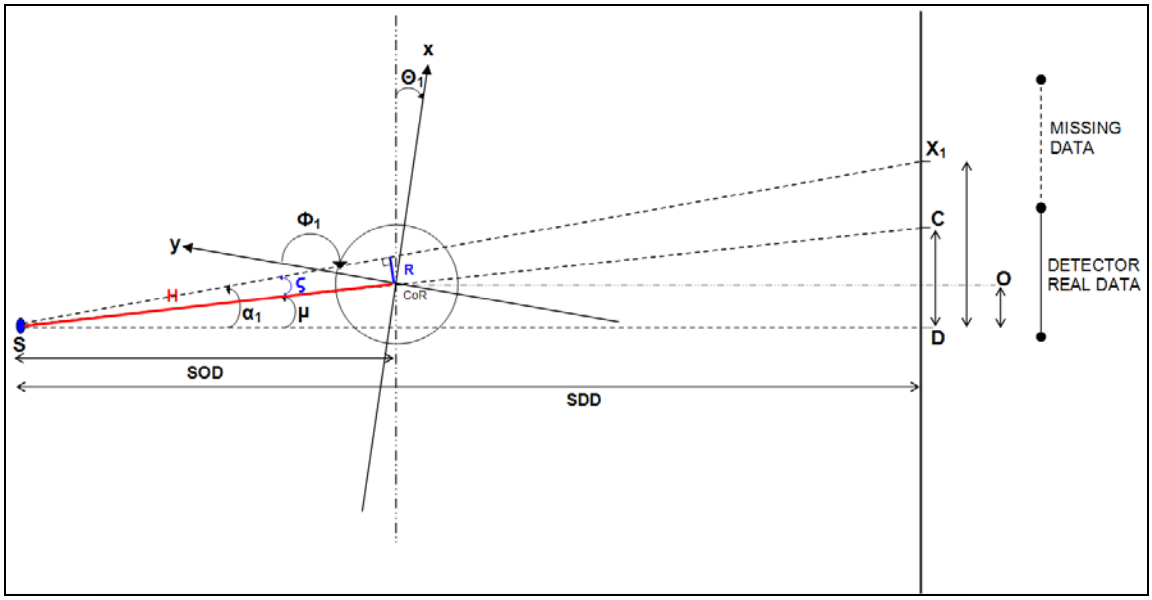

Figure 4.29: Offset CT setup at projection angle θ_1 showing the angles used when estimating a pixel located at X_1 within the missing data.

The first step was to calculate, Φ_1, the angle of the ray path in relation to the object axis. The angle, Φ_1, was used to find the projection angle, θ_2, which contains the redundant ray path.

This involved the following calculations (θ_1 is known):

$$\alpha_1 = tan^{-1}\left(\frac{X_1}{SDD}\right) \tag{4.1}$$

$$\Phi_1 = \pi - (\alpha_1 + \theta_1) \tag{4.2}$$

The next step was to calculate, R, the perpendicular distance between the ray path and the centre of rotation. This distance R coupled with the angle, ς, ensured that the correct ray path intersecting the detector at point X_1 was identified. The angle, ς, defines the angle between the desired ray path and the ray passing through the centre of rotation. The following intermediate calculations were performed to derive R and ς:

$$\mu = tan^{-1}\left(\frac{CD}{SDD}\right) \tag{4.3}$$

$$h = \left(\frac{SOD}{SDD}\right) \times \frac{1}{\sqrt{CD^2 + SDD^2}} \tag{4.4}$$

This allowed R and ς to be calculated using:

$$\varsigma = (\alpha_1 - \mu) \tag{4.5}$$

and

$$R = H\ sin(\varsigma) \tag{4.6}$$

Figure 4.30 shows the offset CT setup after the object has been rotated. The new projection angle, θ_2, contains the same ray path through the object as that projected on X_1 in Figure 4.29. At this projection angle the redundant ray path is known and is projected at X_2 within the measured data. This allows the redundant ray in the measured data to estimate the desired ray in the missing data. The red drawing within Figure 4.30 shows the relationship with the previous projection angle, proving the ray paths pass through the same line within the object.

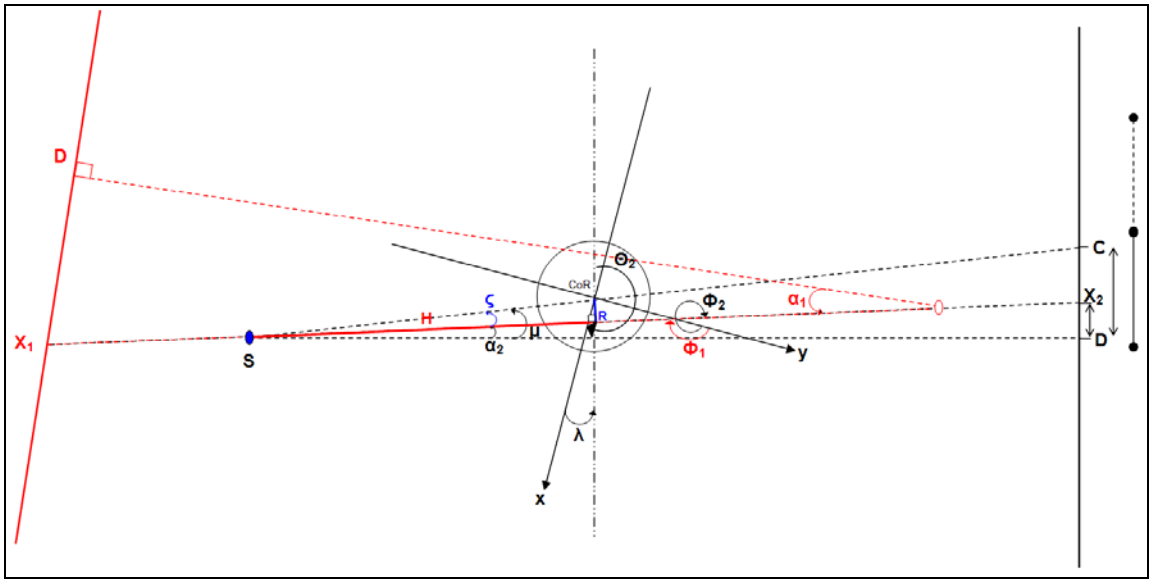

Figure 4.30: Offset CT setup at projection angle θ_2 showing the position of the redundant view and the relationship between the missing ray path in Figure 4.29 and the exact same ray path projected into the measured data at X_2.

Firstly, it was required to find the correct projection angle, θ_2, within the image stack. This was derived by taking advantage of fan beam redundancy properties. The angle of the redundant ray path in relation to the object axis, Φ_2, follows the relationship (as shown in Figure 4.30):

$$\Phi_2 = \pi + \Phi_1 \tag{4.7}$$

Therefore the projection angle, θ_2, can be derived using the following trigonometric calculations:

$$\lambda = \pi - (\alpha_2 + \Phi_1) \tag{4.8}$$

Substitute in Φ_1 from Equation 4.2 gives:

$$\lambda = \alpha_1 + \theta_1 - \alpha_2 \tag{4.9}$$

Using

$$\theta_2 = \pi + \lambda \tag{4.10}$$

The resulting equation to calculate the projection angle, θ_2, was given by:

$$\theta_2 = \pi + \theta_1 + (\alpha_1 - \alpha_2) \tag{4.11}$$

Once the projection angle, θ_2, was known, the point at which the redundant ray path intersects the detector plane (X_2) can be located using the conditions, R and ς. These conditions are based on the position of the desired ray path in the missing data (Figure 4.29). The following calculations were used to find the coordinate, X_2, in the measured data:

At projection angle θ1:

$$\varsigma = \alpha_1 - \mu \tag{4.12}$$

At projection angle θ_2:

$$\varsigma = \mu - \alpha_2 \tag{4.13}$$

Thus

$$\alpha_2 = 2\mu - \alpha_1 \tag{4.14}$$

and

$$X_2 = SDD\tan(\alpha_2) \tag{4.15}$$

The corresponding pixel grey level at the coordinate, X_2, within the measured data was then used as an estimate for the grey value at the point, X_1, within the missing data. This same method was used for each elevation within the cone beam geometry i.e. each 1D horizontal array of pixels was treated as if it was in a fan beam configuration. This concept was illustrated in Figure 4.28.

The reconstruction software required a modified reconstruction "XTekCT" parameter file that had the correct input settings to account for the detector offset. This was essential for alignment purposes. The first step was to calculate the detector offset of the original non-extended offset projections. For example the non-extended offset projections are 2048x2048 pixel images and the detector was offset by half its width (i.e. 1024x0.2mm), giving an offset of 204.8mm, as shown in Figure 4.31(a). The projections also had uncorrected pixel values at the edge of the images due to a prototype detector being used for the experiment. These were removed by cropping 24 pixels from each edge.

The second step was to create the XTekCT parameter file that can reconstruct the new extended projections containing the estimated data. The new estimated projections were 3,994 pixels wide and 2,000 pixels in height (due to the 48 pixels being cropped). This meant the detector offset parameter had to be updated to take into account the new extended data. This required calculating the offset of the new extended data by treating it separately and then finding the difference between the offset of the original non-extended data (-204.8mm) and the new extended data, as shown in Figure 4.31(b).

Detector offset of extended data = (3994-2000)/2 = 997 x 0.2mm = 199.4mm
Therefore "DetectofOffsetX" of new estimated projections = 199.4-204.8 = -5.4mm

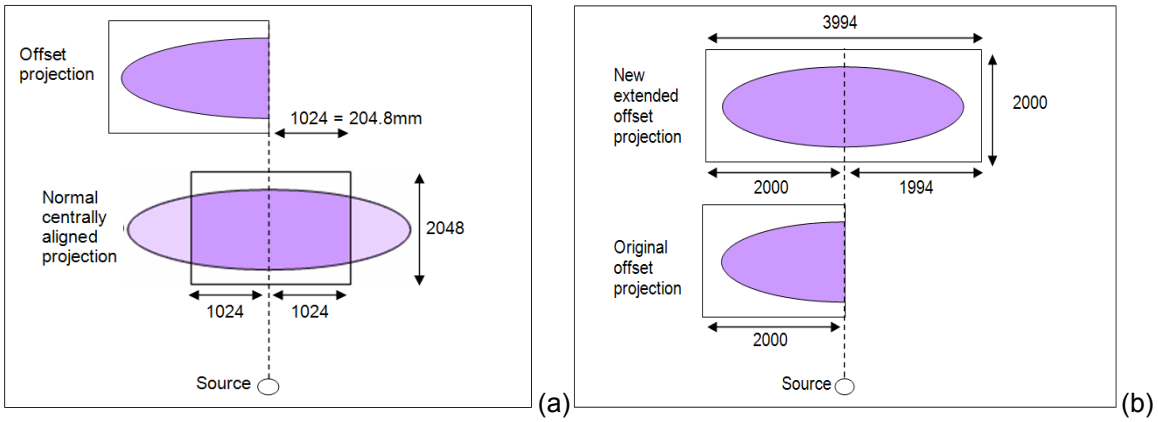

Figure 4.31: Diagram illustrating the calculation of the detector offset parameter for (a) the non-extended offset projections and (b) for the extended offset projections.

Figure 4.32 to Figure 4.35 are example projections following the application of the estimation method. Figure 4.32 and Figure 4.33 are extended projections of the offset aluminium cylinder (with washer attached) and Figure 4.34 and Figure 4.35 are extended projections of the offset WTB. It is clear in Figure 4.35 that the full width of the blade is

over 1.5 times larger than the original size of the detectors FOV; at the minimum geometric magnification allowed by the manipulator table.

This data completion method is accurate for finding the missing data within the mid-plane of the projection and similar ray redundancy based methods are used for fan beam CT. But the accuracy of this estimation will be reduced at locations further from the mid-plane (i.e. increasing the cone angle). This is highlighted in Figure 4.32 where the top of the cylinder appears disjointed at the centre line. Figure 4.33 also shows the shape of the washer is accurate at the bottom (near the mid-plane) but becomes increasingly inaccurate as you move further from the mid-plane.

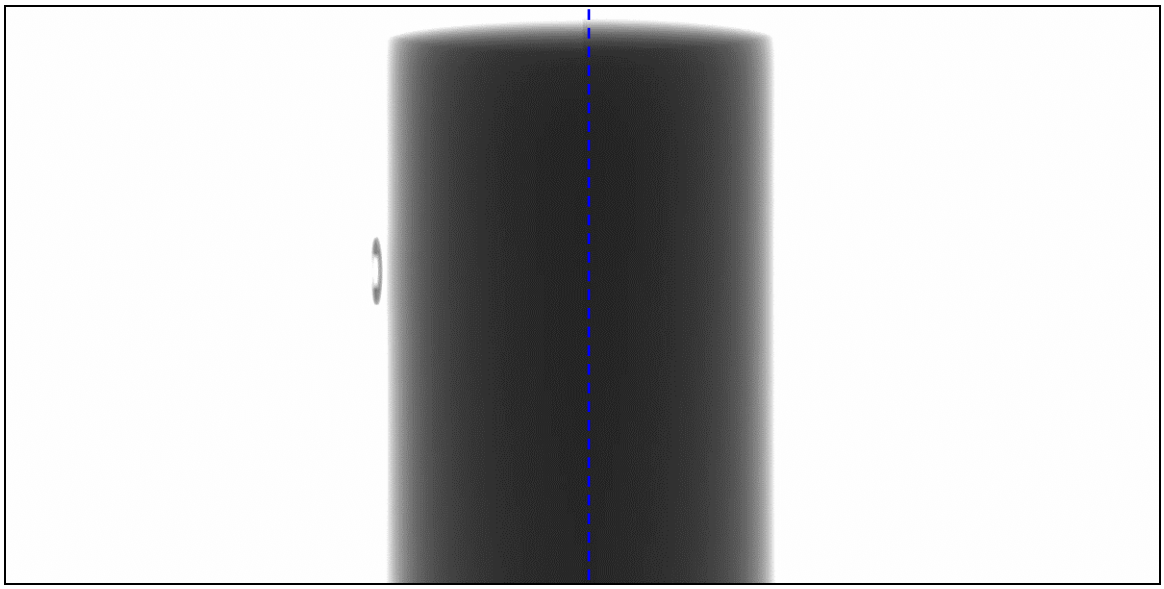

Figure 4.32: Offset projection image of the Aluminium cylinder (at 0 degrees) extended using the estimation technique. The dashed vertical line indicates the threshold between the measured and estimated data.

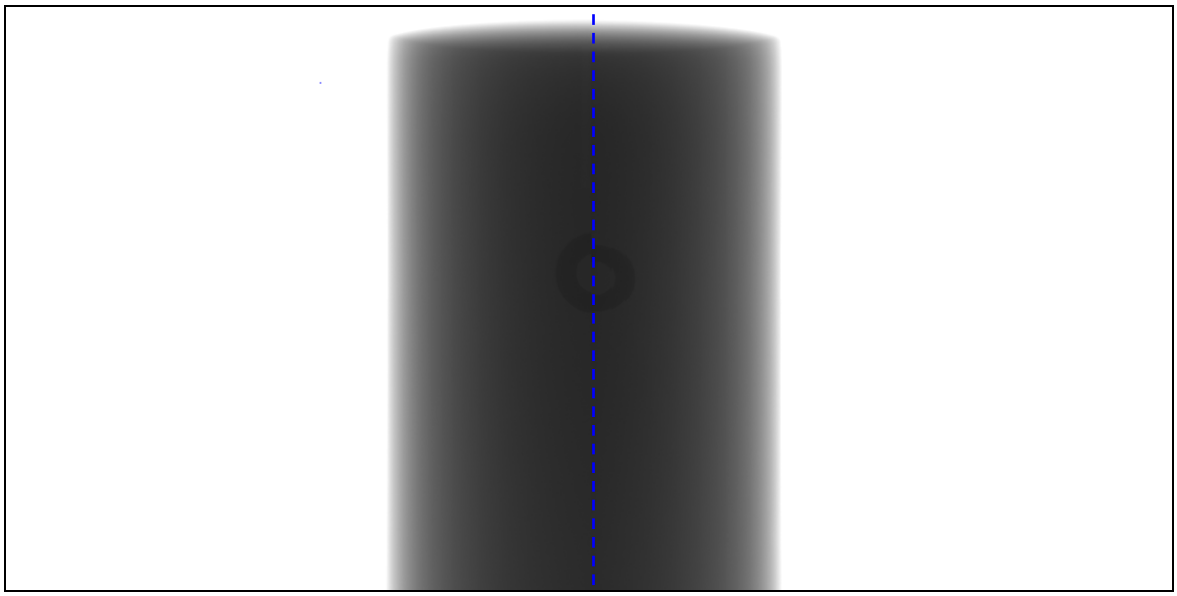

Figure 4.33: Offset projection image of the Aluminium cylinder (at 90 degrees) extended using the estimation technique. The dashed vertical line indicates the threshold between the measured and estimated data.

As mentioned previously, the image stacks used for this experiment contained only 500 projections, whereas projections of this size with an increased reconstructed region require the number of projections to be nearer 3,000 (see section 4.4.3). Estimating the missing data with a lack of projections means that the program chose the nearest available projection to find the required ray-path. This reduced the accuracy of the estimation. Linear interpolation would improve the estimation results when using an image stack with a lack of projections. However, this was not implemented within the program.

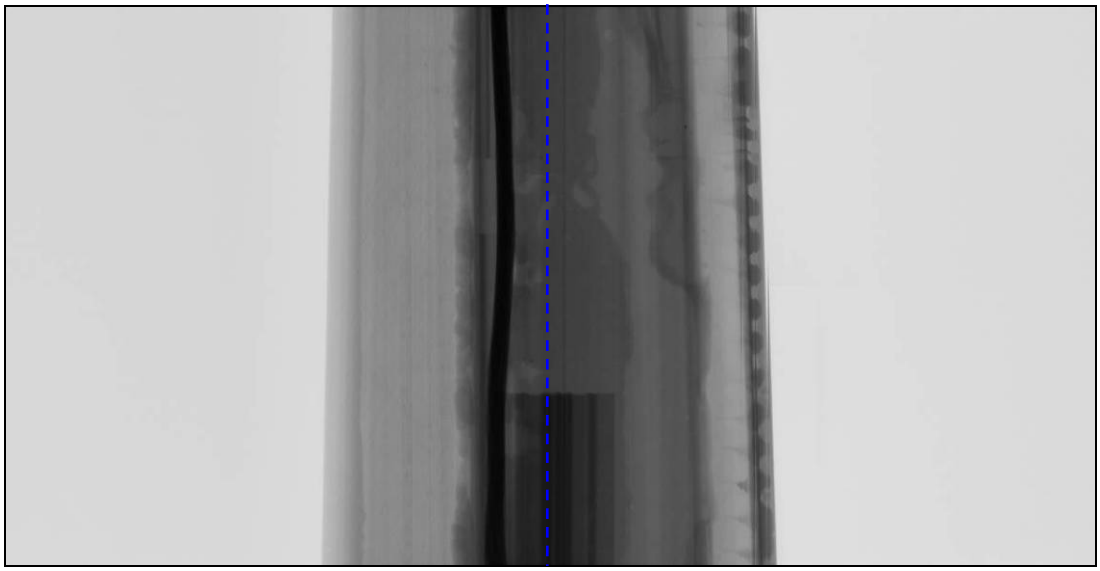

Figure 4.34: Offset projection image of the Wind Turbine Blade (at 0 degrees) extended using the estimation technique. Dashed line indicates the threshold between measured and estimated data.

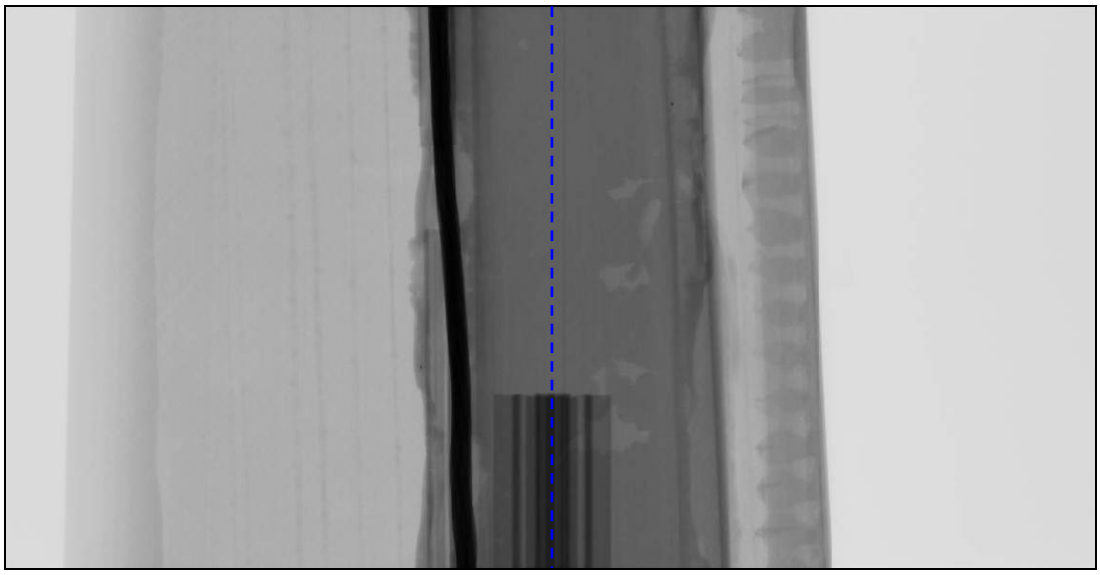

Figure 4.35: Offset projection image of the Wind Turbine Blade (at 90 degrees) extended using the estimation technique. Dashed line indicates the threshold between measured and estimated data.

The image stack for the WTB, as with the aluminium cylinder, contained less than the required number of projections. Without linear interpolation this results in reduced accuracy within the estimated data. However, the estimated data for the WTB appears more accurate than that produced for the aluminium cylinder. This can be seen in Figure 4.34 and Figure 4.35 as no obvious disjointed regions can be found near the mid-plane or at large cone angles.

4.5.2 Alteration of the Reconstruction Algorithm – Blanking

As stated previously the first step of completing the projection data is purely to ensure artefacts are not induced into the measured data as a result of filtration. The second step called blanking is implemented into the FDK algorithm to ensure that only measured data is back projected and that the simulated data is ignored i.e. not reconstructed.

The blanking measure meant that the right hand side of the projection data from the centre of rotation (simulated data) was disregarded. This was done by simply setting all pixels to the right of the centre of rotation to zero at a specific point within the FDK algorithm. This point was after the filtration and before the back projection. To implement this measure required a new line of programming to be input in the CTPro reconstruction software. Metris X-Tek was instructed to carry out this task as they alone have access and the rights to modify this software.

To enable blanking to take place within the reconstruction, the reconstruction parameter file had to be amended. To set all pixels to the left of the centre of rotation to zero “Blanking=1” was input and to set all pixels to the right of the centre of rotation to zero “Blanking=2” was input.

4.5.3 Reconstruction of the Completed Projection Data

Three sets of offset projection data were reconstructed:

(1) Aluminium cylinder with the reference washer;
(2) Aluminium cylinder without the reference washer;
(3) Wind Turbine Blade.

Following the completion of the projection data and the modification of the reconstruction algorithm, the reconstruction XTekCT parameter files had to be amended (explained in section 4.5.1.2). This allowed reconstruction to take place using the normal ‘CT Pro’ software and procedures.

Included in the amended XTekCT parameter file was the new centre of rotation correction values. To find these values a new reference method was developed to optimise the centre of rotation for offset projection data. The incorrect setting of the centre of rotation is usually visualised as a double edge blur within a CT image (see section 2.2.4.5). This double edge is used as a reference for the correction process which positions the data to achieve a single sharp edge. Essentially, the double edge exists as the data consists of

two sets of 180 degree scans, and each scan set needs to be overlaid to obtain an accurate image. However, this double edge cannot be formed because only half of the data exists within the projection, essentially giving only one 180 degree scan. Therefore, a new method was realised by identifying the centre of rotation artefacts. For this new method, the artefacts are either visualised as holes or areas of increased density at the centre of the image (Figure 4.36). Figure 4.36 also illustrates how these 'hole' type artefacts caused normalisation problems with the assigned grey values within the image. The explanation for these new artefacts is due to the fact that if the centre of rotation setting is chosen inside the simulated data, then a hole will be reconstructed in the centre of the CT image. Whereas, if it is set within the measured part of the projection data then a dense cylindrical area will be reconstructed. The correct centre of rotation setting was deduced to be the point at which the hole with no data changed to the hole with increased density. Once the correct centre of rotation was achieved these obvious holes disappeared and the entire image assumed the correct grey level spread.

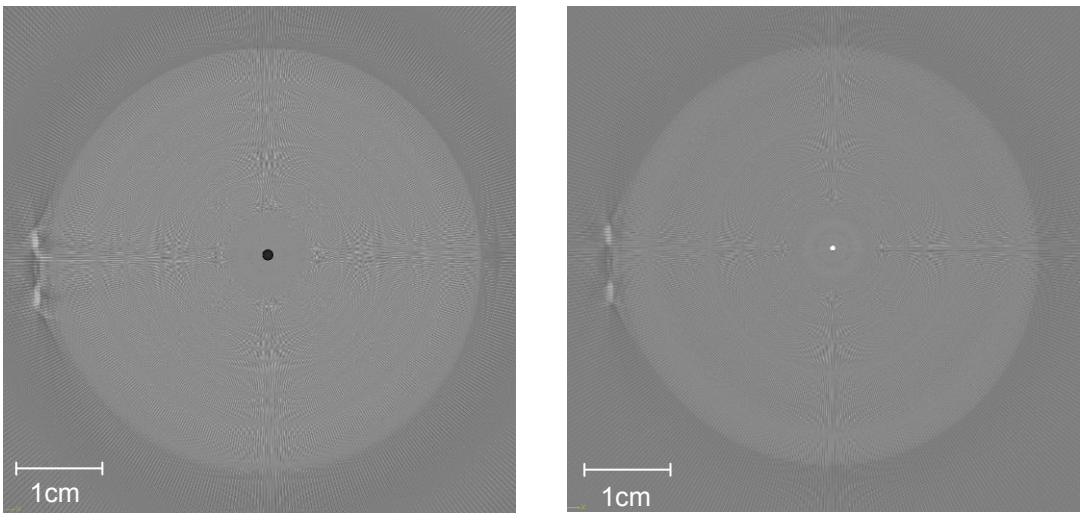

Figure 4.36: The new centre of rotation artefacts were visualised as either holes (left) or areas of increased density at the centre of the image (right).

4.5.4 Results and Discussion

4.5.4.1 Offset CT cylinder (with washer)

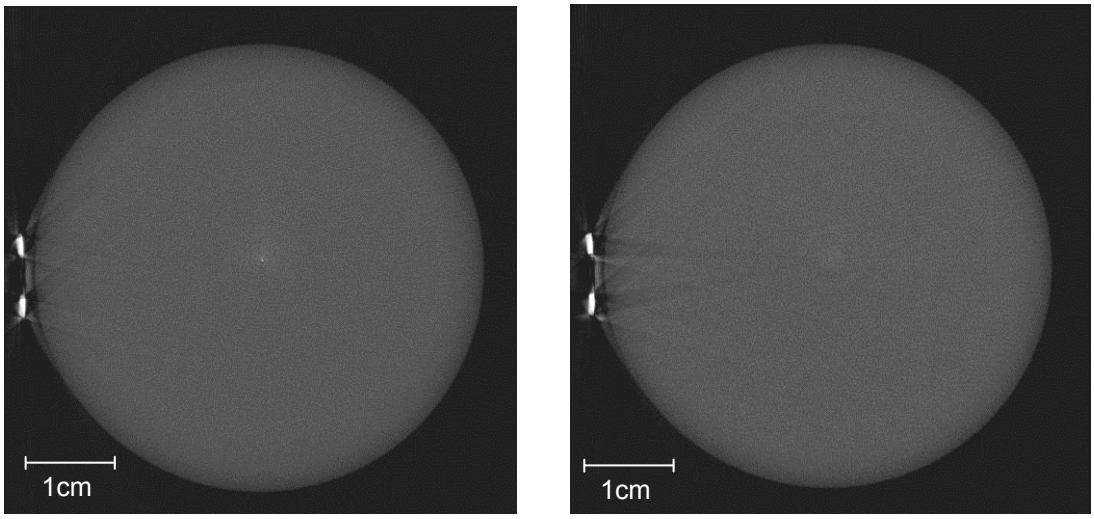

Figure 4.37: CT slices in the axial direction through the aluminium cylinder. Reconstructed image using estimating method (left), reconstructed image using tailing method (right)

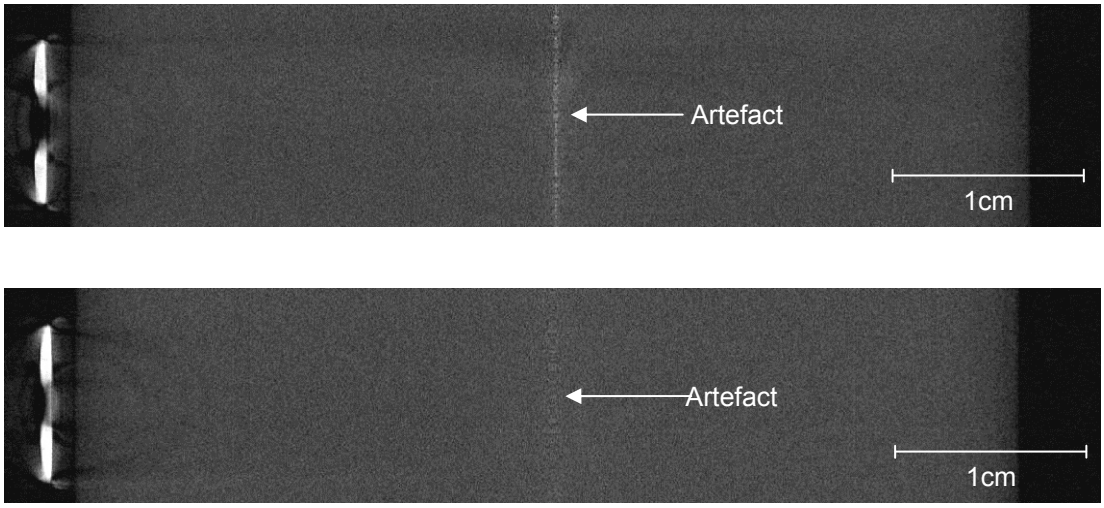

Figure 4.38: CT slices in the frontal direction through aluminium cylinder. Reconstructed CT image using estimating method (top), reconstructed image using tailing method (bottom).

It was identified that the artefacts propagating from the steel washer (Figure 4.37) are predominantly due to lack of penetration and lack of projections used in the reconstructions. This explains why both the estimating method and the tailing method produced very similar artefacts around the washer and on the surface of the aluminium cylinder. The only real difference between the two methods highlighted in these CT

images is the increased centre of rotation artefact found using the estimating method (Figure 4.38). This artefact is more prominent despite the fact that the same centre of rotation was used for both methods (described in section 4.5.3).

A possible explanation for the estimating method producing worse centre of rotation artefacts was due to the small discontinuity or step in grey levels found at the centre line (Figure 4.32 and Figure 4.33). This would potentially cause the filter used in the FDK algorithm to produce artefacts within the measured data.

4.5.4.2 Offset CT Wind Turbine Blade

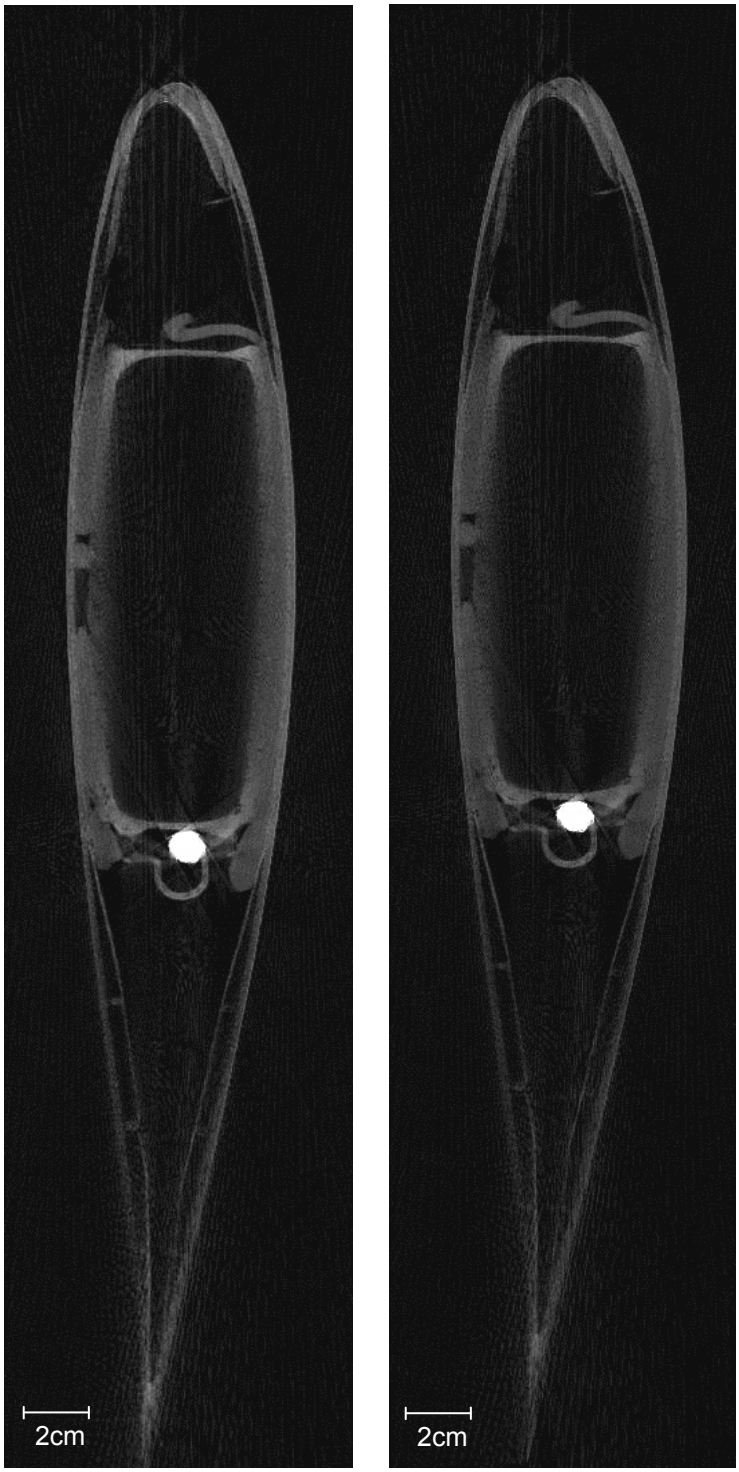

Figure 4.39: CT slices in the axial direction through central region of WTB. Reconstructed image using estimating method (left), reconstructed image using tailing method (right)

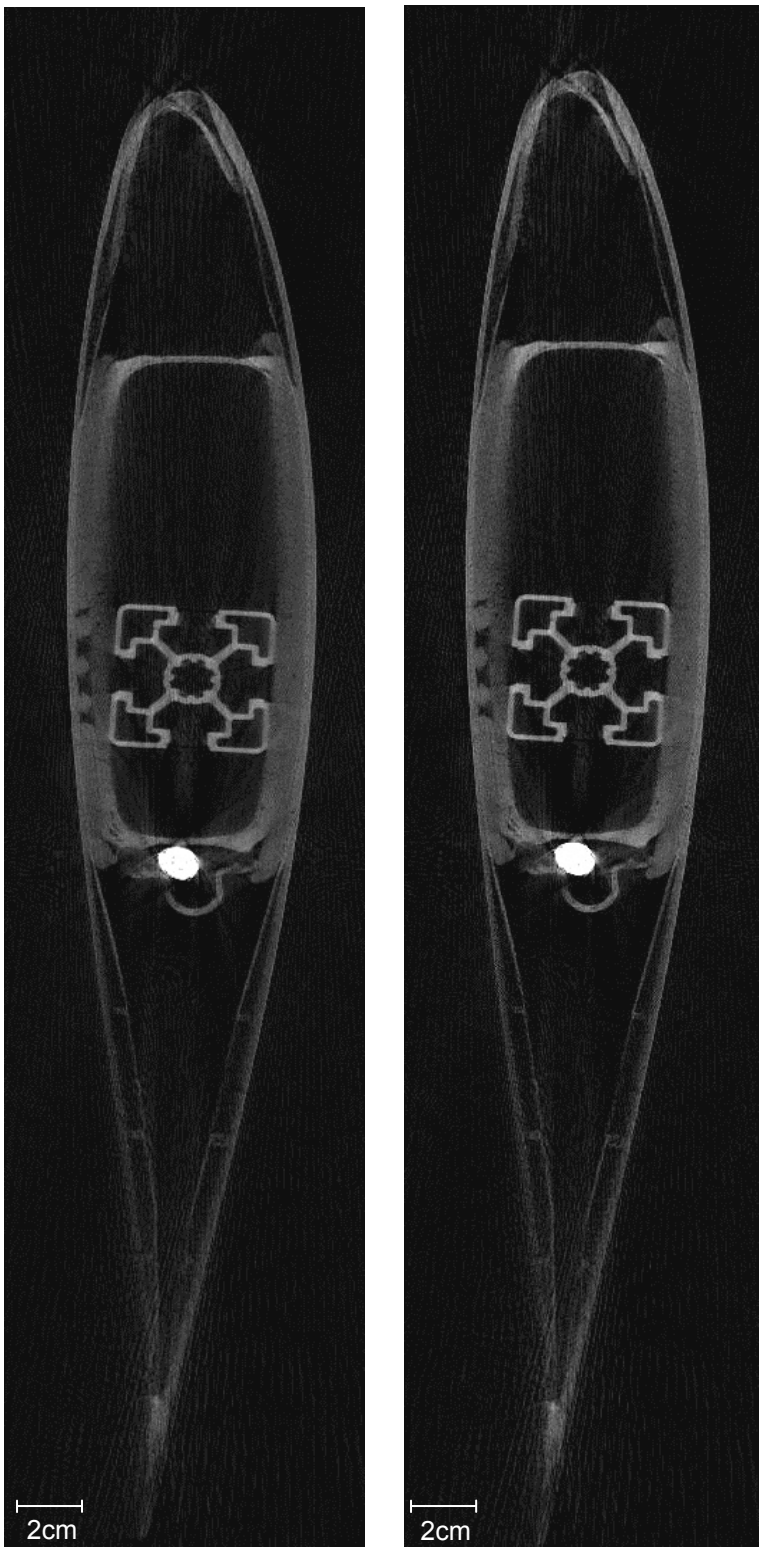

Figure 4.40: CT slices in the axial direction of WTB at large cone angle. Reconstructed image using estimating method (left), reconstructed image using tailing method (right)

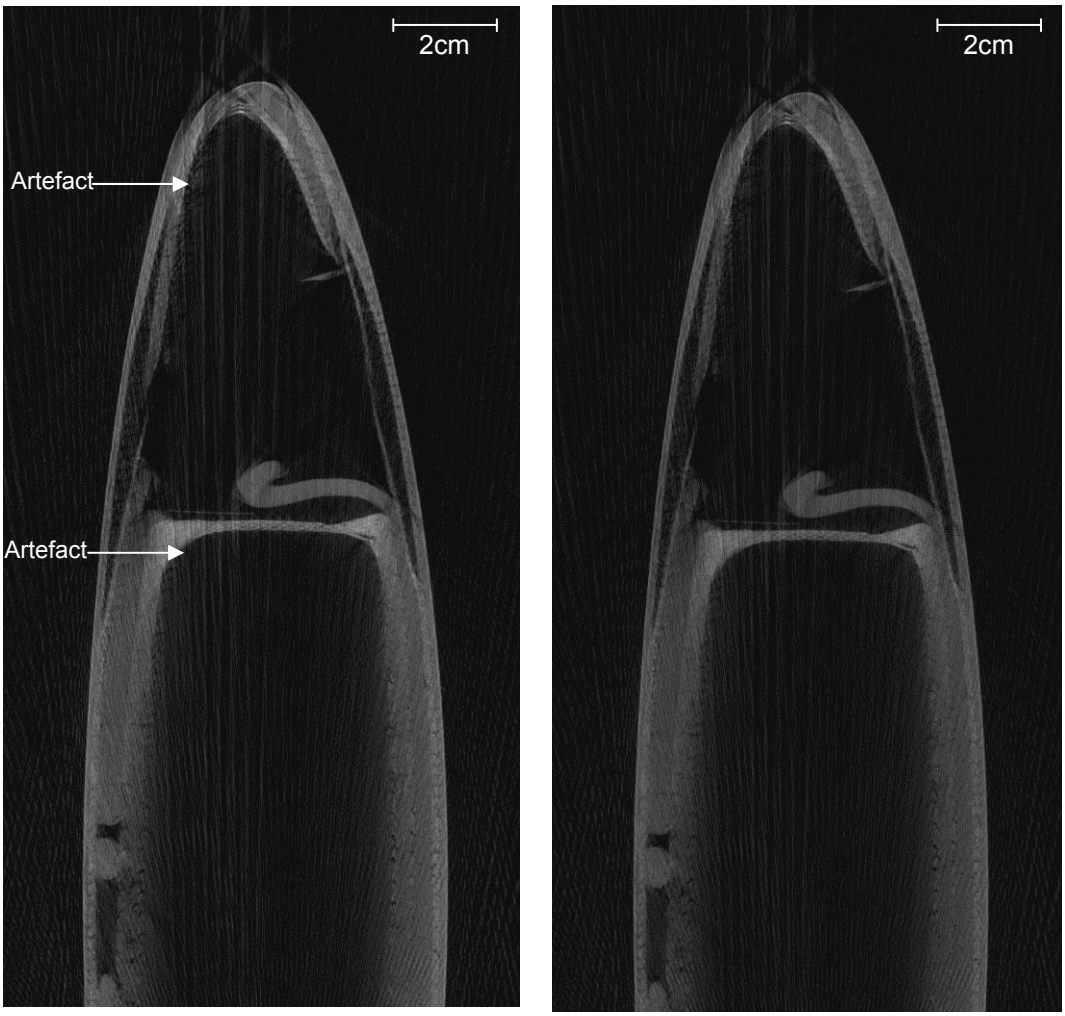

Figure 4.41: Magnified CT slices in the axial direction through central region of WTB. Reconstructed image using estimating method (left), reconstructed image using tailing method (right).

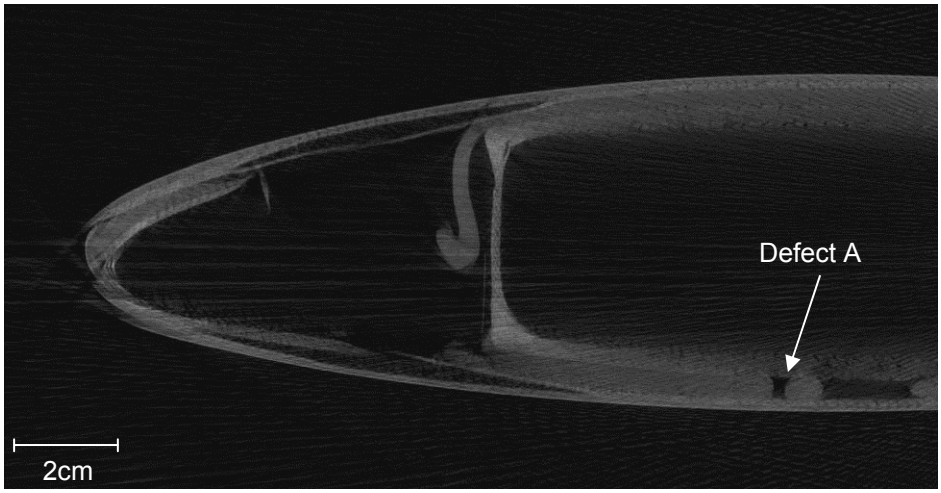

Figure 4.42: CT slice in the axial direction, highlighting defect A within the sandwich structure.

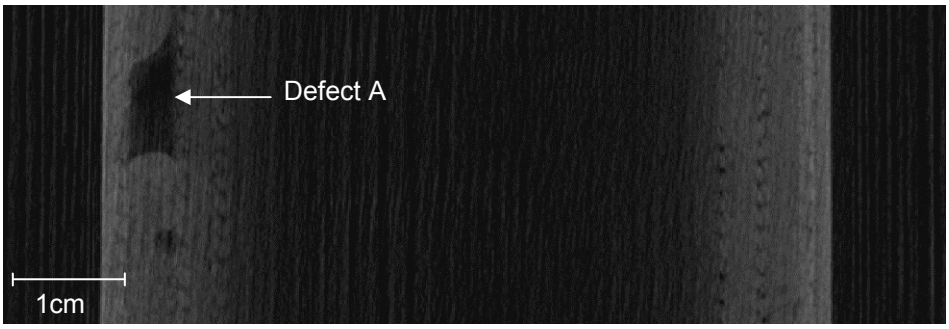

Figure 4.43: CT slice in the frontal direction, highlighting defect A within the sandwich structure.

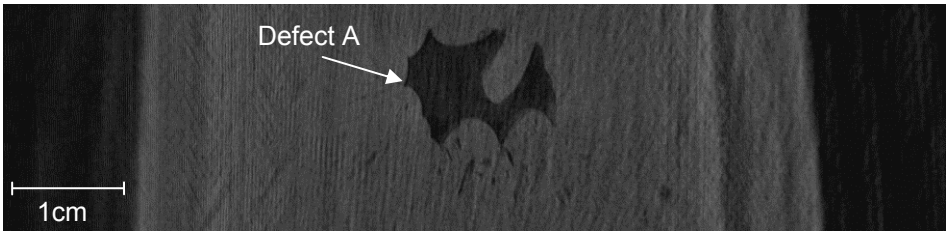

Figure 4.44: CT slice in the sagittal direction, highlighting defect A within the sandwich structure.

Figure 4.39 and Figure 4.40 compare both estimation and tailing methods at the mid-plane of the cone and at a slice taken at a large cone angle, respectively. No significant difference can be seen between the mid-plane slices and the large cone angle slices. The artefacts present appear to be due to lack of projections causing both streaks and loss of edge sharpness, as highlighted at the tips of the blade. However, it could be argued that the reconstruction for the estimation method in Figure 4.41 appears to have more prominent streaking compared to the tailing method (highlighted with arrows).

Figure 4.39 to Figure 4.44 highlight the inspection capability of the experimental offset CT technique and the extensive information that can be extracted. The sandwich structure of the WTB was easily identified and a range of defects were detected. In Figure 4.39 and Figure 4.40 these defects and structural irregularities include: excess glue above the main spar; displaced lightening rod cover; irregular internal structure in the region of the leading edge and missing glue between the GFRP skin layers in the main spar. It should be noted that the strange shaped object inside the main spar in Figure 4.40 was an aluminium pillar used to mount and stabilise the blade on the manipulator table.

The CT images in Figure 4.42 to Figure 4.44 show a specific defect (defect *A*) within the blade. Using all three cross-sectional viewing planes (axial, frontal, sagittal) the information gained about this defect was emphasised. This capability allowed the user to

fully characterise the volumetric shape of the defect and conclude that the defect in this case was a lack of glue in the sandwich structure on the main spar. In addition, the results in Figure 4.43 and Figure 4.44 are able to visualise the fibre detail within the GFRP so potentially important failure modes such as non-intended fibre orientation or kink band can be detected.

4.5.5 Summary

Two different data completion methods have been developed for Offset CT scanning with cone beam geometry. Both of these methods exploited aspects of techniques found in literature for fan beam geometry (see section 4.5.1 and section 2.2.4.5). However, at the time of writing this thesis no similar offset CT techniques for cone beam geometry had been developed. The two data completion methods were qualitatively compared using the results of the projection data completion and the reconstructed CT images. The accuracy of the methods could not be quantified as no original or true reconstruction existed to base the comparison. This was due to the fact that the WTB used in this investigation was physically larger than the digital detector, so a conventional reconstruction was not possible. The qualitative comparison showed that the estimation and tailing methods both produced very similar results in terms of accuracy of the reconstruction and the artefacts present. The only real difference was highlighted in Figure 4.38 of the aluminium cylinder, showing an increased centre of rotation artefact for the estimated method. This artefact was not noticeable within the WTB reconstruction. But this could simply be due to the fact that the centre of rotation artefacts are easily identifiable within the homogenous aluminium but are difficult to locate within the WTB.

It was very difficult to fully compare the performance between the two methods due to the lack of projections within the offset image stack. This lack of projections caused strong artefacts within the reconstruction that could have easily masked artefacts specific to either the tailing or estimating method. This was unavoidable as the limited number of projections was due to the instability of the prototype system. Therefore the next step was the simulation of Offset CT using accurate projection stacks acquired with a commercial fully integrated system. This allowed method specific artefacts to be identified and a more quantitative investigation to take place.

4.6 Simulation of Offset CT

The offset CT techniques described thus far have been applied to experimental projection data acquired using a prototype X-ray system. This system was not fully integrated and

the prototype source was unstable, meaning that the projection data had to be acquired manually. As a consequence a limited number of projections were acquired and, as mentioned previously, this caused artefacts within the offset reconstructions for both the estimation and tailing technique. In addition, the performance of the offset reconstructions could not be quantified as there was no basis for comparison. This required a conventional reconstruction using full non-truncated projection data, which could not be obtained for the WTB. Therefore it was required to measure the performance and validate the two offset methods using a well controlled simulation of offset CT. This meant cropping normal accurate projection images to form half projections, similar to that obtained using the offset CT technique.

4.6.1 Method

Three different CT scans were chosen for comparison. The 'XTekCT' parameter files were altered to crop the projection data at exactly half the full width. However if the centre of rotation was positive i.e. to the right of the image centre, this had to be taken into account. This meant the cropped region of interest had to include the centre of rotation, resulting in projections larger than half the width. These modified parameter files were then used to extend and complete the half projections by both the estimation method and tailing method.

The extended projection data for both estimation and tailing resulted in new image sizes. This again was accounted for when fabricating a new parameter file to reconstruct the new extended projection data. This meant the centre of rotation had to be amended based on the new centre pixel. For example, the original projection width = 900 pixels, the new resultant projection width = 910 pixels, therefore the centre of rotation for the new projection data is an extra 10/2 = 5 pixels to the left of the new centre pixel. This requires the original centre of rotation values to be subtracted by 5 pixels, i.e. the new input value = original centre of rotation – (5 x 0.165mm).The final stage prior to reconstruction was to tell the FDK algorithm to ignore the simulated data by inputting the line "blanking=2" into the parameter file, making it set all pixels to the right of the centre of rotation to zero.

The error mapping method used in Chapter 3 (details in section 3.5.3) to quantify the reconstruction performance could not be utilised for this offset simulation due to the scaling of output images performed by the reconstruction software. This was unavoidable and was related to the different centre of rotation values being used in the parameter setup file. The result was pixels in the original reconstruction could not be mapped

correctly to those in the offset reconstruction, thus rendering any potential error maps meaningless. A reasonable assessment of the performance and the accuracy of the two offset techniques was established using extensive lab testing and intensity line profiles. These enabled any shading artefacts or irregularities to be identified.

4.6.2 Results and Discussion

4.6.2.1 Projection Completion Results

The images below compare the projection completion results using the estimated and tailing methods with the original projection data. The accuracy of the estimation method was quantified by comparing intensity line profiles extracted across the original projection and the estimated projection. The line profiles were positioned in the mid-plane and off the mid-plane at a large cone angle, as illustrated in Figure 4.47. The projection image results for the tailing method was only included for analysis purposes, to ensure the data was extended as expected. The important comparison for this part of the investigation is the accuracy of the estimated data compared to the original full projections.

For the purposes of this investigation the offset projections were all generated so that the left side is the measured original data and the right side is the extended simulated data.

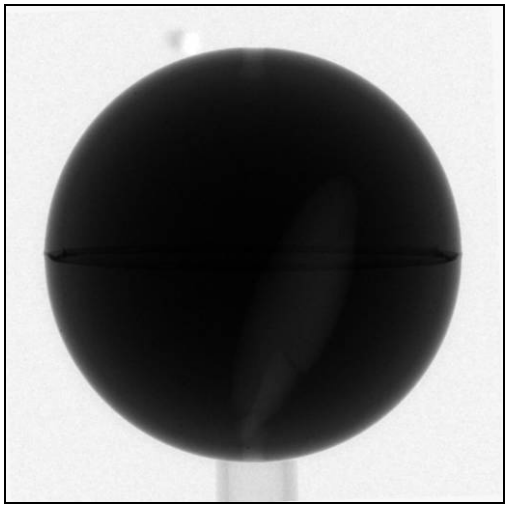

Figure 4.45: Original conventional projection of Object 1

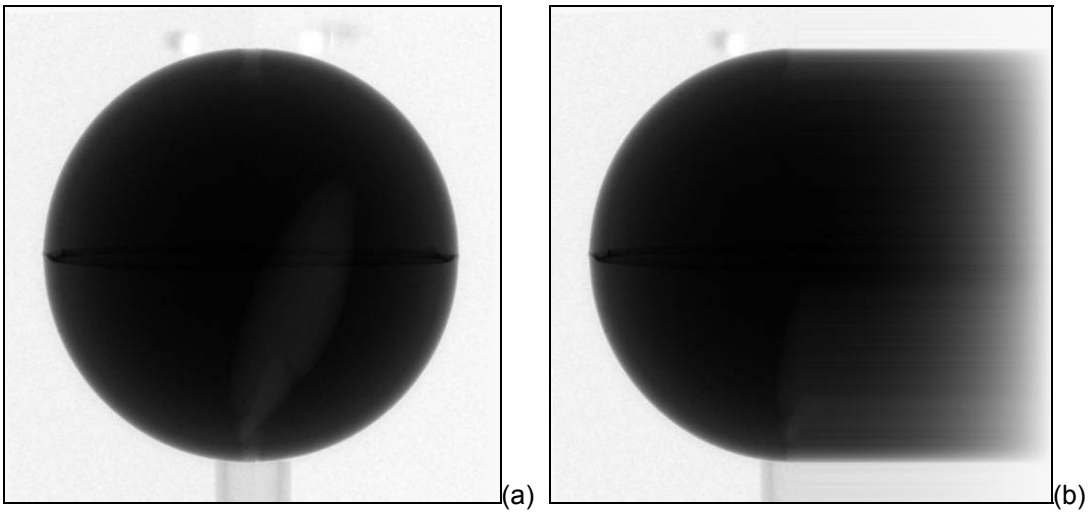

Figure 4.46: (a) Offset projection of Object 1 using the estimation method and (b) Offset projection using the tailing method.

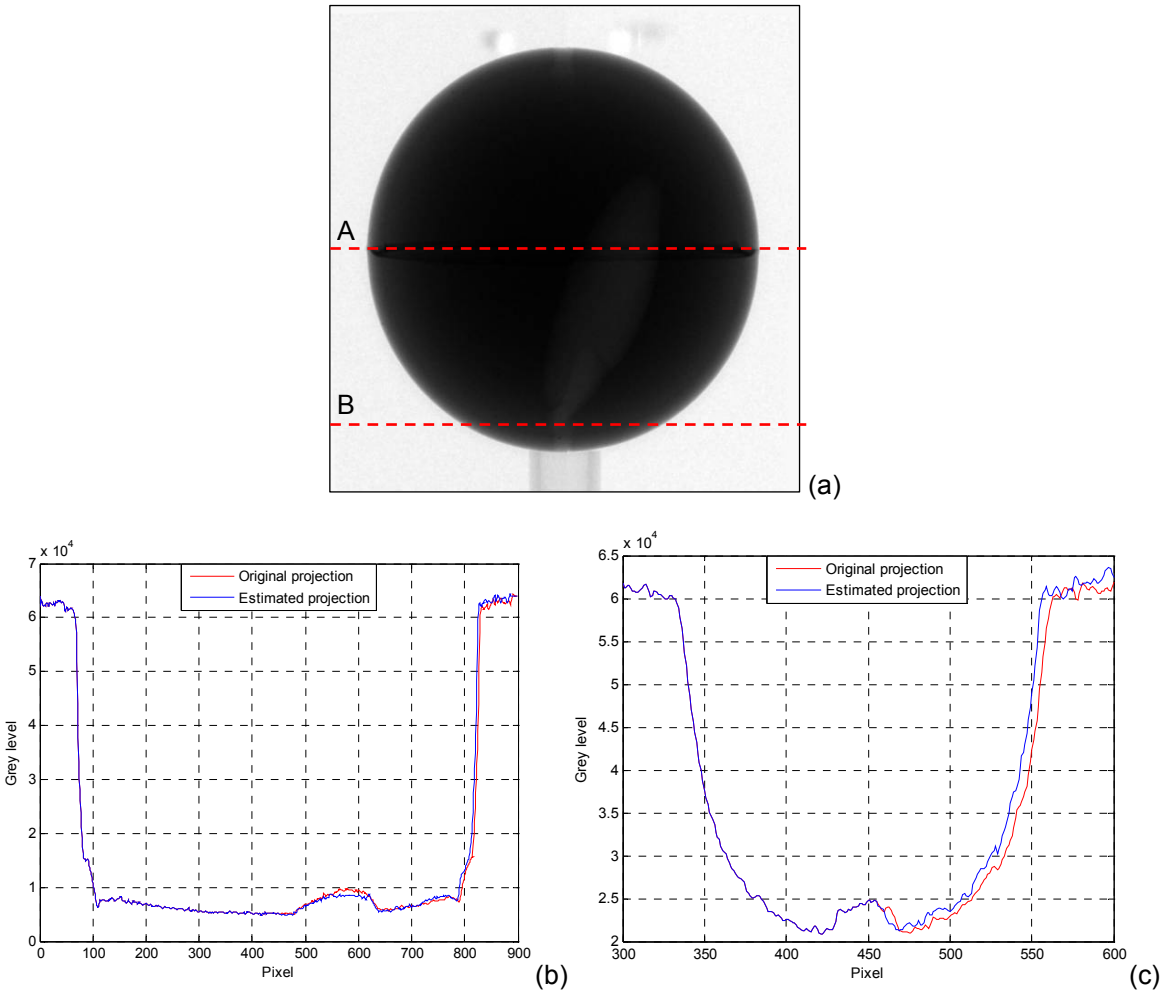

Figure 4.47: (a) Projection image of Object 1 showing location of the intensity line profiles. The line profile results compare the original projection and the estimated projection at different slice positions; (b) line profile *A* placed in the mid-plane and (c) line profile *B* placed at a large cone angle.

Comparing Figure 4.45 and Figure 4.46(a) it can be said that the estimation method for Object 1 produced a very accurate estimation of the missing half of the projection data. This accuracy is emphasised in Figure 4.47 by comparing line profiles extracted across the original projection and the estimated projection. Here, a line profile was placed in the mid-plane (line profile A - Figure 4.47(b)) and out of the mid-plane at a large cone angle (line profile B - Figure 4.47(c)). The object is not disjointed in any way at the threshold between measured and simulated data and the shape remains as represented in the original projection. It was observed that the estimated data is less accurate at a large cone angle, but this was expected as redundant rays are only present in the mid-plane (see section 4.5). Figure 4.46(b) also shows that the tailing has worked as expected for the simulated projections. A low spatial frequency tail off to zero attenuation has been produced from the attenuation found at the cropped edge of the half projection.

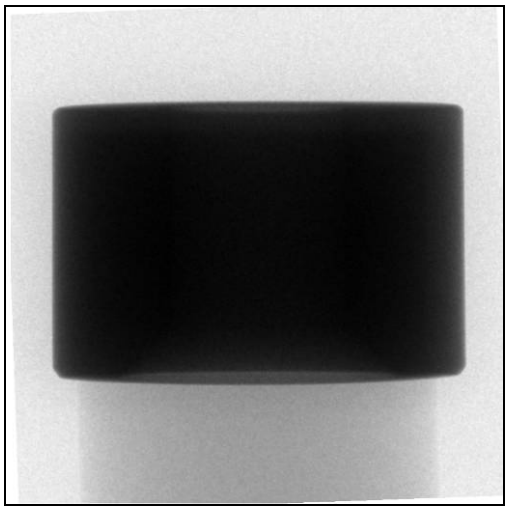

Figure 4.48: Original conventional projection of Object 2.

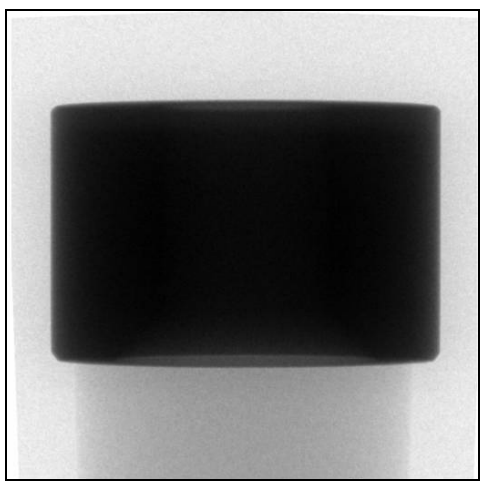
(a)
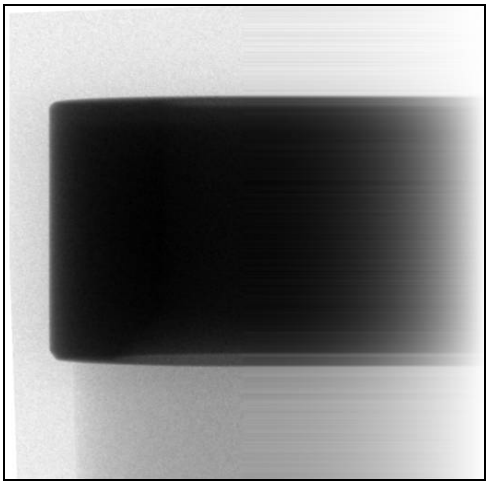
(b)

Figure 4.49: (a) Offset projection of Object 2 using the estimation method and (b) Offset projection using the tailing method.

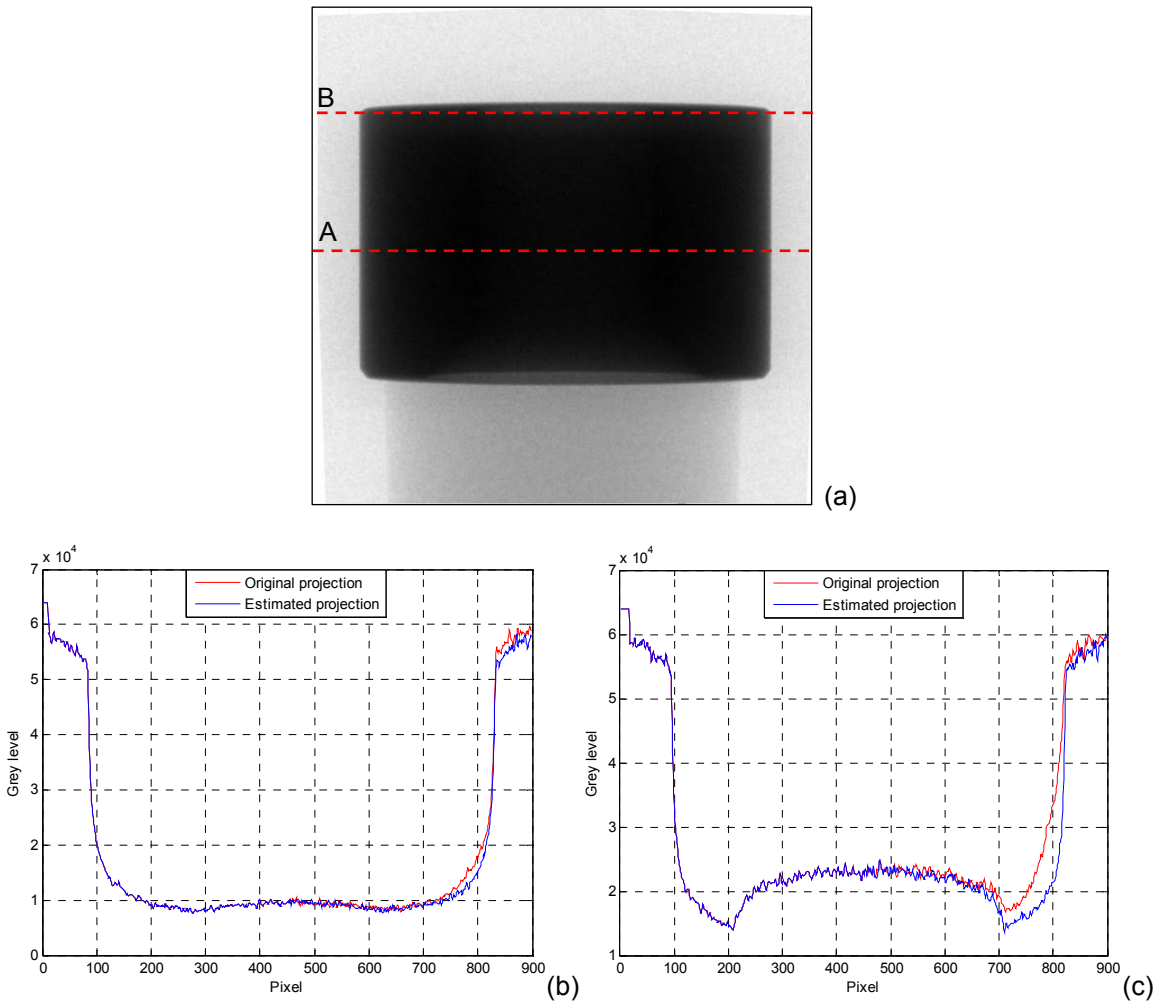

Figure 4.50: (a) Projection image of Object 2 showing location of the intensity line profiles. The line profile results compare the original projection and the estimated projection at different slice positions; (b) line profile *A* placed in the mid-plane and (c) line profile *B* placed at a large cone angle.

Again, comparing the original projection for Object 2 in Figure 4.48 with the estimated projection in Figure 4.49, no obvious differences in the right hand side of the images was observed. In Figure 4.50, the quantitative comparison showed that line profile *A* (Figure 4.50b)) was very accurate but the estimated data in line profile *B* (Figure 4.50c)) differed slightly from the original data. It appears that the estimated technique has essentially mirrored the measured data. For a symmetrical object such as this, the original projection data should also be symmetrical. The fact that this is not the case means the object alignment is off centre. The system uses an automatic pre-processing function to correct this mis-alignment which is illustrated by the white regions at the edge of the projections. If this alignment change is not linear or uniform across the image then it will affect the accuracy of the estimation. Nevertheless, this has only caused a small error and the object structure has been estimated with a high degree of accuracy, even at large cone

angles. The tailing method also produced extended data with no areas of concern (Figure 4.49(b)).

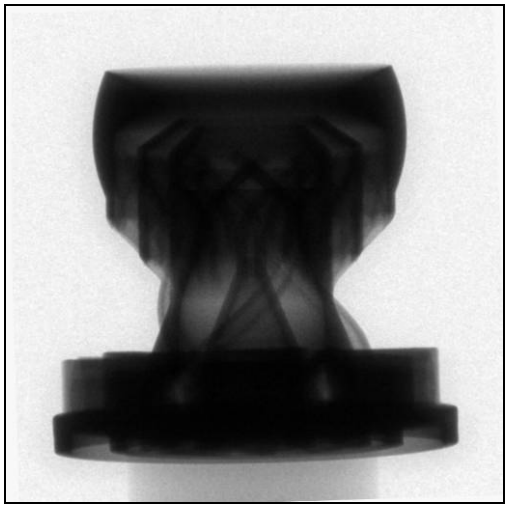

Figure 4.51: Original conventional projection of Object 3.

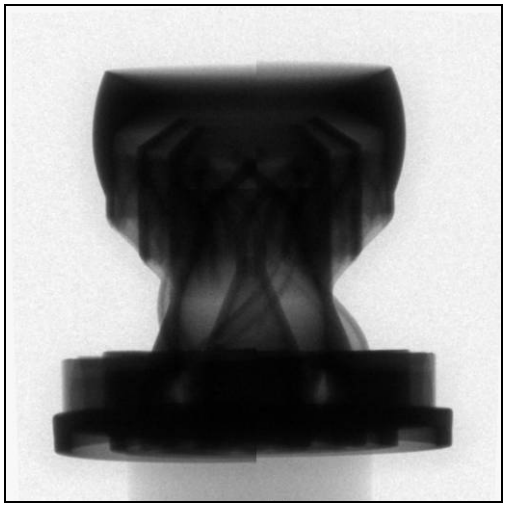

(a)

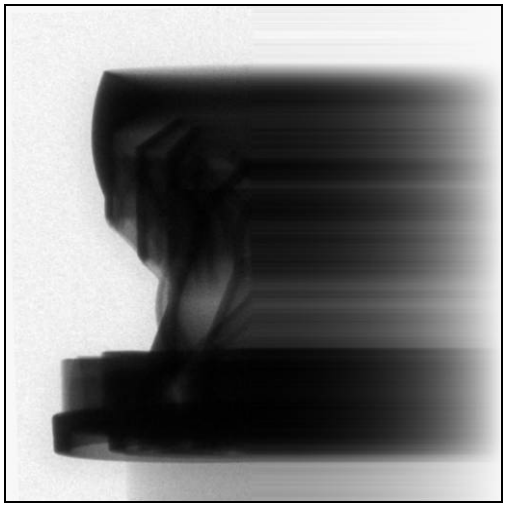

(b)

Figure 4.52: (a) Offset projection of Object 3 using the estimation method and (b) Offset projection using the tailing method.

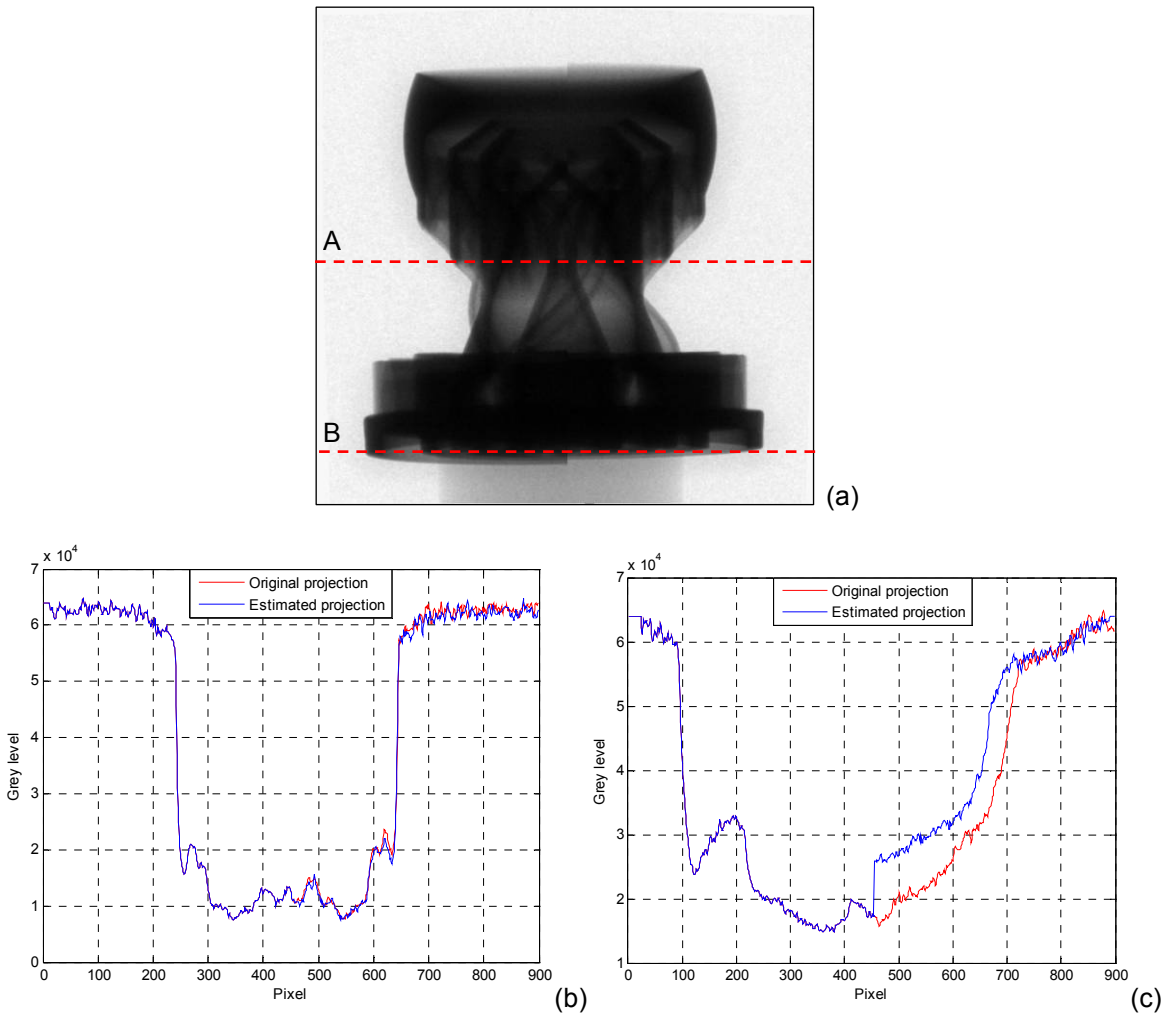

Figure 4.53: (a) Projection image of Object 3 showing location of the intensity line profiles. The line profile results compare the original projection and the estimated projection at different slice positions; (b) line profile A placed in the mid-plane and (c) line profile B placed at a large cone angle.

The estimation method for Object 3 produced interesting results (Figure 4.52a)). In this instance the method has not estimated the missing data with the accuracy observed with Objects 1 and 2. The top and bottom of the object in Figure 4.52(a) are disjointed with a clear step present at the threshold between the measured data and the estimated data. This is emphasised in Figure 4.53(c) for line profile *B*. However it cannot be said that the estimation algorithm has worked incorrectly as the region around the mid-plane has been accurately estimated as verified by the line profile *A* in Figure 4.53(b).

To summarise, the offset projections for Object 1 and 2 had no areas of concerns for either the estimation or the tailing method. However, Object 3 had disjointed areas within the estimated projections, which could potentially cause ringing artefacts (see section 2.2.4.5) to be introduced into the reconstructed images. Currently there is no proven

explanation for the different levels of accuracy for the estimated method. All three objects were acquired using the same system and the method of offset simulation kept the same. However, this system uses a pre-processing method to correct the manipulator alignment and the centre of rotation. This adjusts the alignment of the projection and can be visualised by the white regions at the edge of the projections (Figure 4.50). Therefore the possibility exists that this alignment correction affects the accuracy of the estimation algorithm. The inconsistency found for the estimation method and the methods sensitivity to parameter changes could potentially be a deciding factor for the use of the tailing method in future offset CT scans.

4.6.2.2 Reconstruction Results

The CT images in Figure 4.54 compare the offset reconstructions using the estimated and tailing methods with the original non-truncated reconstruction. The accuracy of the offset methods was quantified by comparing intensity line profiles extracted across all three reconstructions (Figure 4.55). Similar to the projection results in the previous section 4.6.2.1, the line profiles were positioned in the mid-plane (line profile *A*) and off the mid-plane at a large cone angle (line profile *D*).

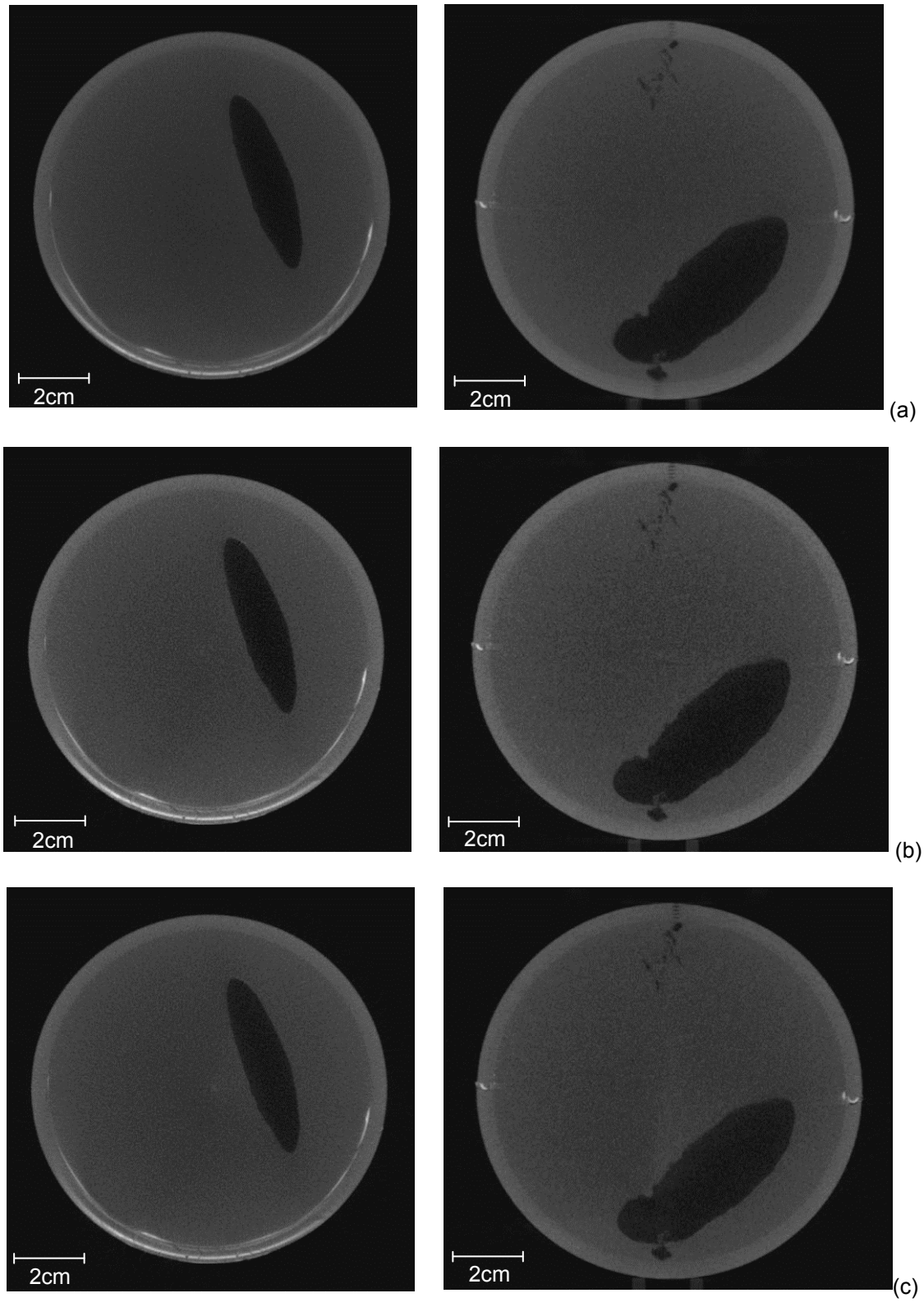

Figure 4.54: CT cross-sectional images taken of Object 1 in the axial direction (left) and in the frontal direction (right). Reconstructed using (a) Original, (b) estimation and (c) tailing.

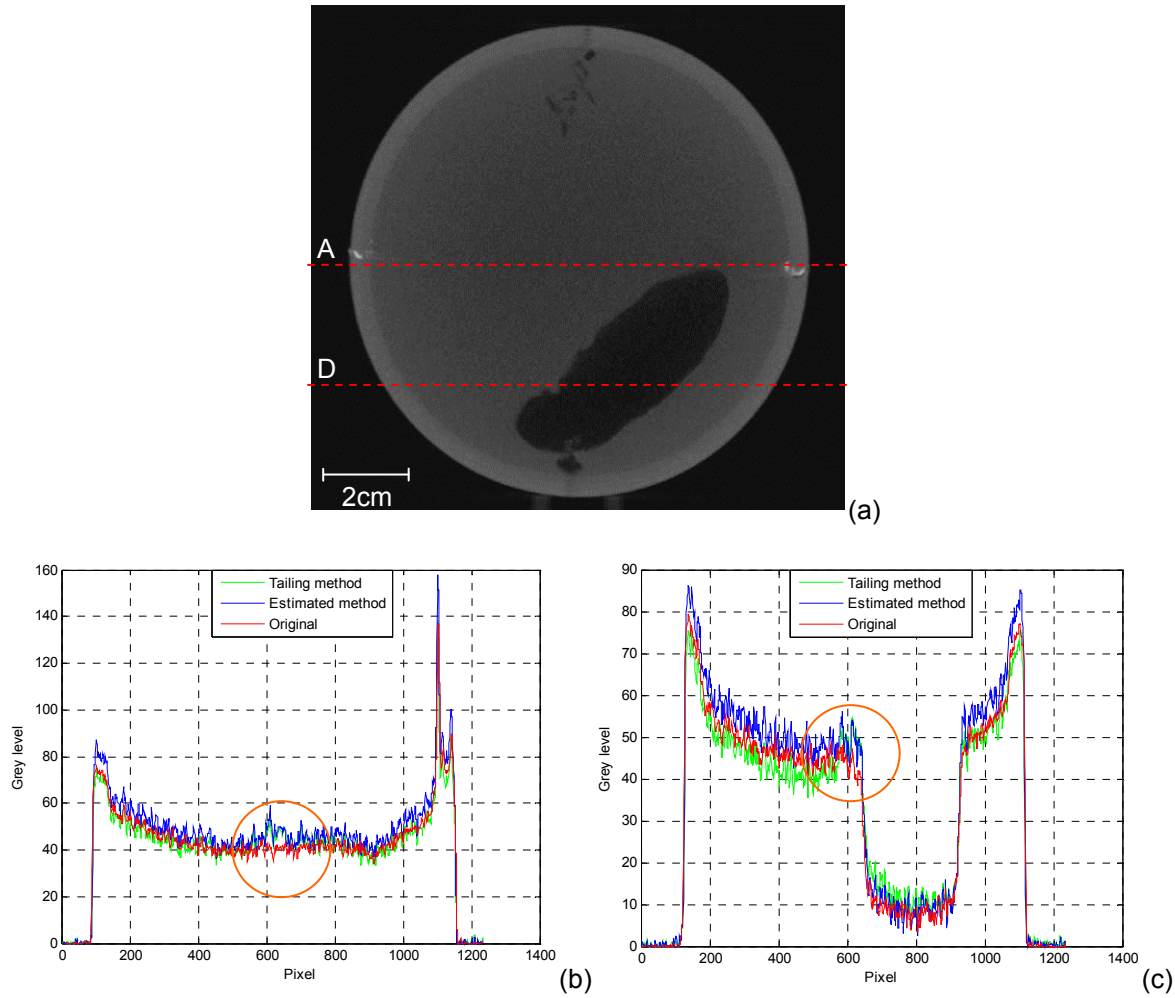

Figure 4.55: (a) CT image of Object 1 showing location of the intensity line profiles. The line profile results compare all three reconstructions at different slice positions; (b) line profile *A* placed in the mid-plane and (c) line profile *D* placed at a large cone angle.

The offset reconstructions from Object 1 (Figure 4.54(b) and Figure 4.54(c)), for both estimation and tailing, have produced accurate results that have no prominent artefacts. However, upon careful inspection of all cross-sectional slices within the reconstruction, small almost overlooked artefacts were identified. The estimation method produced a small artefact near the centre of the image (Figure 4.54(b)) in a very small number of slices. The tailing produced a slightly different type of artefact that again was only found in a very small number of slices. This appears as a lighter region propagating out from the centre of the image. The artefacts are emphasised by comparing line profiles extracted across the CT images for all three reconstructions (Figure 4.55). The line profiles were extracted in the mid-plane (line profile *A*) and off the mid-plane at a larger cone angle (line profile *D)*, as illustrated in Figure 4.55(a). Both the line profiles highlighted the shading artefact present near the centre of rotation (circled regions in Figure 4. 55(b) and (c)). Due

to the central location of this artefact an obvious cause would be an incorrect centre of rotation setting.

These line profiles also demonstrated that the reconstructed CT data (i.e. attenuation coefficients), for both tailing and estimation, was slightly different when compared to the original data. This is illustrated in the line profiles by differences in grey level intensity between the three reconstructed CT images. A reasonable assumption for the source of this error is the resulting effect that the simulated data has on the measured data during filtration. It has already been stated that predicting the effect of the filtration process is a difficult task and one of the primary objectives of this work was to develop a data completion method that would ensure minimal impact on the measured data during filtration.

The results for Object 1 indicate that the central shading artefact and the relative error of the attenuation coefficients, for both the estimated and tailing methods, are not prominent and do not interfere with the structure of the object or the detail detectability. So potentially, they could be identified and disregarded during inspection application.

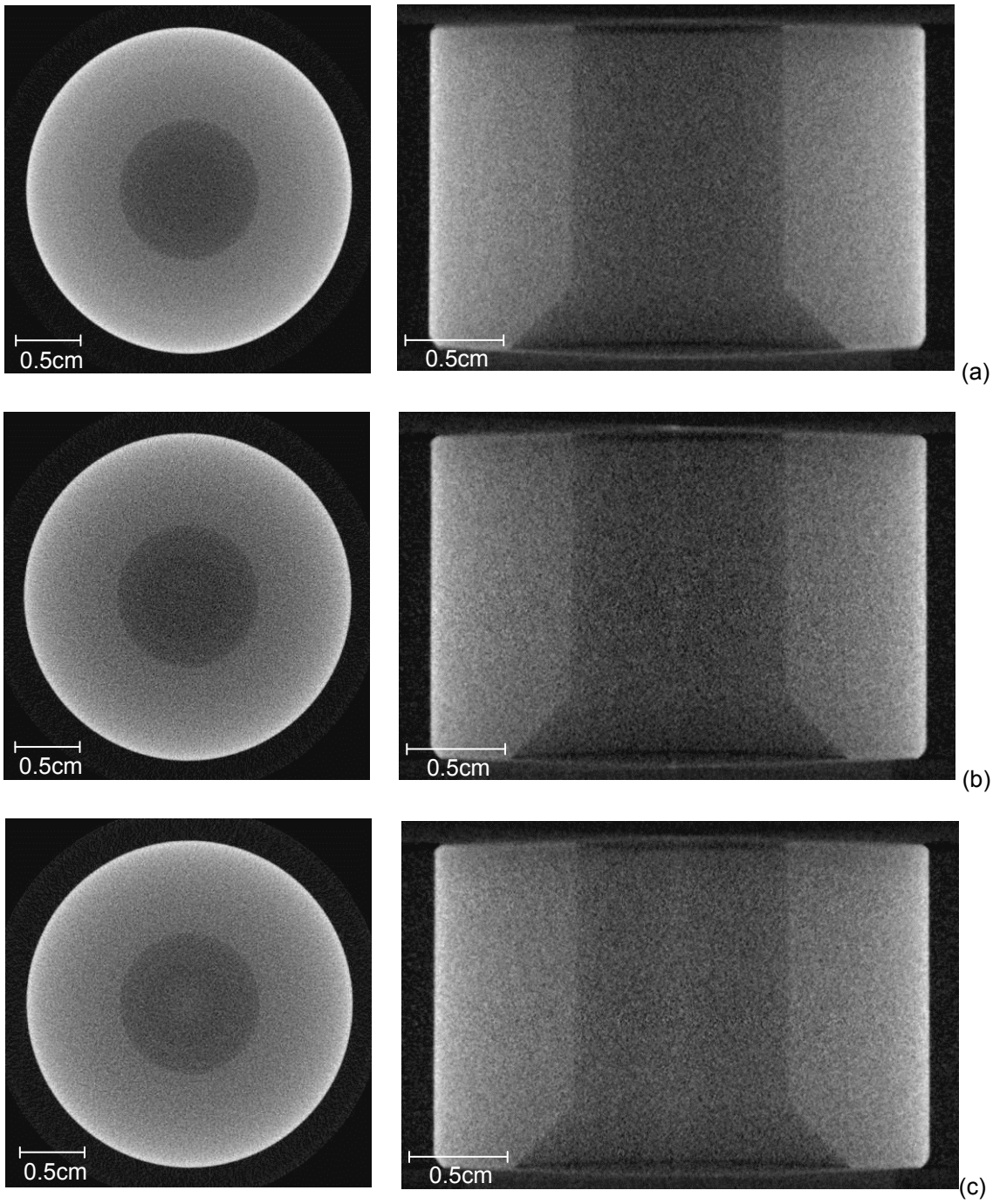

Figure 4.56: CT cross-sectional images of Object 2 taken in the axial direction (left) and in the frontal direction (right). Reconstructed using (a) Original, (b) estimation and (c) tailing.

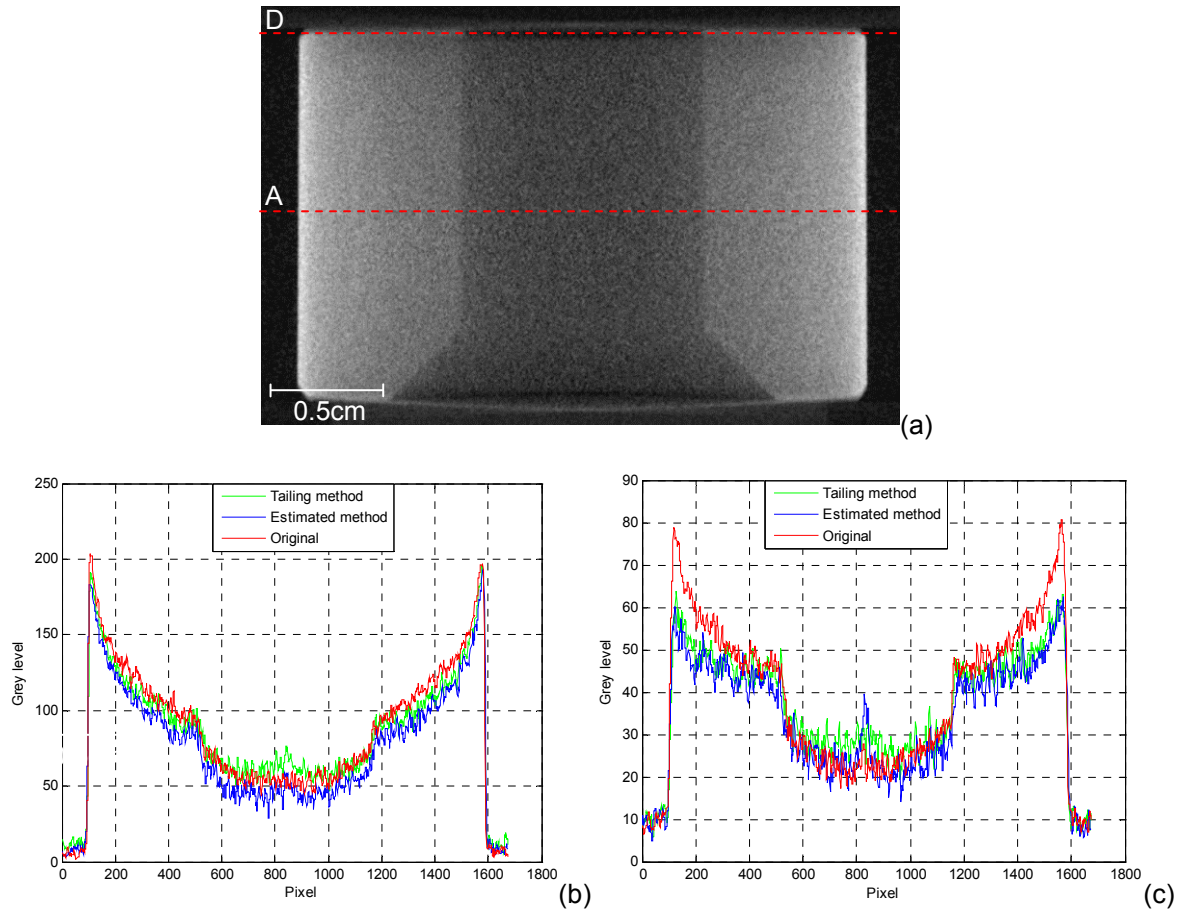

Figure 4.57: (a) CT image of Object 2 showing location of the intensity line profiles. The line profile results compare all three reconstructions at different slice positions; (b) line profile *A* placed in the mid-plane and (c) line profile *D* placed at a large cone angle.

Comparing the results from the original reconstruction and the offset reconstructions for Object 2 in Figure 4.56, it was clear that the estimation method had a centre of rotation artefact within the CT data (Figure 4.56(b)). Upon closer inspection a centre of rotation artefact was also highlighted within the tailing reconstruction (Figure 4.56(c)). This artefact, for both methods, was only found in a very small number of slices near the centre of the object. However, the centre of rotation artefact found for the estimation method is clearly more prominent than the artefact found in the tailing method, especially at increased cone angle locations (i.e. top and bottom edge of the object). This was confirmed in line profile *D*, Figure 4.57(c), showing a spike in the intensity at the centre of the image for the estimated method. The comparison of the projection data completion results for Object 2 (Figure 4.49) shows the simulated data to be very accurate with no discontinuities. Therefore, the possibility that this strong artefact was caused solely by inaccurate estimated data can be eliminated.

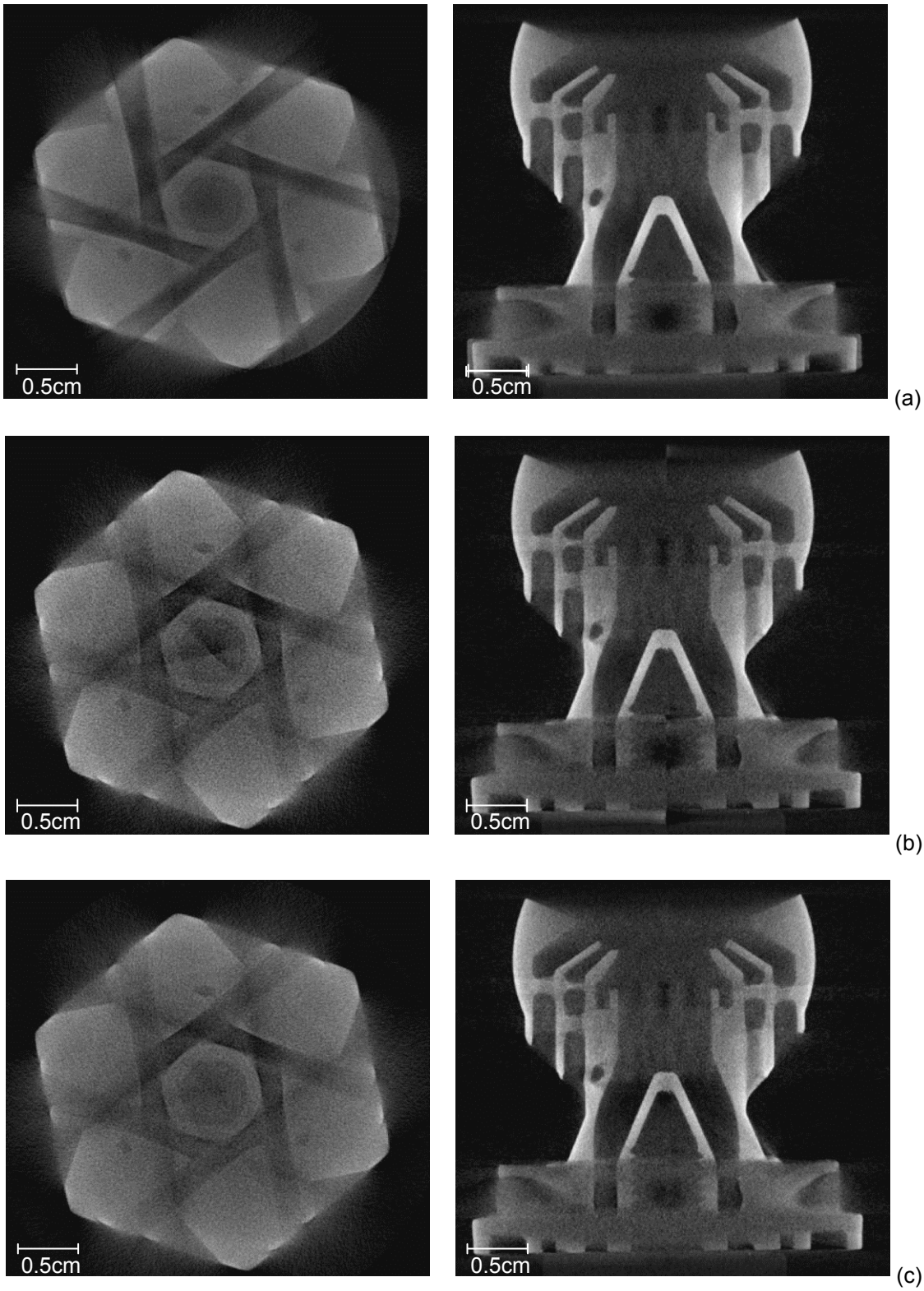

Figure 4.58: CT cross-sectional images of Object 3 taken in the axial direction (left) and in the frontal direction (right). Reconstructed using (a) Original, (b) estimation and (c) tailing

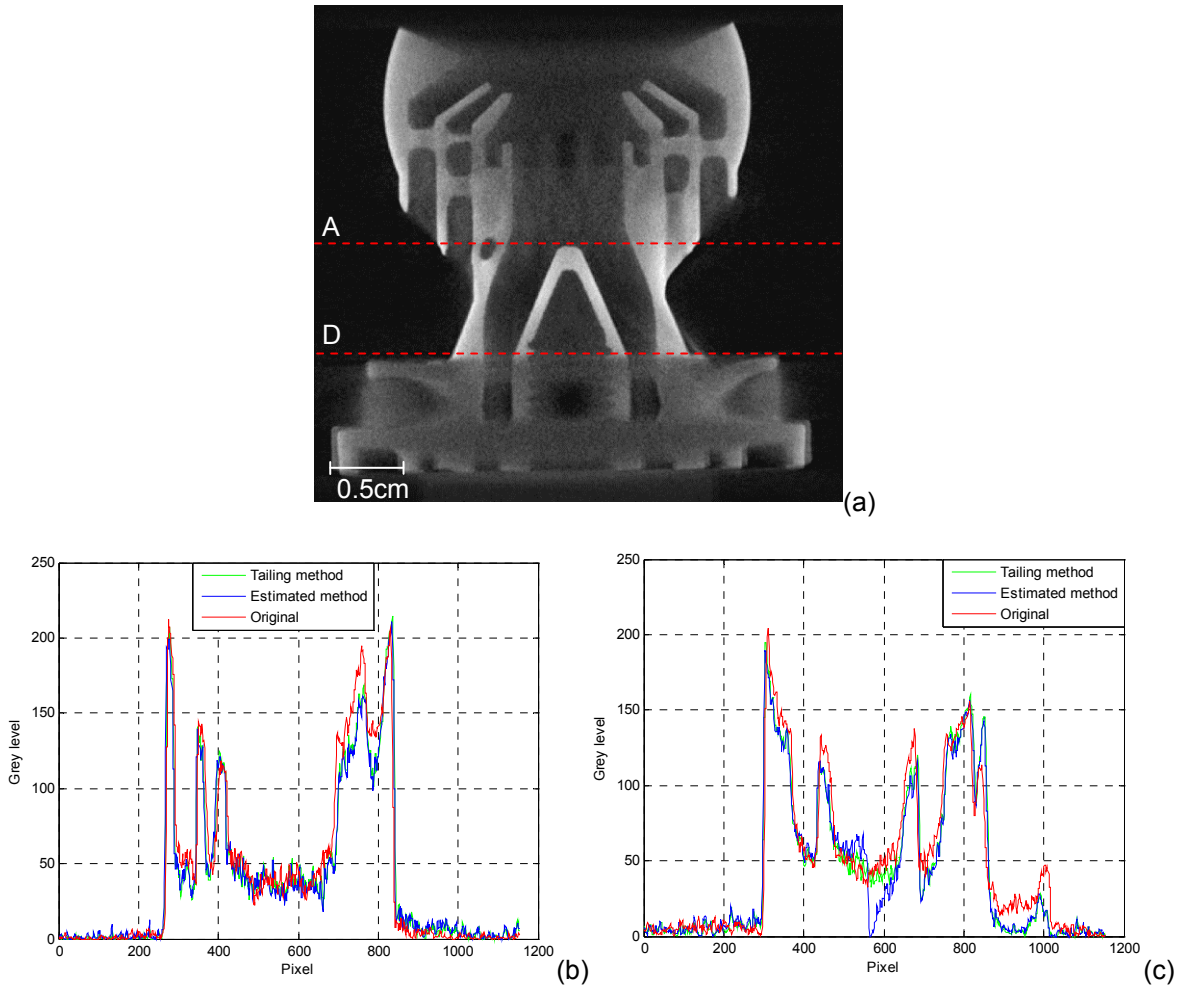

Figure 4.59: (a) CT image of Object 3 showing location of the intensity line profiles. The line profile results compare all three reconstructions at different slice positions; (b) line profile *A* placed in the mid-plane and (c) line profile *D* placed at a large cone angle.

Out of the three objects, the least accurate estimated projection data was found to be Object 3 (Figure 4.52). This was probably the reason why the reconstruction of Object 3 for the estimated method (Figure 4.58(b)) had the strongest artefacts out of all the reconstructions. The intensity profiles confirmed this with line profile *D* revealing a large dip in intensity near the centre of the image (Figure 4.59c)). However, the inaccurate estimate of the missing data is not the sole reason for this artefact, as discussed previously for Object 2. The estimated reconstruction for Object 2 had very similar artefacts but less prominent, even though the estimated projection data was very accurate. This means another cause exists but has not yet been identified. The tailing method for Object 3 resulted in an accurate reconstruction of the object structure but again a small error was reconstructed across the attenuation coefficients within the CT data. This was visualised as a reduction in the reconstructed grey levels across the CT

image, as indicated by the line profiles in Figure 4.59. The same reduction was evident in the reconstruction for the estimated method.

All three of the objects for both tailing and estimation displayed different levels of artefacts introduced into the CT data. The prominent shading artefact is always central in location which, as discussed in section 4.5.3, indicates a centre of rotation issue. The offset reconstructions showed the estimation method to cause an increase in this central artefact. This was the case even though the centre of rotation used was the same for both, estimation and reconstruction. Based on these observations it is probable that there is a centre of rotation issue for both, but the estimation method is more sensitive to the problem than the tailing method. It was also noted that both methods caused the attenuation coefficients within the CT data to be slightly different to that reconstructed in the original CT data. This was attributed to the effect the simulated data has on the measured data during the filtration process. However, this did not affect the structural accuracy or the detail detectability of the reconstruction. It would only present a problem if accurate density measurements had to be inferred from the attenuation coefficients.

4.7 Conclusions

The offset CT technique, presented in this chapter, has nearly doubled[2] the width of objects that could previously be inspected using conventional cone beam CT scanning. The experimental work undertaken successfully increased the CT scan FOV to allow the inspection of a WTB approximately 150mm wider than the detector panel. This resulted in a CT scan FOV that was 1.5 times larger than the FOV permitted by conventional CT.

At the time of writing this thesis, only one company in Europe, BIR ACTIS™ (BIR Ltd 2008), could be found that offers an industrial CT system with the capability to extend the CT scan FOV larger than the detector panel. This method, similar to that of Fu and Lu (2005), is based on an offset detector position and fan beam geometries. Where ray redundancy is used to complete the missing data once the projection data has been rebinned to parallel beam. However, fan beam CT systems only allow single 2D cross sections to be reconstructed at a time. So for the entire length of an object to be reconstructed it would be very extensive in terms of time and computation. Therefore, the cone beam offset CT technique has two main benefits compared to fan beam methods: Firstly, the greatly improved scanning time that is offered by direct 3D reconstruction and

[2] Not exactly double due to geometric magnification.

secondly its applicability, as the vast majority of industrial CT systems use cone beam geometry.

Including the offset CT capability as an inspection tool means increasing the scope of objects that can be inspected using the technique of CT. Previously, objects such as wind turbine blades, large composite panels, engine blocks, etc, would not be an option for CT inspection unless sectioned to smaller dimensions. Another advantage of offset CT is the ability to inspect not only objects larger than the detectors FOV, but also adequately sized objects at high geometric magnifications. This means a very high spatial resolution can be obtained that would not be possible with conventional CT inspections.

Many achievements were made within this project to enable a successful offset CT scan, these include:

- Successful acquisition of actual Offset projection data using a prototype system.
- The development and implementation of two different data completion methods that extending the offset projection data to overcome the truncation problem i.e. tailing and estimation.
- A new method for optimising the centre of rotation parameter
- The inclusion of the blanking function within the FDK reconstruction algorithm
- The successful inspection of the full width of a WTB larger than the detectors FOV. This inspection was able to detect and characterise a large range of defects and structural irregularities within the blade structure. Currently, this level of inspection can not be achieved non-destructively by any other means.
- Suitable validation of the offset CT technique by simulating offset reconstructions using full non-truncated projection data. This allowed intensity line profiles to be analysed, which provided a quantitative measure of the performance and highlighted any errors that were induced by the offset CT reconstructions.

The negative aspects of the two data completion methods have also been discussed within this chapter. Analysing the simulation and actual offset reconstructions, both qualitatively and quantitatively, it was apparent that a central shading artefact existed for both methods. This could be easily identified and disregarded for some of the reconstructions but was more prominent and therefore problematic for others. An explanation for the artefact was identified as the possible incorrect setting of the blanking function to the centre of rotation. This was investigated by further simulating offset CT reconstructions i.e. applying just the blanking to full original projection data and observing any artefacts induced. This simulation concluded that the blanking function used in the

reconstruction algorithm is not the source of the artefacts. Therefore the likely cause can be attributed to the effect the data completion method (i.e. simulated data) has on the measured data. It has been observed that the estimation method causes the central artefact to be more prominent than the tailing method. In fact, the artefact was found not to be significant in any of the reconstructions where the tailing method was applied. This was one of the primary reasons for the conclusion that the tailing method will be used for future offset CT inspections. Other additional factors in this decision were the setup simplicity and the consistency of the results. In contrast, the estimation method was more difficult to setup, very sensitive to changes in input parameters and produced stronger artefacts

Aside from the notable shading artefact, the line profiles also demonstrated that both data completion methods caused the attenuation coefficients within the CT data to be different to that reconstructed in the original CT data. This error highlights the impact that the simulated data has on the measured data during reconstruction. Procedures were in place to minimise this error and ensure that only the accurate measured data was back projected. But it is very difficult to predict the effect that the filtering process will have on the measured data once simulated data has been included. This is the reason for the majority of data completion methods found in literature using as accurate an estimate as possible, whether it is via ray redundancy or prior full CT data (see section 2.2.5). Therefore, to refine the offset technique and improve the accuracy of the reconstructed data it is recommended that the problems encountered with the estimation technique is investigated further. As this technique has the potential to supersede the tailing method in terms of reconstruction accuracy.

The implementation of two further measures within the estimation method would help improve the estimate and reduce these artefacts: (1) Add an interpolation function when estimating the redundant ray paths (see section 4.5.1.2). This will improve the accuracy of the estimate and help remove the disjointed regions present at the threshold between the measured data and the estimated data (see section 4.6.2.1). (2) Add a small faded taper to bridge the gap between the measured data and the estimated data. This will suppress the sharp transition at the disjointed regions thus reducing the risk of ringing artefacts (see section 2.2.4.5).

The results presented in this chapter have shown that the offset CT technique using the tailing data completion method can be performed reliably and the reconstructed CT images are sufficient for the majority of NDT inspections. The small errors in the

reconstructed attenuation coefficients will only present a problem for applications requiring accurate density measurements.

Finally, the successful offset CT technique developed in this work has led to Metris X-Tek including it as an option for customers requiring specialised bespoke CT systems for inspection of large components. The findings have also been passed onto Metris' main R&D department in Belgium with the ultimate goal being to implement the technique as a software add-on without the need for the detector shift.

Chapter 5

Computer Tomography using a Dual Energy Approach for the Inspection of Highly Contrasting Materials.

5.1 Introduction

This Chapter describes the development and validation of a dual energy type image processing algorithm that was implemented into the CT reconstruction process of single energy CT scanning systems. The aim of this technique was to effectively increase the optimum dynamic range of the CT acquisition to improve defect detection and characterisation in multi-density components. The work described here was specifically tailored to meet the inspection requirements of Fibre-Reinforced-Plastic (FRP) composite-Titanium Comeld™ joints.

Comeld™ is a new joining process between FRP composite materials and metals that was developed by TWI Ltd in 2007 (more details in section 5.3). The process involves pre-treatment of a metal surface using a technique called Surfi-sculpt™, to which the composite is directly cured (Smith *et al* 2007). This interlocking structure produces excellent mechanical properties but it also provides opportunities for defect formation during fabrication. NDT inspection of complex structures like this is often very difficult as defects within both the composite and the metal joint section need to be identified. TWI has investigated a number of different NDT techniques for the inspection of the joints, of which CT was one (Smith *et al* 2007). However, due to problems with the inspection of multi-density components (discussed in detail within this chapter), the quality of the results did not meet the requirements. The aim of this work was to overcome the multi-density limitations and develop a CT procedure for the inspection of Comeld™ and other multi-density joints.

As mentioned previously, CT is based on the measured attenuation of X-rays as they pass through an object. These measured attenuation coefficients are based on Beers Law (Equation 2-2) and are dependent on the X-ray source energy spectrum, as well as the thickness and density of the material being inspected.

For the CT reconstruction algorithm to represent these attenuation coefficients accurately within the final image, it is required that the X-ray energy level results in the full penetration of all parts of the test object. This also demands that no part of the image is saturated i.e. the resultant signals are within the effective dynamic range of the detector system (see section 2.1.6.2), If these conditions are not satisfied, then the resultant CT image will be dominated by artefacts. Furthermore, it has been shown that the use of the correct energy setting for the material being imaged optimises the detail detectability of the CT inspection (Macdonald 2004). Therefore, when imaging a multi-density component with a single energy CT system it is very difficult to optimise the energy setting for the different materials present within the object. This will inevitably reduce the overall quality of the inspection. The problem is amplified when inspecting an object made up of two materials of very different densities, such as the composition of CFRP-Titanium Comeld™ joints.

The X-ray exposure required to fully penetrate the high density material results in the ratio between the un-attenuated background signal and that transmitted through the dense part often reaching the limit of the effective dynamic range of conventional X-ray detectors. Consequently, this exposure is outside of the optimum dynamic range of detectability for any low density material present. This results in reduced detail detectability and increased image noise, thus reducing the SNR and contrast in the low density region.

In other words, choosing an optimum X-ray setting for the low density part would result in under penetration of the higher density part. The same applies for the optimum settings of the high density part. As the increase in energy would result in either over exposure for the low density part or, at the very least, increased image noise (reduced SNR) and reduced low density contrast.

This suggests that Dual Energy Computer Tomography (DECT) could be utilised to overcome these constraints by effectively increasing the optimum dynamic range of detectability of the CT acquisition. In doing so, it would also provide a very effective tool for enhanced defect detection in Comeld™ joints and other multi-density components. Currently DECT is a highly developed technique in the medical industry (Hounsfield 1973; Kalender *et al* 1986; Petersilka *et al* 2008) and has NDT applications in the food industry and airport baggage control (Eilbert and Krug 1992; Kroger *et al* 2005; Ying *et al* 2007). In these industries it is mainly used for material composition analysis, where the attenuation data gathered is used to identify the density and atomic number of the materials present. The technology requires specialised systems involving dual sources or the use of multiple

detectors (Rebuffel and Dinten 2007). At the time of writing this thesis, these systems have not been applied for defect detection purposes.

The state-of-the-art systems for conventional CT address the limitations associated with multi-density components through the use of improved detectors with increased dynamic range and improved contrast sensitivity. This increased latitude means that previously overexposed areas will now contain enough detail to use in the CT reconstruction, meaning improved detectability. However, the improved dynamic range offered by these state-of-the-art detectors is still limited and this problem is viewed as being a major obstacle for most industrial applications (Sivers 1995).

Other novel techniques have been developed that attempt to effectively increase the dynamic range of the CT acquisition by taking multiple scans at different detector positions in an attempt to optimise the energy settings for the different aspects of the object under inspection (Sivers 1995). This is then followed by a type of image registration scheme to merge the data to form a single reconstructed CT volume.

The problem of satisfactorily imaging components with a large range of thicknesses or densities has been overcome for film radiography by a method known as a multi-loading. This involves loading a cassette with two films of different film speeds and simultaneously exposing them with a single energy. The result is two films with different exposures that are more suited, or optimised, to the different thicknesses or densities present in the component. These can then be overlapped and viewed on a light box as a single radiograph, known as multiple composite viewing. This novel method has been used to setup procedures for a range of medical (such as mammography) and industrial applications. An EU funded collaborative research project, called HEDRad[1] (High Energy Digital Radiography) is currently adapting the multi-loading technique to Computed Radiography (CR) using phosphor plates. The aim is to increase the latitude of component thicknesses and densities that can be imaged to a high quality using high energy digital radiography. In order to apply this technique to CR, software is required to average the images produced from the different exposures (replacing the composite viewing of films over a light box). To produce accurate images the software includes an

[1] HEDRad is a collaboration between the following organisations: BAM (Federal Institute for Materials Research and Testing), Blohm & Voss Inspection Service GmbH (BIS GmbH), CIT Limited, EON Kernkraft GmbH, I Know How Informatics SA, Nexus Engineering, Technical University of Sofia and TWI Ltd. The project is co-ordinated and managed by TWI Ltd and is partly funded by the EC under the Research for the Benefit of Specific Groups Project ref: FP7-SME-2007-1-GA-222240.

alignment function, to shift the separate images into the correct orientation prior to averaging (HEDRad 2008).

The dual energy technique developed in this research is not DECT in the usual sense referred to in literature. The research presented in this chapter is based on acquiring two complete sets of projection data at two different energies (High Energy, HE, and Low Energy, LE). This allows X-ray settings to be chosen that are optimised to the different material densities present. As a result the ratio between the un-attenuated background signal and the attenuation caused by the chosen material density is within the optimum dynamic range of detectability for both sets of projection data. An image processing algorithm is used to combine the HE and LE X-ray projection stacks to produce a single, optimised projection stack to be reconstructed. The image processing algorithm achieves this by applying an iterative thresholding technique to each stack to segregate the unwanted density from the projection data. A scaling process is then applied to reduce any degradation when the two projection stacks are merged. The resultant merged projection data effectively stretches the optimum dynamic range of detectability for the reconstructed CT inspection thus improving the SNR.

The premise of the technique is that a LE scan produces optimised projection data for the low density region and the HE scan produces optimised projection data for the high density region. However, the problem exists because reconstructing these two projection sets separately will not result in one CT reconstruction with an optimised low density region and the other CT reconstruction with an optimised high density region. The actual result would be an optimised high density region for the HE scan, but the LE reconstruction would cause the entire CT image, including the low density regions, to be dominated by artefacts. These artefacts would be due to the CT requirement of full penetration of the X-ray beam through all angles of the object not being satisfied. Therefore a method was implemented that allowed the extreme high density regions within the LE projection data to some extent be replaced by the optimised high density regions from the HE scan. This resulted in a single stack of optimised projection data that, when reconstructed, provided both minimum penetration in the high density regions and improved detail detectability within the low density regions – effectively stretching the optimum dynamic range of detectability.

The first part of this chapter concentrates on the experimental method used to merge the optimised regions from the projection data of a HE and LE CT scan, to form a single complete stack of optimised projection data. The second part of the chapter focuses on

the validation procedure used to verify the improved performance. This validation procedure consisted of known statistical performance methods applied to a specially made reference phantom to compare the new technique with conventional CT. The two performance measures chosen for the comparison were the detail SNR (Graeff and Engelke 1991; Mangard 2000) and the Modulation Transfer Function (MTF) (ASTM E1695 2006). Further validation was then provided in the final part of the report by comparing real inspection results of two different multi-density components. The first component was a Copper-Aluminium HVAC component (Heating, Ventilation and Air Conditioning) and the second was the CFRP-Titanium Comeld™ lap joint.

5.2 Objectives

The aim of this work was to develop a novel dual energy image processing algorithm that produces optimised projection data of multi-density components by combining image stacks acquired at two different energies. Specifically to;

- Develop an image processing algorithm that allows the CT projection data to be optimised for low density regions without the reconstruction being dominated by artefacts caused by under-penetrated high density regions.
- Effectively increase the optimum dynamic range of detectability of the CT acquisition by producing projection data that ensures sufficient penetration of the high density regions without over exposing the low density regions.
- Implement the dual energy technique with a standard single energy CT scanning system and Filtered Back Projection (FBP) type FDK reconstruction algorithm.
- Validate the improved performance using statistical performance measures on a specially fabricated reference phantom.
- Apply the experimental dual energy method to Comeld™ joints as an advanced NDT procedure for defect detection and characterisation.
- Provide other case studies of the technique application with multi-density component inspection.

5.3 Comeld™ Joints

The key advantage of composite materials is there retention of high strength and stiffness at a reduced weight. However, this can be compromised when attaching them to metallic structures due to the joining processes involved. Currently, the majority of such structural joints rely on a combination of adhesive bonding and mechanical fastening which require

the use of holes, creating stress concentration points that weaken the material. Comeld™ joints were developed with the aim of effectively joining FRP composites to metals by maximising the load carrying capacity of the joint, without the need for fasteners and holes. This involved pre-treatment of the metal surface using a technique known as Surfi-sculpt™. This technique uses an electron beam to allow controlled displacement of the metal to produce a pattern of protrusions and intrusions that the composite can be directly fabricated onto.

Investigations performed at TWI have demonstrated an improvement in mechanical properties for joints using Comeld™ technology (Smith *et al* 2007). The CFRP and Titanium (CFRP/Ti) double step Comeld™ lap joints, as shown in Figure 5.1, demonstrated improved strength, displacement before failure and energy absorbing characteristics compared to control joints when subjected to either tensile or bend loading. Under both types of loading, the Comeld™ joints withstood loads up to twice that of the control joints and absorbed up to 13 times more energy before failure (Smith *et al* 2007).

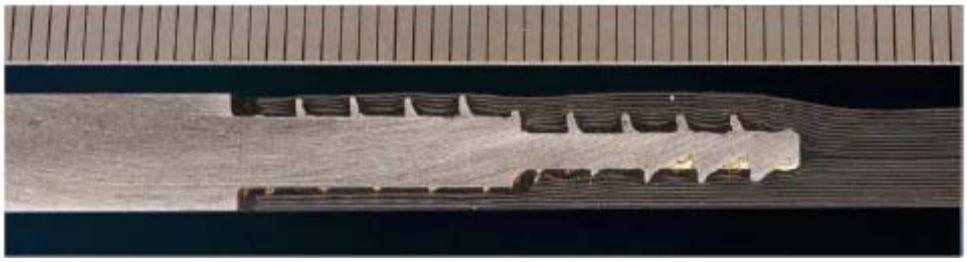

Figure 5.1: Photograph of a Ti/CFRP, double step, Comeld™ joint cross section (mm scale shown). The full details of this sample are described in section 5.3.1.

Although the interlocking structure of a Comeld™ joint produces excellent mechanical properties, it also provides opportunities for defect formation during fabrication. This requires a reliable NDT technique to be identified that can be used for defect detection and characterisation purposes.

5.3.1 Joint Fabrication

Comeld™ joints have been developed for high performance engineering applications. CFRP and Titanium are both used in high strength, low weight applications and therefore combining these without compromising design is beneficial. The joint samples used in this investigation were fabricated by a specialist team at TWI's head office in Cambridge. The

following steps were taken to fabricate the CFRP/Ti double step Comeld™ joints using CFRP pre-preg and autoclave curing:

1. The individual Titanium specimens were machined into the double step shape with the dimensions shown in Figure 5.2. Titanium alloys based on the Ti-6Al-4V system are one of the most widely used and therefore ASTM alloy grade 5 was chosen for the purpose of this work.

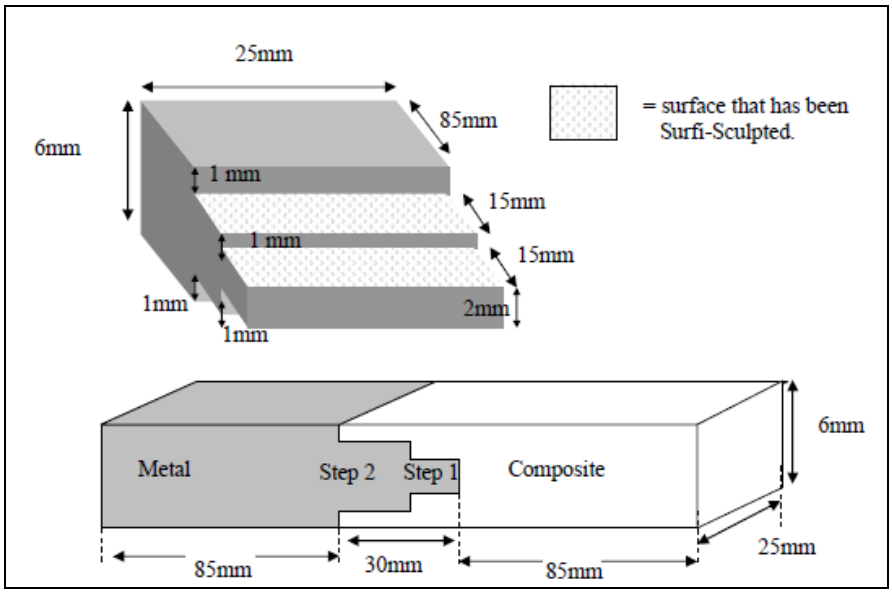

Figure 5.2: Schematic drawing showing the dimensions of the Comeld™ double step lap joint.

2. The Surfi-sculpt™ technique was applied to the surface of the Titanium joint section using TWI's 6kW 150kV HS2 upgraded facility. The process involves the electron beam visiting the same location many times during a single treatment. At that location the beam is focused and then translated in a set direction, causing a protrusion and an intrusion to be created. This is repeated many times until the desired height of the protrusion is met. The resultant surface is shown in the SEM images provided in Figure 5.3.

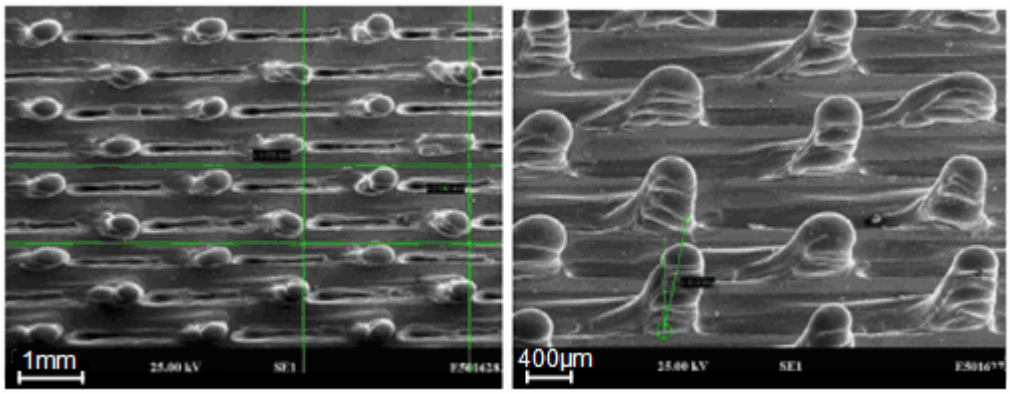

Figure 5.3: SEM images of Surfi-Sculpted, double step, Ti specimen (Nominal magnification is shown).

3. Further surface preparation was needed following the application of the Surfi-sculpt [TM] technique to enhance adhesion between the composite and the metal. This involved washing the Titanium joint section with a detergent solution and immersing in an appropriate echant.

4. Prior to laying up the CFRP pre-preg, the individual joint sections were fixed with plastic spacers between each of them to allow easy separation/cutting of the joints into test specimens.

5. The pre-preg used was Hexply 8552 with IM7 fibres from Hexcel composites (Hexcel n.d.). The composite lay-up chosen for the test specimens was $(0/90)_{12S}$ as shown in Figure 5.4. In this setup, (0/90) indicates that one ply of pre-preg was laid up with the fibres orientated in the 0° direction, followed by another ply perpendicular at 90° degree. The 12S subscript indicates that this was repeated 12 times and then that whole lay-up was repeated with mirror symmetry

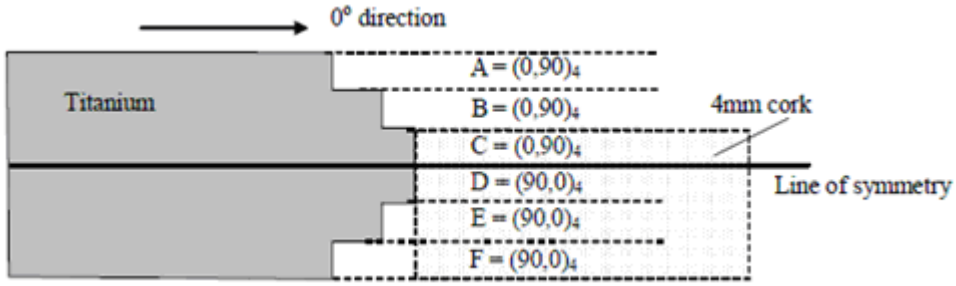

Figure 5.4: Schematic of the Ti/CFRP double step joint showing the CFRP pre-preg lay-up.

6. The method used to lay-up the pre-preg involved combining each set of eight plies as a section. A roller was then used to consolidate each section onto the Titanium protrusions at the correct positions to form the joint. At this stage it does not properly consolidate due to the density of protrusions on the surface. However, the curing process results in a drop in resin viscosity and the high pressures used will cause the pre-preg to consolidate onto the protrusions.

7. Once the lay-up was complete, the whole assembly was placed on a metallic plate and the standard lay-up for autoclave cure completed (Hexcel n.d.). The assembly was left overnight to facilitate consolidation and air removal. The assembly was cured in the autoclave according to the manufacturer instructions, which consolidated the pre-preg onto the Titanium surface.

8. The final step, after the cure cycle, involved cutting the resultant panel into Comeld™ joint test specimens (Figure 5.5).

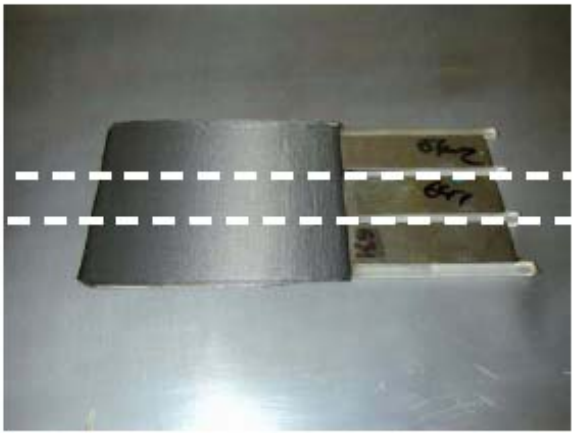

Figure 5.5: Photograph showing the cured panel prior to cutting into test specimens.

5.4 Experimental Approach

The CT system used for this work was a HMX 225 supplied by X-Tek Systems Ltd (X-Tek Group, 2006), the instrumentation and setup is described in full in section 2.2.6.1 All the necessary calibration checks were performed before acquiring the CT projection data. These included; spatial distortion corrections, system alignment and beam focusing (see section 2.2.6.2).

5.4.1 CT Data Acquisition

The sample was placed into the CT system and two full scans were completed; one with the X-ray source at high energy, the other with the source at low energy. Both the HE and LE sets of raw projection data were inputted into the dual energy image processing algorithm. The projection data for both scans was gathered using the exact same acquisition settings other than the energy setting. Object position, number of projections, frames per position and scan region of interest were the same in both scans.

5.4.1.1 Low Energy Scan

Conventional CT demands full penetration of the X-rays through the entire object and a minimum intensity reading of approximately 10,000 grey levels (for a 16 bit detector system) through the longest path length. Furthermore, the transmitted radiation must at no point saturate the detector i.e. the un-attenuated radiation reaching the detector (through free space) should not register an intensity reading greater than 64,000 grey levels. These requirements have to be satisfied to avoid the introduction of artefacts and improve the CT image quality (Ramsey 2008). However, the LE scan is aimed at optimising the energy settings for the low density material, ignoring the requirements for the high density material in the object. Therefore, a minimum 10,000 grey level constraint is not observed and the high density part will remain under penetrated.

5.4.1.2 High Energy Scan

The HE setting ensured minimum penetration through the longest path length (≥10,000 grey levels) and was aimed at optimising the image quality for the high density material. This was achieved at the expense of over exposure and increased noise in the low density material.

5.4.2 Dual Energy Image Processing Technique

The experimental dual energy algorithm consisted of three separate aspects; thresholding, scaling and merging of the raw projection data.

The thresholding segregated the unwanted density within the raw projection data using the assigned grey values. These thresholded values were then scaled using a separate algorithm, effectively mapping the extreme pixels to a different grey level range. This was applied to the projection data from both scans before the merging process. This work was performed in Matlab (R2008a).

5.4.2.1 Image Segmentation by Histogram Thresholding

Segmentation divides an image into its constituent regions or objects. For the purpose of this experiment, it was required to segment the raw projection images. The objective being to split the images into the parts representing the different materials present within a multi-density component. The intensity distribution within a radiographic image relates to the densities present within the component. This means that intensity is a distinguishing feature that can be used to extract different density regions from the image. Therefore, a thresholding technique becomes a strong candidate for efficient radiographic image segmentation. Many computational methods of segmentation exist with the simplest method being thresholding. Grey scale thresholding is typically used to create binary images (Shapiro and Stockman 2002). However, for this experiment this step was not necessary and the thresholding was only used to calculate the threshold value required to segment the images.

Thresholding techniques have been studied extensively due to their efficiency in performance and their theoretical simplicity (Nacereddine *et al* 2005). Generally, thresholding methods are either global or local, and are point or region dependent (Sahoo 1988). Global thresholding algorithms choose one threshold for the entire image while local thresholding algorithms partition the image into sub images and select a threshold for each sub image. Point-dependent thresholding algorithms only analyse the grey level distribution of the image while region-dependent algorithms also consider the location of the pixels.

Sezgin and Sankur (2004) categorised thresholding methods into six groups based upon the information which each method manipulates:

- Histogram based methods involve analysing the peaks, valleys and curvatures present within the image histogram.
- Clustering based methods require the grey-level samples to be either clustered in two parts as background and foreground (object), or modelled as a mixture of two Gaussian distributions.
- Entropy based methods involve algorithms that use the entropy of the foreground and background regions and the cross-entropy between the original and binarised image.
- Object attribute based methods seek a degree of similarity between the grey level and the binarised images, such as edge coincidence and fuzzy shape similarity.

- Spatial methods use higher-order probability distribution and/or correlation between pixels
- Local methods adapt the threshold value on each pixel to the local image characteristics.

Finding the correct threshold value to separate an image into its constituents remains a very important step in image processing. The idea behind threshold techniques is to use the statistics of an image to accurately distinguish its constituents, and an image histogram is the most direct and meaningful statistics of an image (Nacereddine *et al* 2005). Therefore a histogram based method was identified as the most suitable method of thresholding for the purpose of this work.

An image histogram shows how often each grey value occurs within an image. A generic histogram is constructed by splitting the range of the data into equal-sized bins (called classes). Then for each bin, the number of points in the data set that fall into each bin is counted. For a grey level image, the vertical axis represents the frequency (i.e. counts for each bin) and the horizontal axis represents the grey scale, as illustrated in Figure 5.6.

By definition (Nacereddine *et al* 2005):

Let the pixels of a digital image, *f,* be represented by *L* grey levels {0, 1, 2, …, *L*-1}. The number of pixels in level *i* is denoted by k_i and the total number of pixels is denoted by *N*. To simplify, the grey level histogram is normalised and regarded as a probability distribution function

$$p_i = \frac{k_i}{N},\ p_i \geq 0,\ \sum_{i=0}^{L-1} p_i = 1 \tag{5.1}$$

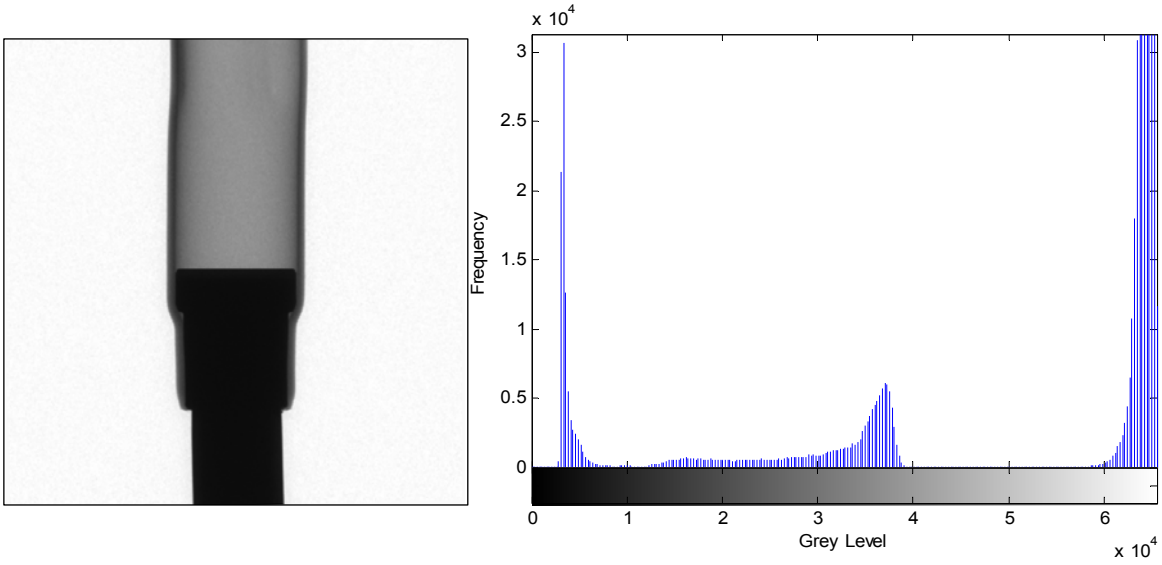

Figure 5.6: Example of a radiographic image (left) and the associated image histogram (right).

The purpose of histogram based thresholding is to find the valleys between the peaks within the histogram. The peaks in the histogram can represent various homogenous regions (phases), often referred to as modes, and thresholds can be set between the peaks to segregate these regions (Russ 2007). However, histograms may not have clearly defined valley points, often making the selection of an accurate threshold difficult, as shown in Figure 5.7.

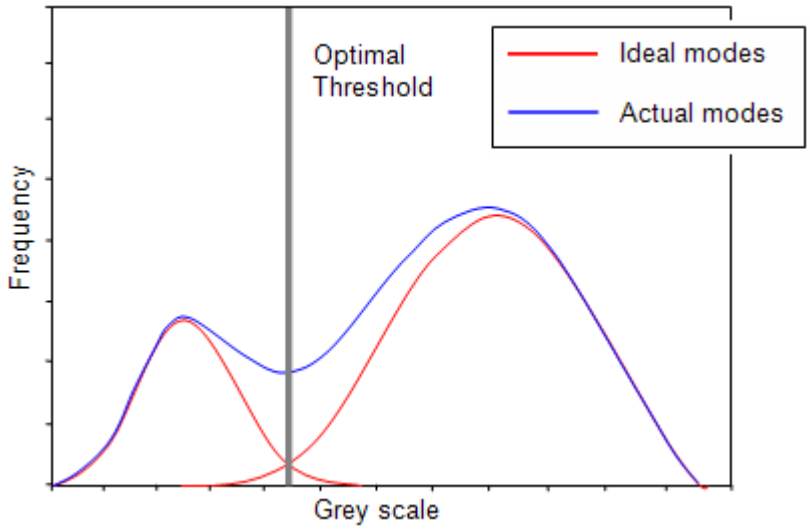

Figure 5.7: Diagram showing optimal threshold intersecting two modes in an image histogram

The following is a list of different methods for histogram based thresholding:

1. P-Tile method

The p-tile method is designed to split object pixels from the background and requires some prior information on the image. The method determines a threshold, *T*, such that at least (100-p)% of the pixels map into the foreground, where p is the percentage of pixels the object(s) of interest is known to occupy (Hale 2004; Henden 2004).

2. Mode method

The highest local maxima are identified and a threshold detected as a minimum between them. To avoid detection of two local maxima belonging to the same global maximum, a minimum distance in grey levels between these maxima is usually required or techniques to smooth histograms are applied (Sonka *et al* 1998; Hale 2006).

3. Iterative or optimal methods

Iterative methods select a threshold value that is statistically optimal based on the contents of the image. The method is based on initially guessing the valley point between modes within the histogram and iteratively improving the solution until convergence i.e. local minima is located (Shapiro and Stockman 2002; Henden 2004; Ridler and Calvard 1978).

4. Adaptive methods

Adaptive or variable thresholding divides the image into sub images and a threshold value is determined independently in each sub image. A global thresholding algorithm can then be used for each of these sub images such as an iterative method (Shapiro and Stockman 2002; Sonka *et al* 1998; Henden 2004).

The choice of histogram thresholding method depends mainly on whether the image distribution is bi-modal or multi-modal and whether the illumination or shading is uniform (Russ 2007). If two dominant modes characterise the image histogram then it is called a bimodal histogram and only one threshold is enough to partition the image. If the image has more than two dominant modes it has a multi-modal distribution and therefore requires a more complicated method of thresholding. The image histograms obtained from the projection data of a multi-density component are always multi-modal as illustrated in Figure 5.6. The materials present are each represented by a dominant mode and so is the background, resulting in three or more dominant modes.

The method of thresholding used for this work is known as adaptive thresholding. This approach divides the original image distribution into sub images, allowing a bi-modal iterative thresholding method to be applied (Sonka *et al* 1998).The resultant threshold value is the point at which the two modes within the sub image intersect. The benefits of this method are that it is relatively simple to implement compared to other multi-modal methods and it is robust against image noise (Shapiro and Stockman 2002).

The calculation used for adaptive thresholding can be derived by the following:

Let R represent the entire spatial region occupied by the image. Adaptive thresholding requires R to be divided into n sub regions $R_1, R_2, \ldots, R_n$, such that;

$$\bigcup_{i=1}^{n} R_i = R. \tag{5.2}$$

For the purpose of this experiment the sub image, R_1, R_2, was required and the background mode, R_3, was disregarded, as illustrated in Figure 5.8.

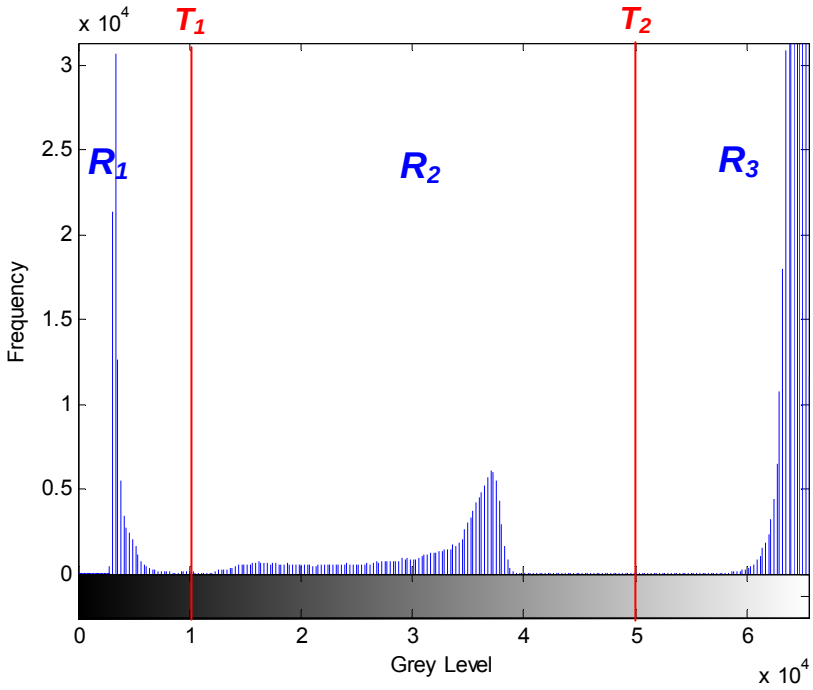

Figure 5.8: Image histogram with a multi-modal distribution, R_1, R_2, R_3. The radiographic image used to produce this histogram is shown in Figure 5.6.

The following iterative method was then performed on the sub image, R_1, R_2, to obtain an accurate threshold value to segregate the two modes (Ridler and Calvard 1978):

1. An initial threshold, T_1, was selected by estimating the point of intersection or valley between the modes.

2. The sub image was segmented using the initial value for T_1, creating two sets:
   $R_1 = \{f(i,j): f(i,j) \leq T_1\}$ (material 1)
   $R_2 = \{f(i,j): T_1 < f(i,j) < T_2\}$ (material 2)
   With $f(i,j)$ being the pixel values of the image f.

3. For iteration number t, the mean grey level $\bar{x}_{R_1}^t$ and $\bar{x}_{R_2}^t$ was computed for the pixels in regions R_1 and R_2, respectively, where segmentation for iteration t is defined by the threshold value, T_1^t, determined in the previous step.
   $$\bar{x}_{R_1}^t = \frac{\sum(i,j) \in R_1}{N_{R_1}} \tag{5.3}$$
   $$\bar{x}_{R_2}^t = \frac{\sum(i,j) \in R_2}{N_{R_2}} \tag{5.4}$$

4. An update threshold value, $T_1^{(t+1)}$, was then created:
   $$T_1^{(t+1)} = \frac{\bar{x}_{R_1}^t + \bar{x}_{R_2}^t}{2} \tag{5.5}$$

5. Steps 3 and 4 were then repeated, increasing t upon each iteration, until the difference between T_1^t and $T_1^{(t+1)}$ in successive iterations was negligible, i.e. until convergence had been reached.

The above iterative algorithm has been proven to converge to a local minimum, but is dependent on the initial threshold value (Ridler and Calvard 1978). This means that a different initial threshold may give a different final result i.e. the local minimum may not be the global minimum. However the possibility of this occurring is massively reduced if the valley points are easily approximated, i.e. the valley points are clearly visible.

The thresholding process for this technique is not easily automated due to the fact that as the object rotates many X-ray projections are taken and the threshold value has to be determined for each of them. To achieve this the threshold needed to be calculated at angular increments within the image stack and these values used to set up an interpolated look up table to be automatically linked into the algorithm. This thresholding process was applied to both sets of projection data, HE and LE, to segregate the radiographically optimised density from the unwanted density, where the unwanted density is outside the effective dynamic range of detectability.

5.4.3 Grey Level Mapping (Scaling)

Before the thresholded regions from the two sets of projection data (HE and LE) could be merged, the grey levels needed to be adjusted to an approximately common scale. The process of taking the original data numbers and changing them to new values is called mapping. A mathematical description of the mapping is called a mapping function (Milanova n.d.). The following is a description of the grey scale mapping function performed on the projection data within the dual energy image processing algorithm. For the purposes of this research, the grey level mapping is referred to as scaling.

An original grey scale image, *f,* was taken from the LE projection stack with $[f_1, f_2]$ being a particular range of grey levels set by the LE threshold value, Th_{LE}, within the image *f*. So $[f_1, f_2] = \{f(i,j) : f(i,j) \leq Th_{LE}\}$, with $f(i,j)$ being the pixel values of the image *f.*

This range of grey values $[f_1, f_2]$ is then mapped onto a new grey scale range $[g_1, g_2]$ by means of a transformation function, Ψ (or mapping function):

$$[g_1, g_2] = \psi[f_1, f_2] \tag{5.6}$$

The grey scale mapping function, Ψ, involves scaling of the new grey level range $[g_1, g_2]$ and takes the form:

$$[g_1, g_2] = \psi[f_1, f_2] = ((Th_{LE} - f(i,j)) \cdot s) + f(i,j) \tag{5.7}$$

This transformation is performed on a pixel by pixel basis. With $0 \leq s \leq 1$ and *s* being the scaling factor used to adjust the grey values of each pixel closer to the chosen threshold value, Th_{LE}, but without exceeding it. The scaling factor, *s*, is based on the amount of

under penetration or saturation within the thresholded region, i.e. the more extreme, the higher the value to increase the scaling.

The result is a new LE grey scale image, *g*, with all grey levels below the LE threshold scaled depending on the input factor, *s*.

The effect which this algorithm has on the projection data can be illustrated by analysing the image histogram after the grey scale mapping function has been applied. Figure 5.9 shows the histogram of the original projection image and Figure 5.10(b) shows the histogram after a threshold of Th_{LE} =10,367 and a scaling factor of *s* = 60% has been applied. The grey level range below the threshold value has been mapped to a higher range of grey levels.

A comparison of Figure 5.10(a) to Figure 5.10(d) highlights the effect the chosen scaling factor, *s,* has within the algorithm. Figure 5.10(c) has the scaling set to *s* = 80% causing all pixels under the threshold grey value (10,367) to be mapped to a higher grey level range than Figure 5.10(b) at *s* = 60%. Further analysis using line profiles (Figure 5.11) also underlines this point.

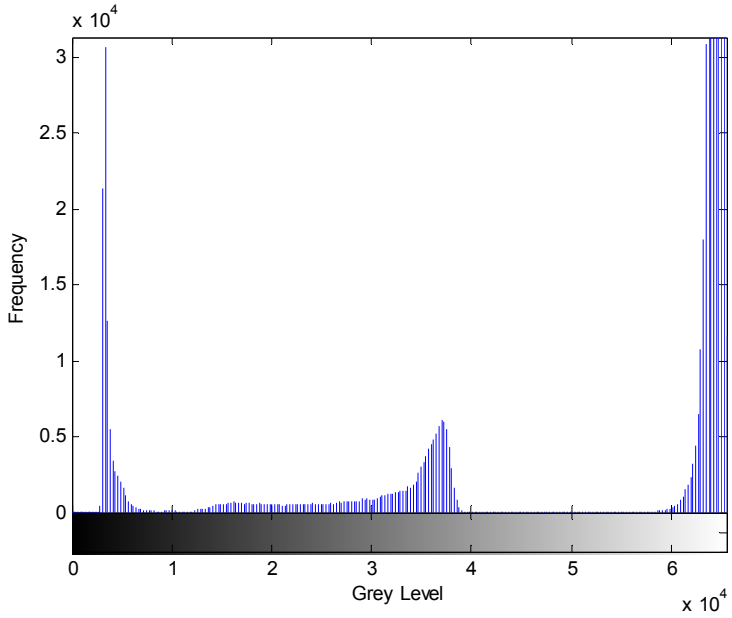

Figure 5.9: Original image histogram, with no thresholding and scaling applied (same as in Figure 5.6)

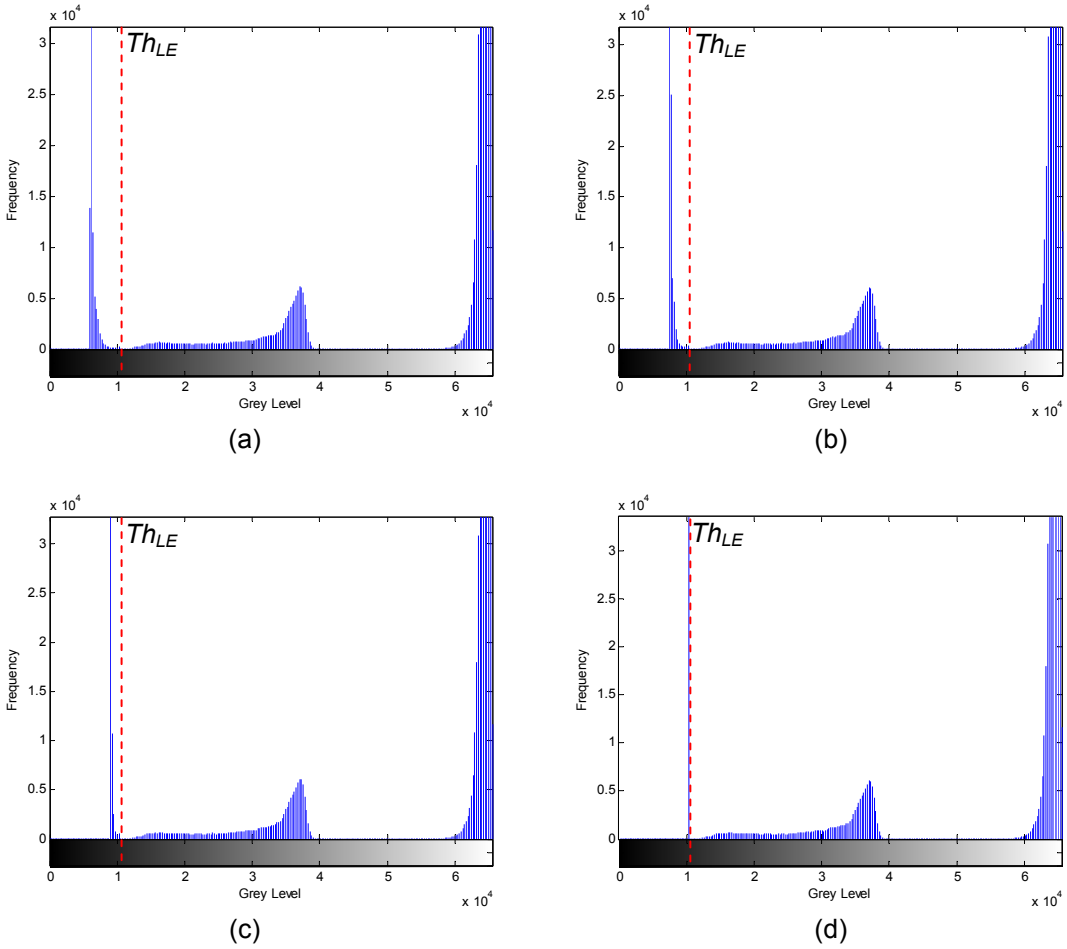

Figure 5.10: Image histogram after thresholding (Th_{LE} = 10,367) and different levels of scaling has been applied, (a) s = 40%, (b) s = 60%, (c) s = 80% and (d) s = 100 %.

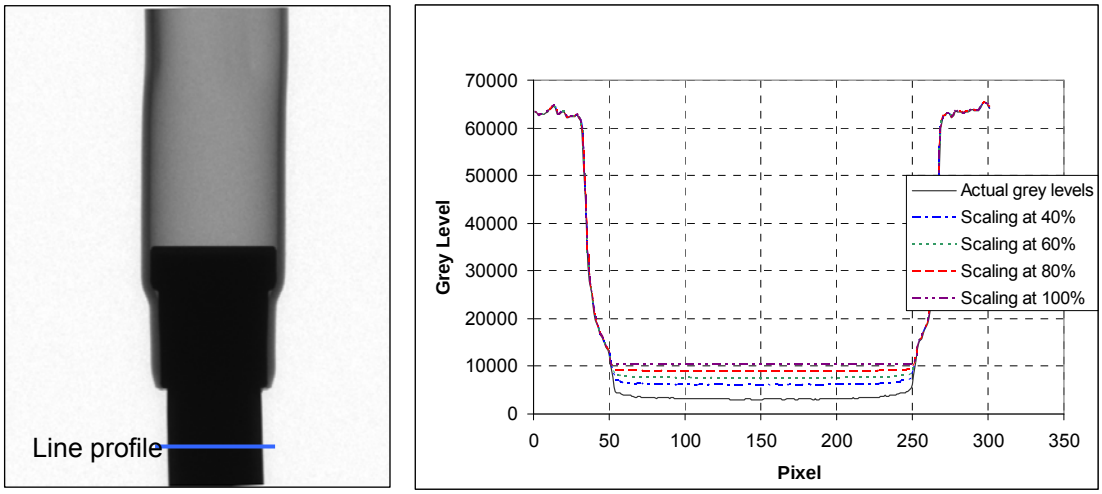

Figure 5.11: An Intensity line profile taken across dense material highlighting affects of scaling % (s).

A similar algorithm applies for the HE projection data except the aim is to scale the grey levels above the HE threshold (Th_{HE}).

In this instance, *h* is an original grey scale image taken from the HE projection stack and $h(i,j)$ is the pixel values for that image. So $[h_1, h_2] = \{h(i,j) : h(i,j) \geq Th_{HE}\}$ with $[h_1, h_2]$ being a particular range of grey levels set by the HE threshold value, Th_{HE}.

As above the grey scale mapping function is applied to give:

$$[m_1, m_2] = \psi[h_1, h_2] = ((Th_{HE} - h(i,j)) \cdot s) + h(i,j) \tag{5.8}$$

The resultant is a new HE grey scale image *m*.

The grey level scaling process aims to modify the extreme threshold regions to a more favourable grey level range while still keeping any detail detected. This means that any good information present within the extreme regions will not be disregarded and will be used to improve the amount of contrast reduction caused to the optimised region when averaged together. The effect this setting has on the raw projection data was observed comparing line profiles and histograms, as shown in Figure 5.10 and Figure 5.11. From this a set of simple guidelines were produced depending on the level of under penetration observed in the high density region. For CT imaging the minimum intensity level required for minimum penetration of the longest path length in the high density material is 10,000 grey levels (Ramsey 2008). Moreover, the black reference intensity level of the detector has been calculated at approx 3,500 grey levels. This black level is obtained when the X-rays are turned off and hence is seen as the point at which no photons are reaching the detector i.e. no penetration of the test object. Based on this information, the range of grey levels between no penetration and sufficient penetration was established which could then be directly linked to the scaling percentage. For example, 10,000 grey levels means sufficient penetration so no scaling is required i.e., *s*=0%, and 3,500 grey levels means no penetration so 100% scaling is required. The scaling setting for the HE data is similar except the intensity range over which the scaling is set is based on the following information: The saturation point for CT imaging is set at 64,000 and over-exposure of the test object is considered to be for intensity readings above 50,000 grey levels (Ramsey 2008). This simple approach for the scaling level was applied for all dual energy reconstructions presented in this chapter.

5.4.4 Merging of the Resultant High Energy and Low Energy Projection Stacks

The next step was to merge the two new projection stacks forming a single optimised stack. This was achieved by averaging each projection image from the new LE stack with the exact angular projection image from the new HE stack.

The new optimised projection image;

$$d_p(i,j) = \frac{\left(g_p(i,j) + m_p(i,j)\right)}{2} \tag{5.9}$$

With *p* being the projection number within the image stack.

The thresholding and scaling of the unwanted extreme regions of the projection data allows averaging to take place with the optimised regions without degrading the final reconstruction. The final step then reads each X-ray projection as a matrix of pixels and averages each pixel from every projection with the correct corresponding pixel from the second projection set.

Averaging was chosen as the method to merge the two projection sets as other methods explored caused artefacts to dominate. Specifically, merging the projection images using an addition method was investigated. In this instance all the pixels in the extreme regions were set to zero (instead of scaled) and the HE and LE projection data were added together so the extreme regions in one projection were replaced with the optimised regions from the other. A resulting projection following the addition procedure is shown in Figure 5.12(a). It is clear that this method of merging the projection data has caused sharp transitions at the edge of the thresholded regions; emphasised by the line profile shown in Figure 5.12(b). As discussed in section 2.2.4.5, this will cause truncation artefacts to dominate the reconstructed CT image. This is illustrated in Figure 5.13. Here, the reconstructed CT image has been produced using the combined projection data resulting from the addition method. The CT image shows that the thresholded edge regions contain significant artefacts that are masking detail within those areas. In contrast, merging the projection data using the scaling and averaging method will inherently not cause sharp transitions at the thresholded edges; removing the risk of these artefacts occurring.

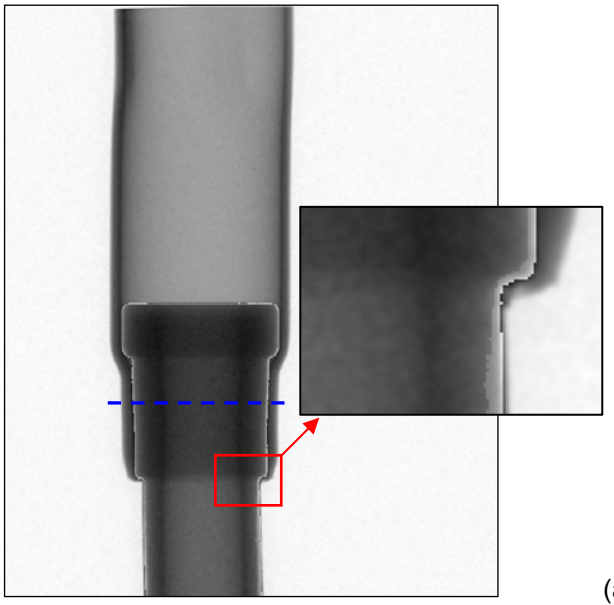

(a)

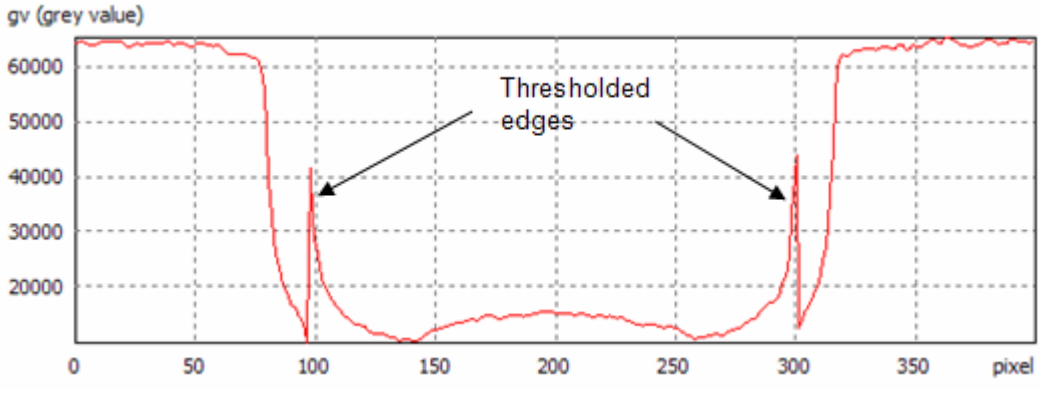

(b)

Figure 5.12: (a) Raw projection image resulting from the addition method of merging the projection data and (b) line profile drawn across the sharp transitions located at the thresholded edges.

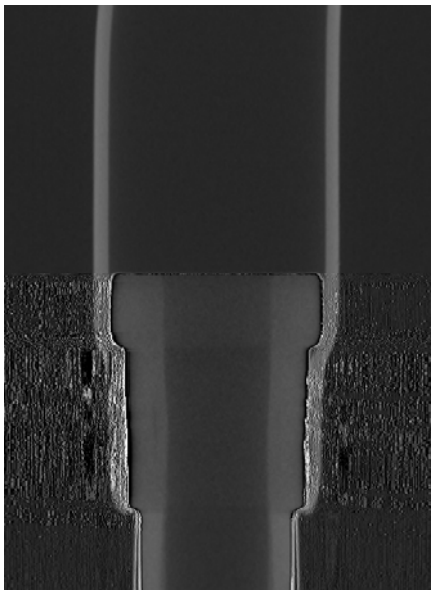

Figure 5.13: A reconstructed CT slice resulting from the addition method of merging the projection data, (see Figure 5.12), scale as in Figure 5.20.

5.5 Dual Energy Technique Validation

Part of the development procedure of any new NDT inspection technique requires a validation process to provide sufficient evidence that the new method does in fact work and give improved performance for the intended purpose. The validation process for this dual energy image processing algorithm consisted of known statistical performance methods being used on a specially made reference phantom to compare the new technique with conventional CT.

Further validation is provided in section 5.6 by comparing real inspection results of two different multi-density components. The first component was a Copper-Aluminium HVAC and the second was the CFRP-Titanium ComeId™ lap joint. The cylindrical shape of the Copper-Aluminium HVAC provided a good starting point for preliminary application of the dual energy algorithm because the threshold value should be easier to determine and it should stay the same for all projection angles. Based on the findings of this investigation the dual energy algorithm could then be tailored to suit the inspection of the more complex ComeId™ joints.

5.5.1 CT Performance Measurement

CT inspection is growing in acceptance as an NDT technique but is still classed as a relatively immature inspection method compared to other techniques. It also suffers from a

lack of standards and guidelines on the subject, as outlined in Chapter 1, section 1.3.2. However, for the validation purposes required in this work, literature was found covering different performance measures (Faulker and Moores 1986; Goodenough and Weaver 1981; Boone and Seibert 1994; Graeff and Engelke 1991; Guan *et al* 1998; Mangard 2000) and American ASTM standards were also found for some system performance parameters such as the MTF (ASTM E1695 2006). The technique developed in this work was specifically aimed at enhanced defect detection and characterisation. Therefore, the chosen test had to be a measure of the detail detectability within the CT image.

To enhance the detail detectability within the final CT image requires the signal difference between the detail and the surrounding base material to increase. Therefore, the correct X-ray spectrum must be chosen (source anode and tube potential) and shaped with filters so that the contrast from a detail within an object increases more than the image noise. Macdonald (2004) states that each individual object material and geometry has its own optimum X-ray tube potential and filter material/thickness. This indicates a dual energy approach would offer the opportunity to improve the detail detectability of multi-density components.

A statistical method exists called the '*detail SNR'* (Graeff and Engelke 1991; Mangard 2000). This calculation provides a measure of the detail detectability within a CT image by calculating the SNR of both the detail within an object and the surrounding base material. The full derivation of the detail SNR can be found in section 2.1.6.2 along with the actual equation used (Equation 2.27).

The MTF was also included in this validation process to compare the edge sharpness and resolution resulting from the dual energy technique. This will measure if any spatial degradation was caused by the averaging used to merge the projection stacks in the algorithm. The MTF is described in full in section 2.1.6.3.

5.5.2 Reference Phantom Fabrication

The reference phantom was made of two different materials, Copper (density ρ=8.96 g/cm^3) and Aluminium (density ρ=2.7 gm/cm^3). Both materials had exactly the same dimensions to ensure X-ray path lengths were kept consistent and an accurate comparison in performance results could be deduced. The performance measure chosen for this study required some kind of 'detail' within the component to be used as an Image Quality Indicator (IQI). Therefore a 2mm hole was drilled at the centre of both the Copper

and Aluminium rod to provide the 'detail' necessary, see Figure 5.14. It should be noted that the Copper and Aluminium ray paths do not overlap using this phantom. The performance of the dual energy technique under these circumstances is tested in section 5.6.

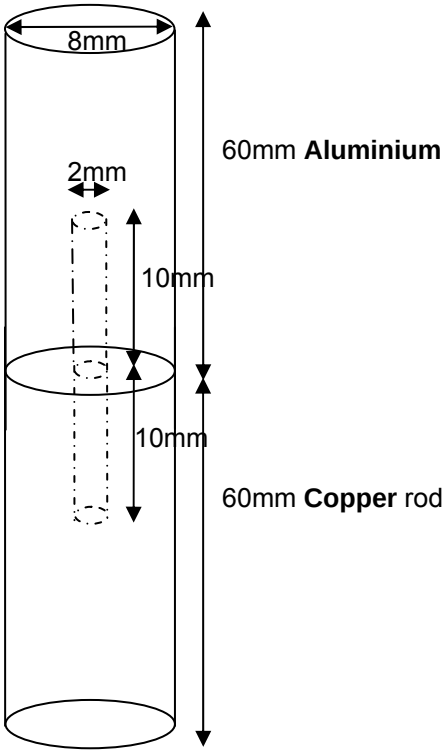

Figure 5.14: Schematic of fabricated reference phantom.

5.5.3 Method

Five conventional CT scans were acquired for the reference phantom at different energy settings and filters. The settings used ensured the minimum requirement of full penetration (≥ 10,000 grey levels) of the more dense material Copper but without saturating the detector. Table 5.1 shows the settings used for all conventional CT scans plus the HE and LE scan for the dual energy approach.

Table 5.1: CT scan settings used for the reference phantom

Scan Type	Inspection Settings					Dual Energy Algorithm	
	Anode	Energy	Filter	Scan ROI (voxels)	Voxel size	Threshold	Scaling %
LE	Silver	70kV 100µA	4mm Al	695x721x738	16µm	14190	80%
HE	Tungsten	195kV 105µA	5mm Cu	695x721x738	16µm	-	-
Conventional 1	Tungsten	120kV 120µA	2mm Cu	695x721x738	16µm	n/a	n/a
Conventional 2	Tungsten	135kV 125µA	3mm Cu	695x721x738	16µm	n/a	n/a
Conventional 3	Tungsten	150kV 175µA	4mm Cu	695x721x738	16µm	n/a	n/a
Conventional 4	Tungsten	165kV 135µA	5mm Cu	695x721x738	16µm	n/a	n/a
Conventional 5	Tungsten	180kV 105µA	5mm Cu	695x721x738	16µm	n/a	n/a

Conventional scan 1 and conventional scan 2 were acquired using a low filter level but still ensuring the signal intensity was kept within the effective dynamic range of the detector. A higher tube potential with increased filtration is regularly used in radiographic imaging to increase the penetration of the test object without saturating the detector. This same premise was applied to increase the penetration of the high density copper without saturating the low density aluminium. The aim was to find the point where an optimal trade-off is achieved between the image quality of the copper and the aluminium. This approach was applied to conventional scans 3, 4 and 5.

A LE and HE scan were then acquired and threshold values calculated before the resultant projection stacks were input into the dual energy algorithm. Example projection images taken from both the LE and HE stack are shown in Figure 5.15. The LE scan resulted in optimum exposure for the low density Aluminium and complete under penetration of the dense Copper part. Similarly the HE scan resulted in optimum exposure of the Copper part with overexposure of the Aluminium.

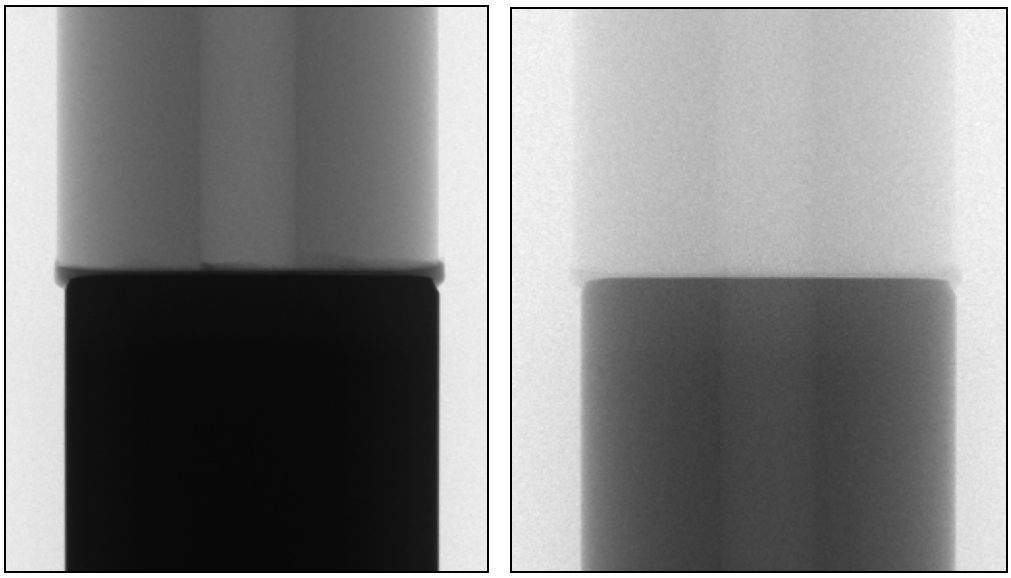

Figure 5.15: X-ray projections taken from the LE scan (left) and from the HE scan (right). See Table 5.1 for the HE and LE acquisition settings.

The threshold values were calculated at 18 degree increments (i.e. 50 projection intervals) using the iterative method described in section 5.4.2.1. This was to observe if the threshold changed during the object rotation. As the reference phantom was cylindrical in shape, the difference in threshold values with rotation was negligible. This resulted in a singular global threshold value (Th_{LE}=14190) to be input into the dual energy algorithm. The scaling percentage applied to the under penetrated region of the LE projection data was 80%. This was based on a minimum intensity reading of 4855 grey levels within the dense copper part (see section 5.4.3 for full details on the scaling setting). In this instance, the scaling was not applied to the HE projection data as it was apparent the over-exposed aluminium region of the image still had considerable information present. This meant that averaging could take place with the optimised LE projections with little reduction in image quality.

The source energy setting and filter was the only parameter that changed between the conventional and dual energy CT scans. All other parameters remained constant to enable an accurate performance comparison. The settings used for all scans are presented in Table 5.1.

The detail SNR results for both the Copper and Aluminium were compared between the dual energy technique and five conventional reconstructions. The detail SNR results were taken using the exact same region of interest and at the exact same cross sectional point

within the reference phantom. To ensure an accurate comparison the detail SNR measurements were taken over ten slices at each point within the Copper and Aluminium.

A comparison between the MTF of the dual energy technique and the conventional method was also performed using the edge method described in section 2.1.6.3. The exact same edge region and cross sectional slice from both CT reconstructions was used for the comparison.

5.5.4 Results and Discussion

5.5.4.1 Detail Signal-to-Noise-Ratio

Figure 5.16 and Figure 5.17 are examples of cross sectional slices taken from the reference phantom so that performance measurements could be applied. The line profiles were drawn across the object detail (i.e. the hole) used for the detail SNR measurements. These line profiles also allowed deviations in pixel values to be easily identified. Figure 5.16(a) and (b) resulted from the dual energy technique and Figure 5.17(a) and (b) resulted from conventional scan 3 (see Table 5.1). To illustrate the noise and artefacts present within the CT images below (Figure 5.16 and Figure 5.17) required a post processing step to improve the visualisation of the object grey levels. This is common practice for interpreting CT images and in no way does it affect the measured attenuation coefficients displayed in the line profiles or the data used in the performance measurements.

Dual Energy Technique

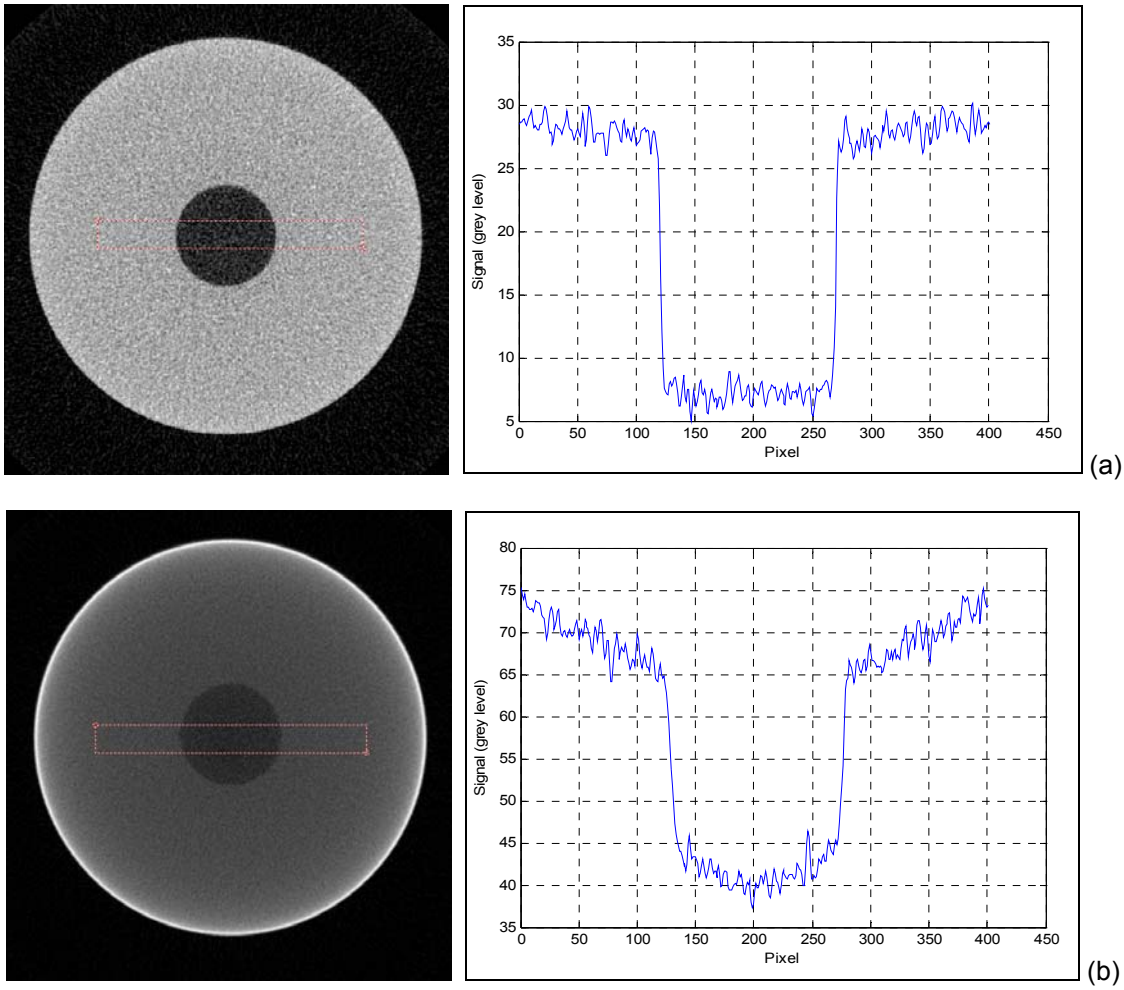

Figure 5.16: CT cross sectional slices of the reference phantom using the dual energy algorithm, with a line profile drawn across the region used for the 'detail SNR' measurement (a) CT cross sectional slice from the Aluminium section and (b) CT cross sectional slice from the Copper section.

Conventional Scan 3

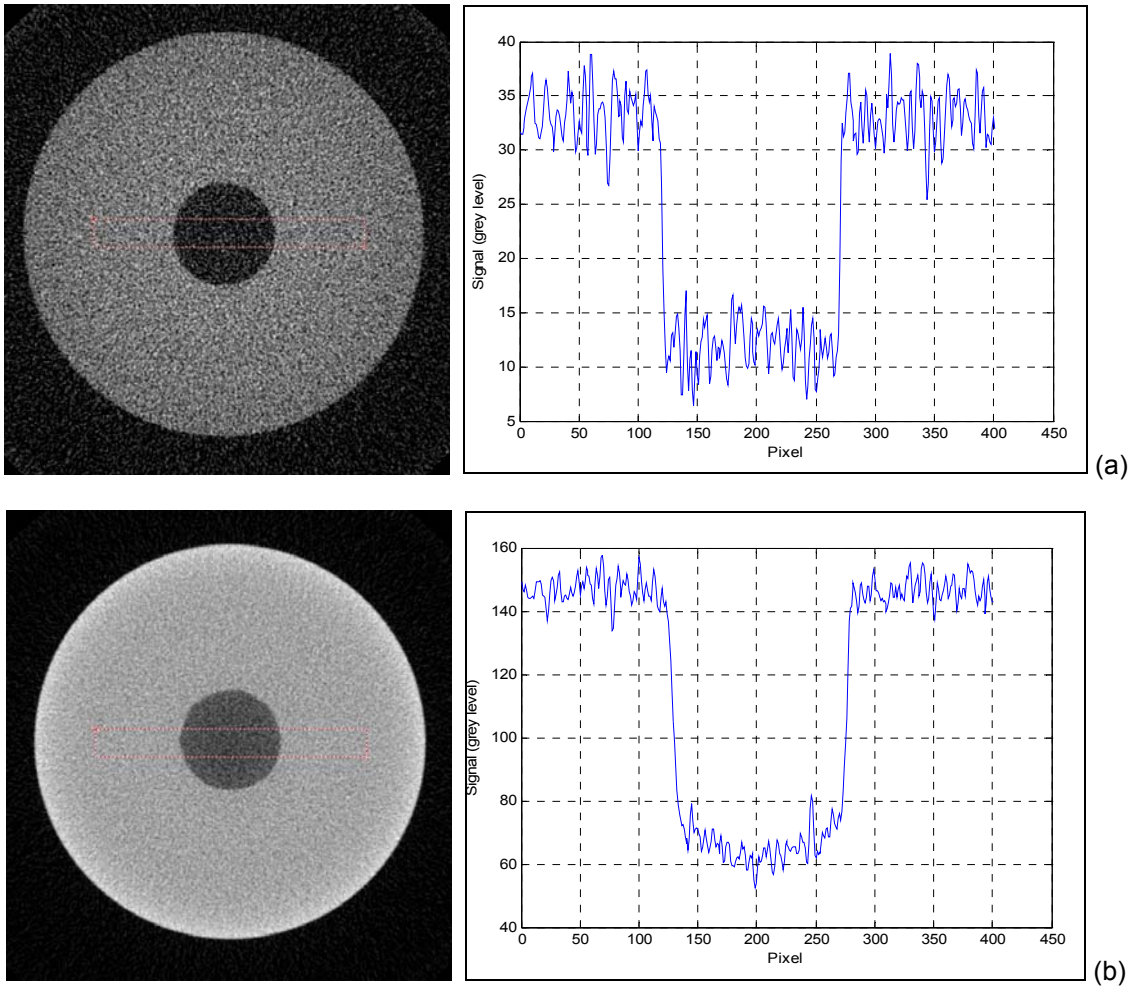

Figure 5.17: CT cross sectional slices of the reference phantom using the conventional scan 3 (see Table 5.1), with a line profile drawn across the region used for the 'detail SNR' measurement (a) CT cross sectional slice from the Aluminium section and (b) CT cross sectional slice from the Copper section.

The dual energy method resulted in a detail SNR of 4.6 for the low density Aluminium and 4.0 for the high density Copper. The detail SNR results for the conventional scans differed significantly between each scan. Based on the findings it was apparent that conventional scan 1 provided the best compromise in terms of image quality obtained for both the copper and the aluminium. Comparing the SNR results for conventional scan 1 with the results for the dual energy method, it was observed that the dual energy method increased the detail SNR by 32% for the low density aluminium and improved the detail SNR by 5% for the copper section. In fact, when compared to all the results for the conventional scans, the dual energy method increased the detail SNR for the aluminium, by a minimum of 32%.

These results were as expected and can be explained as follows: With conventional CT scanning a very important parameter is the full penetration of all parts of the component. This means that when imaging a multi-density component with a single energy CT system it will always be the low density that suffers and results in reduced image quality. The dual energy algorithm addresses this balance by ensuring full penetration of the high density material without the degradation normally caused to the image of the low density material. This is clearly visible when comparing the difference between the low density line profiles for the Aluminium, as shown in Figure 5.16 and Figure 5.17. The dual energy technique has resulted in reduced image noise and improved contrast detail.

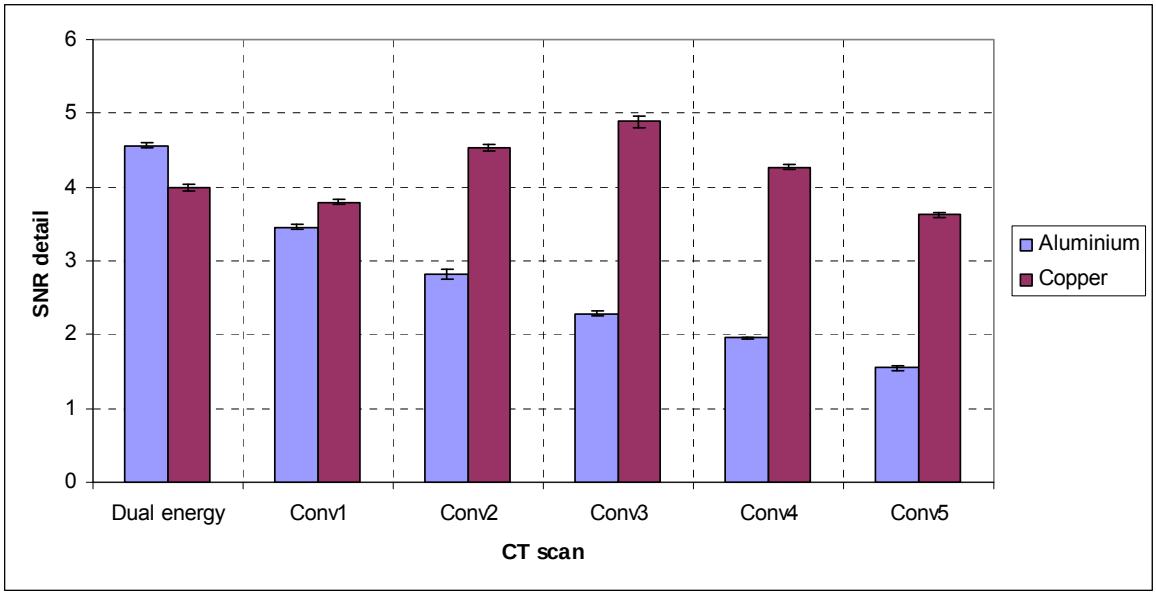

Figure 5.18: Plot of the SNR detail results using the reference phantom. The results from all five of the conventional scans and the dual energy method are displayed. The settings used for these CT scans are shown in Table 5.1.

These performance measurements did highlight that the dual energy method is causing a beam hardening type artefact within the reconstruction (see section 2.2.4.5). This artefact is shown in Figure 5.16(b) as a false density gradient mapped across the material. Here, the edges of the Copper appear denser than the centre. The likely reason for this artefact can be attributed to the edge intensity of the under-penetrated region in LE projection data. If part of this edge remains and is not thresholded with the rest of the under-penetrated region it will strongly influence the intensity at the edge of the combined projection data. Consequently, this will induce a false density gradient across the high density region which will be reflected within the reconstruction. However, currently, this is

an acceptable drawback as the purpose of the dual energy technique was enhanced defect detection and not extrapolating quantitative density measurements from the attenuation coefficients.

5.5.4.2 Modulation Transfer Function

The purpose of the MTF comparison was to deduce whether any spatial degradation was caused when the resultant HE and LE projection stacks are averaged together in the dual energy algorithm.

The MTF measurement displayed in Figure 5.19 produced similar results for both the dual energy technique and the conventional method. The quantitative value of the measured MTF at 10% modulation infers a measure of the spatial resolution (ASTM E1695-2006). This value was compared for both methods giving ~17 line pairs/mm (lp/mm) for the dual energy technique and a value of ~15 lp/mm for the conventional method. Converting this measurement into an interpretable value in microns gave a spatial resolution of ~29µm for the dual energy technique and ~33µm for the conventional method. Therefore the difference in spatial resolution measurements is negligible (~4µm) and it can be concluded that no significant spatial degradation is caused from the averaging used in the dual energy algorithm.

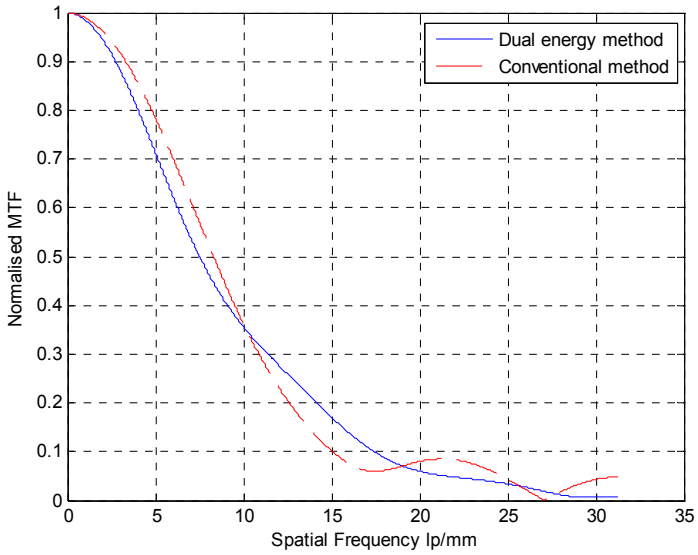

Figure 5.19: MTF as a function of spatial frequency calculated from reconstructed CT slices obtained using the dual energy and conventional method.

5.6 Dual Energy Technique Application

5.6.1 Copper- Aluminium Magnetic Pulse Welded HVAC Component

The manufacturers of the magnetically pulse welded Heating Ventilation and Air-Conditioning (HVAC) units were interested in identifying an NDT technique capable of inspecting the integrity of the weld. The component inspected had approximate dimensions of 85mm length and a diameter between 10-15mm, see Figure 5.20.

A magnetic pulse weld is created by using a high energy current that is discharged through a coil surrounding the component. This high and rapidly changing current creates magnetic forces between the coil and the work piece that accelerate the outer work piece towards the inner one thereby generating a solid state weld. This electromagnetic pulse welding process is executed at very high speed and takes just milliseconds (Kallee and Amos 2008). One benefit of magnetic pulse welding is the ability to rapidly join dissimilar metals to each other. This particular weld was joining Copper and Aluminium.

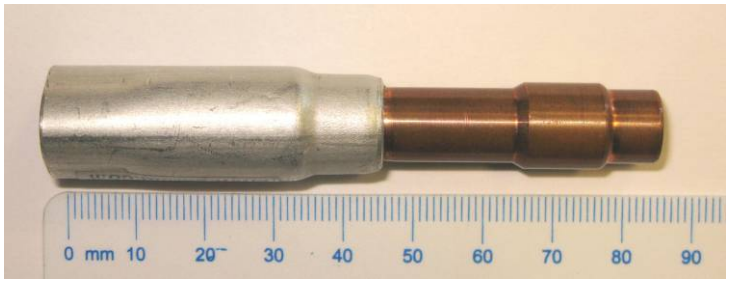

Figure 5.20: Photograph of the magnetic pulse weld component, mm scale shown.

5.6.1.1 Method

Two conventional CT scans were acquired. The energy settings used for the first scan were intended to be a compromise between the thin wall Aluminium and thicker Copper (see Table 5.2 for details). Full penetration was ensured by placing a lead marker[2] on the back of the Copper section, but the condition ≥10,000 grey levels was not satisfied as this caused over exposure of the Aluminium. The second conventional scan was acquired at

[2] The placement of a lead marker on the back of the test object is used in conventional radiography to ensure the test object is sufficiently penetrated by the incident photons. If the test object is not fully penetrated then the lead marker will not be detected within the radiographic image.

an energy (see Table 5.2 for details) setting that ensured the minimum penetration condition of ≥10,000 grey levels was satisfied.

The LE and HE scan were then acquired and threshold values calculated before the resultant projection stacks were input into the dual energy algorithm. The LE energy scan resulted in optimum exposure for the low density Aluminium and complete under penetration of the dense Copper part. Similarly, the HE scan resulted in optimum exposure of the Copper part with overexposure of the Aluminium (Figure 5.21).

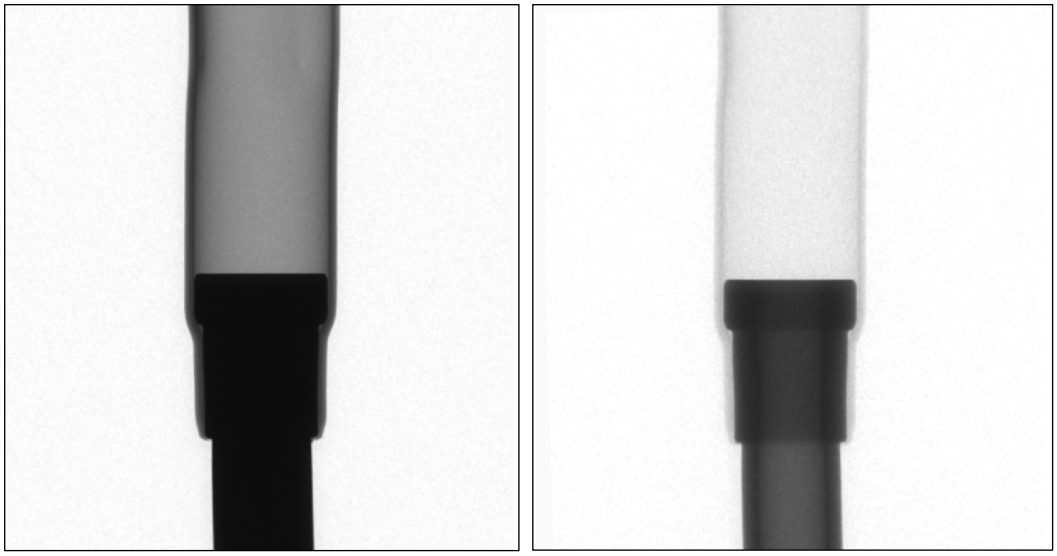

Figure 5.21: X-ray projections taken from the LE scan (left) and from the HE scan (right), scale as in Figure 5.20.

The threshold values for the LE projection data were calculated at 18 degree increments (i.e. 50 projection intervals) using the iterative method described in section 5.4.2.1. This was to observe if the threshold changed during the object rotation, as described for the tests on the phantom in section 5.5.3. The HVAC was cylindrical in shape so the difference in threshold values was again negligible. This allowed a singular global threshold value to be input into the dual energy algorithm. The scaling percentage used for each projection set was based on the approach described in section 5.4.3. The X-ray energy settings and algorithm settings are given in Table 5.2 below.

Table 5.2: CT scan settings used for the HVAC unit inspection

Scan Type	Inspection Settings					Dual Energy Algorithm	
	Anode	Energy	Filter	Scan ROI (voxels)	Voxel size	Threshold	Scaling %
Conventional Scan 1	Tungsten	102kV 65 µA	1mm Cu	554x571x652	57µm	n/a	n/a
Conventional Scan 2	Tungsten	135kV 95µA	2mm Cu	554x571x652	57µm	n/a	n/a
LE	Silver	45kV 200µA	1mm Al	554x571x652	57µm	10,367	80%
HE	Tungsten	155kV 107µA	3mm Cu	554x571x652	57µm	50,000	40%-

5.6.1.2 Results and Discussion

An example of the resulting X-ray projection data following the application of the dual energy algorithm is shown in Figure 5.22. It is evident that the optimised dual energy X-ray projection has provided sufficient penetration of the dense copper part (≥10,000 grey levels as shown in the line profile) and excellent contrast in the less dense aluminium.

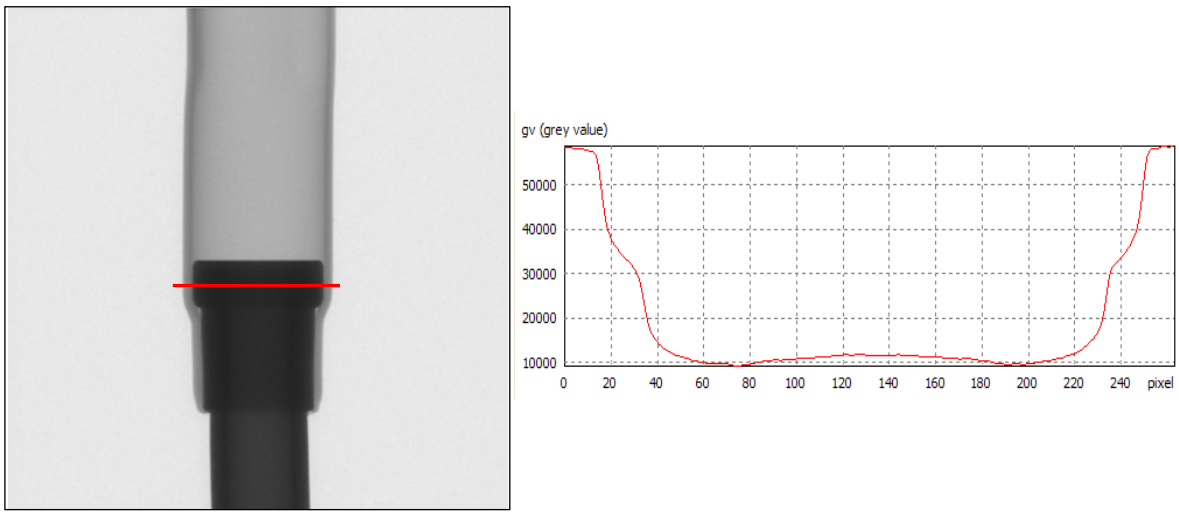

Figure 6.22: X-ray projection taken from the optimised dual energy image stack (left) and an intensity line profile extracted across the dense copper to illustrate that sufficient penetration has been achieved (≥10,000 grey levels) (right), scale as in Figure 5.20.

Figure 5.23 and Figure 5.24 compare the resultant CT images obtained from the reconstruction of the dual energy projection with the two conventional scans (details in Table 5.2).

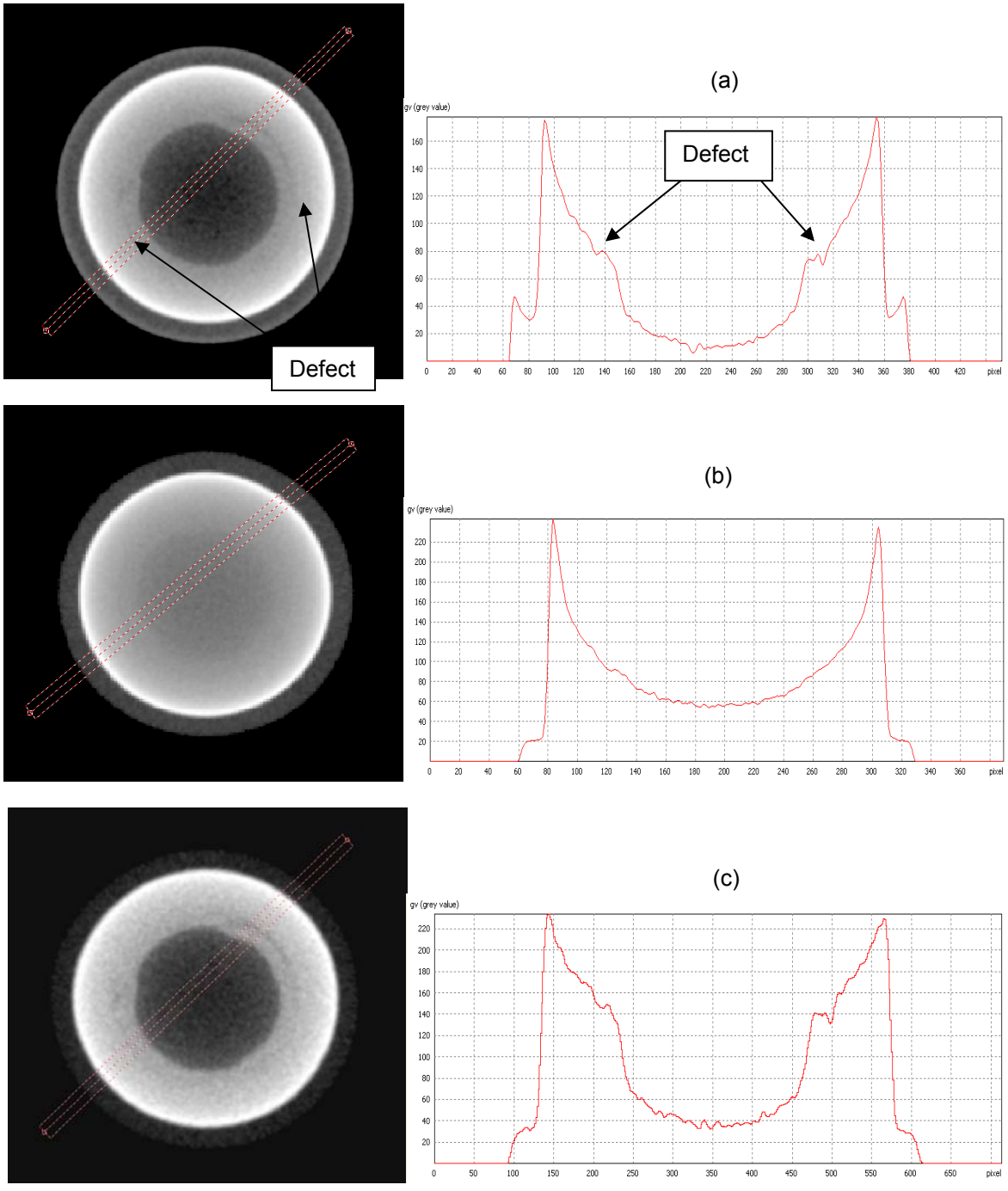

Figure 5.23: Axial 2D cross-sections taken through the defect, which include intensity line profiles. (a) Dual energy CT slice (b) CT slice taken from conventional scan 1 (see Table 5.2) with Copper slightly under penetrated and (c) CT slice taken from conventional scan 2 with Copper penetrated (scale as in Figure 5.20).

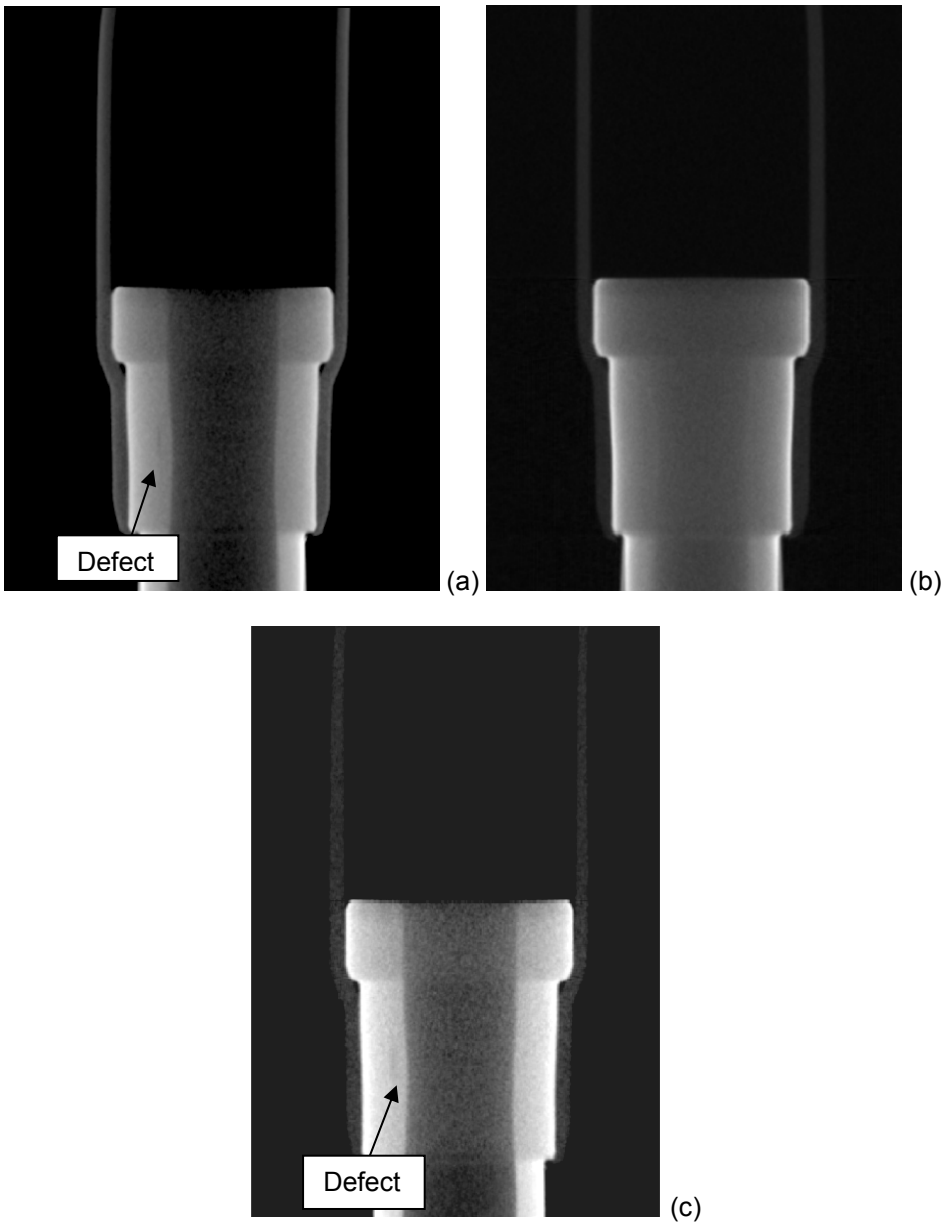

Figure 5.24: Frontal 2D cross section taken through the defect. (a) Dual energy CT slice (b) CT slice taken from conventional scan 1 (see Table 5.2) with Copper slightly under penetrated and (c) CT slice taken from conventional scan 2 (see Table 5.2) with Copper penetrated (scale as in Figure 5.20).

The HVAC results highlight the difficulty in finding energy settings that compromise for objects containing largely varying densities. This is partly due to the CT reconstruction process requiring a large level of penetration (minimum 10,000 grey levels through the longest path) and the limited effective dynamic range of commercially available detectors. It is clear from Figure 5.23(b) and Figure 5.24(b) that trying to compensate the energy settings for the low density does not work. In this reconstruction it has resulted in slight under-penetration and a defect possibly going undetected. The second conventional CT

scan that ensured sufficient penetration of the high density Copper has resulted in the low density Aluminium being over exposed and the image noisy (Figure 5.23(c) and Figure 5.24(c)). This increased image noise within the Aluminium affects the detail detectability reducing the probability of detecting small defects. It should also be noted that although there appears to be no artefacts within the Aluminium regions for the under-penetrated CT scan this could be misleading. The simple cylindrical shape of the HVAC component combined with the circular scanning geometry of the CT acquisition could cause any shading artefacts present to be radial. Therefore resulting in the pixel values within the outer Aluminium to be raised, masking any potential defects, without any obvious streaking.

CT was chosen as the most suitable NDT technique for this inspection due to its ability to detect and visualise volumetric defects. As with most NDT techniques, conventional CT does have limitations that have been identified in these results and discussed. The experimental dual energy method aimed at reducing these limitations by optimising the energy settings has produced impressive results (Figure 5.23(a) and Figure 5.24(a)). Both the Copper and Aluminium had good detail present with reduced noise due to the averaging process. However, the algorithm still caused the beam hardening type artefact, which altered the density gradient across a material. This was highlighted in both the axial and frontal 2D cross sections (Figure 5.23 and Figure 5.24) shown as an increase in grey level intensity towards the edge of the wall diameter. This type of artefact presents the biggest problem when the purpose of the CT inspection is to provide accurate density measurements of a material. However, the HVAC unit inspection presented in this section and the majority of CT inspections performed at TWI are focused on defect detection and characterisation which the beam hardening type artefact will only effect in extreme cases.

As mentioned previously, the HE and LE scans cannot be reconstructed separately to produce a CT image optimised to the low density and a CT image optimised to the high density. In fact even if this was an option, developing a technique that could combine them into a singular reconstructed volume would still be beneficial from a visualisation and interpretation point of view. The problem lies with the LE scan, as under-penetrated parts of the object will cause artefacts to dominate the final reconstructed image. These artefacts are displayed as streaks and areas of inflated pixel values that propagate off the high density regions into the rest of the CT image (see section 2.2.4.5).

5.6.2 Carbon Fibre Reinforced Plastic - Titanium Comeld™ Joint

Following the development and validation of the dual energy algorithm using simple cylindrical multi-density components, the algorithm was then applied and optimised to a CFRP-Ti Comeld™ joint. The Comeld ™ fabrication method and the difficulties with inspecting such a complex component have been discussed in detail within this chapter both from a CT point of view and generally in terms of NDT. The double step lap joint used in this investigation was fabricated using the procedure outlined earlier in section 5.3.1, with approximate dimensions of 23mm x 195mm x 7mm (as shown in Figure 5.1).

5.6.2.1 Method

Based on the findings from the magnetic pulse weld inspection, the conventional CT scan was set up to satisfy the minimum penetration intensity of 10,000 grey levels for the longest path length. As in the previous application, the LE and HE scan was then acquired and the resultant projection stacks were input into the experimental dual energy algorithm.

The threshold values for the LE stack were calculated at 18 degree increments (i.e. 50 projection intervals) using the iterative method described in section 5.4.2.1. The resultant threshold values were plotted as a function of the projection number, as shown in Figure 5.25. A polynomial was fitted to the resultant data and inputted to the dual energy algorithm. By fitting a polynomial to the data the threshold value is variable depending on the rotation angle (i.e. projection number), resulting in a more accurate segregation.

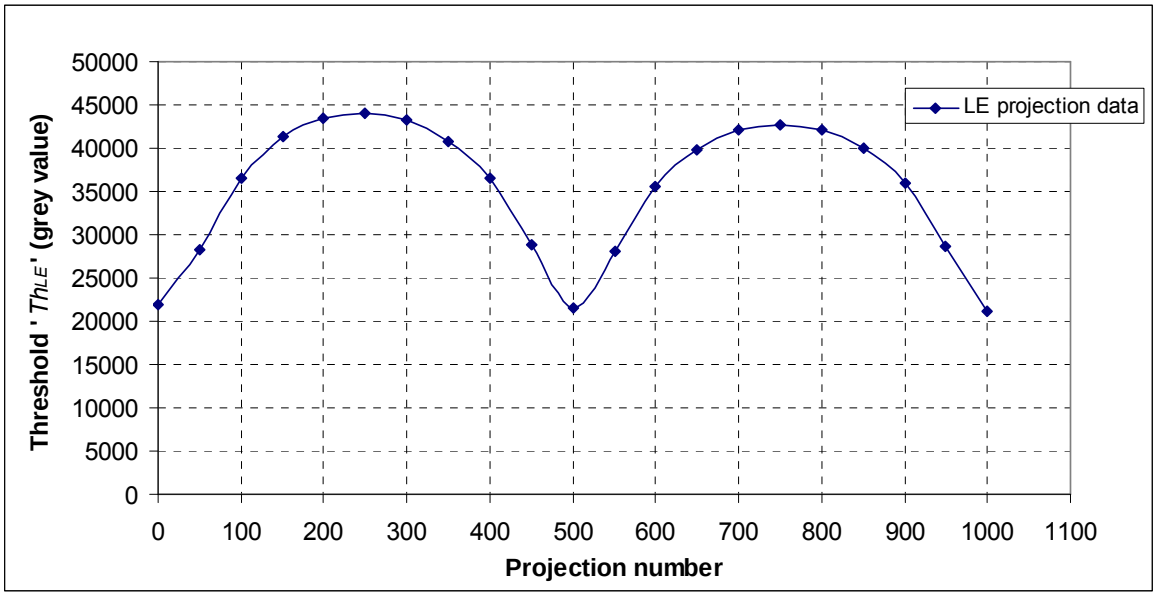

Figure 5.25: Plot of threshold value, Th_{LE}, as a function of the projection number within the LE image stack (see Table 5.3 for details).

The equation of threshold input for the ComeId™ LE projection stack (Th_{LE}) had to be split into two separate polynomials due to the aspect ratio of the component;

$$Th_{LE} \begin{cases} -0.3712p^2+185.64p+21207 & \text{for } p \leq 500 \\ -0.3516p^2+527.74p-15494 & \text{for } p \geq 501 \end{cases} \quad (5.10)$$

Where p is the projection number of the image within the stack. A 2nd order polynomial resulted in the most accurate fitting when compared with 3rd, 4th and 5th order fittings. The aspect ratio of the ComeId™ joint is illustrated in Figure 5.26 displaying the X-ray projection image at 0º and at 90º.

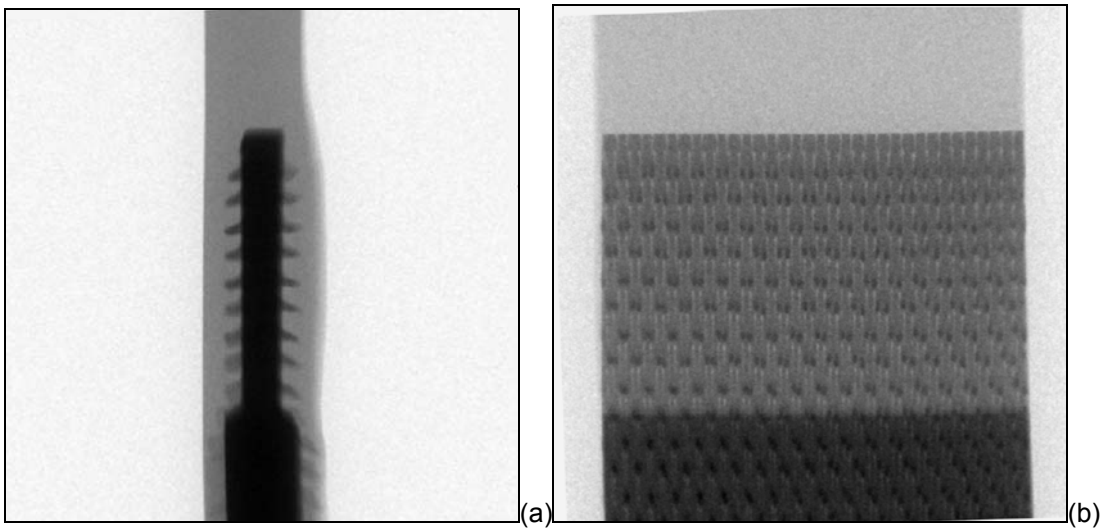

Figure 5.26: (a) Raw projection image (HE scan) of the ComeId™ joint taken at 0º and (b) raw projection image (HE scan) of the ComeId™ joint taken at 90º degrees. Scale as in Figure 5.1.

The X-ray energy and algorithm settings for all the CT scans are given in Table 5.3 below.

Table 5.3: CT scan settings used for the Comeld ™ joint inspection

Scan Type	Inspection Settings					Dual Energy Algorithm	
	Anode	Energy	Filter	Scan ROI (voxels)	Voxel size	Threshold	Scaling %
Conventional	Tungsten	160kV 120µA	4mm Cu	286x828x805	28µm	n/a	n/a
LE	Silver	104kV 120µA	1mm Cu	286x828x805	28µm	Eq.5.10	70%
HE	Tungsten	179kV 130µA	5mm Cu	286x828x805	28µm	-	-

No thresholding/scaling was performed on the low density regions in the HE stack as the scan did not result in saturation of these regions. This meant that enough detail was present in the image to allow averaging with the optimised LE stack with little reduction in quality. In this instance, the resultant image of the low density regions can be viewed as a direct comparison to the improved images produced using the multi loading film technique (or multiple composite viewing) described in section 5.1.

5.6.2.2 Results and Discussion

Projection Images

The ability of the dual energy algorithm to combine the optimised densities from the LE and HE scan was determined using intensity line profile comparison (Figure 5.29 and Figure 5.30). Line profiles were drawn across detail detected within both an optimised high density region from a HE projection and an optimised low density region from a LE projection (Figure 5.27). These line profiles were then compared with profiles taken over the exact same regions within the dual energy projection data (Figure 5.28).

The line profile A was taken across the ply detail within the lay-up of the low density CFRP. The detail detected within this region was compared between the LE projection image and the dual energy projection image (Figure 5.29). The line profile B was taken across the high density Titanium highlighting the internal detail created by the Surfi-sculpt ™ treatment process. The detail detected in this region was compared between the HE projection image and the dual energy projection image (Figure 5.30).

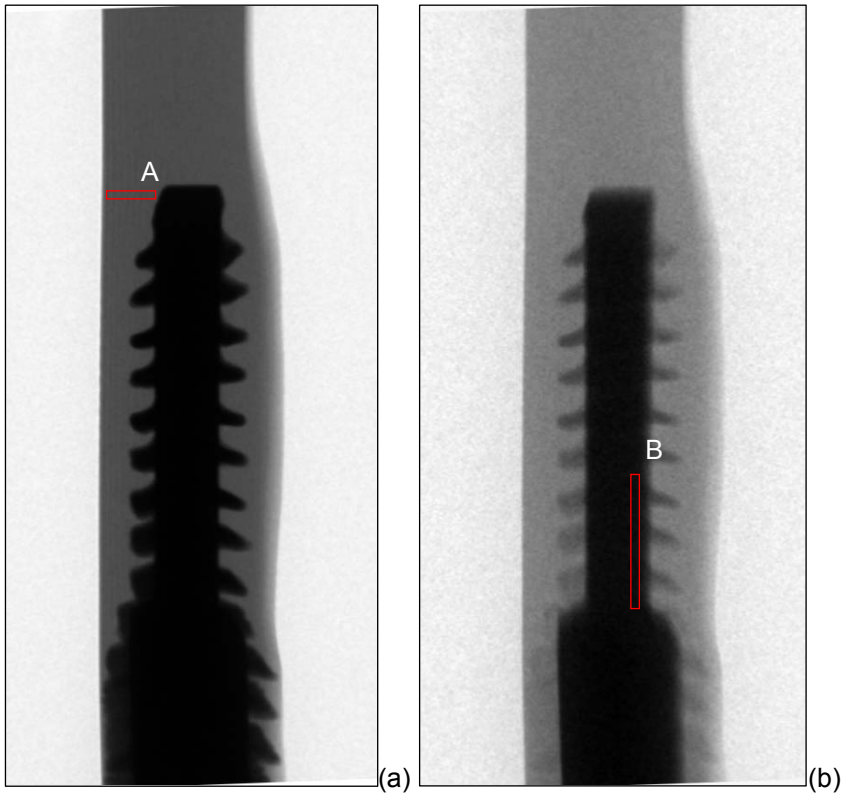

Figure 5.27: Raw X-ray projection images taken of the Comeld^{TM} joint (scale as in Figure 5.1). (a) Projection image taken from LE scan with line profile (*A*) in optimised low density region and (b) projection image taken from the HE scan with line profile (*B*) in the optimised high density region

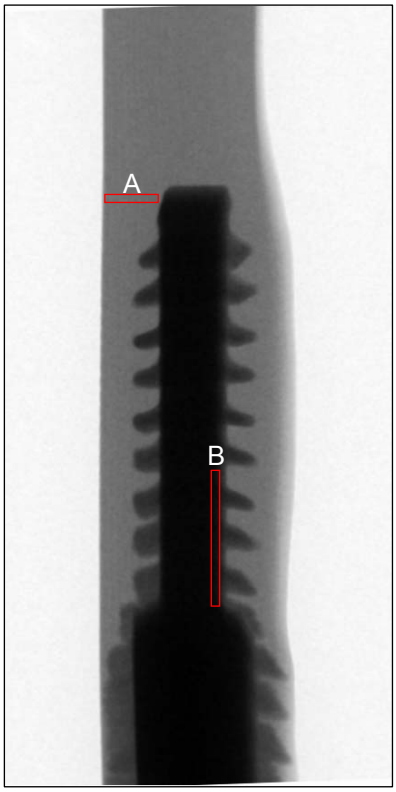

Figure 5.28: X-ray projection image resulting from the application of the dual energy processing algorithm (scale as in Figure 5.1). Both of the line profiles A and B are represented in the image.

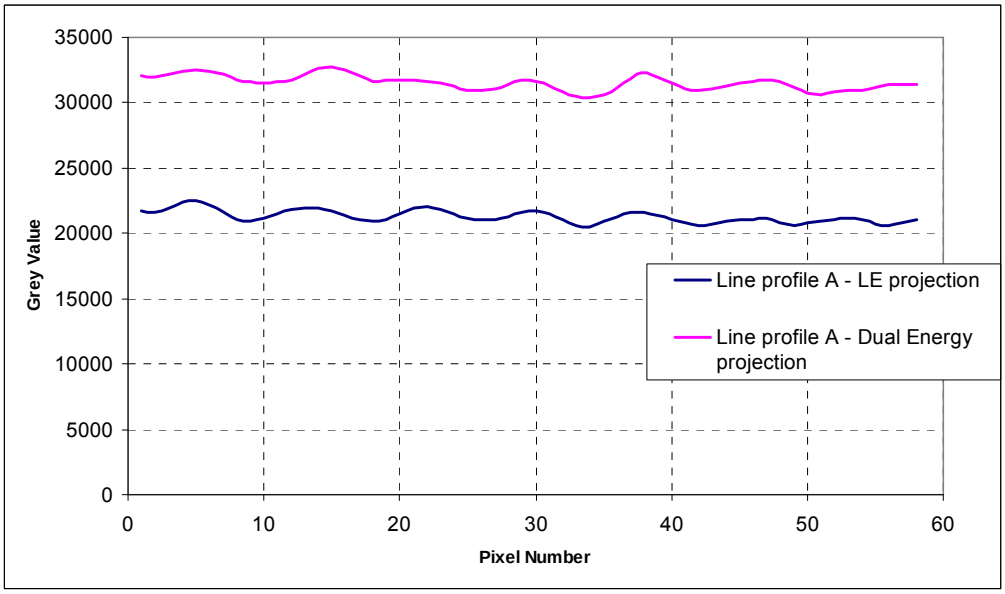

Figure 5.29: Line profile *A* comparison for a low density region in the LE projection image and the dual energy projection image.

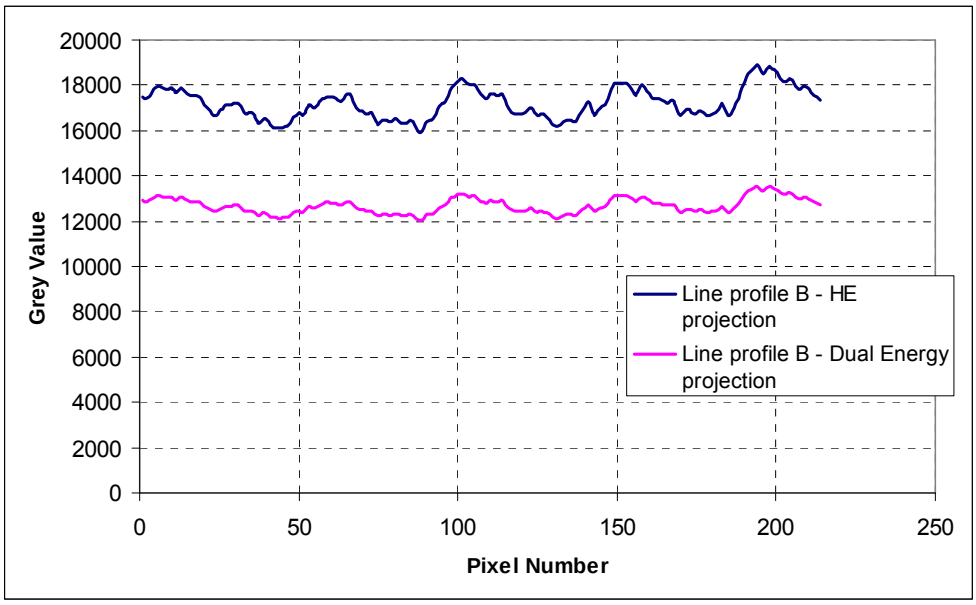

Figure 5.30: Line profile *B* comparison for a high density region in the HE projection image and the dual energy projection image.

The fibres within the CFRP region of the joint provided a measure of the low density contrast within the projection data. Therefore, this was an ideal detail on which to determine the ability of the dual energy algorithm to retain the optimised low density region from the LE projection. The comparison of line profile A in Figure 5.29 showed that the fibre detail within the CFRP was present in both the LE projection image and the dual energy. This was illustrated by similar line profiles showing the small oscillations caused by the density difference found between the carbon fibre plies and the surrounding epoxy matrix. The two profiles did contain some variation, including increased pixel values for the dual energy projection image. But this was expected and is caused by the scaling and averaging process within the algorithm.

Intensity line profile B was taken over the internal detail within the Titanium, providing a useful measure of the high density contrast within both the HE projection data and the dual energy projection data. The comparison showed very good similarity between both profiles meaning the detail detected within the optimised high density region of the HE scan had been successfully preserved by the algorithm (Figure 5.30). Again, small differences are visible and the detail is degraded slightly but this is due to merging the optimised regions with the extreme regions. Steps were taken to reduce this affect within the algorithm, such as the thresholding and scaling, but some deterioration is unavoidable.

CT Images

The reconstructed CT images shown in Figure 5.31 to Figure 5.35 detected numerous small defects that were used to compare the detail detectability between conventional CT scanning and the experimental dual energy technique outlined in this chapter. Included in this comparison is the reconstruction of the LE projection data. This set of CT images are to illustrate the statements made earlier, that it is not possible to optimise the CT inspection for different densities by simply reconstructing separate scans taken at different energies.

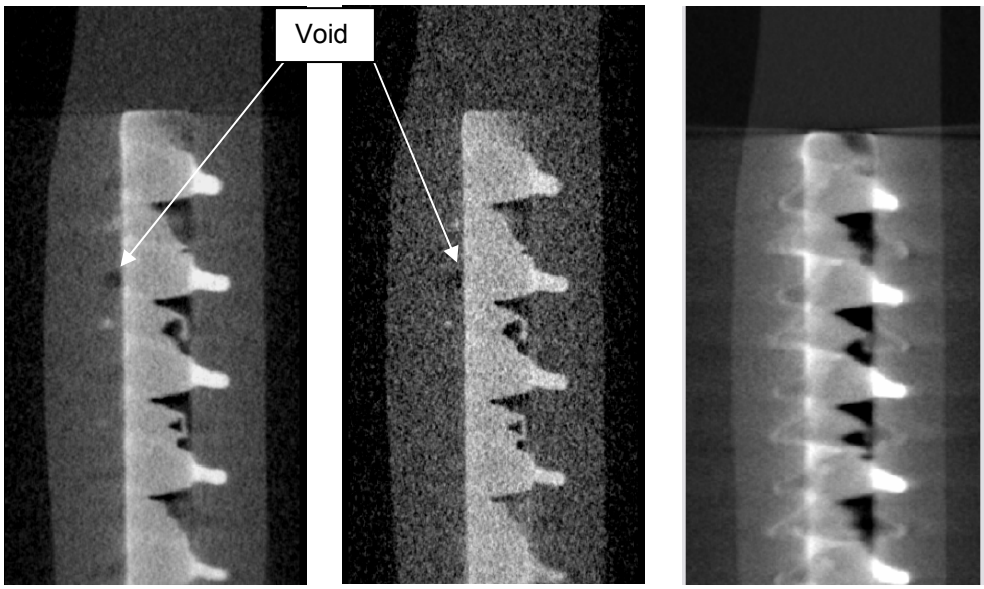

Figure 5.31: Sagittal cross sectional CT slices through the Comeld^{TM} joint (a) Dual energy CT slice (b) conventional CT slice and (c) LE scan CT slice, scale as in Figure 5.1.

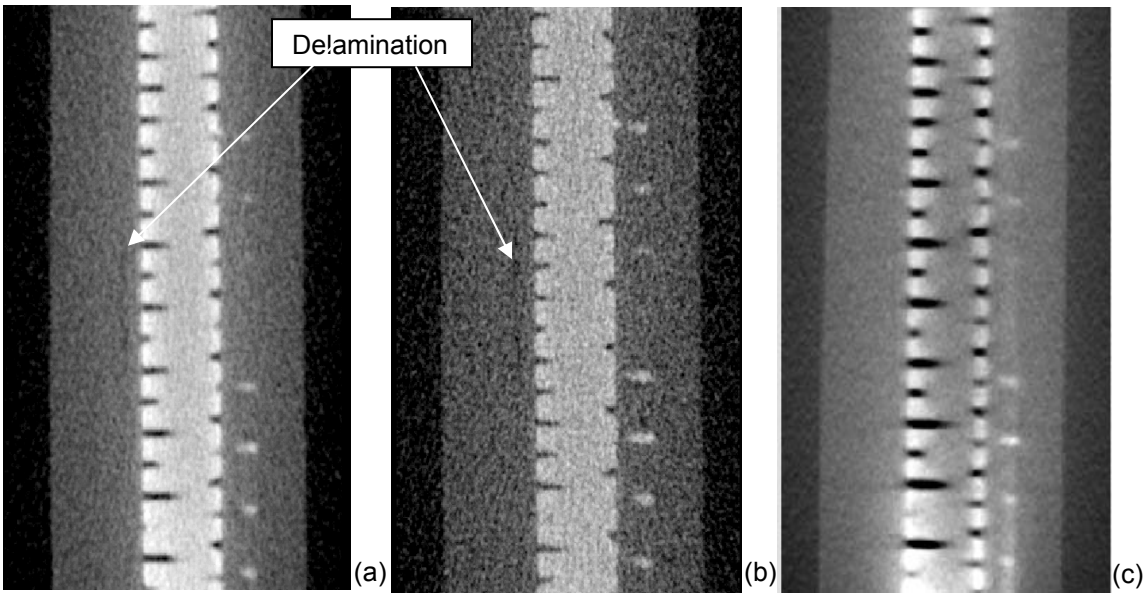

Figure 5.32: Axial cross sectional CT slices through the Comeld™ joint showing a delamination within the CFRP. (a) Dual energy CT slice, (b) conventional CT slice and (c) LE scan CT slice, scale as in Figure 5.1.

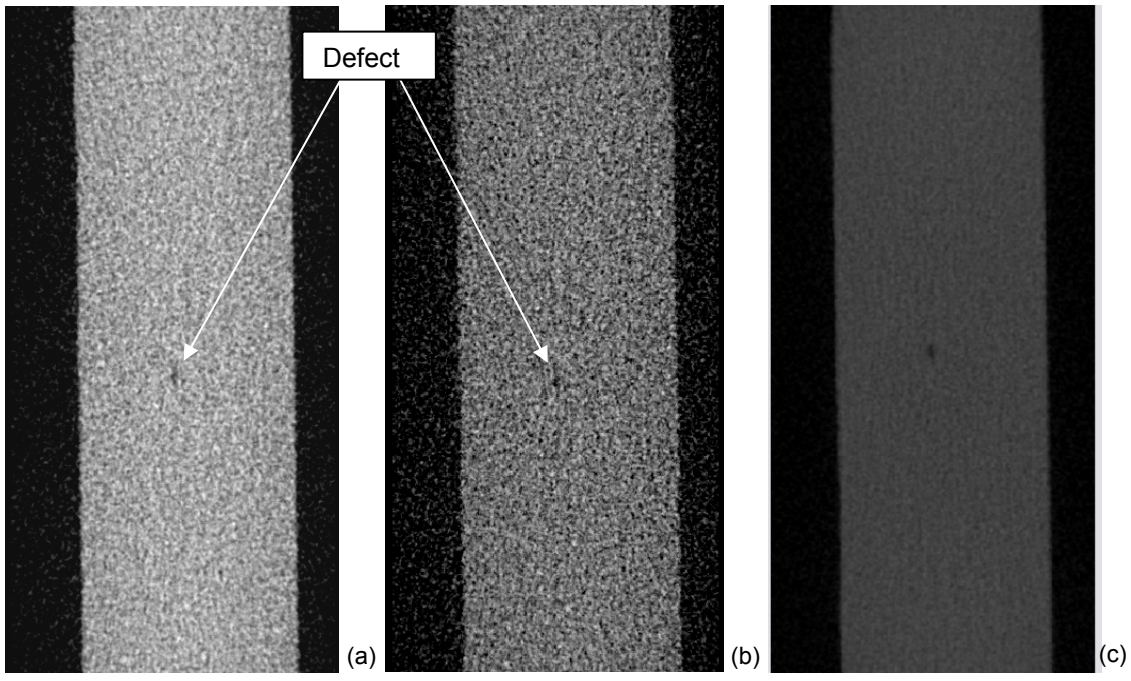

Figure 5.33: Axial cross sectional CT slices through a small discontinuity found within the CFRP section away from the joint itself. (a) Dual energy CT slice, (b) conventional CT slice and (c) LE scan CT slice, scale as in Figure 5.1.

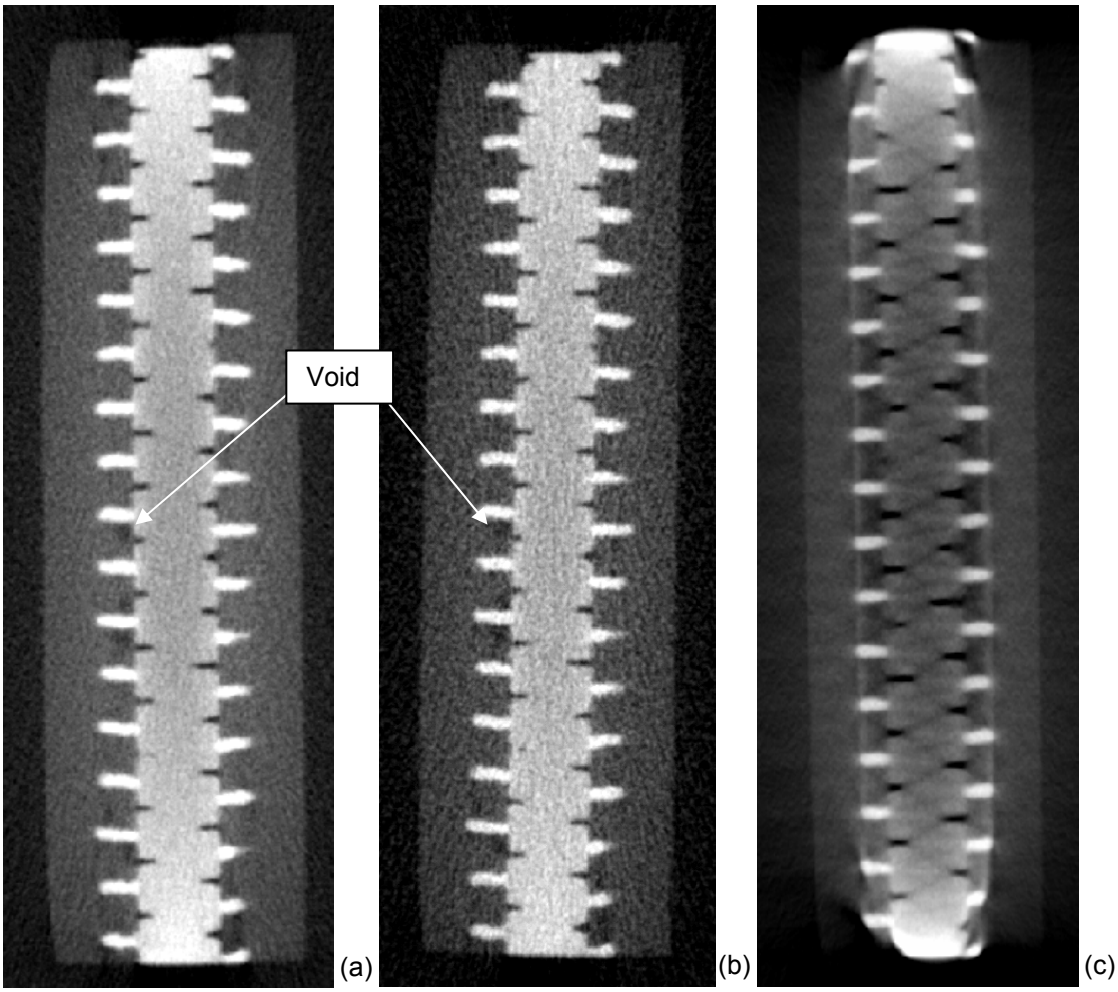

Figure 5.34: Axial cross sectional CT slices through the Comeld™ joint showing defects between the Titanium protrusions within the CFRP. (a) Dual energy CT slice, (b) conventional CT slice and (c) LE scan CT slice (right), scale as in Figure 5.1.

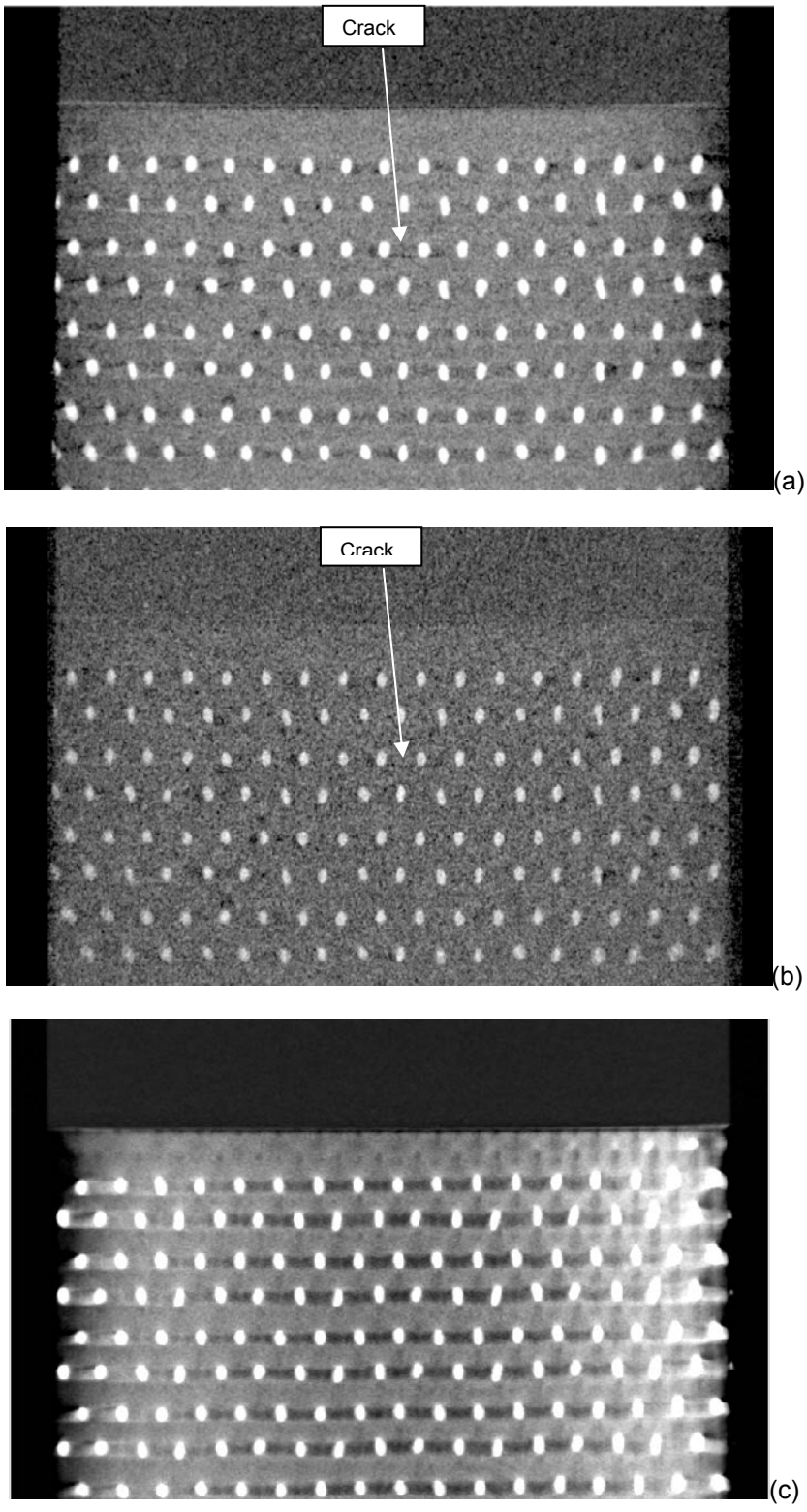

Figure 5.35: Frontal cross sectional CT slice through the Titanium surface and surrounding CFRP. (a) Dual energy CT slice, (b) conventional CT slice and (c) LE scan CT slice, scale as in Figure 5.1.

It is evident from the LE reconstructed CT images, displayed in Figure 5.31(c) and Figure 5.34(c), that although the projection data may have contained optimised low density regions, these regions cannot be reconstructed accurately due to the shading artefacts propagating from the under penetrated high density regions. The only exception to this is found in Figure 5.33(c), showing the LE scan to have increased the contrast between the defect and the low density CFRP. This is simply due to the defect being positioned away from the join nowhere near any high density Titanium.

It is clear the conventional CT reconstruction, that satisfied the intensity condition of ≥10,000 grey levels, has increased image noise affecting its ability to resolve fine details. This is highlighted when comparing a fine crack detected in the CFRP (Figure 5.35). The crack was easily identified in the experimental dual energy reconstruction, Figure 5.35(a), but was very difficult to detect in the conventional scan.

A void was also detected between the CFRP and the Titanium using both the dual energy method and the conventional scan. This void is shown in Figure 5.31 in a sagittal cross sectional slice. Comparing the two slices it is clear that gaining reliable information on the volumetric shape of the void is not possible using the conventional CT reconstruction, whereas an accurate representation of the shape has been provided by the dual energy method. The same applies for a delamination detected in the axial direction of the CFRP (Figure 5.32). The increased energy settings required to fully penetrate the Titanium in the conventional scan have resulted in over exposure and image degradation of the less dense CFRP, making it difficult to diagnose the defect detected.

The beam hardening type artefact mentioned previously is also evident in the dual energy reconstruction of the Comeld™ joint. In general, the beam hardening artefact would be amplified for Comeld™ joints due to the aspect ratio of the component resulting in largely different penetration levels through different angles (Figure 5.34). However this artefact did not significantly affect fine details within the CFRP and still allowed the structure of the Titanium to be accurately reconstructed.

The main drawback of this new method highlighted from both the Comeld™ joint and HVAC results, was the increased beam hardening type artefact within the high density regions. The presence of this artefact means that accurate density measurements cannot be performed. The algorithm causes an increase in this artefact due to the LE scan not requiring full penetration of the high density part. But the removal of this constraint is integral to the experiment because, otherwise, the energy setting could not be optimised

for the low density part. However, it should be noted that this method was never intended as a tool for density measurements but for enhanced defect detection. In addition it has been shown that these problematic areas appear to be offset by the improvement in the detail detectability offered by the optimised projection sets.

5.7 Conclusions

The aim of this work was to improve the detail detectability for CT of multi-density components and more specifically for advanced inspection of Comeld™ joints. This meant implementing a method that allowed a CT reconstruction to take place with different energy settings optimised to the materials present. Dual energy CT was highlighted as a potential method and an approach had to be realised that could provide beneficial results and stretch the optimum dynamic range of detectability - without the hardware and software costs associated with such a specialised system.

The advanced inspection procedure developed in this work permitted a dual energy approach to be implemented on a standard single energy CT system with FDK reconstruction software. The dual energy image processing algorithm allowed extreme regions (under-penetrated and overexposed) within the projection data to be merged with optimised regions without any significant reduction in quality. Therefore, the optimum dynamic range of detectability of the CT acquisition was effectively increased by producing projection data of a multi-density component that resulted in both sufficient penetration of the higher density material without overexposing the low density material.

A validation process was undertaken using known statistical performance measures to qualify the improved results. This was performed on a reference phantom and showed that compared to five conventional CT scans the dual energy technique improved the detail SNR by a minimum of 32% for the low density material. The dual energy technique also resulted in an improvement of 5% for the high density material when compared to the optimal conventional scan. This scan was optimal in the sense that it provided the best compromise in terms of image quality between the two densities. The validation procedure also required a measure of the MTF which showed that no spatial degradation was caused by merging the projection data.

The experimental dual energy method was applied to two different multi-density components and the results showed improved detail detectability within the low density regions and sufficient penetration for the high density region, further validating the

performance measurements. Specifically, the application to the CFRP-Ti ComeId™ joints showed a marked improvement in the detail detectability within the CFRP lay-up when compared to conventional CT results. This advanced inspection procedure has since been implemented by TWI as a design process optimisation tool for ComeId™ joint fabrication due to the improved performance and lack of other suitable NDT techniques that can provide the required sensitivity on such a complex structure.

The main drawback of this new method, as identified in the results, was the increased beam hardening type artefact within the high density regions. The presence of this artefact means that accurate density measurements cannot be performed. The removal of this amplified artefact could be possible with further investigation into improved thresholding techniques and scaling in the algorithm. Improved thresholding could mean full and accurate segregation of the intensity gradient found at the edge of objects within radiographic images. This would remove the inaccurate grey values found at the edges caused by the under penetration in the LE scan. Thus, eliminating the false intensity gradient causing the beam hardening type artefact.

Chapter 6

Conclusions and Further Work

6.1 Conclusions

The research has made important advances and has significantly increased the scope of Fibre-Reinforced-Plastic (FRP) composite structures that can be inspected using industrial cone beam CT. The following section summarises the main outputs of the research and the contributions made.

Chapter 3 developed two data completion methods to overcome the truncation artefacts and the missing data errors associated with Region-of-Interest (ROI) CT inspection of CFRP laminates. The cosine tail method was a simple extension method based on the attenuation found at the truncated edge. The cosine extension provided a simplified assumption to the missing data and a low spatial frequency tail off to zero attenuation. This effectively suppressed the strong 'glowing' truncation artefacts associated with the sharp transition at the truncated edge. But a general error across the ROI still remained due to the simplified approximation of the missing object data. This error did not effect the detectability of defects within the inspection but was considered problematic for applications requiring accurate density measurements. The 'estimation from model' technique was a more sophisticated approach that used prior knowledge of the object to build a model and create a set of projection data to accurately estimate the missing data. This technique suppressed both errors associated with truncated data; the truncation artefacts and the inherent error due to the missing attenuation data. Following validation, the techniques were successfully applied to cone beam projection data and the performance of the reconstruction results was quantified using intensity line profiles. It was evident that both data completion methods produced reconstructions that were virtually indistinguishable from the reconstruction that utilised the full (un-truncated) projection data. This was consistent with the results obtained from the fan beam reconstructions. In addition, no significant difference was seen between the reconstructed model results at the mid-plane and the model results at a large cone angle. This provides evidence that although the model was an imperfect match outside of the mid-plane it did not significantly effect the accuracy of the reconstruction. The ROI techniques developed in this research allow (1) the accurate inspection of regions on objects larger than the Field-of-View (FOV) of the detector and (2) the inspection of regions with high geometric

magnification. The use of such high magnifications is essential for the detection of many defects formed in CFRP panels.

In Chapter 4, the truncated data problem was approached from another angle for extending the CT scanning FOV. A novel technique was developed for industrial cone beam systems that used an asymmetrically positioned detector to effectively nearly double the CT scanning FOV compared to conventional CT. Two data completion methods were investigated and their performance compared. One was based on the cosine extension method described in Chapter 3 and the other utilised ray redundancy properties (for fan beam geometry) to estimate the missing data. In this application the extended data was used for filtration only and was disregarded prior to back-projection. The errors could not be quantitatively compared in the same manner as the ROI techniques due to the unavoidable scaled outputs with the reconstruction software being used. However, extensive lab tests and simulated reconstructions were undertaken and the results were compared both qualitatively and using intensity line profiles. Both techniques produced similarly effective results providing evidence that an accurate reconstruction was possible. In this respect, the cosine extension method was found to be more consistent so it was identified as currently the method to use for offset reconstructions. The techniques were then applied to the inspection of a large FRP Wind Turbine Blade (WTB) over 1.5X larger than the maximum CT scan FOV permitted by the detector. The full width of the WTB was reconstructed which included the projection data that extended beyond the FOV. A large range of defects were detected within the sandwich structure highlighting the inspection capabilities of CT for such complex structures. The main drawback identified from the offset reconstructions was a centrally located shading artefact. Further measures have been identified that may help remove this artefact based on the results in Chapter 3. It should be noted that this shading artefact was not prominent and does not obscure any detail within the image. This would only be problematic for the detection of very small relative density changes in a material.

In Chapter 5, a dual energy approach to CT inspection was investigated to stretch the optimum dynamic range of detectability and improve the SNR for multi density objects. This procedure was applied to CFRP/Titanium lap joints, specially fabricated using the Comeld^{TM} joining technique developed at TWI Ltd. The results from the dual energy technique showed a marked improvement in the detectability of both volumetric and planar defects within the CFRP layup when compared to conventional CT results. These results were then reinforced following a validation procedure showing a significant improvement in the detail SNR. Until this point no suitable NDT technique had been

identified for use with Comeld™ joints due to their complex structure. Therefore, the dual energy procedure has since been implemented by TWI as a design process optimisation tool for Comeld™ joint fabrication. The main drawback of this developmental procedure was the beam hardening type artefacts within the high density material. This artefact meant that accurate density measurements could not be obtained from these regions. However, this artefact did not significantly effect the structure of the object features in any way, meaning that accurate defect detection was still possible. The cause of the artefact was found to be the remaining attenuation data at the edge (following segregation) which resulted in a false intensity gradient. The removal of this artefact is possible with further investigating into improved thresholding and scaling.

6.2 Further Work

In order to further the research presented in this thesis, the aforementioned limitations should be addressed. For ROI CT, two critical areas of future work have emerged. Firstly, it was noted in Chapter 3 that the developed ROI techniques have been focussed solely on the simple geometry of a composite panel. Clearly, this does not cover the full spectrum of desirable inspection subjects. The next logical stage of this research programme would be to investigate ROI and data completion methods for complex geometries and multi-density objects. Both of these areas will present new challenges for the estimation from model technique. From an industrial standpoint, one of the possibilities would be to import a CAD model of the object for inspection. This could open up the technique to any possible object geometry. For cone beam applications it might also be practical to use a different model for each of the tilted fan angles within the cone beam setup. The current method assumes mid-plane geometry for each elevation within the cone. Determining the corresponding tilt angle within the model would improve the accuracy of the estimation at large cone angles, which may be required for more complex test objects. Measures could also be employed to improve the cosine based extension method. For instance, the gradient of the cosine extension at the site of truncation could be better matched with the projection profile using the derivatives of the function at that location. Additionally, the cosine tail length could be modified to correspond with the amount of missing data for each individual projection (instead of the maximum extent). This would increase the accuracy of the resultant sinogram prior to reconstruction.

Secondly, as the work on data completion methods for ROI CT progressed it became evident that the resultant image quality for high aspect ratio composite panels is also affected by the limited effective dynamic range of the detector. A dual energy approach to

CT inspection to overcome this limitation for multi-density objects was investigated in Chapter 5. This method showed an improvement in the SNR and detail detectability, indicating an increase in the optimum dynamic range. Therefore, it is beneficial to extend the work in Chapter 5 and investigate application with high aspect ratio objects. As identified in Chapter 5 the main obstacles that need to be overcome to improve the dual energy technique and extend its scope of application is the thresholding and scaling. Again, if these are performed accurately the two sets of projections data can be effectively merged and mapped to a whole new intensity range, increasing the optimum dynamic range of the inspection without obvious artefacts.

The limitations associated with the cone beam Offset CT technique for extending the CT scanning FOV have been discussed in Chapter 4. To refine the offset technique and improve the accuracy of the reconstructed data it is recommended that the problems encountered with the estimation technique are investigated further. As this technique has the potential to supersede the cosine tailing method in terms of reconstruction accuracy. Specifically, two further measures are recommended for implementation to improve the estimation method and reduce the notable artefacts: (1) Add an interpolation function when estimating the redundant ray paths. This will improve the accuracy of the estimate and help remove the disjointed regions present at the threshold between the measured data and the estimated data. (2) Add a small faded taper (similar to the cosine blend in Chapter 3) to bridge the gap between the measured data and the estimated data. This will suppress the sharp transition at the disjointed regions thus reducing the risk of truncation artefacts.

The main limitation restricting the implementation of offset CT for extending the FOV in many industrial systems is the required detector shift to an asymmetrical position. This is not an option for cabinet systems where the detector is in a fixed stationary position. Therefore, it is of great interest to extend the developed technique for shifting the test object instead of the detector. This requires further investigation to amend the ray redundancy estimation algorithm inline with this geometric setup.

Finally, in order to make full, practical use of the research results, some effort needs to be invested in a more robust implementation of the developed techniques. This may take the form of either stand alone software or as an add-on to commercial reconstruction software.

Publications

Amos, M., Woods, S., Cooper, I. and Withers, P.J. (2010a). An ROI X-ray CT technique for defect characterisation in Carbon-Fibre-Reinforced-Plastic laminates. *Proceedings of the 37th International Conference on Quantitative Non-Destructive Evaluation, QNDE.* San Diego, California, USA. 18th – 23rd July 2010.

Amos, M., Woods, S. and Withers, P.J. (2010b). A Region of Interest X-ray CT technique for defect characterisation in CFRP laminates. *Proceedings of the 7th International Conference on Quality, Reliability and Maintenance, QRM*. University of Wales, Swansea. 19th – 20th April 2010.

Jasiūnienė, E., Raišutis, R., Šliteris, R., Voleišis, S., Vladišauskas, A., Amos, M. and Mitchard, D. (2009). NDT of wind turbine blades using adapted ultrasonic and radiographic techniques. *Journal of the British Institute of Non-Destructive Testing – Insight* 51(9), 65-68.

Amos, M., Rasserkorde, E.M., Pain, D. and Withers, P.J. (2009a). Enhanced computer tomography of multi-density components using a developmental dual energy image processing technique. *Proceedings from the 6th International Conference of the British Institute of Non-Destructive Testing (BINDT - CM/MFPT).* Dublin, Republic of Ireland. 23rd -25th June 2009.

Amos, M., Rasserkorde, E.M., Pain, D. and Withers, P.J. (2009b). Validation of an X-ray Computer Tomography Based Image Processing Technique by Statistical Performance Analysis. *Proceedings of the 36th International Conference on Quantitative Non-Destructive Evaluation, QNDE.* University of Rhode Island, USA. 26th – 31st July 2009.

Mitchard, D. and Amos, M. (2009). Medical scanning technique keeps wind turbines healthy*. Journal for Science, Engineering and Technology in Wales - Advances* **60**, 22-24.

Kallee, S. and Amos, M. (2008). Magnetic Pulse Welding as an Enabler of Light-Weighting in the Automotive Industry. *Proceedings of the 1st Technical Conference on Industrialised Magnetic Pulse Welding and Forming*. Munich, Germany. 3rd July 2008.

References

Abrate, S. (1998). *Impact on Composite Structures*. UK: Cambridge University Press.

Ali, A. M., Melegy, Z., Morsy, M., Megahid, T., Bucherl, A. and Lehmann, E. H. (2004). Image reconstruction techniques using projection data from transmission method. *Annals of Nuclear Energy* **31**, 1415-1428.

American Society for Nondestructive Testing, ASNT. (1991). *Non-destructive Testing Handbook, 2nd Edition: Volume 7, Ultrasonic Testing*. ASNT.

American Standards Institution – ASTM. (2006). ASTM E1695:2006 Standard test method for measurement of computer tomography (CT) system performance.

Anastasio, M A., Zou, Yu., Sidky, E. Y. and Pan, X. (2007). Local cone beam tomography image reconstruction on chords. *Journal of Optical Society of America,* **24**(6), 1569-1579.

Anbarasu, A. (2008). *Characterization of Defects in Fiber Composites Using Terahertz Imaging*. MSc. Georgia Institute of Technology.

Andersen, A. H. and Kak, A. C. (1984). Simultaneous Algebraic Reconstruction Technique (SART): a superior implementation of the ART algorithm. *Ultrasonic Imaging* **6**, 81-94.

Anoop, K. P. and Rajgopal, K. (2009). Image reconstruction with laterally truncated projections in helical cone-beam CT: Linear prediction based projection completion techniques. In: *Computerized Medical Imaging and Graphics,* **33**(4), 283-294.

Arabi, H., Kamali, A. R. and Aghamiri, S. M. (2010). The effect of focal spot size on the spatial resolution of variable resolution X-ray CT scanner. *Iran Journal of Radiation* **8**(1), 37-43.

Badel, E., Letang, J. M., Peix, G. and Babot, D. (2003). Quantitative microtomography: measurement of density distribution in glass wool and local evolution during a one-dimensional compressive load. *Measurement Science and Technology* **14**, 410-420.

Balasubramaniam, K. and Whitney, S. C. (1996). Ultrasonic Through-Transmission Characterization of Thick Fiber-Reinforced Composites. *NDT&E International* **29**, 225-236.

Bartolac, S., Clackdoyle, R., Noo, Frederic., Siewerdsen, J., Moseley, D. and Jaffray, D. (2009). A local shift-variant Fourier model and experimental validation of circular cone-beam computed tomography artefacts. *Journal of Medical Physics* **36**(2), 500-512.

Beutel, J., Kundel, H.L. and Van Metter, V.L. (2000). *Handbook of Medical Imaging, Volume 1*. Bellingham: SPIE Press.

BIR ACTIS. (2008). Offset- *Rotate CT Scanning* [online]. Available from http://www.bio-imaging.com/Rotate-Only_CT_Scanning.asp [Accessed 19 December 2008]

Blakely, B. and Konstantinos, S. (2006). Digital radiography for the inspection of small defects. *BINDT Journal Insight* **48**(2), 22-29.

Boone, J. M. and Seibert, J. A. (1994). A comparison of mono- and poly-energetic X-ray beam performance for radiographic and fluoroscopic imaging. *Journal of Medical Physics* **21**, 1853–1863.

Borum K. K., McGugan M. and Brondsted, P. (2006). Condition monitoring of wind turbine blades. *Proceedings of the 27th Riso International Symposium on Materials science: Polymer composite materials for wind power turbines.* Denmark. 2006.

British Standard Institution – BS EN (2005). BS EN 14784-1:2005 Non-destructive testing – Industrial computed radiography with storage phosphor plates – Part 1: Classification of systems.

Brooks, R. A. and Di Chiro, G. (1976a). Principles of computer assisted tomography (CAT) in radiographic and radioisotropic imaging. *Journal of Physics in Medicine and Biology* **21**, 689–732.

Brooks, R. A. and Di Chiro, G. (1976b). Beam Hardening in X-ray Reconstructive Tomography. *Journal of Physics in Medicine and Biology* **21**(3), 390-398.

Bushberg, J. T., Seibert, J. A., Leidholdt, E. M. and Boone, J. M. (2002). *The Essential Physics of Medical Imaging.* 2nd ed. Lippincott, Williams and Wilkins, USA.

Chia, C. C., Lee, J. R. and Bang, H. J. (2008). Structural health monitoring for a wind turbine system: a review of damage detection methods. *Journal of Measurement, Science and Technology* **19**(12). Available from: http://iopscience.iop.org/0957-0233/19/12/122001/pdf [Accessed 10 December 2009]

Chlewicki, W. (2001). *3D Simultaneous Algebraic Reconstruction Technique for Cone-Beam Projections.* MSc. University of Patras, Greece.

Chotas, H. G., Dobbins, J. T. and Ravin, C. E. (1999). Principles of Digital Radiography with Large-Area, Electronically Readable Detectors: A Review of the Basics. *Journal of Radiology* **210**(3), 595-599.

Cho, S., Yu, L., Pelizzari, C. A. and Pan, X. (2006). Circular Cone-beam Micro-CT for Small Animal Imaging with truncated with Truncated Data. *Proceedings of the IEEE Nuclear Science Symposium and Medical Imaging Conference.* San Diego, USA. 29th October – 4th November 2006.

Choudhry, R. S. and Li, S. (2008). Modelling and Characterization of Impact Damage in Quickstep cured single lap joints. Available from:
http://www.ndt.net/article/v12n02/choudhry.pdf [Accessed 15 October 2009].

Chun, K. I., Cho, M. H., Lee, S. C., Cho, H. M. and Lee, S. Y. (2004). X-ray micro-tomography system for small animal imaging with zoom-in imaging capability. *Journal of Physics in Medicine and Biology* **49**, 3889-3902.

Clackdoyle, R., Noo, F., Guo, J. and Roberts, J. (2004). A Quantitative reconstruction from truncated projections in classical tomography. *IEEE Transaction Nuclear Science*. **51**(5), 2570-2578.

Coenen, V. (2005). A feasibility study of Quickstep processing of an aerospace composite material. *Proceedings of the 26th Sampe-Europe conference*. Paris 2005.

Cohen, G. and Di Bianca, F. (1979). The Use of Contrast-Detail-Dose Evaluation of Image Quality in a CT Scanner*. Journal of Computer Assisted Tomography,* **3**(2), 189-195.

Computerised Information Technology Ltd (CIT). (2008). CR Phantom Specification, [online] Available from: http://www.cituk-online.com/acatalog/CR_Phantom_SpecSheet_13thMarch2010.pdf [Accessed October 2008].

Cormack, A. M. (1963). Representation of a function by its line integrals with some radiological applications. *Journal of Applied Physics* **34**, 2722-2727.

Dainty, J. C. and Shaw, R. (1976). *Image Science: principles, analysis and evaluation of photographic-type imaging processes.* London: Academic Press.

De Man, B., Nuyts, J., Dupont, P., Marchal, G. and Suetens, P. (1999). Metal Streak Artifacts in X- ray Computed Tomography: A Simulation Study. *IEEE. Transactions on Nuclear Science* **46**(3), 691-696.

Dongbo, W., Jian, F., Lei, G. and Ming, J. (2006). Industrial CT imaging method for large objects*. Journal of Beijing University of Aeronautics and Astronautics* **32**(12), 1477-1480.

Dutta, S. S. (2006). *Nondestructive Evaluation of FRP Wrapped Concrete Cylinders using Infrared Thermography and Ground Penetrating Radar.* MSc. Department of Civil and Environmental Engineering, West Virginia University,USA.

Ebert, M. (2001). *Non-ideal projection data in X-ray computed tomography*. PhD. University of Mannheim, Germany.

Eilbert, R. R. and Krug, K. D. (1992). Aspects of image reconstruction in Vivid Technology's dual-energy x-ray system for explosives detection. *Proceedings from SPIE* **1824**, 127–143.

Elbakri, I. A. (2003). *Statistical Reconstruction Algorithms for Polyenergetic X-ray Computed Tomography*. PhD. Electrical Engineering Department, University of Michigan.

Evans, R.D. (1955). *The Atomic Nucleus.* McGraw-Hill Book Company, New York.

Ewert, U., Zscherpel, U. and Osterloh, E. (2003). Unsharpness characteristics of digital detectors for industrial radiographic imaging. [online] Available from: http://www.ndt.net/article/ct2003/v22/v22.htm [Accessed 10 September 2007]

Ewert, U. BAM. (2009). Private communication. BAM Federal Institute for Materials Research and Testing (BAM Headquarters) Unter den Eichen 87, 12205 Berlin, Germany.

Faridani, A., Ritman, E. L. and Smith, K. T. (1992). Local tomography. *SIAM Journal of Applied Mathematics* **52**, 459–484.

Faridani, A., Ritman, E. L. and Smith, K. T. (1992). Examples of local tomography. *SIAM Journal Applied Mathematics* **52**, 1193–1198.

Faridani, A., Buglione, K., Huabsomboon, P., Iancu, O. and McGrath, J. (2001). Introduction to local tomography. In: *Contemporary Mathematics: Radon Transforms and Tomography.* American Mathematical Society.

Faridani, A. and Ritman, E. L. (2000). High-resolution computed tomography from efficient sampling. *Journal of Inverse Problems* **16**(3), 635–650.

Faulkner, K. and Moores, B. M. (1986). Contrast-detail assessment of computed tomography scanners. *Journal of Physics in Medicine and Biology* **31**(9), 993-1003.

Feldkamp, L. A., Davis, L. C. and Kress, J. W. (1984). Practical cone-beam algorithm. *Journal of the Optical Society of America* **1**(6), 612-619.

Finch, D. V. (1985). Cone beam reconstruction with sources on a curve. *SIAM Journal of Applied Mathematics*, 1985, 655-673.

Flisch, A., Wirth, J., Zanini, R., Breitenstein, M., Rudin, A., Wendt, F., Mnich, F. and Golz, R. (1999). Industrial Computed Tomography in Reverse Engineering Applications. *Proceedings from the International Symposium on Computerised Tomography for Industrial Applications and Image Processing in Radiology.* Berlin, Germany. 15th-17th March 1999.

Fu, J. and Lu, H. (2005). Half-scan mode for industrial CT. *Journal of Beijing University of Aeronautics and Astronautics* **31**(9), 966-969.

Fu, J., Lu, H., Li, B., Zhang, L. and Sun, J. (2007). X-CT Imaging method for Large objects using double offset scan mode. *Nuclear instruments and methods in Physics and research: Section A* **572**, 519-523.

Gieske, J. H. and Rumsey, M. A. (1997). Non-Destructive-Evaluation (NDE) of composite/metal bond interface of a wind turbine blade using an acousto-ultrasonic technique. Musial, W. and Berg, D. E. eds. *ASME wind energy symposium*. AIAA/ASME, 249-254.

Gilbert, P. (1972). Iterative methods for the three-dimensional reconstruction of an object from projections. *Journal of Theoretical Biology* **36**, 105-117.

Gordon, R., Bender, R. and Herman, G. T. (1970). Algebraic reconstruction techniques (ART) for three-dimensional electron microscopy and X-ray photography. *Journal of Theoretical Biology* **29**, 471-481.

Goodenough. D. J. and Weaver, K. E. (1981). Introduction to Computed Tomography. In: Ling, C. C., Rogers, C. C. and Morton, R. J, eds. *Computed Tomography in Radiation Therapy.* New York: Raven Press, 121–127.

Graeff, W. and Engelke, E. (1991). Microradiography and microtomography. In: S. Ebashi, M. Koch and E. Rubinstein, eds. *Handbook on synchrotron radiation*, *Volume 4*. Elsevier Science Publishers, 361-405.

Guan, H. and Gordon, R. (1996). Computed tomography using algebraic reconstruction techniques (ARTs) with different projection access schemes: a comparison study under practical situations. *Journal of Physics and Medical Biology* **41**, 1727-1743.

Hasiotis, T., Badogiannis, E. and Tsouvalis, N.G. (2007). Application of Ultrasonic C-Scan Techniques for Tracing Defects in Laminated Composite Materials. *Proceedings of the 4th international conference on NDT.* Chania, Crete-Greece. 11th-14th October 2007.

Hale, S. (2006). Unsupervised Thresholding and Morphological Processing for Automatic Fin Outline Extraction in DARWIN (Digital Analysis and Recognition of Whale Images on a Network), *ACM MemberNet* **5**(2), [online] Available from: http://src.acm.org/subpages/gf_entries_06/ScottHale_src_gf06.pdf [Accessed April 2009]

Hammersberg, P. and Mangard, M. (1998) Correction for beam hardening artefacts in computerized tomography. *Journal of X-ray Science and Technology* **8**, 51-73.

Hammersberg, P., Strenstrom, M., Sandborg, M. M., Matscheko, G. and Alm-Carlsson, G. (1995). A theoretical model for determination of the optimum irradiation conditions for computerised tomography. *BINDT Journal - Insight,* **37**, 978-985.

Hanson, K. M. (1979). Detectability in Computed Tomographic Images. *Journal of Medical Physics,* **6**(5), 441-451.

Hayman, B., Berggreen, A., Shenoi, N., Tsouvalis, N. and Wright, P. (2007). Production Defects and Production Process Modelling for FRP Single Skin and Sandwich Structures. *MARSTRUCT Network of Excellence,* Report No. MAR-W4-3-DNV-04(5), January 2007.

HEDRad. (2008). HEDRad Project Workpackages, [online] Available from: http://www.hedrad.com/project/work_packages.jsp [Accessed: 3 November 2008]

Henden C (2004). Exercise in Computer Vision A Comparison of Thresholding Methods, [online] Available from: http://www.pvv.org/~perchrh/papers/datasyn/paper2/report.pdf [Accessed May 2009]

Herman, G. T. (1980). *Image Reconstruction from Projections: the fundamentals of Computerised Tomography*. New York: Academic Press.

Hexcel Composites (n.d.). *Product Data sheet for HexPly 8552*. [online] Available from: http://www.hexcelcomposites.com [Accessed 9 May 2008].

Hounsfield, G. (1972). *A method of apparatus for examination of a body by radiation such as x-ray or gamma radiation.* US Patent 1283915. British patent 1283915, London. Issued to EMI Ltd.

Hounsfield, G. (1974). *Computerized Tomography comprising laterally shifting detected beams within a rotated fan of radiation.* US Patent 4041315. Issued to EMI Ltd.

Howard, M. (2007). *Structural Diagnostics of CFRP Composite Aircraft Components by Ultrasonic Guided Waves and Built-In Piezoelectric Transducers.* PhD. University of California San Diego.

Hsieh, J., Chao, E., Grekowski, B., Horst, A., McOlash, S. and Myers, T. J. (2004). Novel approach to extend the scanner coverage beyond detector Field-of-view. *Proceedings of the SPIE conference, Medical Imaging 2004: Physics of medical imaging.* San Diego, USA. 14th February 2004.

Hu, H. and Zhang, J. (2009). Exact Weighted-FBP Algorithm for Three-Orthogonal-Circular Scanning Reconstruction. *Sensors* **9**, 4606-4614.

Jasiūnienė, E., Jasiūnienė, E., Raišutis, R., Šliteris, R., Voleišis, S. and Vladišauskas, A., Amos, M. and Mitchard, D. (2009a). NDT of wind turbine blades using adapted ultrasonic

and radiographic techniques. *Journal of the British Institute of Non-Destructive Testing – Insight* **51**(9), 65-68.

Kak, A.K. and Slaney, M. (1988). *Principles of Computerized Tomographic Imaging.* IEEE Press.

Kalender, W. A., Seissler, W., Klotz, E. and Vock, P. (1990). Spiral volumetric CT with single-breathhold technique, continuous transport, and continuous scanner rotation. *Radiology* **176**, 181–3

Kalender, W. A. (2006). X-ray Computer Tomography. *Physics in Medicine and Biology* **51**, 29-43.

Kallee, S. and Amos, M. (2008). Magnetic Pulse Welding as an Enabler of Light-Weighting in the Automotive Industry. *Proceedings of the 1st Technical Conference on Industrialised Magnetic Pulse Welding and Forming*. Munich, Germany. 3rd July 2008.

Katsevich, A. (2002a). Analysis of an exact inversion algorithm for spiral cone-beam CT. *Journal of Physics and Medicine and Biology* **47**, 2583-2597.

Katsevich, A. (2002b). Theoretically exact filtered backprojection type inversion algorithm for spiral CT. *SIAM Journal of Applied Mathematics* **62**(7), 2012-2026.

Ketcham, R. A. and Carlson, W. D. (2001). Acquisition, optimization and interpretation of X-ray computed tomographic imagery: applications to the geosciences. *Computers and Geosciences* **27**(4), 381-400.

Kroger, C., Bartle, C. and West, J. (2005). Non-invasive measurement of wool and meat properties. *BINDT Journal Insight* **47**(1), 25-28.

Kropas-Hughes, C.V. and Trent Neel, S. (2000). *ASNT - Basics of CT* [online].
Available from:
http://www.asnt.org/publications/Materialseval/basics/may00basics/may00basics.htm
[Accessed 10 March 2006]

Kyrieleis, A., Titaremko, V., Ibison, M., Connelley. Withers, P. J. (2010). Region-of-interest tomography using filtered backprojection assessing practical limits. *Journal of Microscopy Online publication* DOI : 10.1111/j.1365-2818.2010.03408.x.

Lading, L., McGugan. M., Sendrup, P. Rheinländer, J. and Rusborg, J. (2002). *Fundamentals for remote structural health monitoring of wind turbine blades - a preproject* ANNEX B Risø-R-1341(EN) Report Risø National Laboratory, Denmark 2002.

Lewitt, R. M. and Bates, R. H. T. (1978). Image Reconstruction from Projections: III: Projection Completion Methods (theory). *Optik – International Journal for Light and Electron Optics* **50**(3), 189-204; IV: Projection Completion Methods (Computational Examples), *Optik – International Journal for Light and Electron Optics* **50**(4), 269-278.

Leng, S., Zhuang, T., Nett, B. E. and Chen, G. H. (2005). Exact fan-beam image reconstruction algorithm for truncated projection data acquired from an asymmetric half-size detector. *Journal of Physics in Medicine and Biology* **50,** 1805-1820.

Li, B. and Hsieh, J. (2007). Comparison of Reconstruction Algorithms to Extend CT Reconstruction Field-of-View. *Proceedings of the IEEE Nuclear Science Symposium and Medical Imaging Conference.* Honolulu, Hawaii, USA. 7th October – 3rd November 2007.

Li, L., Chen, Z., Kang, K. and Zhang, Li. (2007). Investigation of exact truncated data image reconstruction algorithm on parallel PI-line segments in fan beam scans. *Tsinghua Journal of Science and Technology* **12**(3), 337-344.

Lloyd, P. A. (1989). Ultrasonic system for imaging delaminations in composite materials. *Ultrasonics* **27**(1), 8-18.

Macdonald, S. (2004). *The Application of X-ray Micro-Tomography to study Damage Development and Deformation in Ti/SiC composites and Al foams.* PhD. Materials Department, University of Manchester.

Macovski, A. (1983). *Medical Imaging Systems*. Englewood Cliffs: Prentice Hall.

Mangard, M. (2000). *Optimised performance of industrial high resolution computerized tomography.* Linkoping Studies in Science and Technology, Dissertation No. 659. University of Linkoping, Sweden.

Mangard, M. and Hammersberg, P. (1998). Optimised detail detectability in computerised tomography. *Journal of X-ray Science and Technology* **8**(1), 51-73.

Milanova M [n.d.]. Grey Level Enhancement ppt [online] Available from: http://cpsc.ualr.edu/milanova/image_processing/Week2/Grey_Level_mapping.ppt [Accessed April 2009]

Mueller, K., Yagel, R. and Wheller, J. J. (1999a). Anti-Aliased 3D Cone-Beam Reconstruction Of Low-Contrast Objects With Algebraic Methods. *IEEE Transactions on Medical Imaging* **18**(6), 519-537.

Mueller, K., Yagel, R. and Wheller, J. J. (1999b). Fast implementations of algebraic methods for the 3D reconstruction from cone-beam data. *IEEE Transactions on Medical Imaging* **18**(6), 538-547.

Mueller, K. (1998). *Fast and Accurate Three Dimensional Reconstrcution from Cone Beam Projection Data using Algebraic Methods.* PhD. Ohio State University, USA.

Muralidhar, C. and George, S. (1999). Evaluation of defects in composite components using Computed Tomography. *Proceedings of the 9th international symposium on nondestructive characterization of materials.* Sydney, Australia. 28th June –2nd July 1999.

Nacereddine, N., Hamami, M., Tridi, M. and Oucief, N. (2005). Non-Parametric Histogram-Based Thresholding Methods for Weld Defect Detection in Radiography. *Proceedings from the World Academy of Science, Engineering and Technology* [online] 9th November 2005. Available from: http://www.waset.ac.nz/journals/waset/v9/v9-39.pdf [Accessed May 2009]

Nassi, M., Brody, W. R., Medoff, B. P. and Macovski, A. (1982). Iterative Reconstruction-Reprojection: An Algorithm for Limited Data Cardiac-Computed Tomography. *IEEE Transaction on Biomedical Engineering* **29**(5), 333-341.

Netsch, T., Rose, G. and Schomberg, H. (2008). *Cone Beam CT Apparatus using Truncated Projections and a previously acquired 3D CT image*. US Patent No. US 7,440,535 B2.

Noo, F., Clackdoyle, R. and Pack, J. D. (2004). A two step Hilbert transform method for 2D image reconstruction. *Physics in Medicine and Biology* **49**, 3902-3922.

Nosach, Y. (2006). *CTDI and ELP measurements in Estonian Tomography Cabinets.* MSc. Faculty of Physics and Chemistry, University of Tartu, Estonia.

Ohnesorge, B., Flohr, T., Schwarz, K., Heiken, J. P. and Bae, K. T. (2000). Efficient correction for CT image artifacts caused by objects extending outside the scan field of view. *Journal of Medical Physics* **27**(1), 39-46.

Oster, R. (1999). Computed Tomography as a Non-destructive Test Method for Fiber Main Rotor Blades in Development, Series and Maintenance. [online] Available from: http://www.ndt.net/article/v04n07/bb67_4/bb67_4.htm

Pan, Y., Whitaker, R., Cheryauka, A., Ferguson D. (2009). Feasibility of GPU-assisted iterative image reconstruction for mobile C-arm CT. *Proceedings from SPIE* **7258**, 72585J.

Parker, D. L. (1982). Optimal short scan convolution reconstruction for fan-beam CT. *Journal of Medical Physics* **9**(2), 254-257.

Paul, T. and Zhenhui, H. (2008). Advanced NDT with high resolution Computed Tomography. *Proceedings from the 17th World Conference on Nondestructive Testing*. Shanghai, China. 25th-28th October 2008.

Petersilka, M., Bruder, H., Krauss, B., Stierstorfer, K. and Flohr, T. G. (2008). Technical principles of dual source CT. *European Journal of Radiology* **68**(3), 362-368.

Radon, J. (1917). Ber. Sachsischen Akad. Wiss., 69, 262-277. Translation: Radon, J. and Parks, P.C (translator) (1986). On the Determination of functions from their integral values along certain manifolds. *IEEE Transactions in Medical Imaging* **5**(4), 170-176.

Raišutis, R., Jasiūnienė, E., Šliteris, R. and Vladišauskas, A. (2008). *The review of non-destructive testing techniques suitable for inspection of the wind turbine blades. Ultrasound*. ISSN1392-2114. Kaunas: Technologija. **63**(1), 26-30.

Ramamurthi, K. and Prince, J. L. (2003). Region of Interest Cone Beam Tomography with Prior CT Data. *Proceedings of the IEEE 37th Asilomar Conference on Signals, Systems & Computers.* California, USA. 9th-12th November 2003.

Ramsey, A. (2008*). Advanced CT training booklet*. X-Tek Systems Ltd, August 2008.

Ramsey, A. (2009). Private communication. Metris X-tek Ltd, Enterprise Way, Tring, Herts, HP23 4JX, 2009.

Rao, M.R. (2007). *Review of Non-Destructive Evaluation Techniques for FRP Composite Structural Components.* MSc. College of Engineering and Mineral Resources at West Virginia University.

Ravishankar, C., Hoffmann, K. R., Rudin, S. and Bednarek, D. R., (2005). Artifact reduction in truncated CT using sinogram completion. In: J.M. Fitzpatrick, J.M. Reinhardt, eds. *Medical Imaging 2005: Image Processing. Proceedings of the SPIE* **5747**, 2110-2117.

Rebuffel, V. and Dinten, J. M. (2007). X-ray Imaging - Dual-energy X-ray imaging: benefits and limits. *BINDT Journal – Insight* **49**(10), October 2007.

Richardson, M.O.W. and Wisheart, M.J. (1996). Review of low-velocity velocity impact properties of composite materials. *Applied Science and Manufacturing* **27A** (12), 1123-1131.

Ridler, T. W. and Calvard, S. (1978). Picture thresholding using an iterative selection method. *IEEE Transactions on System, Man and Cybernetics* SMC-**8**, 630-632.

Robb, R. and Ritman, E. L. (1979). High speed synchronous volume computed tomography of the heart. Radiology **133**, 655–61.

Rowe, T., Carlson, W. D., Ketcham, R. A. and Colbert, M. W. (2003). Applications of high resolution X-ray CT in petrology, meteorites and paleontology. In: Mees, F., Swennen, R., Van Geet, M. and Jacobs, P. (eds) 2003. *Applications of X-ray Computed Tomography in the Geosciences*. Geological Society, London, Special Publications, 7-22.

Rosenfeld, A. and Kak, A.C. (1982). *Digital Picture Processing, 2nd Edition.* New York: Academic Press.

Russ, J. C. (2007). *The Image Processing Handbook.* 5th Edition. CRC Press.

Sahoo, P. K., Soltani, S. and Wong, A. K. C. (1982). A Survey of Thresholding Techniques. *Computer Vision, Graphics, and Image Processing* **41**(1). 233-260.

Sawicka, B. D., Murphy, J. G., Taheri, F. and Kanary, L. E. (1991). γ-ray CT examination of density gradients in slip cast ceramics: correlation with stress distribution. *Nuclear Instruments and methods in Physics Research* **B69**, 365-369.

Schillinger, B., Kardjilov, N. and Kuba, A. (2004). Region of interest tomography of bigger than detector samples. *Journal of Applied Radiation and Isotopes* **61**, 561-565.

Schneberk, D.J., Azevedo, S. G., Martz, H. E. and Skeate, M. F. (1990). Sources of error in industrial tomographic reconstruction. *ASNT - Materials Evaluation* **48**, 609-617.

Schretter, C. (2010). *Correction of Non-Periodic Motion in Computed Tomography*. PhD. Otto-Von-Guericke University, Magdeburg, Germany.

Sekihara, K., Kohno, H. and Yamamoto, S. (1982). Theoretical prediction of X-ray CT image quality using contrast-detail diagrams. *IEEE Transactions on Nuclear Science* NS-**29**, 2115-2121.

Sezgin, M. and Sankur, B. (2004). Survey over image thresholding techniques and quantitative performance evaluation. *Journal of Electronic Imaging* **13**(1), 146–165.

Shapiro, L. and Stockman, G. (2002). *Computer Vision*. Prentice Hall.

Shepard, R. R. (2006) Practical Radiography – Digital Radiography and CMOS Flat Panel Detectors. *ASNT – The NDT Technician* **5**(2).

Shepp, L. A. and Logan, B. F. (1974). The Fourier reconstruction of a head phantom. *IEEE Transactions on Nuclear Science* **21**, 21-43.

Shepp, L. A. and Stein, J. A. (1976). *Simulated Reconstruction Artefacts in Computerized X-Ray Tomography.* Baltimore, USA: University Park Press.

Simon, M., Sauerwein, C. and Tiseanu, I. (2004). Extended 3D CT method for the inspection of large components. *Proceedings from the 16th World Conference on Nondestructive Testing.* Montreal, Canada. 30th August – 3rd September 2004.

Sivers, E. A. (1995). Use of multiple CT scans to accommodate large objects and stretch dynamic range of detectability. *Nuclear Instruments and Methods in Physics Research, Section B* **99**, 761-764.

Smith, F. C., Buxton, A. L., Dance, B. G. I. and Spence, C. L. (2007). *Developments in Manufacturing and Characterisation of Comeld™ Joints.* The Welding Institute (TWI) Ltd Research Report.

Sonka, M., Hlavac, V. and Boyle, R. (1998). *Image Processing, Analysis, and Machine Vision.* 2nd Edition. Thompson Engineering.

Sourbelle, K., Kachelriess, M., and Kalender, W. A. (2005). Reconstruction from truncated projections in CT using adaptive detruncation. *Journal of European Radiology* **15**(5), 1008-1014.

Stenström, M. (2000). *Computerised Microtomography: Non Non-invasive imaging and analysis of biological samples, with special reference to monitoring development of osteoporosis in small animals*. Ph.D. Linköping University, Sweden.

Stone, D. E. W. and Clarke, B. (1975). Ultrasonic attenuation as a measure of void content in carbon-fibre reinforced plastics. *NDT & E International* **8**(3), 137-145.

Stone, D. E. W. and Clarke, B. (1987). Non-destructive evaluation of composite structures - an overview. *Proceedings of the 6th International Conference on Composite Materials.* London. July, 1987.

Subbarao, P. M. V., Munshi, P. and Muralidhar, K. (1997). Performance if iterative tomographic algorithms applied to non-destructive evaluation with limited data. *NDT&E International* **30**(6), 359-370.

Tam, K. C. (1988). Reducing the fan-beam scanning angular range. *Journal of Physics in Medicine and Biology* **33**(8), 955-967.

Tasto, M. and Schomerg, H. (1978). Object Reconstruction from Projections and Some Nonlinear Extensions. In: C. S. Chen, eds. *Pattern Recognition and Signal Processing*. Sijthoff and Noordhoft, Amsterdam, 485-503.

Tuy, H. K. (1983). An inversion formula for cone beam reconstruction. *Journal of Applied Mathematics* **43**, 546-552.

Van de Casteele, V., Van Dyck, D. and Sijbers, E. R. (2004). The effect of beam hardening on resolution in X-ray micro-tomography. *Journal of X-ray Science and Technology* **12**, 53-57.

Ved, H. R. (2002). *A Computer-Based Cascaded Modeling and Experimental Approach to the Physical Characterization of a Clinical Full-Field Digital Mammography System.* MSc. Worcester Polytechnic Institute, USA. Available from: http://www.wpi.edu/Pubs/ETD/Available/etd-0920102-144012

Wang, G., Snyder, D. and Vannier, M. (1996). Local computed tomography via iterative deblurring. *Journal of Scanning Probe Microscopy* **18**, 582–588.

Wang, G. and Yu, H. (2008). An outlook on x-ray CT research and development. *Journal of Medical Physics* **35**(3), 1051-1062.

Wang, G., Snyder, D. and Vannier, M. (1996). Local computed tomography via iterative deblurring. *Journal of Scanning Probe Microscopy* **18**, 582–588.

Weska, J. S. (1978). A survey of threshold selection techniques. *Journal of Computer Graphics and Image Processing* **7**(2), 259-265.

Weigert, J., Bertram, M., Wulff, J., Schafer, D., Weese, J., Netsch, T., Schomberg, H. and Rose, G. (2004). 3D ROI imaging for cone-beam computer tomography. *International Congress Series* **1268**, 7-12.

Wong, B.S. (n.d.). *Non-destructive testing of fiber reinforced composites and honeycomb structures.* Dissertation. Nanyang Technological University, Singapore. Available from: http://www3.ntu.edu.sg/mae/Research/.../Sensors/NDT/dmms-paper.PDF [Accessed 10 October 2009]

X-tek Group. (2006). *HMX CT System Details* [online]
Available from: http://www.xtekxray.com/products/systemdetail_hmx.html [Accessed December 2006]

Yaffe, M. J. and Rowlands, J. A. (1997). X-ray detectors for digital radiography. *Physics in Medicine and Biology* **42**, 1-39.

Yan, X. H. and Leahy, R. M. (1991). Derivation and Analysis of a Filtered Backprojection Algorithm for Cone Beam Projection Data. *IEEE Transactions on Medical Imaging* **10** (3), 462-472.

Ying, Z., Naidu, R., Guilbert, K., Schafer, D., and Crawford, C. R. (2007). Dual Energy Volumetric Xray Tomographic Sensor for Luggage Screening. *Proceedings from IEEE Sensors Applications Symposium,* San Diego, California, 6th-8th February, 2007.

Yu, L., Zou, Y., Sidky, E. Y., Pelizzari, C. A., Munro, P. and Pan, X. (2006). Region of Interest Reconstruction From Truncated Data in Circular Cone-Beam CT. *IEEE Transactions on Medical Imaging* **25**(7), 869-881.

Zamyatin, A. A. and Nakanishi, S. (2007). Extension of reconstruction field-of-view and truncation correction using sinogram decomposition. *Journal of Medical Physics* **34**(5), 1593-1604.

Zeng, L., Zou, X., Wang, J., Wang, P. and Hunziker, P. R. (2007). Improved Scanning and Reconstruction of Large Objects by Cone-Beam Industrial Computed Tomography. *Proceedings of the signal and image processing SIP*. Honolulu, Hawaii, USA. 20-27th August 2007.

Zou, Y. and Pan, X. (2004a). Exact image reconstruction on PI-lines from minimum data in helical cone-beam CT. *Journal of Physics in Medicine and Biology* **49**, 941-959.

Zou, Y. and Pan, X. (2004b). Image reconstruction on PI-lines by use of filtered backprojection in helical cone-beam CT. *Journal of Physics in Medicine and Biology* **49**, 2717-2731.

Zhu, L., Yoon, S. and Fahrig. R. (2007). A Short-Scan Reconstruction for Cone-Beam CT using Shift-Invariant FBP and Equal Weighting. *Journal of Medical Physics* **34**(11), 4422–4438.

Appendix A

Cosine Extension Length

Chapter 4 provides details of an experiment to determine the optimum tail length of the cosine extension with respect to different levels of truncated data (see section 4.6.1.1). The truncations levels were set at 20% increments from 10% to 70%. The graphical outputs for all four of the investigated truncation levels are displayed in Figures A1 to A4. Each output shows the mean error as a function of tail length and zero-padding length.

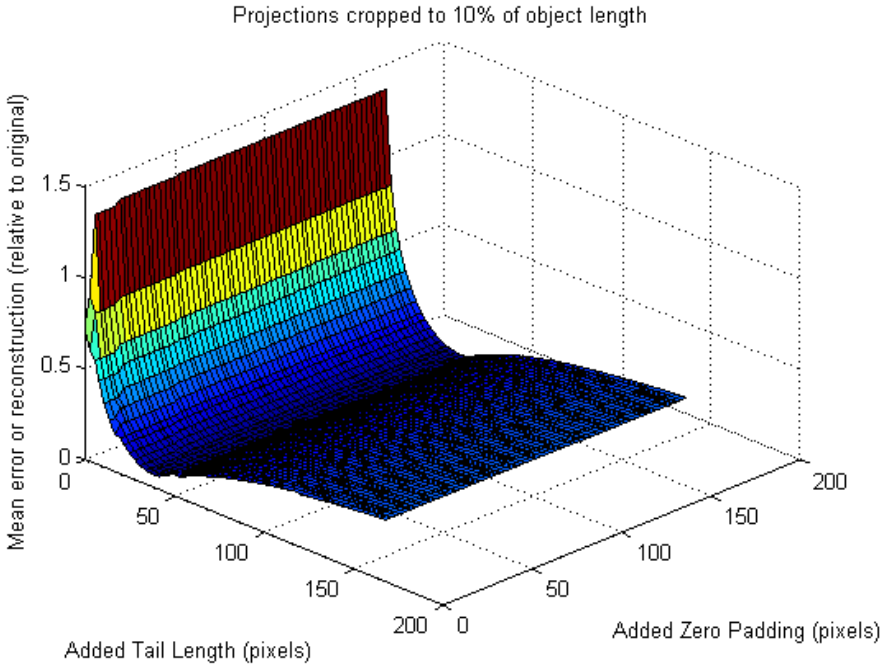

Figure A1: Reconstructed mean error results for 10% truncation with cosine tail and zero padded extension**.**

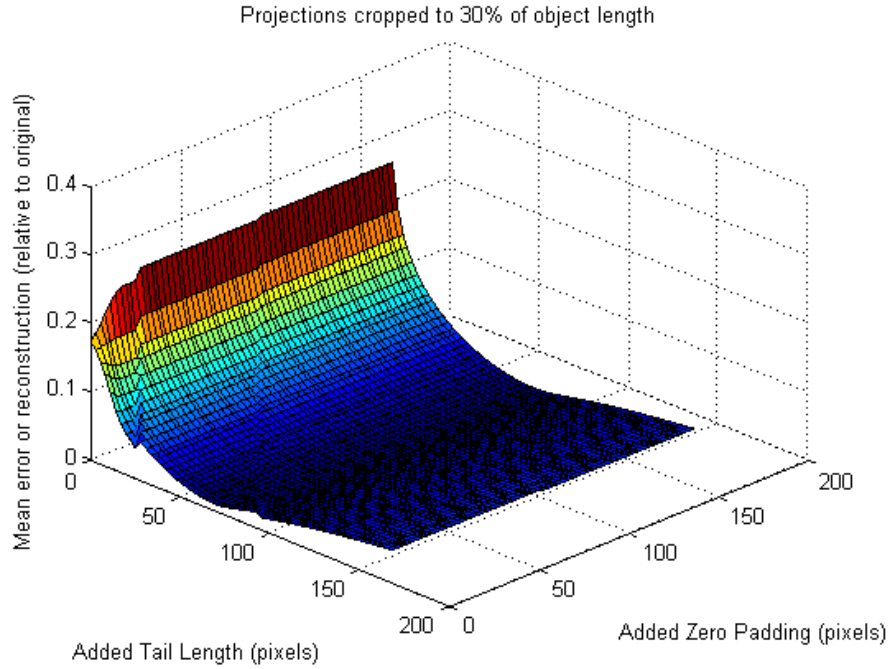

Figure A2: Reconstructed mean error results for 30% truncation with cosine tail and zero padded extension.

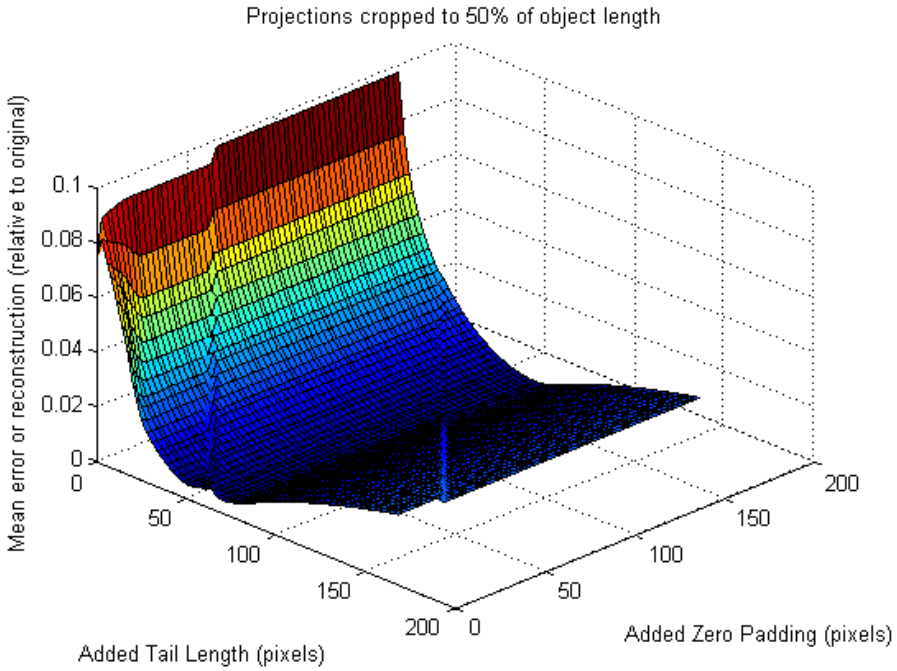

Figure A3: Reconstructed mean error results for 50% truncation with cosine tail and zero padded extension.

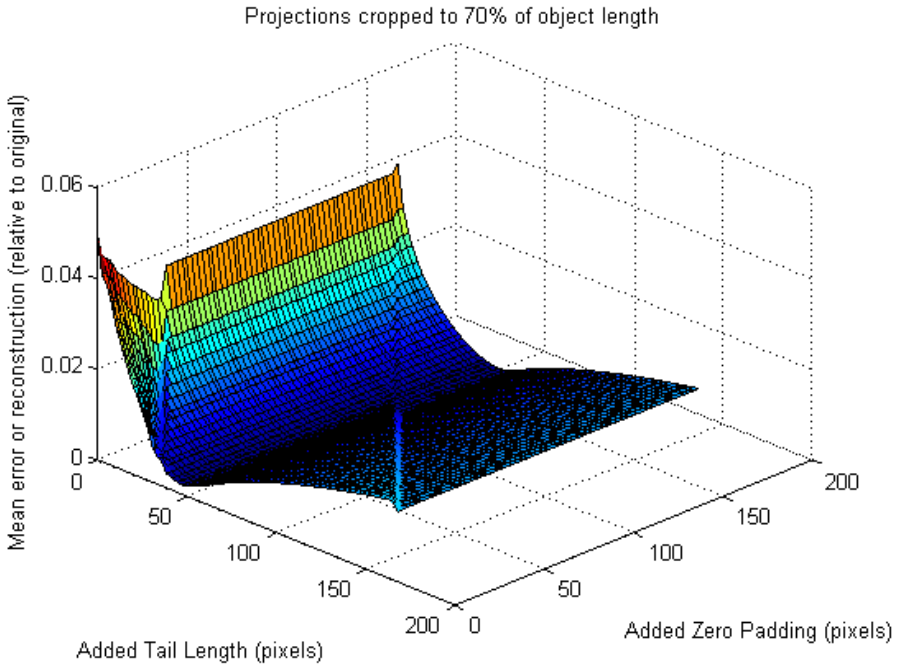

Figure A4: Reconstructed mean error results for 70% truncation with cosine tail and zero padded extension.